Ultracold Fermi gases : next generation experiment and impurity physics

Ragheed Alhyder

PSL UNIVERSITÉ PARIS

THÈSE DE DOCTORAT
DE L'UNIVERSITÉ PSL

Préparée à l'École Normale Supérieure

Ultracold Fermi gases: Next generation experiment and impurity physics

Soutenue par
Ragheed ALHYDER
Le 4 décembre 2020

École doctorale n°564
Physique en Ile-de-France

Spécialité
Physique quantique

Composition du jury :

Denis BOIRON Professeur des Universités Université Paris-Saclay	*Président*
Mathilde HUGBART Chargée de recherche au CNRS Université Côte d'Azur	*Rapporteur*
Michael URBAN Chargé de recherche CNRS Université Paris-Saclay	*Rapporteur*
Markus HOLZMANN Directeur de Recherche au CNRS. Université Grenoble Alpes	*Examinateur*
Georg BRUUN Professeur assistant Université d'Aarhus	*Examinateur*
Christophe SALOMON Directeur de Recherche au CNRS École Normale Supérieure	*Directeur de thèse*
Frédéric CHEVY Professeur École Normale Supérieure	*invité*
Xavier LEYRONAS Maître de Conférences Sorbonne Université	*Invité*

1794 ENS ÉCOLE NORMALE SUPÉRIEURE

PSL UNIVERSITÉ PARIS

Contents

Introduction **4**

1 Ultracold Fermi gases: From few to many **10**
1.1 Two-body problem . . . 10
1.1.1 Universal dynamics and scaling . . . 11
1.1.2 Scattering theory . . . 12
1.1.3 Feshbach resonances . . . 16
1.2 Three-body problem . . . 21
1.2.1 Two-channels model for the three identical bosons . . . 22
1.2.2 Efimov trimers properties and domain . . . 24
1.2.3 Experimental evidence of Efimov physics . . . 26
1.3 Ultra-cold Fermi gases . . . 26
1.3.1 Non-interacting Fermi gas . . . 27
1.3.2 Interacting Fermi gas and the BEC-BCS crossover . . . 29
1.4 Impurity physics . . . 31
1.4.1 Bose polaron . . . 32
1.4.2 Fermi polaron . . . 34
1.4.3 Impurity in a two-component Fermi gas . . . 36

I The Lithium Experiment **39**

2 A new generation Lithium machine **41**
2.1 Overview of the setup . . . 41
2.2 The ^{6}Li atom . . . 42
2.2.1 Level structure . . . 42
2.2.2 Feshbach resonances of ^{6}Li . . . 44
2.3 Vacuum setup . . . 45
2.4 671 nm Laser setup . . . 45
2.5 Absorption imaging . . . 46
2.6 Magneto-optical trap . . . 48
2.6.1 Atomic beam . . . 48
2.6.2 Zeeman Slower . . . 49
2.6.3 Magneto-optical trap (MOT) and compressed MOT . . . 51
2.7 Optical molasses . . . 53
2.7.1 D_2 molasses . . . 53

2.7.2 D_1 gray molasses and sub-Doppler cooling 54
2.8 Optical dipole traps 57
2.8.1 Optical transport 59
2.8.2 Cross dipole trap 63
2.9 Evaporative cooling 65
2.9.1 Working principle 66
2.9.2 State populations 67
2.9.3 Magnetic fields in the science cell 69
2.9.4 Cooling to degeneracy 70

3 From superfluidity to single atom imaging 73
3.1 Thermodynamics of ultracold Fermi gases 73
3.1.1 Equation of state 74
3.2 Quantitative analysis of density distributions 75
3.2.1 Non-interacting Fermi gas in a harmonic trap 76
3.2.2 Unitary Fermi gas 77
3.2.3 Implementation and results 80
3.3 Searching fermionic superfluidity 81
3.3.1 Spin imbalanced systems 81
3.4 Single-atom imaging of fermions 83
3.5 Prospects of the ^{6}Li machine 84

II Impurity immersed in a two-component Fermi sea 85

4 Impurity in an interacting medium: a perturbative approach 87
4.1 Perturbative expansion of the impurity energy 88
4.1.1 Preliminary calculation 88
4.1.2 Asymptotic behavior 89
4.2 Green's function for an interacting system 90
4.2.1 Green's function: Definition 90
4.2.2 Time evolution operator 91
4.2.3 Adiabatic activation 92
4.2.4 Vacuum polarisation 93
4.3 Perturbative expansion using Green's function formalism 94
4.3.1 The impurity's Green function 94
4.3.2 Expectation value of the density-density correlation function . 96
4.3.3 Ladder approximation 100

5 Impurity immersed in a double non-interacting Fermi sea 105
5.1 Variational ansatz of the full problem 107
5.2 Polaron sector 108
5.3 Efimov sector 110
5.3.1 Trimer in vacuum 110
5.3.2 Cooper-like trimer 110
5.3.3 General case 112
5.4 Polaron-trimeron coupling 112

5.5 Dimer energy 116

Conclusion **119**

A Calculation of the first contribution to the diagrammatic expansion **121**

B Ladder diagram terms **124**

C Derivation of polaron-trimeron coupled equations **127**

D Numercial solution of Skornyakov-Ter-Martirosyan's equation **131**

E Cooper-like trimer for different values of $k_F R_e$ **136**

Acknowledgements **162**

Introduction

Fermi gases are ubiquitous systems in nature. In the standard model of elementary particles, fermions make up all elementary constituents of matter, and quantum degenerate gases of fermions are found in many systems in nature, most importantly electrons in solids and nuclear matter. Identical fermions are forbidden from occupying the same quantum state, which is the statement of the famous Pauli exclusion principle [1]. This fundamental principle contributes to keeping objects like neutron stars, solids and atoms from collapsing under gravitational and electrostatic forces and therefore in the stability of matter as we know it [2, 3].

The study of quantum matter has a long history and has given rise to many applications. Since the discovery of superconductivity by Heike Kamerlingh Onnes [4], it has been subject to intense research for over a century and has enabled several technological breakthroughs. In the following decades, many phenomena in quantum many-body systems caused by the strong quantum correlations were discovered. A few examples of unexpected properties are the superfluidity of bosonic liquid ^{4}He under a critical temperature of 2.2 mK, highlighted in the experiments of Kapitza [5] and Allen and Misener [6] in 1938, and the superfluidity of fermionic liquid ^{3}He by Osheroff in 1972 [7]. The non-classical properties of this new phase of matter were mind-boggling for researchers. Indeed, no physicist had yet seen a fluid that would creep out of the recipient it contains, or presents zero viscosity when being stirred.
Another example is 2D electron gases, a field that has strongly impacted fundamental and applied research in solid state physics. These systems are found in field effect transistors, now an indispensable component for modern technological industries, and the quantum Hall effect was discovered in these systems [8]. This effect has become the playground for a plethora of new research in areas ranging from solid state physics to cold atoms.

Quantum simulation and ultracold atoms

Over the past few decades, ultracold atoms have offered new ways of studying quantum systems by providing a flexible and tunable platform for realizing and simulating various quantum models [9]. This goes along Richard Feynman's vision of using hand-built devices to accurately simulate quantum systems and to probe their properties [10].
The idea of cooling dilute gases with radiation pressure is over four decades old [11]. This has come to fruition with the laser cooling of trapped ions [12, 13] and the cooling and trapping of neutral atoms [14, 15]. More advanced laser cooling techniques such as polarisation-gradient cooling [16, 17], velocity-selective coherent population

trapping [18], and sideband cooling in harmonic traps [19] have been employed to overcome the Doppler and recoil limits of laser cooling.
However, these techniques were not sufficient to bring atomic gases to quantum degeneracy. It was the development of magnetic traps for neutral atoms [20] together with evaporative cooling techniques [21, 22] that have enabled the observation of Bose-Einstein condensation (BEC) in ultracold atomic clouds [23–25]. Far-detuned optical traps [26] and evaporative cooling therein [27] offer added flexibility and are now commonly used in cold atoms experiments.
Since the observation of BEC, the field has undergone rapid developments. The phase coherence in BECs was investigated via matter-wave interference [28], and exploited to realize atom lasers [29–31].
In weakly interacting Bose gases, the excitations described by Bogoliubov theory have been investigated [32–35]. Other excitations such as vortices [36–38] and solitons [39, 40] were also observed.
All the aforementioned results can be described in a mean-field context characterized by weakly interacting quasiparticles. In the case of bosons for instance, for interactions much larger than the kinetic energy, one must depart from this picture, but therefore gains access to many rich phenomena with strong correlations between the atoms. This regime can be reached by using Feshbach resonances [41, 42] that modify the low energy scattering properties [43, 44].
Interactions modify in a non-trivial way the basic properties of the system. Strongly interacting Bose gases are still an active subject of research experimentally [45–49] and theoretically [50–55].

Ultracold Fermi gases

The adaptation of the cooling methods to fermionic alkali atoms led to the production of a degenerate Fermi gas via evaporative cooling of spin mixtures [56]. Since then, several Fermi gas experiments have been constructed, where mixtures of different spin components or atomic species were cooled together [57–61]. While accessing the strongly correlated regime using Feshbach resonances with bosons was challenging due to strong three-body recombination, Pauli blocking turned out to stabilise Fermi gases against these losses [62], making Feshbach resonances useful to probe a wide range of interactions.
Hence, interacting ultracold Fermi gases have attracted great theoretical interest [63]. Strongly interacting Fermi gases were soon realised [64, 65], as well as condensates of molecules created from fermion pairs [66–68], Cooper pairs in the attractive BCS regime [69], and superfluids of fermions [70, 71].
Fermi gas experiments have traditionally employed the alkali atoms ^{6}Li and ^{40}K. Later, other fermionic isotopes have been successfully cooled to quantum degeneracy, namely the alkaline earth atoms ^{87}Sr [72, 73], or alkaline earth-like lanthanides such as ^{161}Dy [74], ^{171}Yb and ^{173}Yb [75, 76] with large magnetic dipole moments. This variety of complex level structure together with the ability to tailor interaction potential as needed enable access to many applications and phenomena.

Out of many examples is the Fermi-Hubbard model [77] which represents a key concept in condensed matter physics providing crucial insights into electronic and

magnetic properties of materials. It describes an ensemble of fermions trapped in a periodic potential, within the tight binding approximation. With cold atoms quantum simulators, it became possible to experimentally study the model in a pristine, isolated environment with full control of all Hubbard parameters [78–80]. The advent of quantum gas microscopes for fermionic atoms [81–85], with their single-lattice site resolution, has made possible precision measurement of the equation of state [86, 87] and of spin and charge correlations [88–90] of the two-dimensional Fermi-Hubbard model. More recently, quantum transport measurements were possible using this kind of quantum microscope [91].
Moreover, the realization of Bose [92] and Fermi [93] gases in box-like potentials, making possible the study of these systems in a homogeneous potential, opens new possibilities to study their properties and for instance look for new exotic phases such as the FFLO (Fulde, Ferrell, Larkin, Ovchinnikov) phase [94, 95] characterized by Cooper pairs with non-zero momentum and spatial modulation of the order parameter. This phase can be observed in a two-component Fermi gas with imbalanced spin populations (partially polarized Fermi gas).

Impurity in a many-body quantum system

The limiting case of a partially polarized Fermi gas is a Fermi sea with exactly one impurity. While being one of the simplest problem in many-body physics, the physics of an impurity immersed in a many-body ensemble remains non-trivial and very rich.
One of the most fundamental examples is the polaron problem introduced by Landau in 1933 in a one-page long article [96] describing an electron moving in a metal. In 1948, Landau and Pekar further described the properties of this system [97]. The term *polaron* was introduced to describe the quasiparticle arising from the interactions between the conduction electron and its induced polarization in a polarized ionic crystal. The polaron problem later has taken the form of the study of the interactions between a charge carrier (electron, hole) and the phonons of an ionic crystal, described by a field-theoretical Hamiltonian derived by Fröhlich in 1954 [98]. This quasiparticle has different properties compared to the original impurity: in particular, it is characterized by an effective mass, a binding energy and a renormalized response to an external electric or magnetic field.
The presence of impurities in a many-body system can affect its macroscopic properties in a spectacular way. One important example is the Kondo effect [99] initially suggested to explain the remarkable observation in the properties of gold where at low temperature, the resistivity of the material decreases with temperature until it reaches a minimum at a non-zero temperature and then rises as the temperature is lowered even further [100].
Kondo suggested that this behavior was due to the presence of magnetic impurities in the metallic sample, and the possibility of a scattering process in which the internal spin state of the impurity and a scattered electron are exchanged. This problem, known as the Kondo problem, was revisited in 1975 by Wilson [101], and led to one of the first theoretical developments of renormalization groups. Wilson used a non-perturbative renormalization group method based upon the seminal work of

Anderson on localized magnetic impurities immersed in a Fermi sea [102].

Even the presence of one impurity can drastically modify the properties of the many- body background as introduced in the historical problem of Anderson's orthogonality catastrophe (AOC) in 1967 [103]. Anderson showed that when a motionless impurity is introduced in a Fermi sea, the ground state of this now perturbed system becomes orthogonal to the ground state without the impurity, with an overlap between the two states that decreases with the size of the system with a power law. In cold atoms, an impurity immersed in a Fermi sea can be dressed by the background fermions and forms a polaronic quasiparticle, but due to AOC, a motionless impurity or a heavy impurity will not form a quasiparticle.
An example of a measurement involving this effect is by exciting a *massive* ^{41}K impurity immersed in a Fermi sea of ^{6}Li and measuring its decoherence over time [104,105]. The overlap between the many-body wave function of the Fermi sea before and after a transition in the impurity vanishes as the scattering strength is increased which signals the onset of AOC.
Other impurity problems can be found also in high energy physics, for instance in neutron stars where protonic impurities can interact with the background neutron superfluid [106, 107], or in quantum chromodynamics where the Polyakov loop describes the properties of a test color charge in a hot medium of gluons [108].

An impurity in a system can also be used to probe experimentally the properties of the background system itself, acting as a test particle. For instance, measuring the number of bosonic impurity atoms in a Fermi-Bose mixture provides an insight on the nature of the fermionic background since the loss rate differs as a function of interaction strength between fermions [109]. Moreover, the observation of the crossover from few-body physics to many-body physics of a fermionic ensemble was studied via the measurement of the interaction energy between an impurity and a few indistinguishable fermions [110] in a quasi one-dimensional trap. This study revealed a rapid convergence to the many-body limit of a single impurity in a Fermi sea, showing that the many-body description is already valid for a very low number of fermions in the background.

Experiments in our group on Bose-Fermi mixtures brought focus on impurity physics in two and three component Fermi and Bose gases [109, 111, 112]. The Bose component can be treated as a single impurity moving inside the fermionic superfluid.
In addition to the inelastic decay measurement due to three-body recombination mentioned earlier, the measurement of critical velocity of the Fermi superfluid (the velocity above which dissipation arises) was done by using the oscillation velocity of the Bose component and it matched perfectly models where it is considered as a single impurity immersed in a double Fermi sea [112].
These measurements motivated a theoretical effort to try to understand the properties of an impurity immersed in a two-component Fermi sea, where the phase diagram now includes a trimer sector where Efimov physics comes into play [113–117].

Outline of the thesis

This manuscript covers the essential parts of my work over the last three years in the Ultracold Fermi Gases group at Laboratoire Kastler Brossel (LKB) and at Laboratoire de Physique de l'École Normale Supérieure. It is divided into two main parts, an experimental part that describes the experimental apparatus I participated in constructing over the first two years of my work and a theoretical part regarding two theoretical projects.
It is divided into five chapters structured as follows:

- Chapter 1 presents a general introduction to the physics of ultracold Fermi gases. An overview of two-body collisions is presented within the framework of conventional scattering theory together with a two-channel model treatment of Feshbach resonances. The two-channel model is extended afterwards to include effects of three-body physics and by using this treatment Efimov physics for three-identical bosons is presented, this encapsulates the most important of Efimov's trimers. Then a brief overview of ultracold Fermi gases and the BEC-BCS crossover is presented. The chapter ends with an introduction about the $N+1$ problem which branches off to a description of the Bose and Fermi polarons.

- Chapter 2 presents a description of the experimental apparatus constructed in Lithium 3 team over the last four years. All implemented methods of cooling and trapping are described along with their underlying principle and a brief historical account. It includes a description of the optical setup that is used to create one arm of the crossed dipole trap, which represents one of my contributions to the apparatus.

- Chapter 3 presents the creation and characterization of a strongly interacting Fermi superfluid. An overview of the thermometry method that was used is provided. A measurement of the so-called "superfluid plateau" in a spin imbalanced Fermi gas is presented. Date presented in this chapter were achieved by the team in the course of my theory project.

- Chapter 4 presents a quick overview of a calculation already performed in the group which deals with the energy of an impurity immersed in a fermionic superfluid bath. We show that in order for the problem to be normalized the density-density correlator of the bath fermions has to present a divergent term for large impurity momenta. Afterwards a diagrammatic calculation is presented which takes apart the different interactions in detail in the BCS limit of the fermionic bath and identifies one divergent term.

- Chapter 5 presents a variational calculation describing the phase diagram of an impurity immersed in a non-interacting Fermi sea. The calculation shows the impurity starting off in a polaronic state in the weak attractive impurity-fermion interaction limit and then just after the unitary regime a sharp transition into a trimer state takes place before the interaction strength can support

a two-body bound state, and that is where a smooth transition between the trimer and dimer state happens. This work was reported in [118].

Chapter 1

Ultracold Fermi gases: From few to many

Ultra-cold Fermi gases provide a versatile and simple ensemble to study quantum many-body physics. At the heart of their appeal is the large tunability of their interactions, which allows the system to simulate the physics of a plethora of systems found in nature and then to probe their properties.
The study of interactions in ultracold gases is essential to explain fully their properties. In this chapter an overview of basic concepts related to the study of Fermi gases is presented. We start by the simplest form of interaction, the two-body interaction. Though the simplest, its physics offers many ways to control a system of interacting fermions. The basic tool to control interactions is by exploiting Feshbach resonances, their fundamental properties are derived using a two-channels model.
In addition, the three-body problem or the Efimov problem, which is of particular importance to the scope of this thesis, is presented. Introduced, to stay coherent, using a similar two-channels model.
Then, an overview of ultra-cold Fermi gases and their properties is presented. The non-interacting limit will be discussed and then interactions and their effects of the system will be introduced.
Finally, the physics of an impurity will be presented with a variational calculation which captures the essential properties of such a system. The case of an impurity immersed in a Bose-Einstein condensate, or the Bose polaron, will be discussed along with the case of an impurity immersed in an ultracold Fermi gas, the Fermi polaron. The different theoretical tools will prove useful to understand in more generality the problems this thesis tries to address in the following chapters.

1.1 Two-body problem

In order to describe the dynamics of an interacting many-body system, one has to start by the most basic form of interaction, the interaction between two particles.
In this section an overview of the most important results for the scattering of two particles is presented, together with a detailed treatment of the Feshbach resonances phenomena which will introduce the principles behind the two-channel model which

will be used extensively in Chapter 5.

1.1.1 Universal dynamics and scaling

In general, each atom is typically localized to a volume corresponding to its thermal DeBroglie wavelength [119]:

$$\lambda_{dB} = \sqrt{\frac{2\pi\hbar^2}{mk_BT}} \tag{1.1}$$

where m is the mass of the atom, k_B is the Boltzmann constant and T is the temperature of the gas. For instance, $\lambda_{dB} \approx 0.7\,\mu$m for a ^{6}Li atom in a cloud at a temperature of $1\,\mu$K ($\simeq 10^4\,a_0$ with a_0 the Bohr radius).
Another significant length scale is the interatomic distance $n^{-1/3}$ which is typically on the order of $0.5 - 1\,\mu$m for a dilute gas in a cooling and trapping experiment.
These last two parameters define the degree of degeneracy of the system. Indeed, when particles are localized over a volume λ_{dB}^3 and this volume approaches that defined by the density n (assuming particles are distributed uniformly) i.e. $n\lambda_{dB}^3 \approx 1$ the system is said to reach quantum degeneracy where it can not be described fully by a classical model anymore and quantum effects have to be taken into account in describing the system.

Particles interact via binary interactions where the two particles approach each other, collide then leave the interaction region with different momenta. If the sum of their kinetic energies is conserved the collision is called elastic and if not it is called inelastic.
When the two particles approach each other, they induce dipoles in one another resulting in the well-known isotropic Van der Waals interaction with a general form $V_{vdw}(r) \sim -C_6/r^6$ in the case of neutral atoms in their ground state, where C_6 is a constant which includes the induced polarizability.
The distance between the two particles is limited by the Van der Waals hard core repulsion radius which results from the electronic exchange potential term, and it is on the order of a few Angstroms for alkali metal atoms.
Another relevant length scale is the range of the interaction, also called the Van der Waals length :

$$r_{\text{vdw}} = \left(\frac{m^* C_6}{8\hbar^2}\right)^{1/4} \tag{1.2}$$

where m^* is the reduced mass of the two-body problem. For $r > r_{\text{vdw}}$ only the asymptotic behavior of the potential matters in the scattering process. This length scale is typically on the order of a few nanometers for alkali atoms ($r_{\text{vdw}} \simeq 50a_0$).

Dilute gases at low temperatures treated in the frame of cold atom experiments and theory are in the configuration $n^{-1/3}, \lambda_{dB} > r_{\text{vdw}}$. This translates to the fact that during the scattering process the detailed structure of the interaction potential is not resolved by the interacting particle. This allows a unique freedom in choosing a convenient interaction model to describe the system theoretically.
In addition, a simplification comes from the fact that atoms with a non-zero value for

the orbital angular momentum quantum number ℓ encounter a centrifugal barrier $V_{rot} = \hbar^2\ell(\ell+1)/(2m^*r^2)$ when they approach each other. The range of this barrier exceeds that of the interatomic potential and so atoms with $\ell \neq 0$ do not interact with each other at low temperature in a first order approximation. This leaves only collisions between atoms with $\ell = 0$, the so-called s-wave collisions.

For spin polarized fermions, s-wave collisions are not allowed by Pauli blocking. That means for fermions we need two atomic species or atoms from the same species in different internal states for the scattering process to take place and for interactions to occur in a Fermi gas.

The Van der Waals interaction potential, when modified by the attractive force present between particles due to the induced dipoles, supports several bound states as will be detailed. The number of vibrational states is determined by r_{vdw}. By exploiting these bound states in singlet potentials (potentials between particles with $S = 0$ where S is the total spin of the particles) we can tune the relative energy of the scattered atoms to have a bound state near the threshold of the potential and to increase the interaction strength, this phenomena is known as a Feshbach resonance and will be studied further in this chapter.

1.1.2 Scattering theory

In this section we will present the basic theoretical tools in studying the scattering of two atoms. For a more detailed discussion refer to [120]. Starting with the Schrödinger equation for two atoms in the center of mass frame:

$$\hat{H}\psi(\boldsymbol{r}) = \left[-\frac{\hbar^2}{2m^*}\nabla^2 + V(\boldsymbol{r})\right]\psi(\boldsymbol{r}) = E\,\psi(\boldsymbol{r}) \tag{1.3}$$

where $V(\boldsymbol{r})$ is the interaction potential with an interaction range r_{vdw} and E is the energy of the eigenstate of the hamiltonian.
The solutions with $E < 0$ describe the bound states allowed by the potential V, while the solutions with $E > 0$ describe scattering states with a wavefunction that can be described by the following equation in the asymptotic limit beyond the reach of the potential:

$$\psi(\boldsymbol{r}) \underset{r\gg r_{\text{vdw}}}{\simeq} \frac{1}{(2\pi)^{3/2}}\left(e^{i\boldsymbol{k}.\boldsymbol{r}} + f(\boldsymbol{k}', \boldsymbol{k})\frac{e^{ikr}}{r}\right) \tag{1.4}$$

where $\boldsymbol{k}' = k\boldsymbol{r}/r$ the wave vector of the same length as k but on the axis of $\boldsymbol{r}$, and where we defined with the dimension of a length the scattering amplitude:

$$f(\boldsymbol{k}', \boldsymbol{k}) = -\frac{m^*}{2\pi\hbar^2}\langle \boldsymbol{k}'|\hat{V}|\psi\rangle \tag{1.5}$$

where $|\boldsymbol{k}'\rangle$ denotes a plane wave state with momentum $\boldsymbol{k}'$ with normalization $\langle \boldsymbol{k}|\boldsymbol{k}'\rangle = \delta(\boldsymbol{k}' - \boldsymbol{k})$. We see from the previous description that at a large distance from the scatterer $r \gg r_{\text{rdw}}$, the wavefunction consists of a plane wave plus an expanding scattered spherical wave that vanishes at very large distances from the scatterer.

A detector at one point in space would measure the square of the sum of these two waves at that point. The probability of a particle to be scattered in the direction

of the scatterer within a solid angle $\Theta = (\theta, \phi)$ is called the differential cross section and can be expressed in terms of the scattering amplitude as follows:

$$\frac{d\sigma}{d\Theta} = |f(\boldsymbol{k}', \boldsymbol{k})|^2 \tag{1.6}$$

By integrating the differential cross section over all directions we get the total cross section which gives the fraction of particles which are scattered and is a measure of the overall probability of a scattering process to take place.

Scattering amplitude basic relations and low energy limit with contact potential

We present briefly the derivation of the most relevant formulas in the low energy limit which will be used extensively throughout this manuscript.
We can write naively the solution of Eq. (1.3) as follows:

$$|\psi\rangle = |\phi\rangle + \frac{1}{E - \hat{H}_0 + i\epsilon}\hat{V}|\psi\rangle \tag{1.7}$$

where $|\phi\rangle$ is the solution to the homogeneous noninteracting problem, ϵ is a small positive parameter to avoid a singularity corresponding to the solution of the non-interacting problem. The limit $\epsilon \to 0^+$ is taken at the end of the calculation and $\hat{H}_0$ is the noninteracting part of the hamiltonian $\hat{H}$. This equation is known as the Lippmann-Schwinger equation and its projection on the position space results in Eq. (1.4) far from the scatterer.

By replacing $|\psi\rangle$ in the right hand side by $|\phi\rangle$ we get the first Born approximation which accounts for the effect of the first scattering process on the incoming particle, and as long as the interaction is weak this approximation remains valid. However, in order to characterize the system for any interaction strength we need to go beyond the first term.
We can do that by inserting the expression of $|\psi\rangle$ in the right hand side iteratively in what is called the Born expansion and by writing the energy as E_0 the energy of the incoming particle leading to:

$$|\psi\rangle = |\phi\rangle + \frac{1}{E_0 - \hat{H}_0 + i\epsilon}\hat{T}|\phi\rangle \tag{1.8}$$

where

$$\hat{T} = \hat{V} + \hat{V}\frac{1}{E_0 - \hat{H}_0 + i\epsilon}\hat{V} + \hat{V}\frac{1}{E_0 - \hat{H}_0 + i\epsilon}\hat{V}\frac{1}{E_0 - \hat{H}_0 + i\epsilon}\hat{V} + \dots \tag{1.9}$$

is the $\hat{T}$ operator describing the physical scattering process.
It is related to the full scattering amplitude which describes the amplitude of the scattered wavefunction after a number of scattering processes undergone by the scattered particle. Similarly to Eq. (1.5) which described the scattering amplitude after one scattering process, we can apply iteratively Eq. (1.9) so that we can write Eq. (1.5) as:

$$f(\boldsymbol{k}', \boldsymbol{k}) = -\frac{m^*}{2\pi\hbar^2}\langle \boldsymbol{k}'|\hat{T}|\boldsymbol{k}\rangle$$

We also define the low energy limit of the full scattering amplitude for the incoming particle as minus the scattering length a:

$$\lim_{k\to 0} f(\boldsymbol{k}', \boldsymbol{k}) = -a \tag{1.10}$$

This parameter describes the strength of the interaction and at low energy its value is the only parameter needed to describe the interaction.
The T operator can be written in the form of a self-consistent equation called the Dyson equation:

$$\hat{T} = \hat{V} + \hat{V} G_0 \hat{T} \tag{1.11}$$

where $G_0 = (E_0 - \hat{H}_0 + i\epsilon)^{-1}$ is the resolvent.

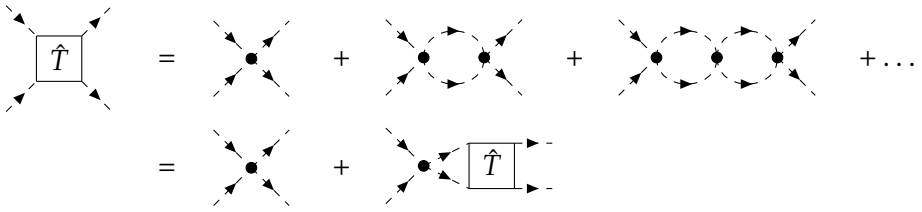

(1.12)

In equation Eq. (1.12) a diagrammatic representation of the Born expansion and the subsequent resummation in the Dyson equation is shown with the two-body interaction g_0 represented by the black disk and the dashed lines representing the propagators of the scattered particles.
In the Born approximation, only the first term is used to describe the two-body interaction, in other words, we take $\hat{T}_{\text{Born}} \simeq \hat{V}$.

Case of zero-range potential

As explained earlier, in dilute systems at low temperatures, scattered particles are not sensitive to the details of the scattering potential. This allows a certain degree of liberty in modeling the potential in a theoretical description of the system. A commonly used potential is simply a contact potential, also known as the zero-range potential:

$$V(\boldsymbol{r}) = g_0\, \delta(\boldsymbol{r}) \tag{1.13}$$

where g_0 is the bare coupling constant indicating the strength of the two body scattering process.
We calculate the scattering amplitude in the Born approximation from equation Eq. (1.5) in the low energy limit:

$$a_1 = \frac{m^*}{2\pi\hbar^2} g_0 \tag{1.14}$$

where a_1 is the scattering length of the single two-body scattering process. However, in order to calculate the true scattering length a we have to include the full scattering amplitude.
Indeed, usually when writing a hamiltonian, the interaction term describes a single scattering process between two particles. Meaning that g_0 is the coupling constant which appears as a coefficient of the interaction term. However, in order to study physical observables, a relation to the physical coupling constant that describes the

whole scattering process has to be established.
This is done by projecting Eq. (1.11) on plane wave states and inserting completeness relations when necessary to get:

$$\langle \boldsymbol{k}|\hat{T}|\boldsymbol{k}\rangle = \frac{g_0}{1 - g_0 \sum_{\boldsymbol{q}} \frac{1}{E_{\boldsymbol{k}} - E_{\boldsymbol{q}} + i\epsilon}} \tag{1.15}$$

where $E_{\boldsymbol{q}} = \hbar^2 q^2/(2m^*)$ is the energy of the scattered particle. We used the vector sum notation $\sum_{\boldsymbol{q}} = \int d^3\boldsymbol{q}/(2\pi)^3$ and $d^3\boldsymbol{q} = d\phi\, d\theta \sin(\theta)\, dq\, q^2$.
By taking the low energy limit of the incoming particle $k \to 0$ and by inserting the scattering amplitude from Eq. (1.5) and Eq. (1.10) we can write:

$$\frac{1}{g_0} = \frac{1}{g} - \sum_{|\boldsymbol{q}|<k_c} \frac{2m^*}{q^2} \tag{1.16}$$

where we introduced the physical coupling constant $g = 2\pi\hbar^2 a/m^*$ for two particles scattering off a potential.
The sum in the second term diverges, in order to remedy this we introduced the UV-cutoff in momentum space (k_c). This comes as a natural outcome of choosing a zero-range potential, and it is related to the inverse of the effective range of the potential. In the case of an infinite-range potential, $k_c \to 0$ and $g = g_0$, which is reflective of the fact that in the case of a mean-field approximation of the system, we consider all particles interacting equally with all other particles, mimicking the infinite ranged potential picture.
Furthermore, when k_c increases, the sum in Eq. (1.16) starts dominating which gives a small and negative g_0. This is reminiscent from the fact that a zero-range approximation is only possible with attractive potentials [121], since repulsive ones need always to keep a finite range. Also, when k_c increases, the range of the potential decreases which means a weaker interaction and smaller g_0.

As for the scattering amplitude $f(k)$, since the interaction potential is isotropic the scattering amplitude depends only on the amplitude of the momentum of incoming particle, we can calculate it from Eq. (1.15), by injecting the expression of g_0 from Eq. (1.16) we find:

$$\begin{aligned} f(k) &= -\frac{m^*}{2\pi\hbar^2} \frac{1}{\frac{1}{g} - \sum_{q<k_c} \left(\frac{1}{E_{\boldsymbol{k}} - E_{\boldsymbol{q}} + i\epsilon} + \frac{1}{E_{\boldsymbol{q}}}\right)} \\ &= -\frac{m^*}{2\pi\hbar^2} \frac{1}{\frac{1}{g} + im^*k/(2\pi\hbar^2)} = \frac{-1}{a^{-1} + ik} \end{aligned} \tag{1.17}$$

where the sum in the denominator is calculated using residues theorem by integrating over the upper half of the complex plane.
To summarize, in order to get this result, we tuned the coupling constant g resulting from the zero-range potential approximation in a way to recover the two-body scattering length a. Furthermore, we see clearly in the last equation that to describe the scattering of two particles in the low energy limit, only one parameter is required

which is the scattering length a.
This constitutes the principle of universality in describing cold atoms systems we talked about earlier in the chapter. To describe two-body interactions only one parameter is required and this goes back to the fact that particles do not resolve the details of the interaction potential and therefore any model which recovers the behavior of the particle's wavefunction far from the scatterer is sufficient.
We also note in the expression of f that the only length scale that appears is the scattering length, which is not surprising since we chose a zero-range potential, characterized by a single coupling constant. In the next section we will see that this is not the case in a finite-ranged potential where its range appears as a coefficient for the second order expansion of $1/f$.

1.1.3 Feshbach resonances

Feshbach resonances have hugely helped popularizing the use of cold atoms systems to model physical phenomena. Their versatility, once the positions of the resonances are known, and them needing no more than an external bias field, made their use in experiments essential. With this powerful tool, interactions can be tuned at will helping us simulate many types of interesting dynamics and hamiltonians and probe their properties.
In the previous discussion the main relevant details of a single two-body interaction at low temperature were introduced. In this picture, atoms enter and leave the interaction region elastically with the sum of their momenta and energies unchanged in what is called scattering into an *open channel*.
However, when taking into account the internal state of the atom, two interacting atoms could scatter into an intermediate bound state, provided the scattering length is positive $a > 0$, that is embedded within the continuum of open channel scattering states. This state usually lies in an energetically unaccessible potential with different internal quantum numbers. The potential could support bound states trapping the atoms before they scatter back out of the scattering region with or without excess energy. This is usually called scattering into a *closed channel*.
Using selective tuning of internal states via an external factor e.g. a magnetic field, one can shift the energy of a closed channel potential close to the open channel threshold, increasing the probability of scattering atoms to change their internal state and to scatter into the closed bound state. In such case, a bound-state resonance is embedded in the scattered states continuum of the open channel. This mechanism is called *Feshbach resonance* in nuclear physics [41] and in atomic physics *Fano resonance* [122]. In molecular physics these resonances give rise to the inverse process of a molecule in an excited state *predissociating* into an open channel [123]. For an extensive review on the subject refer to [42].
Taking for example the scattering of two ^{6}Li atoms [124], the interaction takes the form of a linear combination of singlet and triplet molecular potentials depending on the internal states of the scattered atoms. If the atoms approach each other in the open channel with their unpaired electrons antiparallel and an antisymmetric wavefunction ($\boldsymbol{S} = \boldsymbol{S}_1 + \boldsymbol{S}_2 = 0$) the potential is called a singlet potential, whereas if the spins are parallel ($\boldsymbol{S} = 1$) the potential is a triplet potential (referring to the energy

triple degeneracy of this state in a two spin configuration). In Fig.1.1 the singlet and triplet potentials for ^{6}Li are shown.

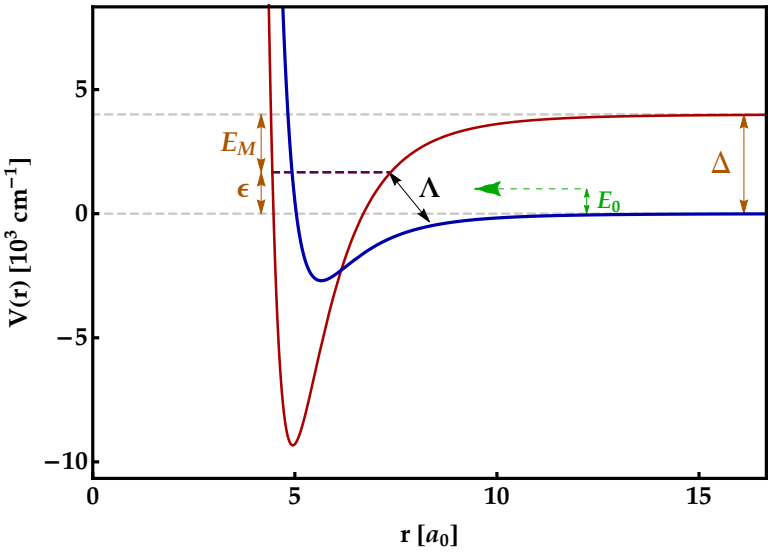

Figure 1.1: Closed and open channel potentials close to a Feshbach resonance. Two atoms in their center of mass frame approach each other with a scattering potential represented by the triplet potential (blue) with an energy E_0 on the order of $h \times 10\,\text{kHz}$. The drawing is not up to scale. A magnetic field is used to shift only the triplet potential by an amount Δ since it does not couple to the total zero spin singlet potential (red). When a bound state E_M in the deep singlet potential is tuned to match to the singlet potential continuum threshold ($\epsilon = 0$) atoms could scatter into the bound state which increases significantly the scattering strength. We also note the coupling constant between the open and closed channel which will be used shortly.

Since $\boldsymbol{S} = 0$ for a singlet potential, an external magnetic field has no effect on its energy, while it shifts linearly the triplet potential (in the case where $m_S \neq 0$). The singlet potential is not accessible for open channel atoms since their energy E_0 is much smaller than the energy barrier. However, applying the magnetic field shifts the energy of the collision state to a place where the bound state is close enough for the atoms to scatter into it, and to scatter back out of it.

^{6}Li has two Feshbach resonances, one at 543 G and the other at 834 G. The former is a very narrow resonance, which means as will be explained later that the scattering length is modified by the resonance in a small interval around the resonance, which hinders the usefulness of such resonance. However, the second resonance is one of the broadest Feshbach resonances in nature [125, 126], this is partly enhanced by the large background scattering length of the triplet potential since if it were just about $h \times 300\,\text{kHz}$ deeper it would support a bound state.

Two-channels model

The two-channels model is often used to treat problems where molecular physics comes into play.

In this framework the molecular state with energy ϵ is explicitly added to the set of possible states in addition to the continuum scattering states. The potential takes the form of a coupling term between the open and closed channel with a coupling constant Λ_k. This coupling constant is real (if not we can always choose the phase of momentum states in a way to cancel its phase) and it is related to the overlap between the scattering states and the molecular state wavefunctions.
We write a two-channel hamiltonian which describes the system [127]:

$$\hat{H} = \sum_{\boldsymbol{k},\sigma} E_k \hat{a}^\dagger_{\boldsymbol{k},\sigma} a_{\boldsymbol{k},\sigma} + \epsilon \hat{b}^\dagger b + \sum_{\boldsymbol{k},\sigma} \frac{\Lambda_k}{\sqrt{\mathcal{V}}} (\hat{b}^\dagger a_{\boldsymbol{k},\sigma} a_{-k,-\sigma} + \hat{a}^\dagger_{\boldsymbol{k},\sigma} \hat{a}^\dagger_{-k,-\sigma} b) \tag{1.18}$$

where $\hat{a}^\dagger_{\boldsymbol{k},\sigma}$ is the creation operator of a fermion in the open channel with momentum $\boldsymbol{k}$ and spin σ and $\hat{b}^\dagger$ is the creation operator of a molecule in a bound state of the closed channel, $E_k = \hbar^2 k^2/(4m^*)$ is the energy of a fermion in the center of mass frame ($m^* = m/2$ in this case), ϵ is the energy of the molecule with respect to the open channel asymptotic threshold, in the center of mass frame the total momentum of the molecule is zero, and $\mathcal{V}$ is the quantization volume. The first two terms represent the energy of the non interacting system $\hat{H}_0$ while the third term represents the interacting part $\hat{V}$.
To study the effects of the two-channels coupling and to recover physical quantities like the scattering length, like in the previous section, we evaluate the matrix element $\langle \boldsymbol{k}'|\hat{T}|\boldsymbol{k}\rangle$ of the T matrix, where the state $|\boldsymbol{k}\rangle$ indicates a pair of atoms in the open channel in the center of mass frame with a relative momentum $\boldsymbol{k}$.
Similar to the treatment in Eq. (1.9) we expand the matrix element iteratively in orders of the interaction potential $\hat{V}$. Since the final state is also in the open channel, each term should include two $\hat{V}$ interactions. A diagrammatic expansion is shown in Eq. (1.19) with the double line indicating the propagator of the molecular state $\hat{G}_{M,0}$ and the black filled point the interaction $\hat{V}$.

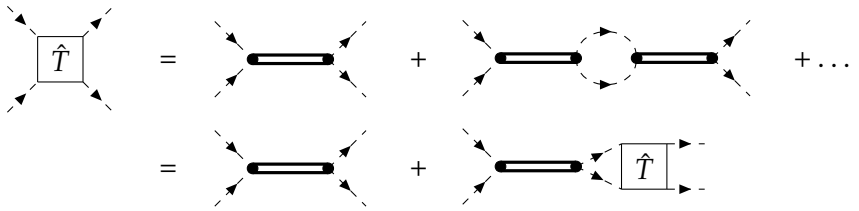

(1.19)

We calculate the first term in the diagrammatic expansion:

$$\langle \boldsymbol{k}'|\hat{V}\hat{G}_{M,0}\hat{V}|\boldsymbol{k}\rangle = \frac{\Lambda_k \Lambda_{k'}}{\mathcal{V}} \frac{1}{E_k - \epsilon + i\eta} \tag{1.20}$$

where we added the term with $\eta \to 0^+$ to select the outgoing (retarded) molecule propagator. Indeed, this parameter appears frequently in scattering amplitudes and it accounts for the fact that the states are not in fact plane waves which have an infinite extension and the effect of the potential on them is immediate, but rather they are travelling wave packets.

Another aspect of this problem is the dependence of the coupling constant on the energy of the incoming fermions in the open channel. Indeed, the energy of atoms is on the order of $h \times 10$ kHz and the coupling to the closed channel depends largely

on the detuning ϵ of the bound state. For broad resonances, the coupling is much stronger than the energy of the incoming atoms and therefore depends very little on it. With this we can replace $\Lambda_k = \Lambda$.

Going back to Eq. (1.20) we sum up the contributions in a Dyson equation as in Eq. (1.11) knowing that the open channel propagator (round dashed circles in Eq. (1.19)) are written as a sum $1/\mathcal{V}\sum_q \Lambda^2/(E_k - E_q)$. With this we can write:

$$\langle \boldsymbol{k}'|\hat{T}|\boldsymbol{k}\rangle = \frac{\Lambda^2}{\mathcal{V}} \frac{1}{E_k - \epsilon - \frac{\Lambda^2}{\mathcal{V}}\sum_q \frac{1}{E_k - E_q} + i\eta} \tag{1.21}$$

Similarly to the case of the zero-range potential, we take the low energy limit with $\langle \boldsymbol{k}'|\hat{T}|\boldsymbol{k}\rangle = -2\pi\hbar^2/(m^*\mathcal{V})f(\boldsymbol{k}) \simeq 2\pi a\hbar^2/(m^*\mathcal{V})$, and with this we write:

$$\frac{1}{a} = \frac{4\pi}{\mathcal{V}} \sum_{q<k_c} \frac{1}{q^2} - \frac{2\pi\hbar^2\epsilon}{m^*\Lambda^2} \tag{1.22}$$

We notice in this expression that when $a \to \infty$ the molecular state should come into resonance with the incoming atoms energy which gives :

$$\epsilon_0 = \frac{m^*\Lambda^2}{\pi^2\hbar^2} k_c \tag{1.23}$$

In this case, ϵ_0 is physical and results from the coupling of the molecular state to the continuum which modifies the energy of the open channel scattering states [128]. At its origin in the singlet-triplet coupling configuration is the non-diagonal hyperfine interaction between the two incoming atoms $V_{\text{hf}} = \alpha\,(\mathbf{s}_1.\mathbf{i}_1 + \mathbf{s}_2.\mathbf{i}_2)$, where $\mathbf{s}_1$, $\mathbf{i}_1$ are respectively the spin and nuclear spin numbers of one of the atoms and α is the hyperfine coefficient. We conclude with that the condition for resonance is $\Delta = E_M + \epsilon_0$.

We write Eq. (1.22) as:

$$a = \frac{m^*\Lambda^2}{2\pi\hbar^2(\epsilon_0 - \epsilon)} \tag{1.24}$$

We can also write the scattering amplitude:

$$f(k) = -\frac{\Lambda^2 m^*}{2\pi\hbar^2} \frac{1}{E_k + \epsilon_0 - \epsilon - \frac{\Lambda^2}{\mathcal{V}}\sum_q \left(\frac{1}{E_k - E_q} + i\eta + \frac{1}{E_q}\right)} = \frac{-1}{a^{-1} + ik + R_e k^2} \tag{1.25}$$

where

$$R_e = \frac{\pi\hbar^4}{m^{*2}\Lambda^2} \tag{1.26}$$

is the resonance range and it represents an effective range of the interaction $\hat{V}$ and it is inversely proportional to the coupling strength $\propto 1/\Lambda^2$. A good scale to compare to in this case is the Fermi energy, meaning for a strong coupling (broad resonance) with respect to the Fermi energy we have $k_F\, R_e \ll 1$ while for weak coupling (narrow resonance) we have $k_F\, R_e \gg 1$. In a typical ^{6}Li experiment we have $k_F R_e \approx 0.01$.

Magnetic tuning of Feshbach resonances

As mentioned earlier, a magnetic field can be used to shift the energy of the open channel with respect to the closed channel. In alkali atoms, this is done by making use of the Zeeman shift in the triplet channel potential (when $m_S \neq 0$) due to its non-zero total spin while the singlet channel undergoes no shift since its total spin is zero.

In Eq. (1.24) we arrived to an expression where the scattering length diverges when the resonance is matched. By writing $\Delta\mu$ as the magnetic moment difference between the incoming open channel state and the closed uncoupled molecular state, we have $\epsilon - \epsilon_0 = \Delta\mu(B - B_0)$.
By taking into account collisions in the open channel in the model we can write the scattering length in Eq. (1.24) around resonance showing explicitly its open-channel bare value without any coupling to the molecular channel (a_{bg}) with respect to the magnetic field change in the commonly used expression [124]:

$$a(B) = a_{\text{bg}}\left(1 - \frac{\Delta B}{B - B_0}\right) \quad \text{with} \quad \Delta B = \frac{m^*\Lambda^2}{2\pi\hbar^2\Delta\mu a_{\text{bg}}} = \frac{\hbar^2}{2\Delta\mu\, m^*\, R_e\, a_{\text{bg}}} \tag{1.27}$$

where B_0 designates the position of the resonance and ΔB the *width* of the resonance, and a_{bg} the background scattering length corresponding to the limit $a(B \to \infty)$, for instance in Fig.2.3 we recover the famous huge scattering length of the triplet channel when $B \to \infty$ for ^{6}Li. Again, the width of the resonance is larger for small resonance ranges R_e and closer magnetic moments between the two channels.
Also, from Eq. (1.27) we notice that when $a = 0$ we get $\Delta B = B - B_0$ which marks the closest zero-crossing point for the scattering length around resonance (as in Fig.2.3). Which adds to the point that for a broad resonance ($\Delta B \gg 1$) the scattering length is modified within a large interval around resonance and for a narrow resonance the scattering length is modified in a very small interval around resonance. For instance in Fig.2.3 there is actually a resonance around 543 G but its width is around 200 mG which makes it invisible on such a scale used in the figure and practically useless.

Resonance strength and narrows vs. broad resonances

As explained previously, the range over which the scattering length changes with respect to the detuning in the vicinity of the resonance is an important parameter. Many methods exist in the literature to characterize and quantify this dependence, and one of the most prominent is using the resonance strength parameter s_{res}. In the case where a Van der Waals potential is used to describe the scattering potential the resonance strength is defined as:

$$s_{\text{res}} = \frac{r_{\text{vdw}}}{R_e} \tag{1.28}$$

where r_{vdw} is the Van der Waals potential range defined in Eq. (1.2) and R_e is the resonance range defined in Eq. (1.26). For singlet and triplet channels r_{vdw} is the same since the dependece of the potential on the spin states of the scattered particles starts only for distances $r < r_{\text{vdw}}$.
We distinguish two asymptotic limits:

- When $s_{\text{res}} \gg 1$ or $R_e \ll r_{\text{vdw}}$ the resonance is said to be broad. The dynamics of the molecular state is completely dissolved in the open channel continuum in the crossover region $-1 < 1/(k_F a) < 1$. The details of the closed channel do not play a role on the dynamics of the system and the scattering length is modified by shifting the magnetic field in a large vicinity around resonance. Eq. (1.27) describes well the change of the scattering length across resonance. The binding energy is given by the universal expression $E_M = -\hbar/(ma^2)$ and the scattering cross section has the universal form $\sigma(k) = 4\pi \frac{a^2}{1+k^2a^2}$. The resonance is dominated by the open channel dynamics and a single channel description is sufficient to describe its dynamics.

- When $s_{\text{res}} \ll 1$ or $R_e \gg r_{\text{vdw}}$ the resonance is known as narrow. The molecular state in this case modifies the many-body physics in the description of the gas. The universal description of the molecule is restricted only to a small interval in the vicinity of the resonance. The system cannot be described by a single channel model and therefore the chosen two-channels treatment is essential. Also, since the time spent in the closed channel bound state is enhanced because the resonance strength is weak and the bound state has to be closer to the open channel threshold ($\epsilon \ll 1$ in 1.1), the probability for the molecule to decay to deeper vibrational levels in the closed channel potential is higher which leads to *bad* inelastic collisions.

We described the Feshbach resonances phenomenon using a two-channels model which encompasses the physics and the mechanism of achieving such resonances in neutral atom systems. In Eq. (1.23) the value of ϵ_0 characterizes the width of the resonance, and k_c is a cutoff related to the potential range between two particles. When $s_{\text{res}} \gg 1$ we have a large value of ϵ_0 and a large value of k_c that leads to a very small potential range and a collapse in the wavefunction known as Thomas collapse [129]. This is the reason why the two-channels model is often attributed to narrow Feshbach resonances description [130, 131].
Since in the course of this thesis problems including an impurity immersed in a double Fermi sea are going to be discussed, two-body interactions alone cannot describe the full extents and properties of such systems and a three body treatment is needed. Indeed, the concept of universality of the interaction potential breaks down in the three-body problem and we see that in order to describe the system we need an additional length scale as we shall see. Therefore, in the next section we will go through the basic tools in studying the three-body problem and we will explore the domain where this problem is relevant in the scope of this thesis.

1.2 Three-body problem

In 1970, Vitaly Efimov, then a junior researcher at the Ioffe Institute in Leningrad, found a remarkable effect in the quantum energy spectrum of three particles [132]. He examined the case of three identical particles interacting through short-range attractive interactions near resonance. In such a case, energy fluctuations (also known as zero-point energy) hinder the possibility of two particles to bind if the binding

energy were too weak as is the case in near resonant interactions.
Under these conditions, Efimov found that an effective long-range three-body attraction arises, and this attraction may support an infinite family of three-body bound states (called Efimov states or Efimov trimers), in which the three particles are bound at larger and larger distances, beyond the range of the interactions.
The Efimov effect, as it became known, is possible at distances exceeding the potential range. In the case of a strongly interacting mass imbalanced system, this happens via an effective interaction mediated between two heavy particles by the third lighter particle moving back and forth between them, extending thus the range over which such an effect takes place.
This translates to the fact that at its origin, the Efimov effect is established by means of the kinetic energy of the particles and thus brings no characteristic length scale of its own to the system. This means that it is not affected by other length scales in the system and therefore it is scale invariant. The energy spectrum of Efimov trimers is discrete and since it has no characteristic length it has no low-energy cutoff and the bound states series is infinite with a peculiar geometric series form that became a distinctive feature of the Efimov effect.
One thing to consider also is that once the two-body interaction becomes strong enough to support a two-body bound state, the Efimov trimer energy merges with the molecular energy spectrum as we shall see more explicitly later, this feature is often called the *Borromean* nature of the Efimov trimer.
However, the problems arising from this infinite series, including the absence of a ground-state energy, mean that a characteristic length scale has to be defined to account for the finite size of the ground state. We will see that this length scale arises naturally by treating the problem using a two-channel model in contrast to other methods where this length scale has to be added manually.
In this section a calculation of the energy spectrum of three bosons in the two-channels model is presented following the one presented in [131]. The energy spectrum of the trimer states is discussed as well as the properties of these trimer in such a system. For an extensive review on the subject of Efimov physics refer to [133].

1.2.1 Two-channels model for the three identical bosons

In the following we will follow closely the calculation presented in [131] rather than the earlier frameworks used by Efimov himself and others. This helps in using the same terminology used previously and also in introducing the work in Chapter 5.

We consider a system composed of three identical bosons with mass m interacting via a contact zero-ranged interaction potential defined as $V_{k-k'} = \Lambda$. We use a two-channel model to write the following hamiltonian in the vicinity of a narrow Feshbach resonance:

$$\hat{H} = \sum_{k} \epsilon_k \hat{a}_k^\dagger \hat{a}_k + \sum_{K} (E_0 + \epsilon_K/2) \hat{b}_K^\dagger \hat{b}_K + \Lambda \sum_{k,K} (\hat{b}_K^\dagger \hat{a}_{k+K/2} \hat{a}_{-k+K/2} + \hat{a}_{k+K/2}^\dagger \hat{a}_{-k+K/2}^\dagger \hat{b}_K) \tag{1.29}$$

where $\epsilon_k = \hbar^2 k^2/(2m)$, E_0 is the binding energy of the molecule with respect to the open channel threshold, $\hat{a}_k^\dagger$ is the creation operator for an open channel boson with

momentum $\boldsymbol{k}$, $\hat{b}^\dagger_{\boldsymbol{K}}$ is that of a closed channel molecular state with momentum $\boldsymbol{K}$. We also mention that the coupling constant is related to a characteristic length scale R_e defined in Eq. (1.26) and to the scattering length with Eq. (1.22) which we write in the following form in this case:

$$\frac{1}{a} = \frac{2k_c}{\pi} - \frac{2\pi\hbar^2 E_0}{m^*\Lambda^2} \tag{1.30}$$

Where a is the two body scattering length in the two-channels model, k_c is a UV-cutoff, its inverse is of the order of the Van der Waals potential range.

The three body ansatz

The problem is solved using an ansatz for the three-body problem in the center of mass frame, that is for a zero total momentum. Because of the conversion of pairs of atoms into molecules and vice-versa, the variational wavefunction is a coherent superposition of three unpaired bosons (all three atoms in the open channel) with coefficient $A_{\boldsymbol{k},\boldsymbol{K}}$ and of one molecule plus one boson (one atom in the open channel and two atoms tightly bound in a molecule in the closed channel) with coefficient $\beta_{\boldsymbol{K}}$ as follows:

$$|\psi\rangle = \Big(\sum_{\boldsymbol{K}} \beta_K \hat{b}^\dagger_{\boldsymbol{K}} \hat{a}^\dagger_{-\boldsymbol{K}} + \sum_{\boldsymbol{K},\boldsymbol{k}} A_{\boldsymbol{K},\boldsymbol{k}} \hat{a}^\dagger_{\boldsymbol{k}+\boldsymbol{K}/2} \hat{a}^\dagger_{-\boldsymbol{k}+\boldsymbol{K}/2} \hat{a}^\dagger_{-\boldsymbol{K}} \Big) |0\rangle \tag{1.31}$$

By solving the Schrödinger equation $\hat{H}|\psi\rangle = E|\psi\rangle$ where E is the trimer energy and considering $A_{\boldsymbol{K},\boldsymbol{k}}$ to be an even function of $\boldsymbol{k}$ we get the following pair of coupled equations:

$$\begin{aligned} \Big(E_0 - E + \frac{3\hbar^2 K^2}{4m}\Big)\beta_{\boldsymbol{K}} + 2\Lambda \sum_{\boldsymbol{k}} (A_{\boldsymbol{K},\boldsymbol{k}} + 2A_{\boldsymbol{k}-\boldsymbol{K}/2,-\boldsymbol{k}/2-3\boldsymbol{K}/4}) = 0\,, \\ \Lambda\beta_{\boldsymbol{K}} + \Big(2\epsilon_{\boldsymbol{k}} - E + \frac{3\hbar^2 K^2}{4m}\Big) A_{\boldsymbol{K},\boldsymbol{k}} = 0 \end{aligned} \tag{1.32}$$

Since we are looking for bound states, we write the energy as $E = -\hbar^2\lambda^2/m < 0$. By solving the second equation and injecting the result in the first we get one equation for $\beta_{\boldsymbol{K}}$ which we integrate over the angular variables to obtain a Skornyakov-Ter-Martirosyan's equation [134] type as follows :

$$\Big(R_e(\frac{3K^2}{4} + \lambda^2) - \frac{1}{a} + \sqrt{3K^2/4 + \lambda^2}\Big)\psi(K) = \frac{2}{\pi}\int_0^\infty dK' \ln\Big(\frac{K'^2 + K^2 + KK' + \lambda^2}{K'^2 + K^2 - KK' + \lambda^2}\Big)\psi(K') \tag{1.33}$$

where $R_e > 0$ is the parameter derived in Eq. (1.26) which is related to the finite range of the inter-channel potential, and $\psi(K) = \beta_{\boldsymbol{K}} K$ and $K = |\boldsymbol{K}|$. With this parameter the problem does not need any additional regularization encountered using other methods [135]. For a narrow resonance $k_c R_e \ll 1$ [136] and here the short-distance regularization does not involve higher angular momentum ($l > 0$) partial waves [137].

A numerical method to solve this equation will be presented in the following chapters, for an analytical derivation of the following refer to [131]. The equation yields on resonance ($a \to \infty$) the Efimov trimers spectrum:

$$\lambda_n^2 = \kappa_*^2 e^{-2\pi n/s_0} \tag{1.34}$$

with κ_* the three-body parameter, $s_0 \simeq 1.00624$ is a scaling parameter. We also note the famous universal ratio $E_{n+1}/E_n = e^{-2\pi/s_0} \simeq 1/515.03$ between subsequent levels with $E_n = -\hbar^2\lambda_n^2/m$ the energy of the Efimov trimer bound states. The three-body parameter can be calculated exactly $\kappa_* R_e \simeq 2.6531$ and the scattering length a_- where the Efimov state joins the three-atom continuum at $\lambda \to 0$ to find $a_-\kappa_* \simeq -1.50763$ which gives the value $R_e/a_- \simeq -1.760$.

1.2.2 Efimov trimers properties and domain

In general , for a given three-particle system, there are three inter-particle interactions. At least two of these interactions are required to be resonant for the Efimov effect to occur. This can be understood simply from the picture of mediated interaction we mentioned earlier where in order for one particle to mediate an effective long-range interaction between two other particles, it must interact resonantly with these two particles. If it interacts resonantly with only one particle, then the mediation to another particle is not possible.

Generally speaking, bosonic particles are favorable to the Efimov effect, whereas fermionic particles tend to prevent the Efimov effect, since their Pauli exclusion may overcome the Efimov attraction.

The lighter a particle is, the better it mediates interaction between other particles. Thus, mass-imbalanced systems tend to enhance the Efimov attraction, and enable the Efimov effect in fermionic systems.

It is useful to add a discussion on the domain of existence of the Efimov trimers. The spectrum in Eq. (1.34) does not have a lower limit, meaning that the energy is not bounded from below and the ground-state energy lies at $-\infty$ giving smaller and smaller trimer sizes. This leads to the mentioned Thomas Collapse [129] encountered in two-body potentials with spatial dependence as $1/r^2$. However, if one accounts for the physical fact of finite range interactions and the limits of the zero-range approximation it is possible to set upper and lower limits on the size of the trimer.

In the case of large binding energies, the trimer size becomes comparable to the range of the two-body potential r_{vdw} defined in Eq. (1.2), in this case the short-range approximation is no longer valid and the Efimov scenario breaks down. For low binding energies, the trimer size becomes larger than inter-particle distance $n^{-1/3}$ and the surrounding atoms create additional interactions which smear the trimer state.

In practice the number of accessible trimers is small, if we take $\lambda_{n_0} = r_{\mathrm{vdw}}$ and $\lambda_{n_1} = n^{-1/3}$ where n is the particle density introduced in 1.1.1 we have $\lambda_{n_1}/\lambda_{n_0} = 1/\alpha^{(n_1-n_0)}$ giving

$$n = n_0 - n_1 = \ln(n^{-1/3}/r_{\mathrm{vdw}})/\ln(\alpha) \simeq 2$$

where $\alpha = \exp(\pi/s_0) \simeq 22.7$ is the recurrent factor encountered in Efimov physics (or its square for energy dependence).

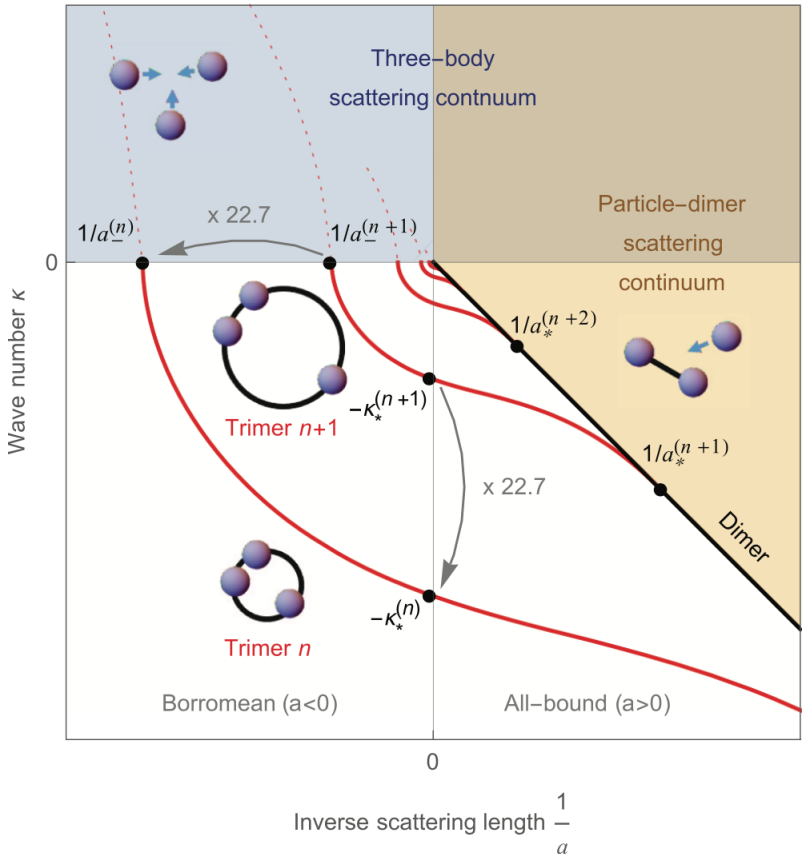

Figure 1.2: Schematic plot of the Efimov scenario. Schematic representation of the so-called *Efimov plot* or *Efimov scenario* showing the discrete scale invariance of the three-body spectrum for identical bosons in the zero-range theory. The wave number $\kappa = E\sqrt{m/(\hbar^2|E|)}$ associated with the energy E of the dimer (black) and trimers (red) is plotted against the inverse scattering length $1/a$. The blue and orange filled regions represent the three-body scattering continuum and the particle-dimer scattering continuum, respectively. Note that these continua overlap for $1/a > 0$ and $E > 0$. Special values of $1/\kappa$ and $1/a$ are indicated by the dots: a trimer appears from the three-body scattering threshold at $1/a_-$, has a binding wave number κ^* at unitarity, and disappears below the particle-dimer scattering threshold at $1/a^*$. Trimer resonances in the three-body continuum are indicated by dotted curves. The discrete scale invariance of the spectrum is indicated by the grey arrows showing the universal scaling ratio between consecutive levels. For clarity, the value of the strength s_0 has been artificially set to 3, instead of 1.00624, thus reducing the spacings between the trimer levels to make them more visible. Figure was taken from [133].

Another known property is the behavior of the energy across resonance (for finite values of the scattering length a). Indeed, by dimensional argument, the energy of the trimers takes the form:

$$E_n = \frac{\hbar^2}{mR_e^2} f_n(R_e/a) \tag{1.35}$$

where the function $f_n(R_e/a)$ should obey the following scaling:

$$f_n(x) = f_0(x/\alpha^n)/\alpha^{2n} \tag{1.36}$$

for E_n to still scale as $1/\alpha^2 = 1/515.03$. This is shown in Fig.1.2. This type of scaling corresponds to a family of functions called the log-periodic functions which have become a signature of Efimov physics.

1.2.3 Experimental evidence of Efimov physics

Efimov physics had stayed for decades a mere theoretical prediction until the first experimental evidence was discovered. We will only focus in this section on experiments in the field of cold atoms relevant to the scope of this manuscript.
Most atomic species have interactions that decay as a $\propto 1/r^6$ Van der Waals potential. Thus, to observe the Efimov trimer described earlier, neutral atoms appear to give an ideal system. As for resonant interactions, this can be achieved by means of the Feshbach resonances studied earlier. Shortly after these techniques were well-established, many groups turned to the old problem of Efimov.

Experimental evidence of the Efimov physics was first obtained with ^{133}Cs atoms [138, 139] by studying the three-body losses in their Bose gas. The basic principle behind the measurement is that each time an Efimov trimer couples to a three-atom or to an atom-dimer threshold, the particle loss dramatically increases, and the corresponding scattering rate coefficients provide well-suited observables to detect Efimov physics in experiments.
Although the experiment observed only one trimer state, its Efimovian nature was convincing since it was observed in regions where the dimer state is known to be unbound.

This experiment was later extended to other atomic species and the scaling factor α was tested experimentally through the observation of multiple resonances and the value of a_- was measured as well as the atom-dimer scattering value which determines the value of a when the trimer state dissolves into the dimer state [140–142]. The binding energy was also directly measured via radio-frequency association, with a three-component Fermi gas of ^{6}Li [143, 144].

1.3 Ultra-cold Fermi gases

The first theoretical study of fermions goes back to Paul Drude's model for the conductivity in solids [145]. Drude considered metals to be composed of *heavy* positively charged particles and *light* electrons[1]. Then he modeled the motion of these particles using a purely classical treatment and using this simple approach, it became possible to explain the basic properties of metals like conductivity and resistance.
However, the observation at the beginning of the 20th century of superconductivity in metals changed this view. It was Heike Kamerlingh Onnes, then a professor at the University of Leiden, who, after having succeeded in liquefying ^{4}He earlier, used his liquid ^{4}He to cool down mercury when he observed the remarkable effect of the resistivity dropping to non-measureable values at low enough temperatures[2].

[1] Electrons were already discovered by Sir Joseph J. Thompson back in 1897.

[2] Onnes received the 1913 Nobel prize in physics for "his investigations on the properties of matter at low temperatures which led, inter alia, to the production of liquid helium"

The condensation of electrons was an utterly strange observation, since for fermions, they cannot be in one and the same quantum state and an obvious scenario for this to happen might be the formation of tightly bound pairs of electrons that can behave as bosons and condense. However, at the time no known interaction could possibly overcome the Coulomb repulsion between electron pairs.
It was not until four decades later that L. Cooper realized that fermions interacting via an arbitrarily weak attractive interaction mediated by the crystal lattice vibrations (phonons) on top of a filled Fermi sea can form a bound pair [146], and by a result could be responsible for superconductivity.
Soon afterwards, Bardeen, Cooper and Schrieffer (BCS) developed a full theory of superconductivity starting from a new, stable variational ground state in which pair formation was included in a self-consistent way [147][3]. Later, Popov [148], Leggett [149] and Eagles [150] realized that the BCS formalism and its variational ansatz provides also a description of a Bose-Einstein condensate of a dilute gas of tightly bound pairs.
In this section, we will describe the rich physics involved in the low temperature interacting Fermi gas, with its asymptotic regimes, the molecular Bose-Einstein condensate, the Barden Cooper Schriefer superfluid, and the unitary Fermi gas. To begin, we will provide some results for non-interacting gases.

1.3.1 Non-interacting Fermi gas

We start with the basic case of a homogeneous system of non-interacting fermions in a box with volume V in three dimensions. The study of the non-interacting (also called ideal) Fermi gas helps understanding the role of interactions in the interacting limit, and provides a playground for many phenomena where the effect of interactions can be neglected, e.g. in a Fermi gas at thermal equilibrium.
To describe a statistical ensemble at thermal equilibrium like a gas of non-interacting fermions we can write the following partition function in the grand canonical ensemble:

$$\mathcal{Z} = \sum_{\lambda} e^{-\beta E_\lambda} \tag{1.37}$$

where λ describes a single mode state in the system, E_λ is the total energy of this state representing the eigenvalue of the single particle hamiltonian of the system $(\hat{H} - \mu N_\lambda)|\Psi_\lambda\rangle = E_\lambda|\Psi_\lambda\rangle$, where μ is the chemical potential and N_λ the number of particles and $\beta = 1/(k_B T)$ is proportional to the inverse temperature, k_B is the Boltzmann constant.
For two identical fermions, by construction, their wavefunction should be antisymmetric with respect to the exchange of the two fermions. This results in the fact that the two fermions cannot be in the same state, this principle is known as *Pauli exclusion principle* or *Pauli blocking*.
This restricts the number of possible states of the particle to two $|\Psi_\lambda\rangle \in \{|0\rangle, |1\rangle\}$ since no more than one fermion with energy $E_{\boldsymbol{k}}$ is allowed to exist in one state.
With this we calculate the probability of having a fermion in a state $\boldsymbol{k}$ representing

[3]The three scientists received the 1972 Nobel Prize in physics "for their jointly developed theory of superconductivity, usually called the BCS-theory."

the wavevector of the fermion if we consider the gas to be composed of free particles since no interaction is present:

$$N_{\boldsymbol{k}} = \langle a^\dagger_{\boldsymbol{k}} a_{\boldsymbol{k}} \rangle = \frac{1}{\mathcal{Z}} e^{-\beta E_k} = \frac{1}{1 + e^{\beta E_k}} \tag{1.38}$$

This is called the Fermi-Dirac distribution describing the occupation number N_λ. When working with in the grand canonical ensemble we have $E_{\boldsymbol{k}} = \epsilon_{\boldsymbol{k}} - \mu$ where $\epsilon_{\boldsymbol{k}} = \hbar^2 k^2/(2m)$ is the kinetic energy of a fermion with mass m and μ is the chemical potential of the gas. In the case of an interacting system, an additional term is added to the hamiltonian to account for the effect of interactions and trapping.
In the limit of low temperature $\beta \to \infty$ fermions start filling up the lowest available energy levels until the last ones reach what is called the Fermi energy ϵ_F and occupation number of a fermion with energy lower than ϵ_F is 1 and above it is 0. This leads the Fermi-Dirac distribution to take the following form $N_{\boldsymbol{k}} = \Theta(\epsilon_F - \epsilon_{\boldsymbol{k}})$ with Θ as the Heaviside step function.
This stacking of fermions creates a sphere with radius $\boldsymbol{k}_F$ called the Fermi wavevector. The volume of this sphere $\mathcal{V} = 4\pi k_F^3/3$ can be related to the total number of fermions $N = \sum_{k<k_F} N_{\boldsymbol{k}}$ by considering the quantization volume in reciprocal space $(2\pi)^3/\mathcal{V}$ giving

$$N\frac{(2\pi)^3}{\mathcal{V}} = \frac{4}{3}\pi k_F^3 \Rightarrow k_F = (6\pi^2 n)^{1/3}$$

where $n = N/\mathcal{V}$ the density of fermions per spin in a volume $\mathcal{V}$.
The Fermi energy could now be calculated as follows:

$$E_F = \frac{\hbar^2 k_F^2}{2m} = \frac{\hbar^2}{2m}(6\pi^2 n)^{2/3} \tag{1.39}$$

It is common to write the last equation in the case where n designates the total number of fermions in a double Fermi gas, i.e. a gas with equal number of fermions in two spin states $|\uparrow\rangle$ and $|\downarrow\rangle$. In that case the factor 6 becomes 3. We can also define the Fermi temperature in a homogeneous system:

$$T_F = E_F/k_B = \frac{\hbar^2}{2mk_B}(6\pi^2 n)^{2/3} \tag{1.40}$$

where k_B is the constant of Boltzmann.
The Fermi energy and therefore the Fermi temperature are an indication of the density of the system and in consequence of the interparticle distance $n^{-1/3}$ previously mentioned in 1.1.1. Thus, the ratio T/T_F, similarly to $\lambda_{dB} n^{-1/3}$, defines a value which can be an indicator of the degeneracy of the system. If $T/T_F < 1$ the system is non-degenerate and a classical treatment is sufficient to describe its microscopic properties. However, if $T/T_F \ll 1$ the system is degenerate and to understand its microscopic treatment more careful treatment taking into account the quantum nature of the degenerate regime is required.
An example of these systems are metals for instance, where the Fermi temperature of the electrons is of several 10^4 K, hence, electrons in metals are in deeply degenerate regimes and quantum many-body effects like superconductivity are manifested in such systems. Another example are the extremely dense neutron stars with a

Fermi temperature of around 10^{11} K compared to typical core temperatures of 10^8 K. Meaning that these systems are deeply degenerate, and that the results obtained in ultra-cold Fermi gases physics can be in some cases extended to such systems.
As for the case of ultra-cold Fermi gases which are used in experiments, in room temperature they are very far from degeneracy. Increasing the density of the gas will increase its Fermi temperature and get it closer to degeneracy, however, this will also increase three-body recombination rate which leads to solidification when the temperature is lowered. This tradeoff is the reason researchers use very dilute gases with densities $< 10^{13}\,\mathrm{cm}^{-3}$ and decrease the temperature of the gas to get a degenerate gas.
The Fermi temperatures for these gases is around 1 μK which means that many steps of cooling have to be performed to bring the gas to degeneracy. In the next chapter we will present a full overview of the steps we use in our experiment to cool the gas.

1.3.2 Interacting Fermi gas and the BEC-BCS crossover

In the case of a gas of fermions composed of two equally populated spin states, interactions arise and become more important and the physics described earlier needs to be modified due to large scale coherence which leads to many-body phenomena arising.
Unlike Bose gases which suffer from huge three-body losses in the limit of strong interactions due to three-body recombination, Fermi gases do not have this problem since Pauli exclusion principle blocks these combinations which leads to gases with life times longer than the times needed to run an experimental sequence in cold atoms experiments.
In the case of strongly attractive interaction $k_F\, a \gg 1$, the ground state of the system should be a BEC of tightly bound molecular pairs. When the binding energy largely exceeds the Fermi energy, the fermionic nature of the gas becomes irrelevant since paired fermions have different momenta and therefore no Pauli blocking happens.
In the other case of weak attractive interactions $k_F\, a \ll -1$, there is no bound state for two isolated fermions, but Cooper pairs form in the medium for fermions close to the Fermi sphere. The ground state of the system is a condensate of Cooper pairs as described by BCS theory. In contrast to the case of molecular condensate, the binding energy of these pairs is much smaller than the Fermi energy and thus the Pauli principle plays a major role.
In between, it crosses the unitary limit where the scattering length diverges and the properties of the gas become scale invariant.

It was then realized by Leggett [151] building upon the work of Popov [148] that the transition from the BCS to the BEC regime is a smooth crossover. In light of what was explained this sounds a bit odd since the two-body physics shows a threshold behavior at the unitary limit, below which there is no bound state for two particles. However, in the presence of the Fermi sea, the transition is manifested simply by a crossover from a regime of tightly bound pairs to a regime where these pairs are of much larger size than the interparticle spacing.

BCS limit

In this regime of weak attractive interactions $k_F a \to 0^-$. Fermions are weakly attracted to each other and will form an ensemble of phase-coherent Cooper pairs protected by the superfluid gap $\Delta/E_F^2 \sim 8\, e^{-\pi/(2k_F|a|)}/e^2$. However, the pairing gap is still exponentially smaller than the Fermi energy, meaning that the pairing is fragile and excitations could break up pairs easily.
The ground state energy per unit volume of the BCS-superfluid is mainly given by:

$$\epsilon_{\mathrm{G,BCS}} = \frac{3}{5} n E_F (1 + \frac{10}{9\pi} k_F a + \frac{4(11 - 2\ln(2))}{21\pi^2} (k_f a)^2) \tag{1.41}$$

where the first term is the energy of the non-interacting normal state, where $3E_F/5$ is the average kinetic energy per fermion in the Fermi sea., the second is a mean-field shift and the next term was obtained by Galitskii, Lee and Yang, in the context of repulsive hard-sphere fermions [152, 153]. The generalization of this expansion to attractive interactions was shown in [154].

BEC limit

In the regime of small positive scattering lengths $k_F a \to 0^+$, opposite-spin fermions are strongly attracted to each other and form tightly bound dimers of size a and binding energy $-\hbar^2/(ma^2)$. The dimers are composite bosons that condense at low temperature and can be described by a Gross-Pitaevskii equation for small scattering lengths. Consequently, the ground state energy per unit volume reads:

$$\epsilon = -\frac{\hbar^2}{ma^2} n_M + \frac{1}{2} g_M n_M^2 \left(1 + \frac{128}{15\sqrt{\pi}} \sqrt{n_M (c_M a)^3} + \dots\right) \tag{1.42}$$

where $n_M = n/2$ is the dimer density, $g_M = 2\pi\hbar^2 c_M a/m$ and $c_M a \simeq 0.6\, a$ is the dimer-dimer scattering length [62, 155]. The first term is the binding energy per molecule in the tightly bound limit. The second term is a mean field contribution describing the repulsive interaction between molecules in the gas [156].

Unitary limit

In the unitary limit, the scattering length drops out as a scaling parameter and we retrieve relations that are analog to the ideal Fermi gas. All the complexity of the interacting system is thus encapsulated in a few universal numerical constants. Indeed, the energy density can be expanded as

$$\epsilon = \frac{3}{5} n E_F (\xi - \frac{\zeta}{k_F a} + \dots) \tag{1.43}$$

The numerical constant ξ is the Bertsch parameter $\xi = 0.376$ [157]. The other numerical constant ζ was measured to give $\zeta = 0.87$ [158]. The analytical or numerical calculation of those two parameters represent a challenging problem as they cannot be obtained by standard perturbative methods due to the lack of small parameters in the system.

The unitary gas is revisited in the third chapter where a presentation of our extrapolation of previous measurements of the equation of state of a unitary Fermi gas is presented. For an extensive review on the BCS-BEC crossover refer to [159].

The previous discussion concerns purely fermionic gases which do not interact with the environment. However, their properties can be modified dramatically if such an interaction is introduced. An iconic problem is the study of the quantum system's properties when one particle is immersed in the system, an umbrella term is *impurity physics*.
In the next section we will explore the main theoretical results in this domain and we will see how the physics of the BEC-BCS crossover affects the state of the impurity.

1.4 Impurity physics

Properties of quantum systems can be modified dramatically when they interact with an environment. One of the first systems in which this phenomenon has been recognized is an electron moving in a deformable crystal. As originally pointed out by Landau and Pekar [97], Fröhlich and Holstein [98,160] a single electron can cause distortion of the ionic lattice that is sufficient to provide a strong modification of the electron motion.
Schematically this can be described as an electron moving together with its screening cloud of collective excitations which take the form of vibrations due to the attraction and repulsion between the electron and the crystal, these vibrations of the crystal are commonly known as *phonons*. This effect not only renormalizes the effective mass of the electron but can also make its propagation (partially) incoherent. The resulting electron dressed by the phonons has been termed *polaron*.

Polaron physics is important for understanding many solid state materials including ionic crystals and polar semiconductors [161–164], and even high temperature superconductors [165]. It has also been discussed in the context of electrons on the surface of liquid helium [164,166].
Furthermore, in several technologically relevant materials, such as organic semiconductors used in flexible displays, unusual temperature dependence of electron mobility arises from the strong coupling of electrons to phonons [167,168].
The idea of polaronic dressing has been extended far beyond electron-phonon systems and has become an important paradigm in physics. One important example is charge carriers in systems with strong magnetic fluctuations, such as holes doped into antiferromagnetic Mott insulators [169,170] or electrons in magnetic semiconductors [171,172], which can be described as magnetic polarons. Even in the Standard Model of high energy physics the way the Higgs field produces masses of other particles [173,174] is closely related to the mechanism of polaronic dressing.
The study of the problem has had major influences on theoretical approaches also. For instance, the Kondo effect [99,102], in which scattering of a localized spin on conduction electrons leads to the formation of a bound state, was the starting point of the application of the renormalization group approach to condensed matter sys-

tems. The crucial aspect of most impurity problems is that simple perturbative and mean-field approaches are not sufficient. Powerful analytical methods have been employed to explore this problem including bosonization (see e.g. [175,176]), renormalization group [101,177,178], and Bethe ansatz solution [179,180].
In a broader perspective, the polaron problem represents a sub-class of quantum impurity problems, in which a single impurity introduces interactions (or at least non-trivial dynamics) in the many-body system which is hosting it. These systems have long been a fertile ground for testing analytical, field-theoretical, and numerical methods for studying quantum many-body systems.

In ultracold atomic gases, the realization of impurity systems has led to a dramatic increase of activity in this topic. Using this platform, researchers have been able to create a large variety of polaronic systems with different impurity masses, bath and impurity types and tunable interactions. When the impurity is immersed in a Bose-Einstein condensate it is called a *Bose polaron* and many experimental realizations using fermionic and bosonic impurity atoms were realized [181–187].
The case of an impurity immersed in a spin polarized Fermi sea is known as a *Fermi polaron* and its first experimental realization was as a side effect of experiments aiming at observing the superfluid transition in a Fermi gas using spin-imbalanced samples [188,189]. In the first experiment, a superfluid core was observed as Cooper pairing dominates the superfluid region and a polarized non-interacting gas was observed on the outer shell of the sample, however, between these two regions a partially polarized gas formed and showed interesting results.
While the physics of this experiment is going to be shown in detail in Chapter 3 it is important to note that the difference between its result and the one in [189] has launched a considerable theoretical effort to understand this problem [190–196]. Later experiments [109,197–199] focused on studying the properties of an impurity immersed in a spin polarized system as well as in a fermionic superfluid with two spin states instead of one using the rich environment of Fermi gases where the BEC-BCS crossover provides a bath where a transition between the Bose polaron and the Fermi polaron can be achieved.
In the following a brief overview of each polaron regime is going to be presented.

1.4.1 Bose polaron

The Bose polaron problem is connected to the original polaron problem investigated by Landau and Pekar [97], for which a conduction electron is immersed in a phonon bath. In cold atoms, the Bose polaron can be realized by considering an impurity immersed in a Bose-Einstein condensate, the interaction is manifested by Bogoliubov excitations in the BEC. For a recent review refer to [200].
A commonly known model is the Fröhlich hamiltonian:

$$\hat{H} = \frac{\hbar^2 p^2}{2m_i} + \sum_{\boldsymbol{k}} \hbar\omega_{\boldsymbol{k}}\, \hat{b}^\dagger_{\boldsymbol{k}} \hat{b}_{\boldsymbol{k}} + \sum_{\boldsymbol{k}} V_k\, e^{i\boldsymbol{k}.\boldsymbol{r}}\, (\hat{b}_{\boldsymbol{k}} + \hat{b}^\dagger_{-\boldsymbol{k}}) \tag{1.44}$$

where $\boldsymbol{r}$ and $\boldsymbol{p}$ are the impurity position and momentum vectors respectively, m_i is the mass of the impurity, $\hat{b}^\dagger_{\boldsymbol{k}}$ is the creation operator of a phonon at wavevector $\boldsymbol{k}$

and energy ω_k and V_k is the matrix element of the impurity-phonon interaction at momentum k.
While this model was originally introduced in the context of electron-phonon systems, the Fröhlich hamiltonian has been shown to describe the interaction between impurity atoms and Bogoliubov modes of a BEC [201, 202] in the limit where the scattering of phonon at finite momentum can be neglected.
This model is characterized by two important parameters: the impurity mass m_i and the impurity-phonon coupling strength. In the weak coupling regime, the polaron can be thought of as a quasi free impurity carrying a loosely bound screening cloud of phonons. It was previously described by a weak coupling mean-field theory [203] and a full description of its properties was shown in [204]. The mean-field expression of the energy is of the form $E_n^{\mathrm{mf}} = g_{ib} n_b$ where $g_{ib} = 2\pi\hbar^2 a_{ib}/m_{ib}$ where a_{ib} is the impurity-phonon scattering length and m_{ib} is the impurity-phonon reduced mass. In this limit, the effective mass m^* of the Bose polaron tends towards m_i.

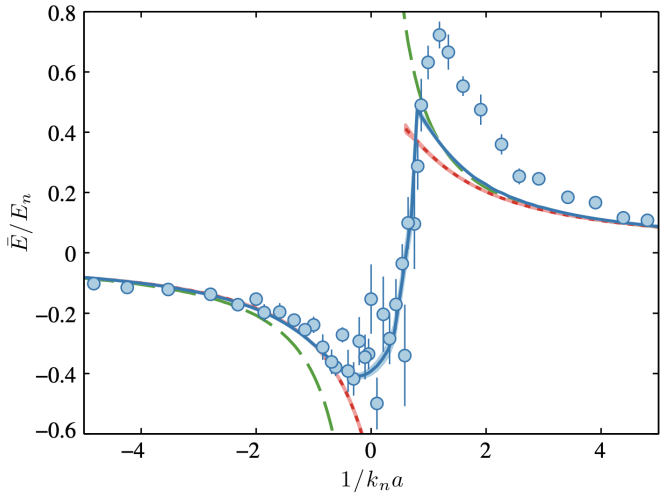

Figure 1.3: Average energy of an impurity immersed in a Bose-Einstein condensate as a function of the interaction parameter. The results are obtained by fitting the spectroscopic signal of the impurity (blue dots), while the blue line is the spectrum calculated using a variational ansatz taking into account three-body correlation [204, 205]. The green dashed line shows the perturbative regime result and the red line shows the result of a variational calculation without considering three-body physics. Figure taken from [206].

In the strong coupling regime, on the other hand, the screening cloud is so large that the impurity becomes effectively trapped in the resulting potential. To explore the strongly interacting regime, a variational ansatz has been used [205, 207], as well as a field theoretical study [208]. These studies are in agreement and determined the energy of the polaron for any interaction strength.
When $a_{ib} > 0$, an impurity-boson dimer can be formed, but contrary to the Fermi polaron case [130], there is no sharp transition expected from the Bose polaron to the molecular state. Both studies expect a smooth transition between the two states: the energy of the polaron tends asymptotically towards that of the shallow dimer energy and the effective mass of the Bose polaron tends smoothly towards $m^* = m_i + m_b$,

signature of the dimer state.
For $a_{ib} > 0$, a repulsive branch of the Bose polaron also exists. While in the weakly interacting regime $a_{ib} \to 0^+$, the Bose polaron is well-defined and can be described with a perturbative expansion, in the strongly interacting regime the Bose polaron is ill-defined for $1/(k_n a_{ib} \ll 1)$, with a strong decay into the lower-lying energy branches.

Moreover, three-body effects were taken into account in [205, 209]. They showed that three-body physics can affect the Bose polaron in the strongly interacting regime with an avoided crossing between the polaronic energy branch and the trimer energy branch, meaning the impurity becomes smoothly bound into an Efimov trimer in this regime. An effect to be contrasted with the first order transition observed between the polaron and the trimer state for an impurity in a normal phase Fermi sea [118] and the smooth crossover in case the Fermi sea allows interactions [130].
The Bose polaron has been investigated experimentally in the strongly interacting regime in JILA with fermionic ^{40}K impurities in a BEC of ^{87}Rb [210] and in Aarhus University with ^{39}K for the impurities and the BEC using two different internal states [206].
In the latter experiment, a clear signal of the Bose polaron was observed by using RF spectroscopy and an energy shift predicted in [204] due to three-body correlations has been observed which means that to describe accurately the physics of Bose polarons three-body effects have to be taken into account.

1.4.2 Fermi polaron

The question of spin-imbalanced Fermi gases has been an intriguing problem for decades. Originally, it was understood that pairing and superfluidity could sustain a certain amount of spin imbalance, above which the system would undergo a quantum phase transition towards a normal state [211, 212]. Four decades later, experiments done at MIT and Rice university [188, 189, 213] have revived the old problem in a way and opened it to new possibilities in another way.
One remarquable feature of [188] is the observation of three different phases in the cloud. At the center, a superfluid core, where the densities of the two spin states are equal was observed, then an intermediate normal shell where the two states coexist with one component acting as a bath and the other component as an impurity and finally an outer rim of the majority component.
The intermediate phase raised many interesting questions regarding the phase diagram of an impurity of minority atoms, and it was known to be as the Fermi polaron problem.
The Fermi polaron is a quasiparticle arising from the interaction of an impurity with a spin-polarized Fermi gas. The impurity in this case is dressed by the particle-hole excitations of the surrounding Fermi sea. For a recent review refer to [214].
Typically, the hamiltonian of the system, also called the $N+1$ body problem, describes simply an impurity interacting with a Fermi sea and is written as:

$$\hat{H} = \sum_k \frac{\hbar^2 k^2}{2m} \hat{a}_k^\dagger \hat{a}_k + \frac{\hbar^2 p^2}{2m} \hat{c}_p^\dagger \hat{c}_p + \frac{g_0}{\mathcal{V}} \sum_{k,k',q} \hat{a}_{k+q}^\dagger \hat{c}_{k'-q}^\dagger \hat{c}_{k'} \hat{a}_k \tag{1.45}$$

where $\hat{a}_{\boldsymbol{k}}^{\dagger}$ is the creation operator of a fermion with momentum $\boldsymbol{k}$ and mass m, $\hat{c}_{\boldsymbol{p}}^{\dagger}$ is the creation operator of an impurity with momentum $\boldsymbol{p}$ and mass m, g_0 is the bare coupling constant of the interaction impurity-fermion, it can be normalized by adding a UV-cuttof as seen in section 1.1 resulting in Eq. (1.16).

Variational approach

As part of the theoretical effort aimed at studying the observations in [188], a variational ansatz was proposed in [191] that described an impurity scattering in a polarized Fermi sea and creating one particle-hole excitation:

$$|\psi\rangle = \left(A + \sum_{\boldsymbol{k},\boldsymbol{q}} B(\boldsymbol{q},\boldsymbol{k})\hat{a}_{\boldsymbol{k}}^{\dagger}\hat{a}_{\boldsymbol{q}}\hat{c}_{\boldsymbol{k}-\boldsymbol{q}}^{\dagger}\right)|\phi_{FS}\rangle \tag{1.46}$$

where A is the amplitude of the state $|\phi_{FS}\rangle = |0\rangle \otimes |FS\rangle$ that describes a non interacting majority Fermi sea plus a minority atom with zero momentum, and $B(\boldsymbol{q},\boldsymbol{k})$ is the amplitude of the second state that describes a perturbed Fermi sea with a majority atom with momentum $\boldsymbol{q}$ (with $|\boldsymbol{q}| < k_F$) excited to momentum $\boldsymbol{k}$ (with $|\boldsymbol{k}| > k_F$).
To determine the properties of the polaron, one finds the amplitudes A and $B(\boldsymbol{q},\boldsymbol{k})$ that minimize the expectation value of the hamiltonian presented in Eq. (1.45).
The minimization leads to an implicit equation for the energy of the minority particle at unitarity $a \to \infty$:

$$E = \sum_{|\boldsymbol{q}|<k_F} \frac{1}{\sum_{|\boldsymbol{k}|>k_F}\left(\frac{1}{\epsilon_{\boldsymbol{k}}+\epsilon_{\boldsymbol{q}-\boldsymbol{k}}-\epsilon_{\boldsymbol{q}}-E} - \frac{1}{2\epsilon_{\boldsymbol{q}}}\right) - \sum_{|\boldsymbol{k}|<k_F}\frac{1}{2\epsilon_{\boldsymbol{q}}}} \tag{1.47}$$

where $\epsilon_{\boldsymbol{k}} = \hbar^2 k^2/2m$ the energy of a fermion with mass m.
At low momentum $\boldsymbol{k}_0$ of the impurity, the dispersion relation of the impurity can be expanded as:

$$E(\boldsymbol{k}_0) = \eta E_F + \frac{\hbar^2 k_0^2}{2m^*} + \dots \tag{1.48}$$

The moving impurity becomes dressed by the Fermi sea and that results in a quasiparticle with an effective mass m^* and binding energy ηE_F and $\eta < 0$.
These two parameters depend on the interaction strength $1/(k_F a)$, where a is the impurity-fermion scattering length. Far in the BCS limit ($1/(k_F a) \ll -1$), the impurity behaves as a free particle with mass m, thus $\eta = 0$.

At unitarity, a numerical solution of Eq. (1.47) yields $\eta \simeq -0.606$ and $m^* \simeq 1.17\, m$. Despite it being a variational calculation and can only give an upper bound for the value of η, it is remarkably close to the results obtained using variational Fixed-Node Monte-Carlo predictions [215] ($\eta = -0.58, m^* = 1.04\, m$), and using diagrammatic Monte-Carlo [216] ($\eta = -0.59, m^* = 1.09\, m$). This can be explained by the relatively weak probability of excitation of a particle-hole pair ($\simeq 25\%$ in the variational calculation), confirmed by an expansion of the polaron energy as a function of the number of excited particle-hole pairs that converges quite fast [216, 217]. Furthermore, experimental measurements from MIT using a density profile analysis [218, 219] and our group using a collective modes study [220] showed that the

effective mass is indeed close to unity, with $m^* = 1.06\,m$ and $m^* = 1.17\,m$ respectively, thus barely modified by the interactions. The results for η are summerized in Fig.1.4.

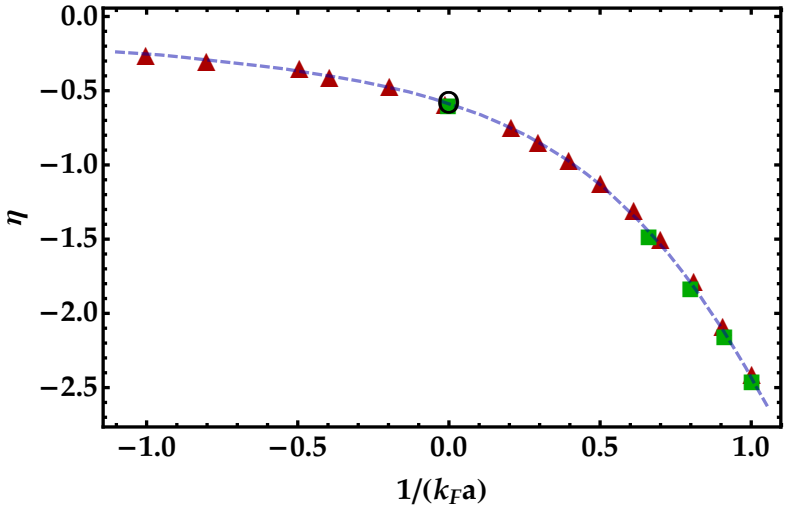

Figure 1.4: Fermi polaron energy. The blue dashed line gives the numerical solution for the ansatz with one particle-hole excitation [221]. Green filled squares show a few points obtained from the diagrammatic Monte-Carlo calculations [216]. Red filled triangles show points resulting from Fixed-Node Monte Carlo calculations [222]. The blue empty circle shows the result corresponds to a RF measurement at unitarity in agreement with the theories [198]. We see full agreement between the results obtained.

In the BEC limit, the impurity can form a dimer with an atom from the majority. It was shown that the phase transition is located at $(1/(k_F a) = 0.91)$, with a sharp crossing between the energy curves of the Fermi polaron and the dimer. Above this critical value, the impurity can be roughly considered as a boson interacting with the Fermi sea with an atom-dimer scattering length $a_{\mathrm{ad}} = 1.18\,a$ [134, 223, 224].

1.4.3 Impurity in a two-component Fermi gas

Experiments on dual superfluids raised many questions regarding the behavior of an impurity immersed in a superfluid of spin $1/2$ fermions [111, 225, 226]. In these experiments, the polaron is weakly coupled to the background superfluid and the interaction could be accurately modeled within mean-field approximation.
Further theoretical works explored the strong coupling regime between the impurity and the background fermions using mean-field theory to describe the fermionic superfluid [114, 117, 130]. They highlighted the role of Efimov physics in the phase diagram of the system and as a consequence some results were plagued by unphysical ultraviolet divergences.
Indeed, in the Fermi polaron case, no three-body effects are possible since Pauli blocking forbids interactions between spin polarized fermions. On the contrary, the Bose polaron is subject to Efimov effects [132] and three-body interactions play an

essential role in the strongly interacting regime.
The nature of the transition between the polaron and the trimer state is intriguing since it depends heavily on the background interactions. Indeed, it was shown in [130] using a mean-field approach to describe the superfluid, that superfluid excitations provide a strong coupling between the polaron and trimer state making for a smooth avoided crossing between the two branches. However, for a background Fermi sea in the normal state, it was shown in [118] that this transition takes the form of a sharp first order transition.

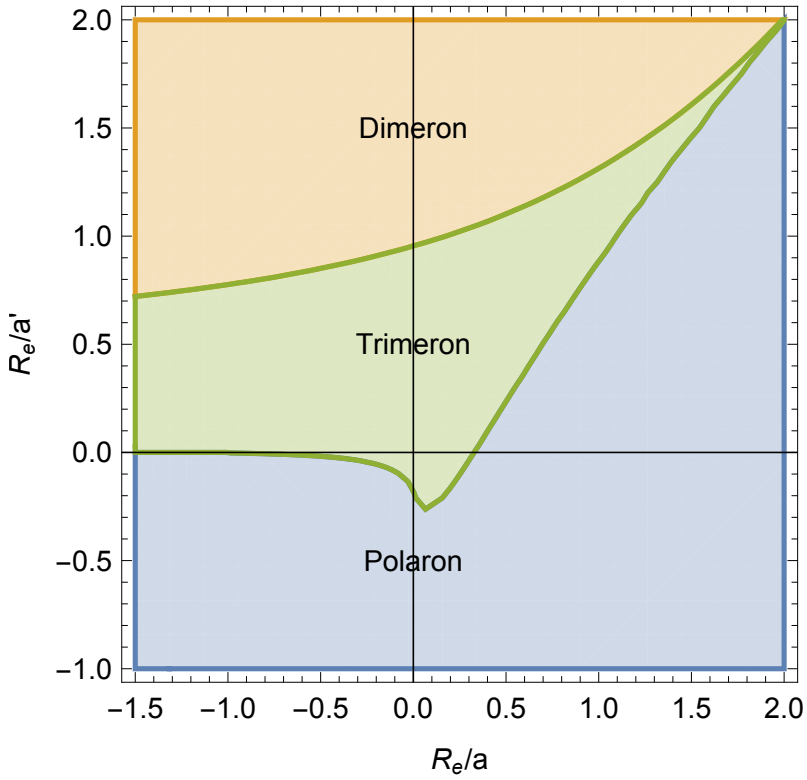

Figure 1.5: Stability diagram for an impurity in vacuum. Polaron, dimer and trimer states in the case of the impurity and two fermions with equal masses, and calculated using a coupled channel model (figure was taken from [117]). Variational approaches based on a mean-field description of the background superfluid suggest that the polaron/trimer transition is a crossover [130]. Here, a' designates the impurity-fermion interaction scattering length, whereas a designates that between the fermions. The diagram was obtained by calculating the energy of the polaron, trimer and dimer states and choosing the lowest value for each impurity-fermions and fermion-fermion interaction.

The presence of the two-component Fermi sea allows access to Efimov effects even for a fermionic impurity and a trimer bound state becomes accessible in the phase diagram of the problem along with the dimer state present in the strongly interacting regime. A phase diagram for the problem without the presence of the Fermi sea is shown in Fig.1.5. It was obtained (See supplemental material in [117]) by searching values where the mean field energies of the three sectors are equal.
Moreover, the presence of the Fermi sea allows us to study the transition between a

polaronic state in the presence of two component fermionic superfluid and a Bose polaron when the fermion-fermion interaction is increased.
The study of a polaron immersed in a two-component Fermi sea will be a central part of this manuscript. We will see how the calculation of the energy of the polaron in an interacting superfluid presents divergent terms which are reminiscent from the three-body physics which will be the main focus of Chapter 4.
The problem mentioned earlier regarding an impurity immersed in a non-interacting Fermi sea is going to be detailed in Chapter 5 where we will use a variational ansatz to explore the phase diagram.

Summary

In this chapter we have presented basic concepts concerning the physics of ultra-cold Fermi gases which are particularly relevant to the objectives of this manuscript.
A description of two-body and three-body physics and a review of the main theoretical results in their respective domains were first presented. These concepts will be used extensively in the last two chapters to help presenting the theoretical calculations done throughout my thesis work.
A particular focus on impurity physics was given, especially the case of a Fermi polaron, which will be relevant to two problems which will be discussed in later chapters.

Part I

The Lithium Experiment

This part deals with the Lithium 3 experiment that I joined as a PhD student from September 2017 to July 2019 under the supervision of Tarik Yefsah (in large majority) and Christophe Salomon.
My work contributed to the completion of the experimental apparatus and the optimization of evaporative cooling down to near quantum degeneracy.
This was a collective effort involving also Shuwei Jin, Julian Struck, Yann Kiefer, Darby Bates, Kunlun Dai, Bruno Peaudecerf and Joris Verstraten.

After I left the experiment to start a theory project, the Lithium 3 team achieved the precise characterization of quantum degeneracy through the analysis of in-situ profile of the gas and the previously measured Equation of state, as well as superfluidity. A more detailed description of the apparatus and results can be found in Shuwei Jin's PhD thesis [227].

Chapter 2

A new generation Lithium machine

The first part of thesis work included participating in building an experimental apparatus aiming at producing a Fermi superfluid of ^{6}Li atoms. To obtain a Fermi superfluid, several cooling steps are needed. This chapter will start with an overview of the ^{6}Li atom, and will mainly focus on the main experimental setup. An explanation of the cooling and manipulation steps will be presented and the technical details of its implementation in our setup will be viewed starting from the generation of a hot vapor of atoms to obtaining a degenerate Fermi gas.

2.1 Overview of the setup

The main goal of the experimental sequence is to achieve an ultra-cold atomic gas of ^{6}Li using laser cooling and manipulation techniques. The full apparatus is under ultra high vacuum $\approx 10^{-9}$Pa, which creates a low pressure environment in which minimal losses of the atoms are observed during the time required to run the experimental sequence, which is on the order of 1 minute.
The ultra-high vacuum system is comprised of several parts designed to produce, cool and image an atomic vapor of ^{6}Li atoms. An overview of the setup is presented in Fig. 2.1.
The sequence starts with the production of a hot Lithium vapor creating a vapor pressure which propels the atoms through a collimation tube. The atomic jet is then slowed down by the Zeeman slower, enough to be captured in the magneto-optical trap (MOT). The atoms are then cooled down further using D_2 and D_1 cooling techniques to a temperature which allows them to be captured efficiently by an optical dipole trap. The atoms are then transported optically to the science cell where they are captured by another optical trap which forms with the transport beam a cross dipole trap. Then the evaporative cooling starts in the cross dipole trap, and afterwards the transport beam is switched off and further evaporative cooling steps are performed on the atoms in the remaining beam.

At the end of the cooling sequence, we end up with a quantum degenerate spin 1/2 Fermi gas of ^{6}Li atoms at a temperature of a few tens of nano Kelvins. For the unpolarized phase the sample is in a superfluid phase.

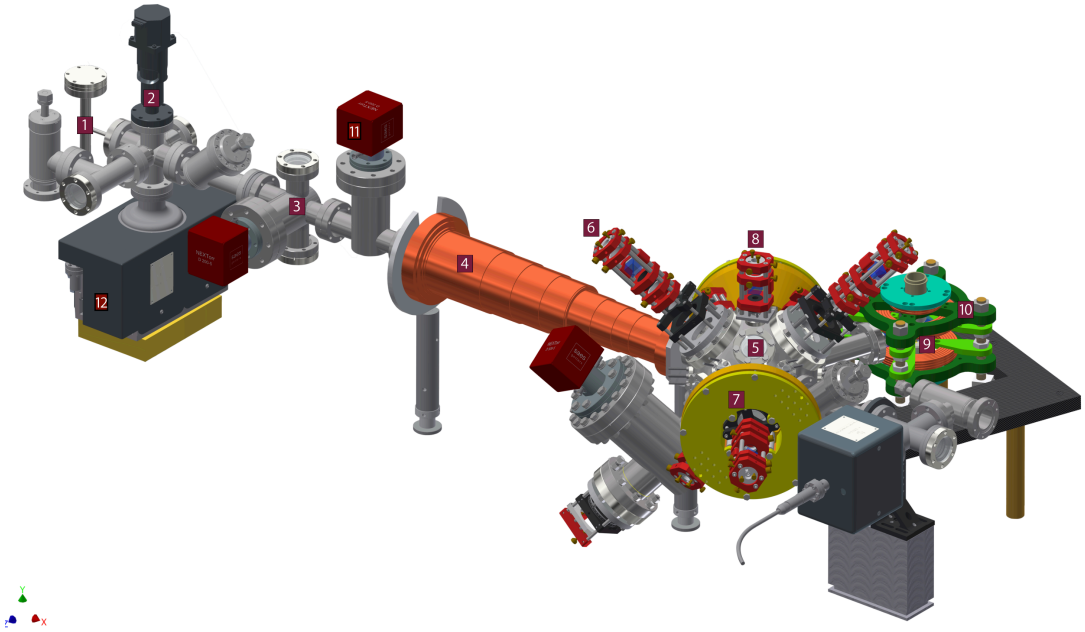

Figure 2.1: 3D CAD model of the main vacuum setup. The main parts are indicated: **1.** Oven. **2.** Atomic beam shutter. **3.** Differential pumping section. **4.** Zeeman slower. **5.** MOT chamber. **6.** MOT beam, 3 in total. **7.** MOT coil, 2 in total. **8.** D1 gray molasses beam, 3 in total. **9.** Science cell. **10.** Feshbach and curvature coils. **11.** Getter pumps. **12.** Ion pumps.

2.2 The ^{6}Li atom

Lithium is an alkali metal with atomic number 3. It appears naturally in two stable isotopes. ^{7}Li with four neutrons, and ^{6}Li with three. Since the two isotopes differ by a single spin-1/2 particle, they exhibit different quantum statistics. ^{7}Li is a composite boson, while ^{6}Li is a composite fermion. This thesis is solely concerned with the fermionic isotope. For more details on ^{6}Li refer to [126].

2.2.1 Level structure

^{6}Li has a single, unpaired valence electron. The ground state configuration is $1s^2 2s^1$, and the lowest excited state configuration is $1s^2 2p^1$. The spin-orbit interaction between the intrinsic angular momentum of the valence electron (spin S) and the angular momentum of its orbit (L) leads to the splitting of this line into the D_1 and D_2 lines, and to the fine structure levels each with an angular momentum $\boldsymbol{J} = \boldsymbol{L} + \boldsymbol{S}$, its possible values give rise to a quantum number $J \in [L - S, L + S]$.

Both of these states have a natural line width of $\Gamma_D = 2\pi \times 5.87$ MHz. These transitions give the excited states $2P_{1/2}$ and $2P_{3/2}$ corresponding to the values $J = 1/2$ and $J = 3/2$ respectively, with a relatively small fine structure splitting of ≈ 10 GHz. The D_2 line is used in the Zeeman slower, the magneto optical trap, the imaging and in repumping atoms during these phases, while the D_1 line is used only for D_1 gray molasses.

By increasing the resolution on the spectroscopic levels, the interaction with the nucleus can no longer be neglected and another splitting is observed. The nucleus spin ($I = 1$) interaction with the fine structure levels gives rise to another quantum number $F \in [J - I, J + I]$ and the hyperfine structure. The ground state $2S_{1/2}$ with $J = 1/2$ splits into two levels corresponding to $F = 1/2$ and $F = 3/2$ with a splitting of ≈ 228.8 MHz. The $2P_{1/2}$ splits also into two levels with $F = 1/2, 3/2$. While the $2P_{3/2}$ splits into three levels with $F = 1/2, 3/2, 5/2$.
Due to the weak coupling of the valence electron to the nuclear spin, the hyperfine splitting of the excited level $2P_{3/2}$ does not exceed the natural line width, which explains the lower limit of the MOT cooling of around the Doppler temperature. The full level structure is depicted schematically in Fig2.2.

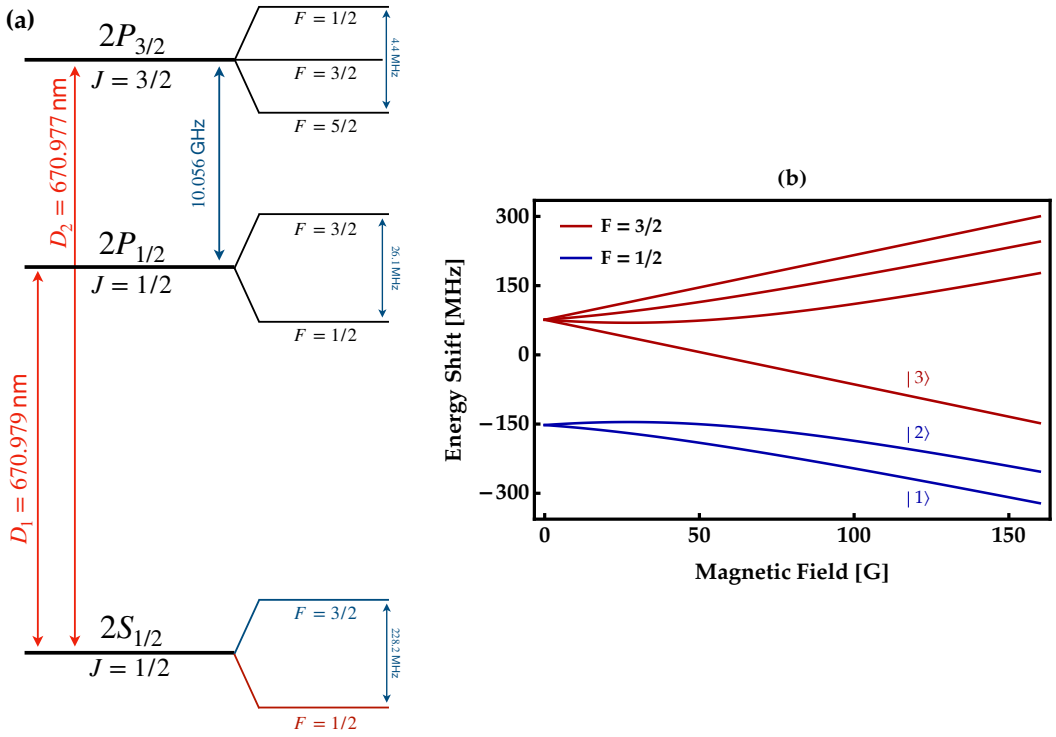

Figure 2.2: Level structure of ^{6}Li. (a): Fine and hyperfine structure of ^{6}Li atom. The ground state and $2P$ excited states are shown. Energy splittings are not to scale. **(b)**: Zeeman sub-levels of the lowest two hyperfine states, the lower two states will be used as two spin states for evaporative cooling.

In the presence of an external magnetic field, a final splitting occurs to the atomic levels, the Zeeman splitting, due to interaction between the intrinsic magnetic moment of the atom (spin) with the external magnetic field.
As the magnetic field increases from zero, the Zeeman interaction is initially small compared to the hyperfine interaction. Thus, we can treat the interaction pertubatively with respect to the hyperfine splitting. In this case, the vector $\boldsymbol{F}$ precesses around the magnetic field vector $\boldsymbol{B}$, and therefore F is still a good quantum number. When the coupling to the field is large compared to the hyperfine splitting, we enter the so-called Paschen-Back regime, where F is no longer a good quantum number. The full Hamiltonian needs to be diagonalized in $|m_S, m_I\rangle$ basis. Traditionally, the

lowest six states stemming from Zeeman splitting of the lowest two hyperfine states are denoted $|1\rangle, |2\rangle, \ldots, |6\rangle$.
This regime dominates in the case of ^{6}Li even for a few tens of Gauss since its hyperfine splitting is weak. In Fig.2.2(b) we show the Zeeman sub-levels of the lowest two hyperfine states. The energies are plotted using the Breit-Rabi formula [228] which is written for a state with $J = 1/2$ as follows:

$$\Delta E_Z(F_\pm = I \pm 1/2, m_F) = -\frac{hA_{FS}}{4} + g_I m_F \mu_B B \pm \frac{hA_{FS}(I+1/2)}{2}\sqrt{1 + \frac{2m_F x}{I+1/2} + x^2} \quad (2.1)$$

where we used the notation $x = \dfrac{(g_J - g_I)\mu_B B}{hA_{FS}(I+1/2)}$, and g_J and g_I are the Landé g-factors and A_{FS} is the magnetic dipole hyperfine constant. Refer to [126] for the values of these constants and for more details on the level structure.
In our setup, we work in the high field regime during evaporation, where we prepare the system in a balanced mixture of states $|1\rangle$ and $|2\rangle$.

2.2.2 Feshbach resonances of ^{6}Li

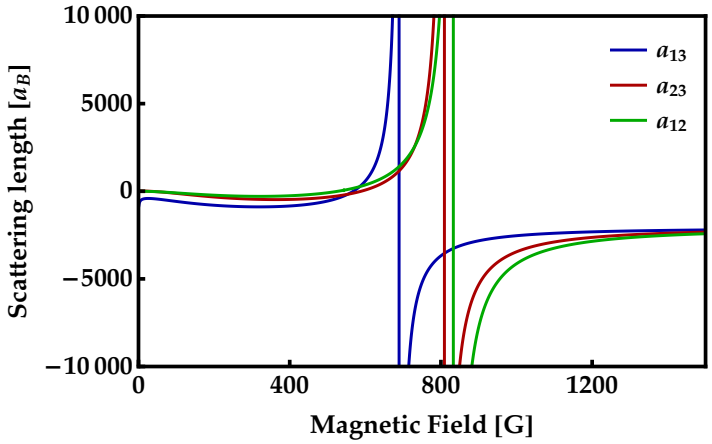

Figure 2.3: Feshbach resonances for ^{6}Li atom. Values of the s-wave scattering length for the three energetically lowest Zeeman sub-levels of the ^{6}Li atom. The scattering length is in units of Bohr's radius. Data was taken from [229].

One of the reasons leading to the wide use of ^{6}Li in cold atoms experiments is its extremely broad Feshbach resonances [42, 230]. For each pair of the three lowest hyperfine sub-levels in Fig. 2.2(b), i.e. $|1\rangle$, $|2\rangle$ and $|3\rangle$, there exists a Feshbach resonance around $\approx 300\,G$ wide.
For the evaporation process, we use mainly the states $|1\rangle$ and $|2\rangle$ after applying a bias field corresponding to the field value on resonance at $832\,G$, and we modify our imaging resonance to correspond to this at high field values.

2.3 Vacuum setup

Maintaining an ultra-high vacuum regime is essential for atomic gas experiments. Indeed, for atoms cooled down to mK or even μK, any collision with molecules from the residual room temperature gas would inflict huge atom losses. For this reason extra care is required in preparing the experimental environment to be extremely isolated and under very low pressure, usually lower than 1 nP (nanopascal).
Continuous pumping is provided by four getter pumps which use chemical absorption to get rid of Hydrogen mainly, which is too light to be pumped by other pumping methods. The getter pumps also have an ionic pump stage, which is mainly warranted by the two ion pumps.

2.4 671 nm Laser setup

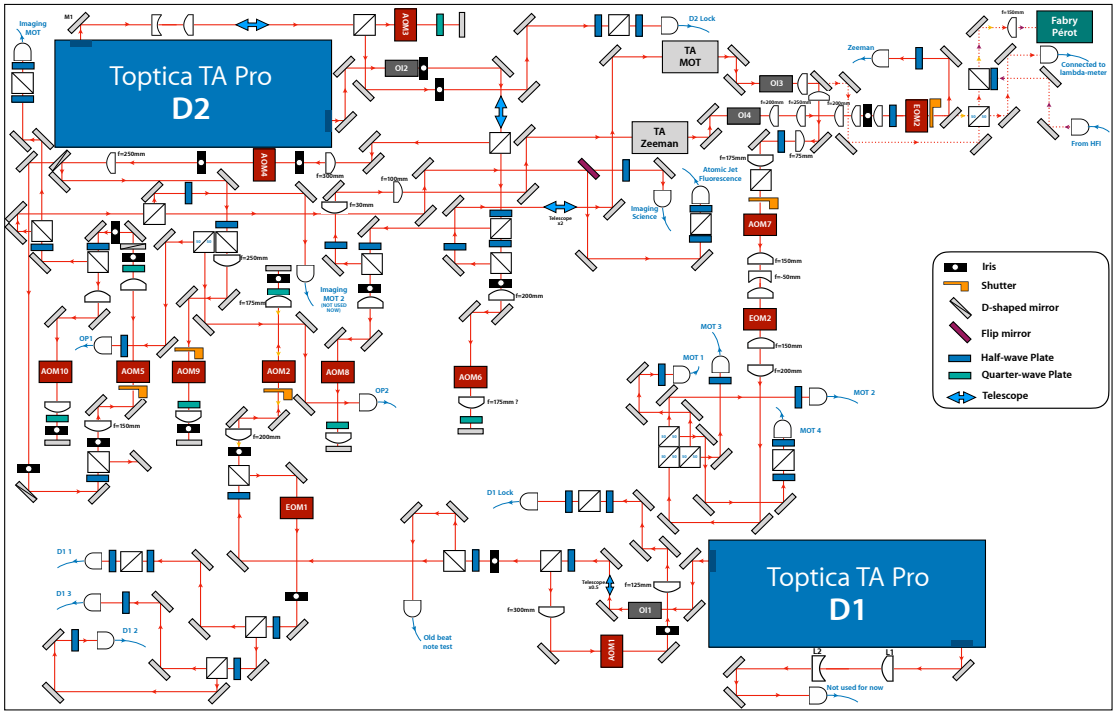

Figure 2.4: ^{6}Li optical table. Detailed reconstruction of the ^{6}Li optical table. The spectroscopy part is left out. We use two master lasers one for the cooling steps which use the D_2 transition (Zeeman, MOT, D_2 molasses), and the other is used solely for the D_1 gray molasses. To make up for the low power output of the Toptica lasers, we use two TA chips placed in the paths of the MOT and Zeeman beams.

We operate a dedicated optical table for all laser setups running at 671 nm used to cool, trap and image the atoms. At this wavelength, available laser diodes have typically 20 mW power, which is usually barely sufficient to capture and cool lithium atoms.
Although a 2.1 W solid state laser was designed and operated at this wavelength

[231], commercially available choices are still limited in their power. For our experiment, we use two Toptica TA pro lasers and two TA chips to deliver the power needed to the various optical setups needed.
The first laser is operated at the D_2 transition wavelength. The secondary output beam is sent through a spectroscopy cell containing Lithium vapor to lock the laser frequency. We use the modulation transfer spectroscopy technique [232] to lock the laser on the transition $|F = 3/2\rangle \rightarrow |F' = 5/2\rangle$.
The primary output power (around 350 mW) is separated into two main paths, one for the Zeeman slower and one for the MOT beams. Each beam is amplified by a TA chip to reach the required intensity.
For the Zeeman and MOT beams, an electro-optical modulator (EOM) is used to generate sidebands with a power equal to 10 % of the main carrier power. The sideband will provide the repumping needed during the Zeeman and MOT phases as we will see in the next section. The MOT beam is separated into four beams to provide the light for all MOT arms.
The second laser is operated at the D_1 transition wavelength. A part of the main output beam is sent also through the spectroscopy cell to lock the laser frequency on the crossover between the transitions $|F = 1/2\rangle \rightarrow |F' = 3/2\rangle$ and $|F = 3/2\rangle \rightarrow |F' = 3/2\rangle$. Similar to the first laser, an EOM is used to generate the repumper sidebands.
A detailed schematic of the laser table setup is shown in Fig.2.4.

2.5 Absorption imaging

Working principle

To get quantitative information regarding the atomic cloud, we take images of the cloud and analyze the resulting density profiles. From that we can extract many experimental parameters e.g. temperature, atom number, velocity distribution, position, etc ...
To that aim we use absorption imaging. In its simplest form, when we shine a resonant laser beam on a cloud of atoms, the absorption of photons of the beam results in an intensity profile which reflects the density profile of the imaged cloud. The atomic density on the camera sensor could be related to the attenuation of the light intensity using Beer-Lambert law which can be written in 3D as:

$$OD(x,y) = -\ln\left(\frac{I_f(x,y)}{I_i(x,y)}\right) = \sigma\,\tilde{n}(x,y) \quad ; \quad \tilde{n}(x,y) = \int_{-\infty}^{\infty} n(x,y,z)dz \tag{2.2}$$

where I_f, I_i are the probe beam intensity values before and after the atomic cloud respectively, and σ is the scattering cross section, defined by the probability of a photon to be scattered by an atom, it is given by:

$$\sigma = \frac{\sigma_0}{1 + I_0/I_{sat} + 4\delta_L^2/\Gamma_D^2} \tag{2.3}$$

where $\sigma_0 = 3\lambda^2/(2\pi)$ is the scattering cross section on resonance, δ_L is the aforementioned laser detuning with respect to the atomic transition, Γ_D is the natural line width, I_{sat} is the saturation intensity of the transition we use for imaging.

Implementation

In practice we take three consecutive images of the atoms, the first one with the atomic cloud and the probe beam, resulting in an intensity profile $I_f = I_{at}$, the second one is only with the probe beam I_i, and the third one without neither the atoms nor the probe beam I_{ref}. We reconstruct the optical density (OD) as follows:

$$OD(x,y) = -\ln\left(\frac{I_{at} - I_{ref}}{I_i - I_{ref}}\right) \tag{2.4}$$

Noting that this designates the optical density integrated over the imaging direction. To calculate the atom number for instance from previous data we simply integrate the whole optical density profile and divide by σ:

$$N_{at} = \int\int \tilde{n}(x,y)\mathrm{d}x\mathrm{d}y = \frac{1}{\sigma}\int\int OD(x,y)\,\mathrm{d}x\,\mathrm{d}y \tag{2.5}$$

To calculate the temperature we use the time-of-flight technique. Using this techniques implies the assumption that the thermal energy of the cloud is much higher than its interaction energy. To perform the measurement, we take several images with different expansion times of the atomic cloud after having turned off the trap. The cloud expands ballistically in time, and its size changes as follows:

$$z(t) = \sqrt{z_0^2 + b^2t^2} \tag{2.6}$$

where z_0 is the root mean squared size of the cloud (assumed to have a Gaussian spatial profile) before expanding, and b is a parameter determined by the velocity of expansion.
The temperature of the cloud is related to the expanded (Gaussian) width by the relation $T = m\sigma_v^2/k_B$. So by fitting several cloud width values at different times we can extract the temperature and initial size of the cloud.

For our imaging system for the MOT we send a resonant laser on the transition $|F = 3/2\rangle \rightarrow |F' = 5/2\rangle$ with linear polarization, the imaging beam is several millimeters wide at the atoms position. Then we place a double convergent lens with equal distance to have the atoms in the object plane and the camera sensor in the imaging plane. Since atoms during the MOT phase could fall down to the $|F = 1/2\rangle$, before each imaging sequence we shine a repumper beam resonant with the transition $|F = 1/2\rangle \rightarrow |F' = 3/2\rangle$ to transfer the atoms to $|F = 3/2\rangle$ state.
As suggested by Eq. (2.2), there is an interplay between the intensity of the probe beam and the maximal optical density (OD) value obtained, since for lower intensity values compared to the saturation intensity we increase the cross section and correspondingly the maximal OD value. However, for low intensities, the number of incident photons becomes lower, for this reason we use special cameras [1] which feature CCD sensors with very high quantum efficiency i.e. incident photon to converted electronic count ratio. Also, we tune our probe beam intensity to around $I = 0.1\, I_{sat}$.

[1] For instance PCO.Pixelfly CCD camera which has a quantum efficiency of 50% for 670nm light.

High field imaging

To probe atoms in the science cell with a bias magnetic field of 832 G during evaporation, the imaging beam frequency needs to be red-detuned of about 1 GHz according to the Breit-Rabi formula. This is done by using another laser source and performing an offset-lock with the D_2 laser [233]. For technical details refer to [234].

2.6 Magneto-optical trap

The MOT loading is the first trapping step towards preparing an ultracold fermionic superfluid of ^{6}Li. It brings down the temperature of the hot atomic vapor to the mK range.
By imaging the cloud at this step many debugging issues could be resolved early and easily. Furthermore, the MOT is the starting phase for further cooling techniques and eventually for optical transport towards the science cell where the experiment actually takes place. As the name suggests, this phase includes the simultaneous trapping and cooling of the slow atomic beam by the MOT beams and the magnetic field gradient created by the MOT coils. The steps towards loading the MOT are presented in moderate detail in this section.

2.6.1 Atomic beam

The oven is a T-shaped tube filled with about 1g of natural Lithium and 1g of pure ^{6}Li. Since the natural abundance of ^{6}Li is around 7.5 %, with this choice we have approximately equal amounts of ^{6}Li and ^{7}Li. An illustration of the oven is found in Fig.2.5.

Its temperature is stabilized using a relay system which reads constantly the temperature of the oven and keeps it close to a predetermined threshold. This is done by connecting to a control module two heating elements wound around the two parts of the tube, the vertical and horizontal ones, and two thermocouples positioned to measure both temperatures. The first vertical part is the main oven chamber, it is heated to about 500°C to get high pressure vapor ($\approx$ 10mP), since Lithium has very low vapor pressure at room temperature [126].

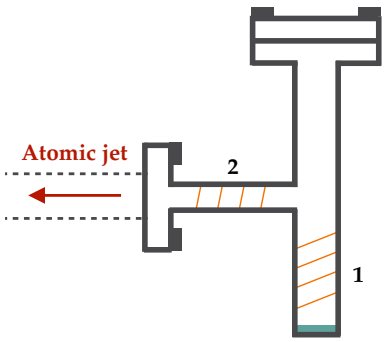

Figure 2.5: The oven. The oven is T-shaped, tube 1 is where Lithium is stocked and it is heated to around 500°C. Tube 2 is the collimation tube and is heated to around 550°C.

The second part is a 5 mm diameter tube which is heated up to 550°C to avoid having Lithium building up and clogging the tube, to create a first differential pumping step which separates the high vacuum oven part from the ultra-high vacuum experiment, and to collimate the atomic jet. For more information about the oven design and function refer to [235].

The pressure build-up produces a collimated atomic beam moving with a mean thermal velocity $v_T = \sqrt{2k_BT/m} = 1700$ m.s^{-1}.

The atomic flux is estimated in these conditions by collecting the fluorescence light scattered by the atomic jet near the output of the oven when shone by a resonant laser beam. The result is about 3×10^{12} atoms/s, which is good when compared to other similar experimental setups [235].

Moreover, in order to avoid the accumulation of atoms on the glass window on the other side of the machine, and more importantly to avoid having collisions between the atomic jet and the MOT atoms once the MOT is loaded, an electronically controllable shutter is positioned at the output of the oven. An electronic circuit receives a TTL signal from the control module connected to the main experiment control computer, which activates an Arduino module controlling a stepper motor which moves the shutter. The shutter is opened during the MOT loading phase only and then it remains closed until the end of the experimental run.

2.6.2 Zeeman Slower

Working principle

The capture velocity of MOT traps is about ≈ 50 m.s^{-1}, so atoms exiting the oven must be slowed down to be collected by the MOT. Consider a two level atom with an atomic transition frequency $\omega_A/2\pi$ moving with a mean thermal velocity v_T = 1700 m.s^{-1}. In order to slow it down, we send a counter-propagating laser beam with frequency $\omega_L/2\pi$ close to the atomic transition frequency $\omega_A/2\pi$. Due to their relative movement, the atomic transition frequency must be shifted from the atomic resonance to account for the Doppler effect by an amount $\mathbf{k}_L.\mathbf{v}$ where $\mathbf{k}_L$ is the wave vector of the laser and $\mathbf{v}$ is the velocity of the atom. As a rule of thumb, an atom moving at 1 m.s^{-1} is shifted by 1 MHz with respect to a light beam with $\lambda = 1\,\mu$m.
If the laser frequency is tuned to match the atomic transition frequency taking into account the Doppler shift, the atom absorbs with large probability a photon with momentum $\hbar\mathbf{k}_A$ and reemits another one in any direction, resulting on average in a reduction of its velocity by an amount $v_R = \hbar k_A/m$ which is the recoil velocity of the ^{6}Li atom in our case. Soon enough, the atom will be slowed down to a velocity which changes the Doppler shift significantly to a point where the laser beam becomes out of resonance with the atomic transition.
To solve this problem we can either chirp the laser frequency or create a laser beam with several sidebands in a given interval which accounts to the Doppler broadening, or apply a fine tuned spatially varying magnetic field which causes the Zeeman sublevels to change their energy splitting values in a way to be always resonant with the laser beam at taking into account the Doppler shift. The latter proposition is the basic idea behind the Zeeman slower [236] [2].
The position dependent magnetic field $B(z)$ should verify:

$$\mu_B B(z) = \hbar(\omega_L - \omega_A) + \hbar\mathbf{k}_L.\mathbf{v}(z) \tag{2.7}$$

where μ_B is the Bohr's magneton.

[2] The Nobel prize in physics in 1997 was awarded to W.D. Phillips, S. Chu and C. Cohen-Tannoudji for the development of methods to cool and trap atoms with laser light.

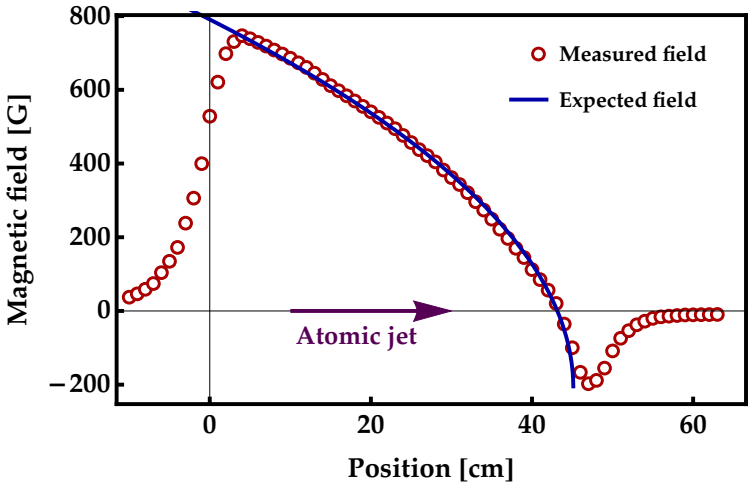

Figure 2.6: Magnetic field of the Zeeman slower. Measured magnetic field values at multiple positions of the Zeeman slower with a current $I = 20A$ (red dots), and expected variation of the magnetic field calculated for the same current value (blue line). Here the position at 0 corresponds to the beginning of the Zeeman slower for atoms coming from the oven. The measured and expected values are in satisfactory agreement. Figure adapted from M. Delehaye's thesis [237] and S. Jin's thesis [227].

Implementation

In the experiment, the slower is a 60 cm tube with 24 layers of copper wires wound around it creating solenoids of decreasing diameter to match a predetermined magnetic profile, a current of 20 A is passed through the slower.
The atomic transition used for slowing down the beam is on the $D2$ line, $|F = 3/2, m_F = 3/2\rangle \rightarrow |F' = 5/2, m_F = 5/2\rangle$. The light used is a locked monochromatic 671nm light (see section 2.4), the source is a Toptica TA Pro laser, then it is amplified by a TA chip to get around 80mW of power on the atoms. The laser beam has a diameter of approximately 1 cm at the entrance of the opposite side of the MOT chamber and it is focused at the position of the oven to account for the divergence of the atomic beam while it propagates to the MOT chamber. The light has a σ^+ circular polarization, driving transitions with $\Delta m_F = 1$, which locks the atoms in a cycling transition $|F = 3/2\rangle \rightarrow |F' = 5/2, m_F = 5/2\rangle$. The chosen magnetic field profile is a spin-flip configuration, see Fig.2.6, where the field starts with a high value $B(z = 0) = 600$ G and has a zero-crossing before the end of the slower tube, where the field is reversed and arrives at a value of -200 G and the field has a non-zero value at the end of the tube $B(z = l) = 4$ G, where l is the length of the slower.
The spin-flip configuration is achieved practically by starting to wind coils with a relatively big diameter, then gradually decreasing that until it is zero, then before the end of the slower tube, repeating the same process backwards, by starting with small diameter coils and finishing with bigger ones, creating an inverted Zeeman slower at the end of the first one to create a field in the opposite direction. The field has a zero in the region between the two 'sub-slowers'.

This configuration has many advantages, on the one hand, an increasing mag-

netic field configuration requires a significant compensation field for its final field value in the MOT chamber, while on the other hand, a simple decreasing field configuration ends with a zero-field value making the Zeeman light resonant with the atoms in the MOT chamber, and is detrimental to the trapping efficiency of the MOT. Moreover, both configurations consume more power than the spin-flip configuration. All of the previous problems are totally avoidable with the spin-flip configuration. However, it has two main problems which need to be taken into account.
First, since the field value at the entrance of the MOT chamber is not strictly zero, we need to add a compensation coil which brings the field value to zero at the position of the MOT cloud.
Second, since there exists a region where the magnetic field vanishes, where due to stray fields from the slower solenoids which become more prevalent now that the strong magnetic field component parallel to the slower axis is zero, the atomic spin could precess around these field vectors and this results in atoms decaying back to $|F = 1/2\rangle$ after having absorbed the slower light which is a dark state for the slower beam.
For the previous reason, this configuration requires an additional beam which we call the repumper beam, which is derived from the main beam and detuned using an EOM at 228 MHz and at around 10 % of the main beam power. This beam works on pumping the atoms in the zero and negative field regions back to a state which the slower beam could target.
The Zeeman slower slows down atoms to a velocity of around 50 m.s^{-1} which is within the capture capacity of the MOT. For more details on the subject we refer to the following theses [235, 237, 238].

2.6.3 Magneto-optical trap (MOT) and compressed MOT

Working principle

Atoms arrive in the MOT chamber with a mean velocity of around ≈ 50 m.s^{-1} after being slowed in the Zeeman slower. The idea behind the trapping method is to imprint the spatial distribution of the slowed atomic jet on different values of Zeeman shifts induced by a magnetic field which brings the atoms transition closer to a red-detuned light which brings back the atoms towards the center [15]. We see in Fig.2.7 an oversimplified illustration of the trapping method in 1D.
Consider an atom with two hyperfine levels $|F = 0\rangle$ and $|F = 1\rangle$ with a transition frequency $\omega_A/2\pi$. In the presence of a magnetic field which changes its sign at the origin (anti-Helmholtz coil configuration), the $|F = 1\rangle$ level splits into three Zeeman sub-levels with $m_F = -1, 0, +1$ with an energy which depends on the position and is proportional to the magnetic field gradient.
The next ingredient is to shine two counter-propagating laser beams parallel to the field vector with frequency $\omega_L/2\pi$. The frequency of the laser is red-detuned with respect to the atomic transition with detuning $\delta_L = \omega_L - \omega_A < 0$. The beams are circularly polarized with σ^+ and σ^- polarizations.
When an atom in the ground state is displaced parallel to the z-axis, the laser beam coming from the opposite direction (with polarization σ^-) becomes resonant with

the transition $|F = 0, m_F = 0\rangle \rightarrow |F = 1, m_F = -1\rangle$ and the radiation pressure force pushes back the atom towards the center of the trap. Similarly, when an atom is displaced in the other direction it is pushed back by the beam with σ^+ polarization. The displaced atoms also loses energy due to emitting a photon in a random direction, which also creates a cooling effect, this is the basic principle behind Doppler cooling.

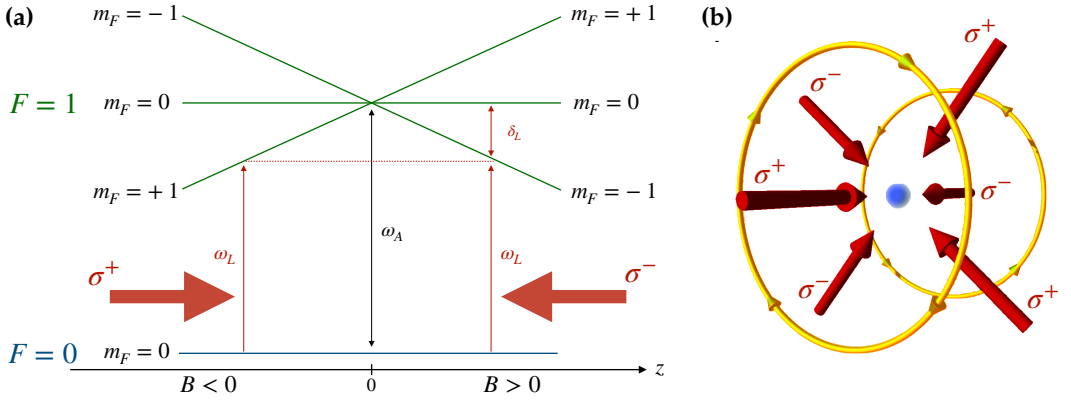

Figure 2.7: Magneto-optical trap. (a). Simplified illustration of the working principle of a MOT. In reality, the situation is more complicated since both the ground and excited states have several Zeeman sub-levels. **(b).** MOT beams configuration schematic, the two coils (in yellow) are in anti-Helmholtz configuration.

The combined effect creates an efficient trapping method capable of trapping and cooling the atoms to temperatures which could theoretically reach the Doppler temperature. This temperature is around 150μK in the case of ^{6}Li.
However, typical temperatures at the end of this phase are 5 or 6 times the Doppler temperature, which is in part due to the unresolved hyperfine structure of the D_2 line in ^{6}Li which causes heating due to atoms depumping from non-targeted levels, also to collective photon scattering phenomena.
Indeed, after a certain atomic density threshold, the probability for a photon emitted by an atom to be reabsorbed by neighboring atoms becomes significant which creates a repulsive effect between the atoms [239]. A possible remedy was the dark-spot technique where the MOT beams are blocked in a diameter smaller than the cloud's diameter, which creates a region where no spontaneous emissions occur [240]. In our case, we do not need this kind of mechanisms because the MOT phase is followed by a gray molasses phase which is much more beneficial in terms of phase space density gains.

Implementation

In the experiment, our setup includes two identical coils to generate a magnetic field gradient on the order of 10 G/cm. The coils are shaped like cones in order to allow more optical access to the main MOT chamber. As for the MOT beams, they are derived from the same beam, red-detuned by -3Γ with respect to the $|F = 3/2\rangle \rightarrow |F' = 5/2\rangle$ transition. They are also superposed with a repumper beam which is detuned by 228 MHz to pump back atoms from the $|F = 1/2\rangle$ state as was the case for the Zeeman slower.

The beams are split into four arms in 3 perpendicular axes. In one direction we install two counter-propagating beams, and we use mirrors in the other two directions to reflect back the beam. The output power per MOT arm is $P_0 \approx 10\,\text{mW}$ with a waist $w_0 = 7\,\text{mm}$, leading to an intensity $I = 2P_0/(\pi w_0^2) \approx 5I_{sat}$, where I_{sat} is the saturation intensity of the D_2 line $I_{sat} = 2.54\,\text{mW/cm}^2$.

During the experimental sequence, we switch on the magnetic field and the MOT beams during 2 s, trapping around 10^9 atoms on average. Afterwards, while keeping the MOT beams power stable, we increase the density of the cloud by ramping up the current in the coils linearly during 50ms, increasing the gradient to 25 G/cm. The compressed MOT cloud at the end of this step has a 2 mm diameter and a temperature slightly more than 1 mK. The last step helps in increasing the density of the cloud without huge temperature jumps, which increases the collision rate, an important parameter for the evaporation as we shall see.

2.7 Optical molasses

The MOT represents an essential step in cooling the atomic gas, at the end of which we have phase space densities on the order of $n\lambda_{dB}^3 \sim 10^{-6}$, and while it is a big step compared to the initial thermal state of the gas in the 500°C oven, it is far from enough for the atoms to be loaded in an optical trap with a depth of 1 mK which is the main objective behind the first cooling steps.
For that we wish to improve the phase space density. To this end, we need to reach sub-Doppler temperatures, and we do that by means of employing gray molasses cooling technique on the D_1 spectroscopic line.

2.7.1 D_2 molasses

Motivation and working principle

The gray molasses technique, as we shall see in 2.7.2, involves light shifts of the Zeeman sub-levels, which are generally orders of magnitude smaller than shifts caused by bias fields. In fact, in their first studies, these shifts were approximated by 'fictitious' bias magnetic fields [241] which cause Zeeman splittings similar to the one we see in weak bias field regimes. This translates experimentally to the fact that all magnetic field gradients should be turned off for the gray molasses to work efficiently.
As the electric current in the large MOT coils is still circulating, turning off these coils includes a transitional phase of several milliseconds where the fields and the subsequent induced fields, eddy fields, go to zero. This brings out the need for a step in the experimental sequence between the MOT phase and the D_1 cooling phase where the atoms are still subject to a friction force confining them, and naturally, this step should not require any magnetic components. In our case we decided to go with an optical molasses on the D_2 line, which requires basically that we keep the MOT beams while turning off the fields.
Optical molasses work similarly to the optical part in the MOT, the only difference is that the spatial Zeeman splitting does not exist anymore due to the absence of the

magnetic field gradient [3]. Instead, the moving atom's transition is shifted only by a Doppler shift resulting from its velocity component towards the light source, which results in the transition becoming resonant with the red-detuned laser soon enough and a radiation pressure force causing friction and cooling.
This method is generally known as Doppler cooling [11].

Implementation

We switch off the MOT coils and keep the beams for a duration of 3 ms, at the same time we change the frequency of the beams by means of commanding a voltage controlled oscillator (VCO) connected to an accousto-optical modulator (AOM) on the path of the beam. This brings the detuning from -3Γ to $-\Gamma$. Also we decrease the beam intensity by 25%. At the end of this phase we obtain an optical molasses with a temperature of around 900μK.

2.7.2 D_1 gray molasses and sub-Doppler cooling

Working principle

As explained in the previous section, the typical phase space density achievable in the MOT phase of ^{6}Li is too low in order for the subsequent optical trapping techniques to work efficiently. Several techniques have been explored, for instance, a lithium quantum gas was produced by exploiting the higher-lying ultra-violet transitions of ^{6}Li [242]. While the narrow transitions give rise to much lower Doppler temperatures, these methods involve many technical difficulties we would rather avoid.

Historically, sub-Doppler temperatures were observed in optical molasses of sodium atoms [16,243], which led to several theoretical studies to explain the observed temperatures. The explanation came as a cooling mechanism in play which was coined Sisyphus cooling or polarization gradient cooling [17,244].

In this scenario, two counter-propagating beams with perpendicular linear polarizations create a spatially dependent periodic polarization gradient. An atom in its ground state with two Zeeman sub-levels g_-, g_+ will see its ground state degeneracy lifted by the effect of the polarization [241]. The atom, depending on its position, will interact with light with different polarization. This creates a periodic potential in which the atom is moving which also changes its pumping rate depending on its position in the potential.
An atom in a state g_+ in an interval with polarization σ^- is in a potential valley by construction for negative detuning of the laser beam. It transforms while moving its kinetic energy to potential energy while climbing the potential, and upon reaching the hill, the polarization changes back to σ^+. Here, the probability of the atom being pumped back into g_- by emitting a photon with an energy which is equal to the energy it spent climbing is maximum at this point. The cycle goes on, and on average the gas cools down. The randomness of the spontaneous emission process gives a

[3] In fact, the mechanism behind the optical molasses was already at play during the MOT phase as we mentioned, which contributed to the cooling of the cloud.

lower bound to the gas temperature, the recoil temperature, which is around 3.5 μK for ^{6}Li.

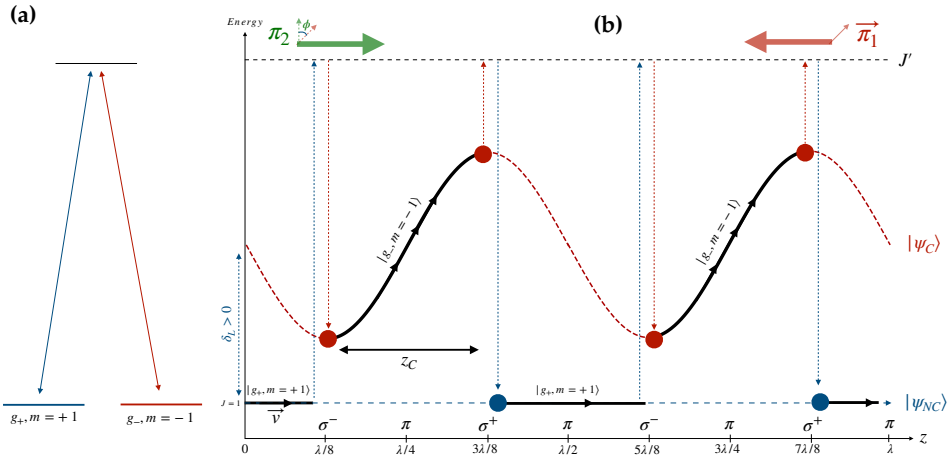

Figure 2.8: D_1 **cooling mechanism. (a).** The ground state configuration without coupling to the light field, $|g_+\rangle$ and $|g_-\rangle$ are degenerate. **(b).** The state configuration after coupling to the light field. For a polarization configuration with two linear polarizations with an angle ϕ, the motion of the atom allows for an atom initially prepared in a state $|\psi_{NC}\rangle$ to have a non-zero probability of decaying into a coupled state, and this coupling is maximal when the two energy levels are close. A second scattering process brings back the atom into the non-coupled state.

The only drawback of the previous method is the persisting coupling between the atoms and the light field, which means that the atoms could still interact with each other by means of multiple photon scattering which could excite atoms back to potential maxima and increase their kinetic energy instead of decreasing it. For this reason people have tried to incorporate dark non-coupled states in which the atoms weakly interact with the light field. Gray molasses is one of these techniques which was first proposed in [245–247] in the follow-up of different experimental schemes using Λ transitions [18].

Consider an atom with a transition $J = 1 \leftrightarrow J' = 1$ moving in a polarization induced potential created by two counter-propagating beams with polarizations forming an angle ϕ. Its Zeeman sub-levels will have a Λ form as in Fig.2.8.b. in which we have a superposition of non-coupled ground states for each polarization value, for instance, for a σ^+ polarized light, atoms in the state $|J = 1, m_J = +1\rangle$ are not coupled to the light field, and the same holds for $|J = 1, m_J = -1\rangle$ when the polarization is σ^-. The coupled state feature the same polarization induced spatially varying potential as in Sisyphus technique, and it is shifted to higher energies if the laser is blue detuned $\delta_L > 0$. An illustration of the mechanism is shown in Fig.2.8.
An atom in a dark state $|\psi_{NC}\rangle$ has a probability of emitting a photon and decaying (with a probability $1/2$) into the coupled state $|\psi_C\rangle$, this results from the motion of the atom in the polarization induced potential, and it is dependent on the angle ϕ, for more details see [246, 248]. This probability is highest in the minima of the periodic potential. Once the atom is in a coupled state, the same Sisyphus cooling scenario plays out, the atom climbs the potential for a distance $z_C = v\,\gamma_C$ with γ_C

the pumping rate of the laser beam. The atom then decays back to a non-coupled state when the polarization changes again. The cycle continues until the atom has very small velocity causing the overall temperature of the gas to cool down. The only inconvenience is that for this configuration, the Doppler mechanism will cause heating due to the positive detuning, which could be negligible if the atoms velocity is sufficiently small at the beginning of this phase.

Gray molasses was first realized experimentally with ^{87}Rb and ^{133}Cs atoms [249, 250], using the D_2 line. For ^{6}Li atom, the excited-state hyperfine splitting on the D_2 transition is small (4.4 MHz for ^{6}Li) compared to the natural width of the transition Γ_D. So any control over these levels is lost if we want to repump atoms which fall in dark states and the overall efficiency of the gray molasses technique falls drastically. An alternative is to use the D_1 line which has larger hyperfine splitting (26.1 MHz for ^{6}Li). Since 2012, D_1 gray molasses has been used by several groups in cooling atomic species like Lithium, Potassium and Sodium, started by our group [251,252]. It has become a standard technique for sub-Doppler cooling due to its easy implementation and high efficiency. For all these species the lowest temperatures achieved are on the order of $10-12$ times the single photon recoil temperature.

Implementation

As we saw, since the gray molasses efficiency is very sensitive to external magnetic fields, all bias fields should be strictly zero before starting this phase. To this end we install three pairs of compensation coils and we use the atom number and temperature of the D_1 cloud to calibrate these fields.

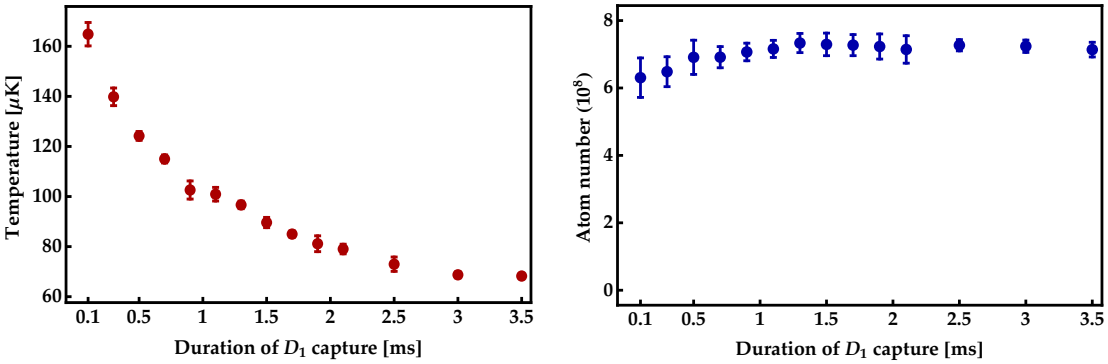

Figure 2.9: Performance of D_1 cooling. Temperature and number of atoms as a function of the duration of D_1 capture. We see that after 3 ms of capture time, we reach a stationary regime where the temperature stabilizes and we do not suffer from atom losses. Figure adapted from S. Jin's thesis [227].

We use three retro-reflected beams in three directions, one of them is superposed with one of the MOT arms with a power of ≈ 80 mW and a waist of 8 mm, while the others are independent and pass through different windows of the MOT chamber with a power of ≈ 20 mW and a waist of 4 mm, giving an intensity $\approx 30 I_{sat}$[4] in

[4] As tradition goes, I_{sat} used for all calculations is the one for the D_2 line.

each direction. The beams are blue detuned with respect to the transition $2S_{1/2}, F = 3/2 \rightarrow 2P_{1/2}, F' = 3/2$, we also install a repumper beam resonant with the transition $2S_{1/2}, F = 1/2 \rightarrow 2P_{1/2}, F' = 3/2$. The repumper is derived from the main beam and its frequency is modulated using a dedicated EOM driven by a DDS circuit with a linewidth of 20Hz, insuring a good coherence between the two beams.
The experimental sequence is the following, first we switch on the compensation coils which reach their stationary regime in about 1 ms. At the same time we switch on the D_1 beams at full intensity during 3 ms to capture the atoms from the D_2 molasses. Afterwards we decrease during 2 ms both the principle and repumper intensity values to 50% of the initial value, we leave them at this value for 1 ms to allow the cloud to thermalize, this step seems to decrease the temperature by about 30% without significant atom losses.
The logic behind the previous steps lies in the fact that the gray molasses capture velocity scales as I/δ^2 and the temperature of the molasses scales as I/δ, with I the beam intensity and δ the beam detuning. That means that first we have to shine a high intensity beam to increase the capture efficiency, then by decreasing the intensity in the second step we cool down the cloud.

The intensity ramp has been optimized by taking different intensity ratios and measuring the temperature and atom number of the D_1 cloud, we noticed that if we ramp down the intensity to $< 50\%$ the temperature continues to drop while atom losses increase slightly. For 10 % of the initial intensity we get a cloud with $T = 20\,\mu$K and less than 10 % of the initial atom number. The final step is turning off the repumper beam alone for $10\,\mu$s, this drives the atom population into the $|2S_{1/2}, F = 1/2\rangle$ state, which means a cloud consisting of a mixture of atoms in states $|1\rangle$ and $|2\rangle$, which will be beneficial for subsequent cooling steps.

At the end of this step the cloud is cooled down to around 70μK and we have an average of 6×10^8 atoms which constitutes about 80 % of the atom number in the D_2 molasses cloud. We report in Fig.2.9 measurements done on the D_1 cloud.

2.8 Optical dipole traps

In previous sections we have encountered trapping techniques relying on the radiation pressure force. These near-resonant traps allow to capture and accumulate atoms even from a thermal gas. However, the performance of these traps is limited in several ways. The reachable temperature is limited by the transition line-width (or recoil energy for narrow lines), the attainable density is limited by light-assisted inelastic collisions, and the overall internal dynamics are perturbed by resonant processes. So in order to be able to manipulate the atomic cloud further, e.g. to perform evaporative cooling or to study the evolution of the system in different trap geometries, one has to resort to non-dissipative trapping methods with which we are able to trap the gas without unnecessary perturbations to its dynamics.

A first example of these non-dissipative methods is magnetic trapping [20, 253]. Relying on the Zeeman interaction between the atomic spin and an external magnetic field, we can trap atoms depending on their spin state by using pairs of coils positioned carefully to create the required potential. Magnetic traps have been pop-

ular in the cold atoms community for their deep potentials, practicality and stability after installation. However, the existence of the coils limits the optical access, the nature of the Zeeman interaction renders the trap state-dependent, the confinement i.e. trapping frequencies are very limited compared to other trapping techniques, and finally the confining magnetic field prevents the usage of Feshbach resonances that are essential for evaporation cooling.

A good alternative is optical dipole trapping which relies on the electric dipole interaction with a far-detuned light, an interaction that is much weaker than the ones discussed above. Although optical dipole traps need high power lasers which were not commonly available until a few years back, they allow more versatility in terms of trapping geometries (harmonic potentials, lattice potentials, box potentials, etc). Hence, for neutral atoms it has become customary to use this trapping method to manipulate the gas at its final stages of cooling and to tailor the final experimental setup.

The first dipole force traps were demonstrated using dieletric spheres[5] [254], while the first observations of optically trapping neutral atoms were made with the trapping of sodium atoms cooled to below 1 mK [26].

The dipole force

When a two-level atom with transition frequency ω_0 and linewidth Γ is placed into laser light, the electric field $\boldsymbol{E}$ induces an atomic dipole moment $\boldsymbol{p}$ that oscillates at the driving frequency ω. The amplitude of the dipole moment is simply related to the electric field amplitude by $|\boldsymbol{p}| = \alpha|\boldsymbol{E}|$ where α is the complex polarizability which depends on the driving frequency ω. The interaction potential of the induced dipole moment $\boldsymbol{p}$ in the driving field in the limit of large detuning $\Delta \gg \Gamma$ is given by:

$$U_{dip}(\boldsymbol{r}, z) = -\frac{1}{2}\langle \boldsymbol{p}.\boldsymbol{E}(\boldsymbol{r})\rangle = \frac{3\pi c^2}{2\omega_0^3}\frac{\Gamma}{\Delta} I(\boldsymbol{r}, z) \tag{2.8}$$

where $\Delta = \omega - \omega_0$ is the detuning, I is the electric field intensity and it has a spatial dependence which determines the spatial form of the potential. For a gaussian beam propagating along the z axis the expression of the intensity profile is as follows:

$$I(\boldsymbol{r}, z) = \frac{2P_0}{\pi w(z)} \exp\left(-\frac{2r^2}{w(z)^2}\right) \quad \text{with} \quad w(z) = w_0\sqrt{1 + \frac{z^2}{z_R^2}} \tag{2.9}$$

with w_0 the waist of the beam defined as the $1/e^2$ radius of the gaussian radial profile, P_0 the total power, and z_R is the Rayleigh range. Also, we consider $r = 0$, $z = 0$ is the focal point position.

The optical dipole force is derived from the potential in Eq. (2.8). It emerges, from the interaction of the intensity gradient of the light field with the induced atomic dipole moment as described in Eq. (2.8). While the radiation pressure force describes the dissipative (imaginary) part of this interaction, the dipole force describes the non-dissipative (real) part.

[5]The first experiments involved a combination of radiation pressure and dipole force, and were the subject of the 2018 Nobel prize of physics "for groundbreaking inventions in the field of laser physics".

As we see, if the laser is red-detuned ($\Delta < 0$), the dipole potential is attractive and the atoms are trapped in intensity maxima, and the opposite case applies to blue-detuned lasers ($\Delta > 0$). We note the dependence of the dipole potential on the ratio I/Δ in contrast to the dependence of the radiation pressure potential on I/Δ^2. From this we see that at large detunings the dissipative part all but vanishes, and the overall weak, yet more important non-dissipative part takes over the light-atom interaction effect.

Although far detuned, the laser beam could still excite atoms with very low probability, which, combined with power fluctuations, sets a limit to the performance of dipole traps, which is one of the reasons the transport beam is turned off after an initial step of evaporation. For these traps we deploy lasers tuned at a frequency several hundred Terahertz away from the atomic transition, and due to the weak nature of the dipole force, these lasers need to have powers ranging from several to hundreds of Watts depending on the required trap depth.

2.8.1 Optical transport

To gain more optical access, a much needed requirement to further manipulate the atoms and perform measurements, we transport the atoms from the main MOT chamber to the science cell.

The most common technique of optically transporting atoms is by shining a high-power far red-detuned laser on the atoms [255–257]. The atoms will see the focus of the gaussian beam as a potential minimum and will fall into the trap if their thermal energy is lower than the trap depth. Then the focus is moved mechanically by changing the length of light travel between its source and the atoms.

Implementation

For our optical transport, we use a high-power laser from IPG photonics with a wavelength $\lambda_{\mathrm{IPG}} = 1070\,\mathrm{nm}$ and a maximum power around 200 W focused down on the atoms with a calculated waist of $62\,\mu\mathrm{m}$. At maximum power we have around 170 W on the atoms. An illustration of the optical table of the transport setup is shown in Fig.2.10.

In order to move the focus of the beam, we use a motorized linear translation stage on which two mirrors are mounted. We can slide the motorized stage over a range of 16 cm, this means an effective focal sliding distance of 32 cm since it has two mirrors, slightly larger than the 31.5 cm required to get from the MOT chamber to the science cell center.

The power of the transport beam is controlled by mounting a half-wave plate on a motorized rotational mount combined with a high-extinction ratio optical cube placed afterwards. The mount is being controlled electronically via a module commanded by analog signals sent from the control computer. This allows to change the power of the laser beam in a range from 50 mW to 170 W. This power control method avoids using AOMs which are susceptible to thermal lensing issues at these high powers. However, it limits the time scale over which we can modulate the beam power. Indeed, although the rotational mount has a maximum speed of around 5

cycles per second, induced vibration in the optical setup limit drastically the speed at which we rotate the mount. This is not completely inconvenient since we keep the laser power constant during the transport and we only change it during evaporative cooling, which requires power modulation on a scale of several seconds, which is feasible using our setup.

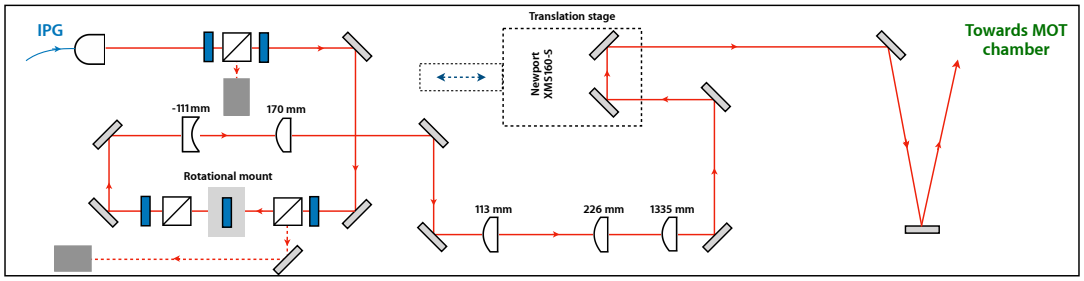

Figure 2.10: Optical transport laser setup. The rotational mount after the fiber provides control over the power of the laser, with the remaining power going into the beam dump. We position two telescopes to change the beam diameter in order to have the correct waist value at the level of the atoms. The translation stage slides the beam's focus from the center of the MOT chamber to the center of the science cell.

During the sequence, the optical trap is switched on during the D_2 molasses step and we keep it at maximum power during the D_1 molasses. We calibrate the centering of the beam using an imaging axis perpendicular to the transport beam, and by changing the horizontal and vertical angles of the last two mirrors in the setup shown in Fig.2.10. Then we optimize the focal position by scanning the atom number in the science cell after the transport for different initial positions of the translation stage. The loading of the trap depends on the trap depth which is in our case at maximum power around 1.5 mK, which gives a ratio of trap depth to temperature of around $\eta = U_0/(k_B T) = 20$ at the end of the D_1 molasses step. We manage optimally to have an elongated cloud of around 5×10^6 atoms at a temperature of around $120\,\mu$K in the science cell after this step is over.

The heating observed at the end of this phase could be explained partly by the influence of the dipole trap inducing a light shift (around 52 MHz for the D_1 line at this power) in the atomic transitions targeted by the gray molasses which renders the cooling process less efficient for the atoms falling in the transport beam. Another reason is the increased density of atoms inside the trap, an effect which is proven to increase the temperature of the molasses [258].
Also, by measuring the intensity noise spectrum, the power noise of the laser we find a peak at around 10 kHz, which means that heating will occur if the trapping frequency is around half of that value [259], which is close to the measured value as we shall see. We tried using a proportional–integral–derivative controller (PID) system to regulate this power but the trials were cut short by comparing the evaporation results before and after this regulation without noticing much difference so we used this beam without power regulation and we tried to limit the effect of the power fluctuations by switching off this beam once we load successfully the atoms in another dipole trap beam in the science cell.

Trapping frequency

Atoms sit at the bottom of the gaussian dipole potential described in Eq. (2.8). For the coldest atoms, this potential could be approximated by two concentric harmonic potentials with frequencies ω_r and ω_a, one along the propagation access of the beam and the other in the plane perpendicular to it at $z = 0$. This is easily derived by expanding the gaussian profile in Eq. (2.9) for small $\boldsymbol{r}$ and z values around zero, we obtain:

$$\begin{aligned} &U_{dip}(\boldsymbol{r}, z) \approx U_0 + \frac{1}{2} m(\omega_r^2 r^2 + \omega_a^2 z^2) \\ &\text{with} \quad \omega_r = \sqrt{\frac{4U_0}{m w_0^2}}, \quad \omega_a = \sqrt{\frac{2U_0}{m z_R^2}}, \quad U_0 = \frac{3c^2}{w_0 \omega_0^3} \frac{\Gamma}{\Delta} P_0 \end{aligned} \tag{2.10}$$

where $U_0 < 0$ denotes the potential depth.

In order to have an estimate of the efficiency of the evaporation in the dipole trap, and to calculate the collision rate and phase space density, we need to know exactly the trapping frequencies of our trap. This is a straightforward calculation using the expressions in Eq. (2.10) and calculating the waist using classical optical laws, but due to thermal lensing problems and the uncertainty on the exact positioning of the optical elements, we opt to experimentally measure the trapping frequency of the trap [256, 257]. This measurement depends on the assumption that atoms occupy a small area at the bottom of the trap where the gaussian intensity/potential profile could be approximated by a harmonic curve as we did above, which is not an ideal approximation in our case given the current parameters of the gas like temperature and atom number, but it helps giving a lower limit of the trapping frequency in our trap.
At this temperature, similar to a classical trap, the gas follows Boltzmann spatial and momentum distributions.
If the dipole trap is switched off, the gas will start a ballistic expansion following its initial velocity distribution. Then, if the trap is switched back on, a breathing mode will be triggered [260, 261]. The atoms will be pulled back to the trap by a force proportional to the square of its radial trapping frequency, then by holding them inside the trap, they will continue to oscillate. An oscillating density profile in the trap which oscillates at the same frequency is obtained if the cloud is probed at several time intervals during this process.
The amplitude of the oscillation is attenuated by atoms exploring anharmonic parts of the potential and thus interacting destructively with atoms at the center of the trap. This is partly evident from the fact that the attenuation happens on a time scale of around 200 μs, which is much shorter than the lifetime of the gas mainly affected by residual heating or collisions with the residual gas at this stage, measured to be several seconds for atoms in the transport dipole trap. This means the trapping frequency in this measurement is slightly underestimated and subsequently the waist is overestimated.

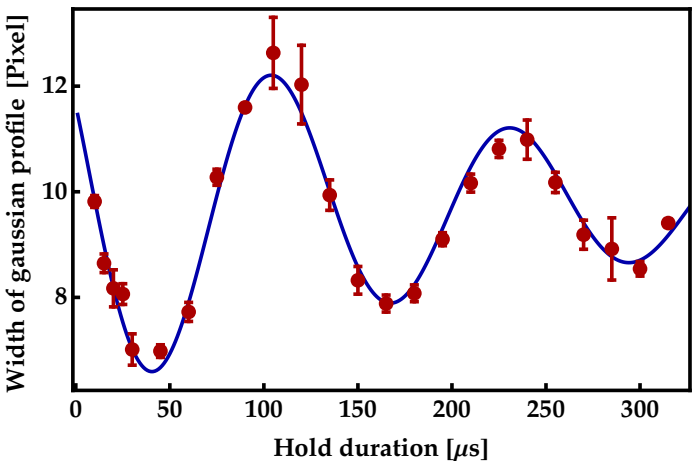

Figure 2.11: Radial frequency measurement. The breathing mode is triggered by deconfining the gas, leaving it to expand for a certain time (between 30 to 50 μs here) and then we hold the atoms inside the trap and measure the radial size of the cloud for different hold time durations. Figure adapted from S. Jin's thesis [227].

The results of this measurement are shown in Fig.2.11. We measure the breathing mode frequency to be $\omega_b = 2\pi \times (7.93 \pm 0.08)$ kHz which is twice the radial trapping frequency value [260,261] which leads to a trapping frequency $\omega_r = 2\pi \times 3.97$ kHz. By calculating subsequently the waist we find a waist of $w = 85.6\,\mu$m at $P = 160\,W$. This differs from the designed value for the reasons cited above. With this waist we can calculate the axial trapping frequency to find $\omega_a = 2\pi \times 8$ Hz which is relatively small and allows the cloud to expand over 3 cm in the axial direction, which decreases the density, and consequently the evaporation efficiency.

Transport ramp

As mentioned previously, to transport the atoms, we send an analog signal to the translation stage, moving the focus of the beam accordingly after trapping the cloud in the optical trap. If one chooses the simplest solution of a linear ramp, sliding the focus causes oscillations of the cloud along the transport axis, and upon arrival the abrupt stop causes sloshing that leads to heating and atom losses. For this reason we use an acutely configured ramp which compensates the axial excitations by decelerating upon stopping in a way that the cloud is at rest at the end of the transport. In literature this effect is called "shortcut to adiabaticity" and it has been studied and observed experimentally [262]. A type of ramp which verifies this condition is the quartic ramp (forth order in time). It is composed of different segments of linear jerks leading to a continuous acceleration ramp which avoids inertial kicks to the atoms during the transport. The stage reaches a maximum velocity of $320\,\text{mm.s}^{-1}$ and a maximum acceleration of $1280\,\text{mm.s}^{-2}$. The minimized kick at the beginning of the ramp is compensated at the end of the ramp by a well calibrated negative acceleration value. This minimizes the inertial force once the focal point arrives at the science cell. We transport the atoms during 1.2 s, a duration which takes into account the speed limitations of the translation stage and the required minimal duration to

perform the quartic ramp.

We transport about 80 % of the atoms trapped in the dipole trap to the science cell, which translates to around 1 million atoms at the end of the transport ramp. The loss of atoms is due to residual atom spilling during the transport duration of 1.2 s. By measuring the temperature we find $T = 150\,\mu$K. The increase in temperature of about $30\,\mu$K is mostly attributed to the transverse shaking of the cloud which occurs during the transport due to the rail-guided translation stage we are using. We note that photon scattering is estimated to be around 7 photons/s which translates to a temperature increase of about $1\,\mu$K/s during the transport.

2.8.2 Cross dipole trap

Once in the science cell, we can start evaporative cooling that requires a high collision rate hence a high density. In order to increase the density, confinement is increased in the axial direction by crossing the first transport beam with another perpendicular high-power beam to provide a second trapping potential decreasing further the trap volume and therefore increasing the atom density. The downside could be loss of atoms if the trapping volume is small compared to the volume of the atomic cloud at its current temperature. That is why we choose a waist not smaller than $60\,\mu$m in the experiment. A schematic illustration of the trap is shown in Fig.2.12.

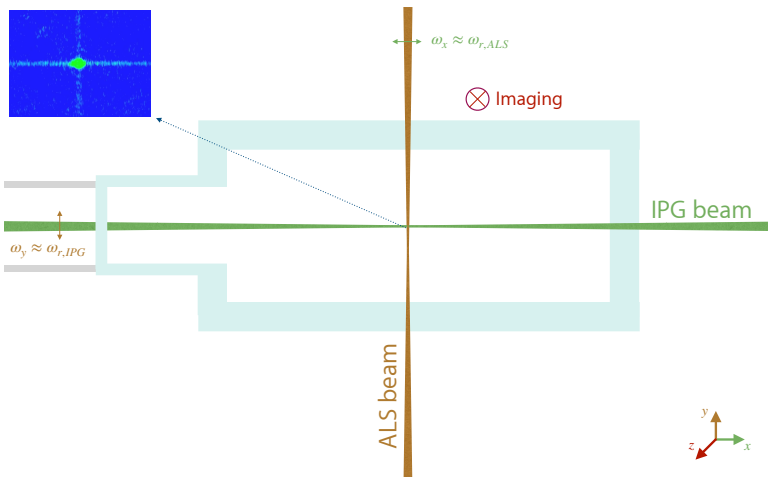

Figure 2.12: Cross dipole trap in the science cell. The transport beam is crossed with a second dipole trap beam in the science cell to create a cross dipole trap. Trapping frequencies at the beginning of evaporation are indicated for each axis.

Optical setup

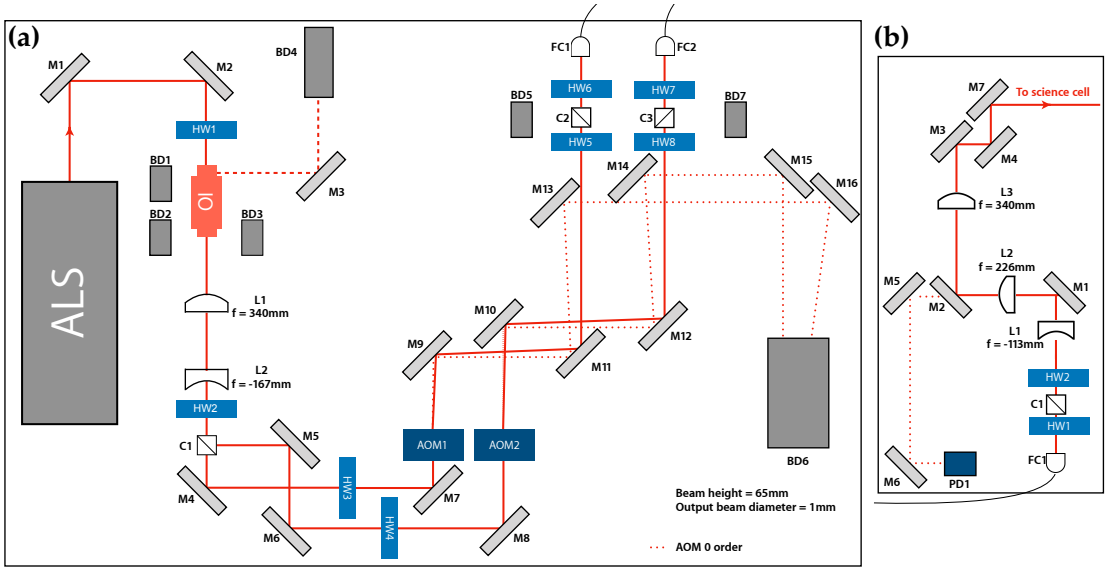

Figure 2.13: Cross dipole trap optical setup. (a). The beam is separated into two paths with perpendicular polarizations using a polarizing beam splitter ($C1$), and on each path an AOM is installed which is used first to control the power by means of a computer-controlled analog signal which feeds the power regulator of a VCO module which controls the AOM. Second, as a fast switch to cut off the power coming from this arm by means of a TTL signal. Finally, each beam's path is coupled in a fiber coupler which goes to the main experimental table. For arm 2, all power is diverted in $FC1$ using $HW2$ while $FC1$ is not used for now. **(b).** Optical setup after the high-power fiber output. The ALS power is monitored using the photodiode $PD1$ which is handy during evaporation to directly measure the power on the atoms.

The laser system used is a high-power continuous wave laser from Azurlight Systems (ALS) with a wavelength $\lambda_{\mathrm{ALS}} = 1064\,\mathrm{nm}$ and a maximum power output of 45 W. An illustration of the optical setup that I have developped is in Fig.2.13. The power is split into two independent paths using a polarizing beam splitter ($C1$), then an AOM is installed in the path of each beam, and the diffracted order (order -1) is coupled into a fiber coupler connected to a high-power fiber.
In practice, the output power is around 38 W. However, at these high power values, fluctuations have been observed inside the optical fiber over time which limited the output. A steady output power is achieved at around 18 W, so the power ratio between the two paths is modified to obtain this power value at the end of the first fiber, and the AOM is switched-off on the second path to dump all remaining power in beam dump 6. The ALS laser is always operated at maximum power to guarantee a stable beam mode shape over all experimental runs.

Implementation and results

The trapping frequency is measured as explained in the previous chapter. Starting by ramping down the power of the transport beam, then proceeding to switch off

the other inducing radial oscillations a value of $\omega_r = 65.0 \pm 1.0\,\mu$m is obtained which is close to the designed value.

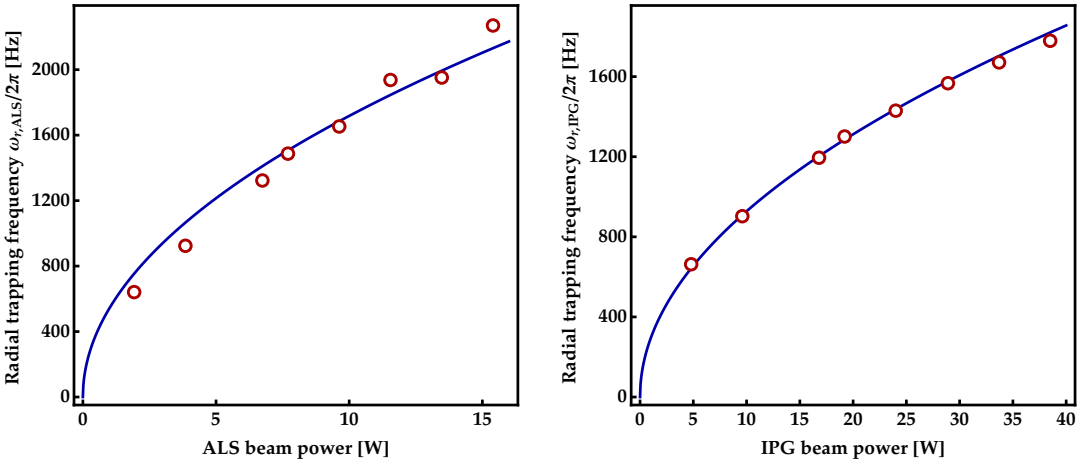

Figure 2.14: ALS and IPG trapping frequencies for different power values. For fitting the curves, a square root function is used to get the trapping frequency value according to the expected curve $\omega_r \propto \sqrt{P}$ to obtain the waists of the beams. The square root behavior of the two curves showcase the limited effect of the experimental factors on the trapping frequencies e.g. thermal lensing, jittering optical table, etc. Figure adapted from S. Jin's thesis [227].

Finally, the waist of the two dipole trap beams is measured directly by measuring the trap frequency for different values of power. This should result in a curve $\omega_r(P) \propto \sqrt{P}$ as seen in Eq. (2.10). By fitting the obtained data the following values for the waists of the two beams are obtained:

$$w_{ALS} = 65.0 \pm 1.0\,\mu m, \quad w_{IPG} = 88.7 \pm 0.3\,\mu m \tag{2.11}$$

The measurement of the IPG waist is compatible with the one reported in Fig.2.11 in the MOT chamber, and the measurement of the ALS waist is compatible with the designed value. Since the measurement in the transport beam is done before shining the cross beam, the waist is still overestimated as was the case in the MOT chamber. However, the waist of the cross beam is compatible with the designed value because of the axial confinement in this trap provided by the transport beam, which in its role prevents the cloud from exploring anharmonic sections of the potential.

2.9 Evaporative cooling

Evaporative cooling describes the process of energetic particles leaving a system with a finite trapping energy [263]. This process happens naturally since there are always high energy particles in the tail of the thermal Maxwell-Boltzmann distribution. If these particles leave the system, it gives rise to a redistribution of energy in the system and an overall cooling of the system.

Evaporative cooling of trapped neutral atoms was suggested for a gas of atomic hydrogen as an efficient way of achieving Bose-Einstein Condensation (BEC) [264]. The technique was extended to alkali atoms a few years later using Sodium and Rubidium atoms [22] and it was the key ingredient which led to achieve BEC in the same year [23, 25][6].

The attractiveness of evaporative cooling comes from its simplicity and more so from the fact that it is applicable to a wide range of temperatures and densities. The only limit is that the thermalization time should be about 30 to 100 times shorter than the lifetime of the sample, which could be determined by loss, heating, and inelastic collision processes.

2.9.1 Working principle

The basic idea is to allow high-temperature atoms to escape the trap, a crossed optical dipole trap in our case detailed in 2.8.2. Many parameters play a role in this process, the density of atoms in the trap, the trap depth, the initial temperature, trap geometry, and the effective cross section of elastic collisions.
The efficiency of evaporation is determined by the combination of all previous parameters and it is in competition with cooling speed. An extreme example that would demonstrate this trade-off is if we imagine an extremely large trap depth to cloud temperature ratio $\eta = U_0/k_BT$, if we wait enough, there is a probability that the whole energy of the cloud is carried by one particle which escapes the trap and therefore the whole system is cooled to zero temperature [263], this event could take an infinite amount of time to actually happen. Which means that an efficient and slow evaporation is compromised by the finite lifetime of the atoms in the trap. So to strike a balance between evaporation efficiency and duration is the first requirement for evaporation.
A relevant parameter to benchmark the evaporation is the phase space density, which is defined as:

$$PSD = n\lambda_{dB}^3 \tag{2.12}$$

where λ_{dB} is the De Broglie wavelength $\lambda_{dB} = \sqrt{2\pi\hbar^2/(mk_BT)}$, and n is the density at the center of the cloud. We remind that $PSD \approx 1$ in the degenerate regime.
Also, in forced evaporation, an important condition to achieve a sustained evaporation is to maintain or increase the elastic collision rate:

$$\Gamma_{\text{coll}} = n\sigma v \tag{2.13}$$

where n is the density of the gas, $\sigma = 4\pi a^2$ is the elastic cross section in the non-unitary regime for a two-component Fermi gas and a is the s-wave scattering length between the two spin states, v is the mean velocity of atoms in the trap. In the unitary regime in a harmonic trap geometry, which is our case, we write:

$$\Gamma_{\text{coll}} \overset{a\to\infty}{=} \frac{2N\hbar^2\bar{\omega}^3}{\pi(k_BT)^2} \tag{2.14}$$

[6] Eric A. Cornell, Wolfgang Ketterle, and Carl E. Wieman were awarded the 2001 Nobel prize in physics for their realization of Bose-Einstein Condensation for neutral atoms.

where N is the number of atoms per spin state, $\bar{\omega} = (\omega_x\omega_y\omega_z)^{1/3}$ is the geometric mean of the trapping frequencies. The relation is deduced in [265].

Due to Pauli blocking for fermions, having an atomic cloud composed of only one state sets the elastic cross section to zero and no evaporation takes place. For this reason the sample is prepared in the two states $|1\rangle$ and $|2\rangle$ in Fig.2.2.1, and a balanced atomic population in both states is sought.
By insuring a high collision rate, the probability of hot atoms leaving the trap can be maximized. But for a large value of η no atoms could escape the high walls of the potential, that is why the evaporation is forced by lowering the optical trap depth insuring a constant η value during the process.
Another important element is to increase the collision cross section, and this is done by means of creating a bias field to exploit molecular energy levels which exist in the Zeeman-shifted relative energy range of the two spin states in the trap, this phenomenon is known as Feshbach resonance and was explained in detail in 1.1. At resonance, a attains very large values and the collision rate is maximized.
During the final steps of evaporation, the optical dipole potential, which was lowered drastically, is so weak that it cannot trap the atoms anymore against gravity. In order to avoid atom spilling, another curvature field is added which acts as a magnetic confining potential to increase confinement in the axial direction of the cross dipole trap as will be explained.

2.9.2 State populations

As mentioned earlier, it is important to prepare the cloud so that a balanced atomic population in the lower sub-Zeeman levels of the ground state is ensured. After D_1 cooling, which is the last experimental step to change the state populations, a bit more than 65% of atoms are in state $|1\rangle$ and the rest are in state $|2\rangle$. This is a direct result of intentionally switching off the repumper beam of the D_1 gray molasses just before the end of the phase as mentioned previously.
A further step of transferring atoms between the two states to balance the population is thus needed.

For that a Radio-frequency (RF) antenna close to the science cell is used, powered using a signal generated by a high precision frequency generator and then amplified by an RF amplifier of 50 W. The spectral width of the generator signal is negligible compared to the widened atomic transition due to the factors mentioned earlier.
To chirp the frequency of the generator within an interval around the atomic transition frequency, the transition frequency should be well-known. For that the number of atoms in one state (state $|1\rangle$ for instance) is probed while sending a RF signal with fixed frequency in a designated interval. A dip in the atom number points to the transition, which is then measured more precisely by reducing the interval of scanned values. In our case the transition is found at $\omega_A = 2\pi \times 76.267$ MHz with a width at two sigma of $\approx$ 10 kHz. This transition frequency value corresponds according to Breit-Rabi formula in Eq. (2.1) to a bias magnetic field value of 832 G, which is the applied value corresponding to the Feshbach resonance between these two states.

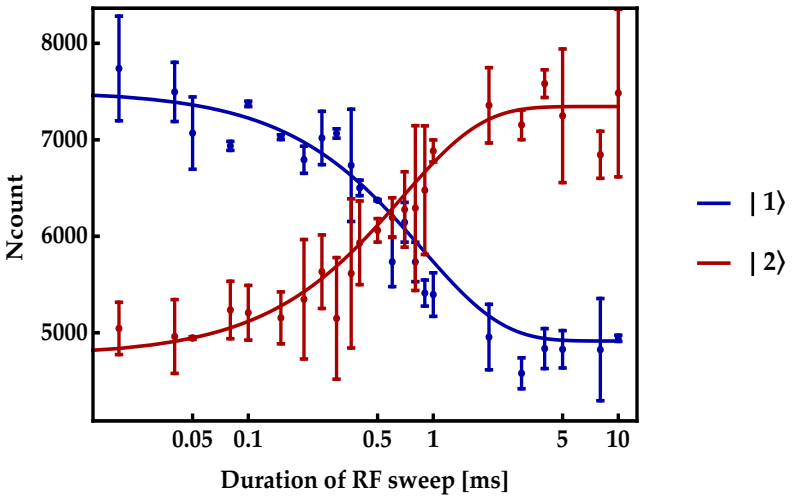

Figure 2.15: Evolution of populations in states $|1\rangle$ and $|2\rangle$ during an RF sweep. At unitarity, an RF sweep of 400 kHz is applied with variable durations and the atom number in each state in measured. For long sweep times the two populations inverse adiabatically in agreement with Eq. (2.15). Figure adapted from S. Jin's thesis [227].

Afterwards, a sweep is performed within an interval of values centered around the measured transition frequency. If the sweep is performed slowly enough (with respect to the Rabi frequency), all atoms are transferred from state $|1\rangle$ to state $|2\rangle$. This process is called adiabatic passage, and the probability of transfer during the sweep is calculated using Landau-Zener formula [266, 267]:

$$P_{|1\rangle\to|2\rangle} = 1 - \exp\left(-\frac{\Omega^2}{4\Delta_\nu}t\right) \tag{2.15}$$

With Ω denoting the Rabi frequency between the two states, Δ_ν/t is the sweep speed, Δ_ν the interval of frequencies and t the sweep duration. The result of this sweep is in Fig.2.15, an exponential evolution in agreement with Eq.(2.15) is observed. The probability of transfer approaches one for very slow sweeps compared to the Rabi frequency $|\Delta_\nu/t| \ll \Omega^2$.

Rabi oscillations

The Rabi frequency can be calculated using the exponential time constant $\tau = 4\Delta_\nu/\Omega^2$ of the probability curve. This is equivalent to the two curves in Fig.2.15. This gives the following values: $\tau_1 = 0.86 \pm 0.08$ ms and $\tau_2 = 0.80 \pm 0.05$ ms, and therefore two Rabi frequency values $\Omega_1 = 2\pi \times (6.86 \pm 0.63)$ kHz and $\Omega_2 = 2\pi \times (7.12 \pm 0.44)$ kHz. To double check this value, which is constant in the setup since the power of the RF signal is not changed, the Rabi frequency can be directly measured by sending resonant RF pulses of different durations, and then measuring the atom number in one of these states. By construction, the atomic population will oscillate with a frequency equal to the Rabi frequency, see Fig.2.16.

With these values the atomic population in states $|1\rangle$ and $|2\rangle$ is balanced by simply applying a RF sweep with a duration corresponding to the point where the

two populations are equal in Fig.2.15. So a single linear RF sweep of 400 kHz centered around the atomic transition during 550 μs is applied which results in around 1.1×10^6 atoms in each spin state with a temperature around 150 μK.

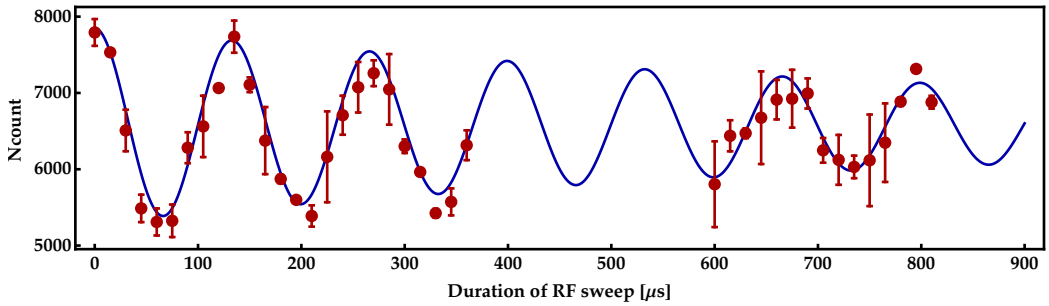

Figure 2.16: Rabi oscillations between state $|1\rangle$ and $|2\rangle$ at unitarity. A coherently driven atomic state by a resonant signal will oscillate with a frequency equal to the Rabi frequency. The value obtained by fitting the curve is $\Omega = 2\pi \times (7.51 \pm 0.03)$ kHz. Figure adapted from S. Jin's PhD thesis [227].

2.9.3 Magnetic fields in the science cell

For efficient evaporation, as mentioned earlier, a bias magnetic field is needed to maximize elastic collisions between the spin states present in the cloud at this stage. For this goal, a pair of coils, named Feshbach coils, are installed in Helmholtz configuration to provide a bias field of 832 G corresponding to the resonance value as detailed in Fig.2.3.
The Feshbach coils provide a field offset of 3.78 G/A, so we need to power them using high current cable with around 220 A. Feshbach coils have a diameter of 86 mm and they are placed closest to the science cell.

As mentioned earlier, decreasing the power of a dipole trap during evaporation causes the trap to become weakly confining in the axial direction. For that we add a pair of coils in Helmholtz configuration but placed at a well configured distance to create a curvature potential to keep the atoms confined during evaporation. In our case, the curvature coils provide a curvature gradient of 0.033 G/cm/A. A plot of the magnetic field values for both pairs of coils is shown in Fig.2.17.

To characterize well the evaporation process, trap frequency values need to be known very precisely. Since curvature coils provide a confining potential, the question of knowing their trapping frequency arises. This frequency is measured by moving the IPG focal point on the ALS axis, then abruptly switching off the IPG beam and leaving the atoms to expand in the ALS alone. Then the triggered axial oscillation in the ALS potential happens in a potential with a frequency equal to the quadratic sum of two contributions: One of the ALS axial trapping potential which is known and the one from the curvature coils $\omega_\perp^2 = \omega_{curv}^2 + \omega_a^2$. Doing this measurement yields $\omega_{curv} = 2\pi \times (23.4 \pm 0.1)$ Hz which is higher than the axial frequency of the ALS, around $\omega_a \approx 2\pi \times 7$ Hz.

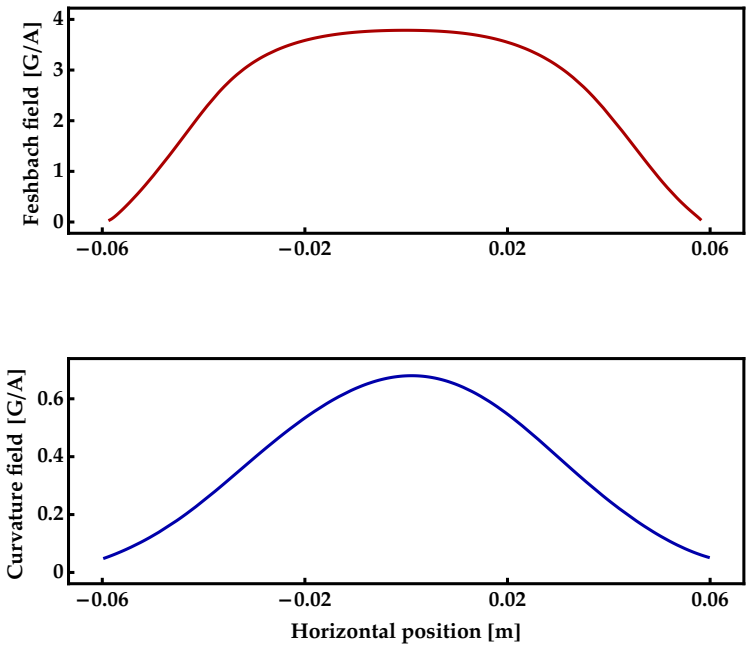

Figure 2.17: Feshbach and curvature fields in the horizontal plane. Due to their Helmholtz configuration, Feshbach coils provide a non-confining bias field, while the curvature coils provide a confining field. These curves are obtained using a numerical simulation taking into account the geometry of the pairs of coils. Along the vertical axis, the magnetic field creates an anti-confining potential. However, this is largely compensated by the optical trap confining potential.

2.9.4 Cooling to degeneracy

Combining all previous ingredients, at the beginning of evaporation, the cloud contains around 1.1×10^6 atoms per state at a temperature of around 150 μK. The crossed beams geometry places the atoms near the center of both traps, which allows us to make the approximation that the cloud is confined in a three dimensional harmonic potential resulting from the cross dipole trap and the curvature coils. The harmonic trapping frequencies are the following:

- On x axis (IPG beam axis), the trapping frequency is a combination of the ALS radial trapping, the IPG axial trapping, and the curvature coils magnetic trapping. At this step the dominating frequency is the ALS radial frequency $\omega_x \approx \omega_{r,ALS} = 2\pi \times 2.2$ kHz.

- On y axis (ALS beam axis), the trapping frequency is a combination of the IPG radial trapping, the ALS axial trapping, and the curvature coils magnetic trapping. At this step the dominating frequency is the ALS radial frequency $\omega_y \approx \omega_{r,ALS} = 2\pi \times 2.7$ kHz.

- On z axis (perpendicular to the XY plane), the trapping frequency is a combination of the IPG radial trapping, the ALS radial trapping, and the curvature coils

magnetic trapping. At this step the dominating frequency is a combination of the ALS and the IPG radial frequencies $\omega_z \approx \sqrt{\omega_{r,ALS}^2 + \omega_{r,IPG}^2} = 2\pi \times 3.4$ kHz.

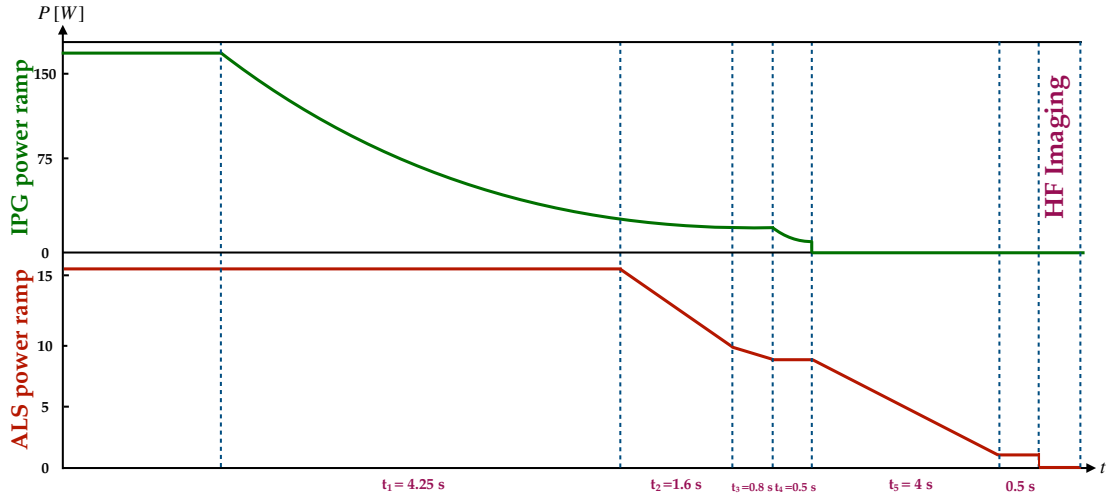

Figure 2.18: Evaporation power ramps. The sequence starts by an exponential ramp decreasing the power of the IPG to around 12% of its initial value while keeping the ALS at constant power. Before the end of the exponential ramp, the ALS powered is ramped down linearly to around 10 W, then we proceed to decrease again the ALS power keeping constant the IPG power. Afterwards the IPG beam after a final exponential ramp is turned off and the evaporation is continued only in the ALS trap. Figure adapted from S. Jin's PhD thesis [227].

With these values we calculate a phase space density using Eq. (2.12) and we find $PSD = 7.4 \times 10^{-4}$ reminding that the regime of degenerate Fermi gas is reached when $PSD \approx 1$. We can also calculate the collision rate using Eq. (2.13) to find $\Gamma_{\text{coll}} \approx 9000\, s^{-1}$, a very good value to start with.
The evaporation starts by ramping up the curvature and Feshbach coils currents, then waiting around 300 ms for the magnetic fields to stabilise. Afterwards the ALS power is kept constant while decreasing the power of the IPG beam by 88% reaching a power $P_{IPG} = 28.5$ W. At the end of this process the cloud has $N = 3.4 \times 10^5$ atoms at a temperature $T = 23\,\mu$K which gives $PSD = 2.2 \times 10^{-2}$ and $\Gamma_{\text{coll}} \approx 3.2 \times 10^4\, s^{-1}$. All atoms at the end of this step are transferred into the cross trap and both of its beams provide similar potential depths (image in Fig.2.12).

Then the power of both beams is decreased linearly, the sequence is reported in Fig.2.18. During the fifth phase of evaporation, the IPG beam is turned off completely and the evaporation is continued solely in the ALS trap. This is because the IPG has significant power fluctuations at this power level which cause heating. The remaining confining forces are those of the ALS beam and the curvature coils. After the IPG is turned off, two additional evaporation steps are performed in the ALS alone, this results in a significant increase in phase space density of which we report the results in Fig.2.19.

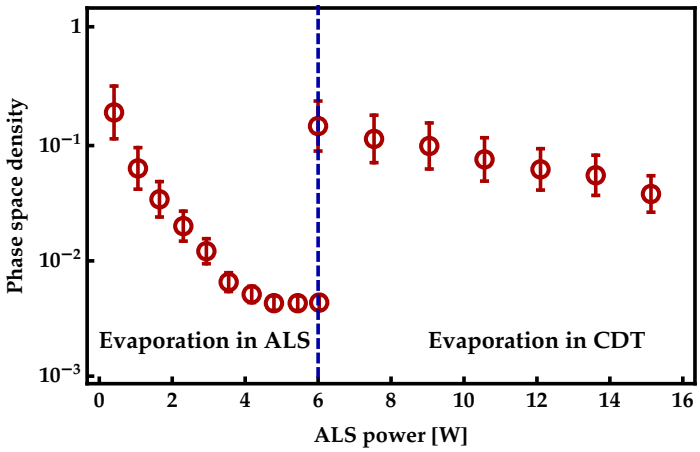

Figure 2.19: Phase space density evolution during evaporation. After switching off the IPG a factor of 2 in temperature is gained, which means a stable ratio $\eta = U_0/(k_B T)$ is maintained since the IPG trapping frequency is very close to that of the ALS at that point in evaporation. At the end of the evaporation sequence, a phase space density of around 0.2 is obtained. Figure adapted from S. Jin's PhD thesis [227].

Summary

In this chapter an overview of the main experimental steps used to obtain a degenerate Fermi gas was presented.
Starting by producing an atomic vapor of ^{6}Li atoms, which are slowed down by a Zeeman slower and then captured by the MOT. They are subjected to two additional cooling steps of D_2 molasses and D_1 gray molasses. Then they are loaded into an optical dipole trap which transports them to the science cell where another optical dipole trap is used to increase confinement and density. An RF sweep is applied to balance populations in the two lowest spin states. Then, a bias field and a curvature field are applied to increase the cross section of the elastic collisions and to increase confinement respectively. Then by ramping down the power of the beams of the cross dipole trap a dense fermionic cloud is obtained.

At the end of the evaporation sequence, a cloud with $N = 6 \times 10^4$ and $T = 2\,\mu$K is obtained which leads to a phase space density of 0.2. We note that in this regime measuring the temperature using time of flight methods is not reliable anymore since the ballistic expansion is no longer a valid model due to two main reasons: Firstly, the strong interactions of the unitary regime at which the imaging is performed redistribute the momentum between atoms in a non-trivial way, and the imprinted velocity distribution measured during time of flight is not closely related to the thermal distribution of the cloud anymore. Second, the expansion time of the cloud at this temperature is limited by the imaging system detection threshold, and getting a good signal-to-noise ratio is quite hard. That is why people resort to other techniques to measure the temperature of the cloud in this regime like the virial theorem and equation of state fitting which will be discussed in the next chapter.

Chapter 3

From superfluidity to single atom imaging

In the previous chapter, a description of the experimental apparatus and its steps was introduced. In the final stages of the evaporative cooling, a cloud of about 60 thousand atoms is obtained, at a temperature measured to be around 2 μK using the time of flight method.
However the ballistic expansion of the gas when released from the trap, which is the basic assumption behind the time of flight method is no longer a valid assumption since the gas is at unitarity ($a \to \infty$) and the dynamics of the system are dominated by its strong interactions.

The transition from a normal phase to a superfluid phase for a Fermi gas cannot be easily observed as for bosonic gases, where bosonic statistics dictate a total collapse of the atoms into a single quantum state which can be directly observed [66, 68, 268, 269]. In a strongly interacting Fermi gas, the emergence of a superfluid alters very little the density profile of the trapped gas, and to observe directly superfluidity, going beyond looking at the density profile of the cloud while it is cooled is needed.

In this chapter the main methods used to probe the properties of the gas at this limit will be explained. Starting by a brief overview of the thermodynamic properties of a Fermi gas, its equation of state, and the different expansion regimes for a Fermi gas in different limits.
The result of the fitting of the experimental density profile using this equation of state will also be presented. Then a discussion over a qualitative characterization of superfluidity using the analysis of the density profiles of a spin imbalanced gas will follow. Finally, we will talk about the prospects of the ^{6}Li machine.

3.1 Thermodynamics of ultracold Fermi gases

For fermions in the ultracold regime, interatomic interactions can be described using a single parameter, the scattering length a. At these low temperatures the thermal wavelength (λ_{dB}) attains large values compared to the interatomic interaction range and the details of this interaction become irrelevant. Leading to the universality

property where the dynamics of the system do not depend on the details of the interaction potential, and therefore the physics of interactions does not a priori depend on the atomic species used in the experiment.
The other natural length scale to consider in these systems is the inter-particle distance $n^{1/3} \propto k_F^{-1}$. The behavior of the Fermi gas is governed by the ratio $1/(k_F a)$ and we can write the chemical potential of the gas as a function of its parameters:

$$\mu = f(m, n, k_B T, a) \tag{3.1}$$

where k_B is the Boltzmann constant and m is the mass of the atomic species in the gas. According to Vaschy-Buckingham theorem, we can always write an equivalent equation to Eq. (3.1) as a function of dimensionless parameters leading to:

$$\frac{\mu}{E_F} = F(\frac{T}{T_F}, \frac{1}{k_F a}) \tag{3.2}$$

where $k_F = (2\pi^2 n)^{1/3}$ is the Fermi wavevector, $E_F = \hbar^2 k_F^2/(2m)$ the Fermi energy, and $T_F = E_F/k_B$ the Fermi temperature .
In the case of resonant interactions, the so-called unitary limit where $a \to \infty$, the scattering length becomes irrelevant and drops out from all physical quantities leaving the average interatomic distance as the only relevant length scale in the system. The only relevant energy scale is the Fermi energy E_F which does not depend on the type of interactions [270]. Thus, at finite temperature, thermodynamic properties like entropy, energy, compressibility and specific heat are universal and depend only on the ratio T/T_F.
Moreover, in this case, a single equation which relates these thermodynamic variables can encompass all the macroscopic properties of the system. Such an equation is called the equation of state (EoS). It was measured in our group at ENS in 2009 and 2010 at zero temperature in the whole BEC-BCS crossover and at finite temperature at unitarity at ENS and Tokyo and later at MIT [157, 271, 272]. We exploit the results of MIT to interpolate our measurements in order to determine T/T_F of our cloud.
It is worth noting that at zero temperature, the chemical potential is related to the Fermi energy simply by a factor:

$$\mu = \xi E_F \tag{3.3}$$

where $\xi = F(0, 0)$ is the Bertsch parameter [273], and determining its value is the solution for the unitary gas problem at zero temperature.

3.1.1 Equation of state

The equation of state is a term used for all expressions relating fundamental thermodynamic properties, and it describes the macroscopic properties of a system in thermal equilibrium. Measuring the EoS marked an important milestone in the field of ultracold atoms and presented an opportunity to validate theoretical models which predicted the behavior of the unitary Fermi gas.
In order to relate the EoS to our measurements, we need to express it in terms of the integrated density distributions that are probed by imaging the cloud (as detailed in section 2.5).

However, taking into account exactly the inhomogeneity of the optical potential is not an easy task. For this reason, approximations are used which allow to compare our results with the homogeneous case, and the most prominent of these methods is the local density approximation (LDA).
In the local density approximation, we consider that over a mesoscopic length scale, smaller than the size of the system and larger than the interatomic distance, the system is homogeneous and in thermodynamic equilibrium. This allows us to define local variables such as pressure and temperature and write a local equation of state. This small system exchanges atoms and energy with the neighboring systems meaning that to describe it we have to work in the grand-canonical ensemble formalism defining a local chemical potential:

$$\mu_\sigma(\boldsymbol{r}) = \mu_{0,\sigma} - U(\boldsymbol{r}) \tag{3.4}$$

where $\mu_{0,\sigma}$ is the global chemical potential of the homogeneous gas of atoms with spin σ, $U(\boldsymbol{r})$ is the trapping potential, in our case the optical dipole potential described in section 2.8, and $n(\boldsymbol{r})$ is the density at position $\boldsymbol{r}$.
In the small volume described by the LDA the grand potential $\Omega(T, \mu_\sigma, \mathcal{V})$ is minimum, where $\mathcal{V}$ is the volume of the small LDA box. A direct result of this minimization is the Gibbs-Duhem relation [159]:

$$\mathcal{V}\,\mathrm{d}P = S\,\mathrm{d}T + N_\uparrow\,\mathrm{d}\mu_\uparrow + N_\downarrow\,\mathrm{d}\mu_\downarrow \tag{3.5}$$

which gives an EoS relating the measured density $n = N/\mathcal{V}$ to the pressure:

$$n_\sigma(\mu_\sigma(\boldsymbol{r}), T) = \frac{\partial P(\mu_\sigma(\boldsymbol{r}), T)}{\partial \mu_\sigma}\Big|_T \tag{3.6}$$

where n_σ and P are the local density and pressure of the untrapped homogeneous gas respectively. This relation has been measured previously [157, 271], and the measured data from [157] will be used for the pressure to interpolate a function to compare the results with and extract the temperature as will be detailed in the next section.

3.2 Quantitative analysis of density distributions

The main purpose of imaging and image analysis is to record density distributions of the atomic gas, whether it is trapped (*in situ*) or after a ballistic expansion. Almost all experimental knowledge about the physics and properties of cold atoms system comes from processing and analyzing these images. In the experiment, we are able to obtain density profiles for each spin state after analysing images of atomic clouds.

In order to evaluate the thermodynamic properties of the gas, and especially the temperature in our case, we need to have an expression for the density profile and to relate it to these properties. Starting by deriving this expression for a non-interacting Fermi gas in a harmonic potential, then we relate this expression to the local unitary regime density in LDA.

3.2.1 Non-interacting Fermi gas in a harmonic trap

For N non-interacting particles with energies ϵ_i, the Fermi-Dirac statistics governs the density distribution. Since in LDA each small volume is allowed to exchange particles and energy with the neighboring volumes, we write the occupation distribution in a state i in the Fermi sea in a small box defined by LDA in the grand canonical ensemble as follows:

$$\bar{n_i} = \frac{1}{\exp\left((\epsilon_i - \mu_0)/k_B T\right) + 1} \tag{3.7}$$

with μ_0 the global chemical potential and k_B the Boltzmann constant. We note that $\bar{n_i} \in \{0, 1\}$ due to Pauli blocking.
Consider these particles confined in a three dimensional harmonic trap, with the trapping potential:

$$V(\boldsymbol{r}) = \frac{m}{2}(\omega_x^2 x^2 + \omega_y^2 y^2 + \omega_z^2 z^2) \tag{3.8}$$

where ω_i is the trapping frequency along the axis i. Supposing the thermal kinetic energy of the particles to be much higher than the quantum mechanical harmonic level spacings in the trap $\hbar\,\omega_i$.
We can neglect the level structure and write the energy of each particle as simply the sum of its kinetic energy and the trapping potential at its position, showing that LDA is a valid approximation in this setting (also called the Thomas-Fermi approximation), and it allows us to write the occupation of a phase space slot $\{\boldsymbol{r}, \boldsymbol{p}\}$ as follows:

$$f(\boldsymbol{r}, \boldsymbol{p}) = \frac{1}{\exp\left(\beta(\boldsymbol{p}^2/2m + V(\boldsymbol{r}) - \mu_0)\right) + 1} \tag{3.9}$$

where $\beta = 1/(k_B T)$. Note that since we have a spin balanced gas of the same species we dropped the σ index.
With this we can calculate the density distribution of a thermal non-interacting gas:

$$n(\mu(\boldsymbol{r}), T) = \int \frac{\mathrm{d}^3\boldsymbol{p}}{(2\pi\hbar)^3} f(\boldsymbol{r}, \boldsymbol{p}) = -\frac{1}{\lambda_{dB}^3}\mathrm{Li}_{3/2}\left(-e^{\beta(\mu_0 - V(\boldsymbol{r}))}\right) \tag{3.10}$$

where λ_{dB} is the thermal De Broglie wavelength and Li_n is the polylogarithm function of n-th order [1] and $V(\boldsymbol{r})$ is the potential in Eq. (3.8).

In our images, the three dimensional density profile is not accessible hence the imaging light already "integrates" the density along its axis of propagation. Then when visualizing the measured data, a general tendency is to integrate the density over one axis to obtain one dimensional graph which is then fitted to extract the

[1] The polylogarithm function is defined as:

$$\mathrm{Li}_n(z) = \sum_{k=1}^{\infty} \frac{z^k}{k^n}$$

temperature. For that we integrate Eq. (3.10) along two of the three axes to obtain:

$$\begin{aligned}\bar{n}_0(z) &= \int_{-\infty}^{+\infty}\int_{-\infty}^{+\infty} \mathrm{d}x\,\mathrm{d}y\, n(\mu(\boldsymbol{r}), T) \\ &= \int_{-\infty}^{+\infty}\int_{-\infty}^{+\infty} \mathrm{d}x\,\mathrm{d}y\, -\frac{1}{\lambda_{dB}^3}\mathrm{Li}_{3/2}\left(-e^{\beta(\mu_0-\frac{m}{2}(\omega_x^2 x^2+\omega_y^2 y^2+\omega_z^2 z^2)}\right) \\ &= -\frac{1}{\lambda_{dB}^3}\frac{2\pi}{m\beta\omega_x\omega_y}\mathrm{Li}_{5/2}\left(-e^{\beta\mu(z)}\right)\end{aligned} \tag{3.11}$$

where $\mu(z) = \mu_0 - m\omega_z^2 z^2/2$ is the local chemical potential encountered in Eq. (3.6) in one dimension.
We can also relate $\bar{n}_0(z)$ to the pressure [274], starting from the first equality in Eq. (3.11) and after making the change of variables $x_1 = \omega_x x/\omega$, $y_1 = \omega_y y/\omega$ and $\rho^2 = x_1^2 + y_1^2$ we write:

$$\int_{-\infty}^{+\infty}\int_{-\infty}^{+\infty} \mathrm{d}x\,\mathrm{d}y = \frac{\omega^2}{\omega_x\omega_y}\int_{-\infty}^{+\infty}\int_{-\infty}^{+\infty} \mathrm{d}x_1\,\mathrm{d}y_1 = \frac{2\pi\omega^2}{\omega_x\omega_y}\int_0^{+\infty}\rho\,\mathrm{d}\rho$$

(the cloud is trapped in a gaussian beam typically and therefore is symmetric by rotation around the beam's axis). With this we can write:

$$\begin{aligned}\bar{n}_0(z) &= \frac{2\pi\omega^2}{\omega_x\omega_y}\int_0^{+\infty}\rho\,\mathrm{d}\rho\, n(\mu(z) - m\omega^2\rho^2/2) \\ &= -\frac{2\pi}{m\omega_x\omega_y}\int_0^{+\infty}\mathrm{d}\mu\, n\Big(\mu(\boldsymbol{r})\Big) = -\frac{2\pi}{m\omega_x\omega_y}\Big[P(\mu)\Big]_{\mu(z)}^{-\infty}\end{aligned}$$

where we used $\mathrm{d}\mu = -m\omega^2\mathrm{d}(\rho^2/2)$. With that we finally get the relation:

$$P_0(\mu(z), T) = \frac{m\omega_x\omega_y}{2\pi}\,\bar{n}_0(z) \tag{3.12}$$

Note that in the derivation of this expression the fact that the pressure and density are parameters of the non-interacting gas were not relevant. Hence, the relation also holds in the strongly interacting limit.
We note also the relation of the pressure for a non-interacting gas:

$$P_0(\mu(z), T) = -\frac{1}{\beta\lambda_{dB}^3}\mathrm{Li}_{5/2}\left(-e^{\beta\mu(z)}\right) \tag{3.13}$$

3.2.2 Unitary Fermi gas

To use the measured data, an expression relating the measured one dimensional unitary gas density $\bar{n}(z)$ to the data in Ku et *al*. [157] is needed. As mentioned earlier, all thermodynamic quantities in the unitary limit depend only of the ratio T/T_F. So we choose the pressure data $h(\beta\mu(z)) = P(\mu(z), T)/P_0(\mu(z), T)$, with P the pressure of the unitary gas and P_0 that of the ideal gas. To this end, we write the pressure equation of state as follows:

$$P(\mu(z), T) = P_0(\mu(z), T)\, h(\beta\mu(z)) \tag{3.14}$$

where the function $h(\beta\mu(z))$ is plotted in Fig.3.1. We see that in the limit of high temperature, $h(\beta\mu(z)) \simeq 1$.

Using Eq. (3.12) we can write a relation for $\bar{n}(z)$, the measured density of the unitary gas:

$$\bar{n}(z) = -\frac{2\pi}{m\omega_x\omega_y\beta\lambda_{dB}^3}\mathrm{Li}_{5/2}\left(-e^{\beta\mu(z)}\right)\, h(\beta\mu(z)) \tag{3.15}$$

This expression turned out to be very useful since it allowed to measure directly the equation of state and to transform each point in the integrated density profile (which is the outcome of one experimental image) to a point in the function $h(\beta\mu(z))$ [271, 274].

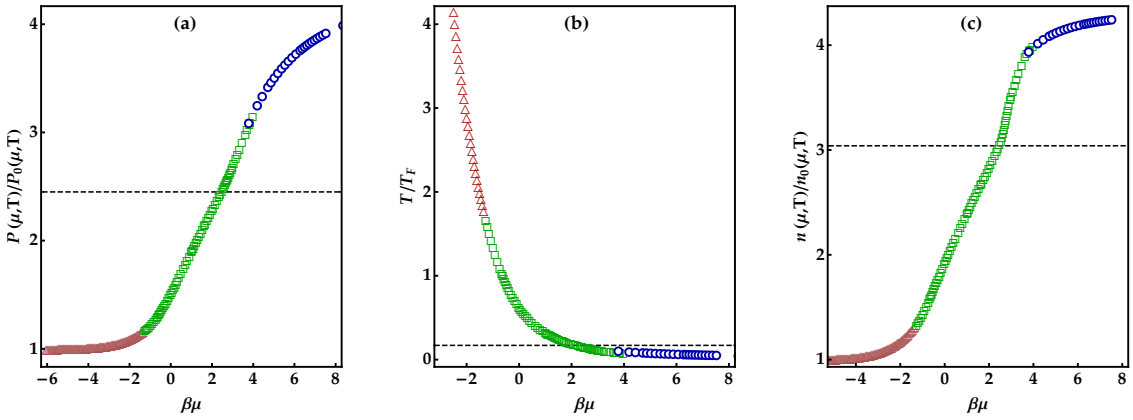

Figure 3.1: Interpolation function used to extract T/T_F. Red triangles: Third order virial expansions derived from Eq. (3.20). Green squares: Data from Ku et *al.* [157] obtained by measuring the equation of state for a unitary Fermi gas. Blue circles: Low temperature extension using the fermionic and bosonic excitations spectrum in the superfluid phase [275]. **(a).** Pressure data with respect to $\beta\mu$. **(b).** Temperature data with respect to $\beta\mu$. **(c).** Density data with respect to $\beta\mu$. The dashed black line marks the limit beyond T_C. Figure adapted from Bruno Peaudecerf (Private communication).

The function in Eq. (3.15) us used to fit the density data and obtain the value $\beta\mu$ for every point in the density profile. Then the value is used at the center of the trap to calculate T/T_F from the relation[2]:

$$\frac{T}{T_F} = \frac{4\pi}{(3\pi^2 n\lambda_{dB}^3(\beta\,\mu))^{2/3}} \tag{3.16}$$

With $T_F = \hbar^2(3\pi^2 n)^{2/3}/2mk_B$ the Fermi temperature and n is the density at the center of the trap.

[2] In practice interpolated data from Ku et *al.* were also used

Superfluid excitations in the low temperature limit

The previous data was restricted to a certain range of fugacity and can be extended to the low temperature limit when $T/T_F < T_C \simeq 0.17\,T_F$ [276] which is the critical temperature for the superfluid transition. We know that in the limit $T = 0$ for a unitary gas, the only relevant energy scale is the Fermi energy and the Bertsch parameter ($\xi = 0.376$ [157]) defines the scaling factor of the energy with respect to it [273] as follows:

$$\mu = \xi E_F \tag{3.17}$$

Beyond this limit, temperature dependence of the energy can be accounted for by the elementary excitations present in the superfluid phase: bosonic Bogoliubov-Anderson phonons and fermionic gapped Bogoliubov quasiparticles. Their contributions are given by [275]:

$$E(n,T) \overset{T\ll T_F}{=} \frac{3}{5} n E_F(n) \left[\xi + \frac{\sqrt{3}\pi^4}{16\zeta^{3/2}} \left(\frac{k_B T}{E_F(n)}\right)^4 + \frac{5}{2}\sqrt{\frac{2\pi\Delta(n)^3 k_B T}{E_F(n)^4}} \exp\left(-\frac{\Delta(n)}{k_B T}\right)\right] \tag{3.18}$$

$$\Delta(n) \overset{a\to\infty}{\approx} \left(\frac{2}{e}\right)^{7/2} E_F(n) \tag{3.19}$$

where Δ is the pairing gap from BCS theory, and $E(n,T)$ is an energy density.

Virial expansion in the high temperature limit

The data from Ku et *al.* can also be extended to the high temperature limit $T/T_F > 1$ using the virial expansion. Though the system is strongly correlated system at low temperatures, with increasing temperatures the correlation between particles becomes weaker.

At sufficiently high temperatures, the scattering cross section is of the order of the square of the thermal de Broglie wavelength, which becomes much smaller than the average inter-atomic distance. As a result, the inclusion of few-body correlations is already sufficient to describe the underlying properties of the system. These few-body correlations can be exactly taken into account using few-particle solutions and virial expansion [277]. The expansion for pressure is written as:

$$P(\mu,T) = \frac{2}{\beta\lambda_{dB}^3} \sum_j b_j e^{j\beta\mu} \tag{3.20}$$

With b_j the j-th virial coefficient. In our data, the first three orders are used with the known coefficient values: $b_1 = 1$, $b_2 = 3\sqrt{2}/8$ [278] and $b_3 = -0.29095295$ [277].

Interpolation curves and comments

With the previous analysis the interpolation curves used in the thermometry are shown in Fig.3.1.

We note that for the limit of high temperature (small $\beta\mu$) the pressure curve tends to unity, which is the expected behavior since the gas would look more and more like

an ideal gas at higher temperature.
At low temperatures, the normalized density shows a dramatic upturn signaling the importance of strong interactions and eventually the superfluid phase (above the dashed line), and afterwards it asymptotically reaches the zero-temperature value $1/\xi^{3/2} \simeq 4.34$. The pressure does not show an upturn but smoothly attains a limiting value. The smooth behavior is expected for a second-order transition, where first derivatives of the pressure with respect to the chemical potential are continuous across the transition.

3.2.3 Implementation and results

An EoS fitting is performed at different levels of the evaporation sequence once the IPG is turned off and the evaporation continues in the ALS (See section 2.9).
In Fig.3.2 images at different final values of the ALS power corresponding to different values of trap depths are shown. The result of the EoS fit during evaporation and the corresponding T/T_F values at the center of the trap are also presented.
As evaporation proceeds, the temperature decreases and reaches the critical value $T_C/T_F \simeq 0.17$ at the center of the trap, with T_F the Fermi temperature of the homogeneous gas below which the system becomes superfluid [157, 271]. The T/T_F value of 0.05 is clearly deep in the superfluid regime.
However, to directly observe superfluidity many methods have been developed. In the following more focus will be brought on the method in which a spin imbalance is created in the system and a superfluid core is distinctly observed in the density profile of the difference between the two spins.

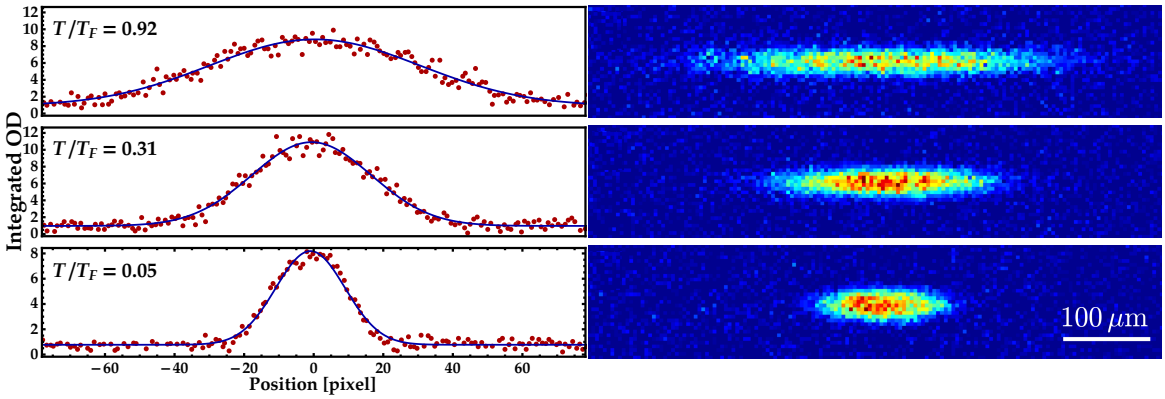

Figure 3.2: EoS fitting of the unitary degenerate gas. The atomic cloud in the ALS at different steps of the evaporation (P_{ALS} = 320, 110, 30 mW). The double integrated density profile $\bar{n}(x)$ is fitted with the EoS to obtain the ratio T/T_F corresponding to the LDA value at the center of the trap. A denser cloud at the center at colder temperatures is observed which corresponds to an increase in the phase space density. Figure adapted from S. Jin's thesis [227].

3.3 Searching fermionic superfluidity

In order to check if the system has reached the superfluid regime, the general consensus was that the system should exhibit some aspect of superfluid flow that would not be possible in a classical system.
Nevertheless, many attempts at observing such kind of behavior have failed due to the complexity of the strongly interacting regimes physics, which could obscure the superfluid transition despite it being known for its dramatic and abrupt indicators. To cite one example of these dramatic signs, the superfluid transition is easily observed in liquid Helium [3], where the liquid shows unusual properties as creeping out of the recipient which contains it and having zero viscosity.
In cold atoms experiments this turned out to be a challenge. One of many examples are the attempts at observing the so-called scissors mode [279] which have been hammered down by later studies showing similar behavior in normal gases deep in the hydrodynamic regime [280,281].
The effort continued and culminated in many experiments which established methods to detect superfluidity. In bosonic systems, merely measuring the condensate fraction [68,269,282] is a reliable measurement to detect bosonic superfluidity, where the density profile presents a clear bimodial distribution. This method would not be useful for a Fermi gas at unitarity since no condensation is allowed.
In fermionic system, one possibility is by using a rapid ramp method in which a swift ramp of the magnetic field to the BEC side to capture the momentum distribution of fermionic pairs by projecting them onto molecules [69,283] gave satisfactory results. A more direct method is to stir the superfluid and to observe vortices which are a signature of superfluidity [71].

3.3.1 Spin imbalanced systems

One of the most common and easy to implement methods to verify superfluidity is inducing a spin imbalance in the system and looking for pairing signatures in the sample [189,213].

In order to understand this method, we need to recall that one of the most prominent features of superfluidity is the emergence of an energy gap Δ in the system. This gap corresponds to the pairing energy of the Cooper pairs which form after the superfluid transition.
In the presence of a spin imbalance in the gas translated to an imbalance in the chemical potential $\delta\mu = \mu_\uparrow - \mu_\downarrow$, an interplay takes place between the gap energy and the chemical potential. If it is less costly to break a Cooper pair and flip its spin ($\delta\mu > \Delta$), a spin polarized superfluid forms and it cannot be detected easily. Whilst if the spin imbalance stays below the gap value ($\delta\mu < \Delta$) an imbalanced superfluid stays the favored state of the system. This problem was first studied in superconductors by Clogston and Chandrasekhar [211,212] and is known as the Clogston-Chandrasekhar limit.

[3] We recommend watching Alfred Leitner's 1963 videos on the superfluid transition in liquid Helium at Michigan state university.

In this regime, the minority atoms will pair up with majority atoms in the core to form Cooper pairs, this pairing induces little changes to the transition frequencies of the atoms at unitarity. The majority atoms in the outer shell form a fully polarized ideal Fermi gas. Between these two shells, the remaining minority atoms will polarize the medium creating polarons which form dimers in the BEC limit [188,284].
In the superfluid core the pairing mechanism imposes the constraint $n_\uparrow = n_\downarrow$ or using the Gibbs-Duhem relation:

$$\frac{\partial P_\uparrow}{\partial \mu_\uparrow} = \frac{\partial P_\downarrow}{\partial \mu_\downarrow} \tag{3.21}$$

Using the fact that the pressure is proportional to the integrated density $\bar{n}(z)$ as in Eq. (3.12) we can get the result in the center region:

$$\frac{\partial(\bar{n}_\uparrow - \bar{n}_\downarrow)}{\partial z} = 0 \tag{3.22}$$

This allows us to detect superfluidity by simply taking two consecutive images of both spin states and subtracting the resulting density profiles. The existence of a constant difference between the density profiles is a signature of pairing and therefore of superfluidity.

Implementation

To induce spin imbalance, a RF sweep is used as explained in section 2.9.2. By modifying the RF sweep duration applied before the evaporation and probing the atom number after the evaporation, a spin imbalance of 2:1 is induced, meaning $N_\uparrow = 2N_\downarrow$.
Afterwards, the camera is used to take two fast successive shots of the two spin states with an exposure of 7 μs each and an interval of 3 μs between them. This is accompanied by a shift in the resonant light frequency by 80MHz corresponding to the Zeeman shift between the spin states $|1\rangle$ and $|2\rangle$ at 832 G.
Typical pictures are shown in Fig.3.3, where a constant difference between the two states indicates a superfluid core in the gas.
The inner shell extending on 30 pixels $\approx$ 180 μm is a superfluid indicated by the plateau in the density difference. The second shell consists of the polaron partially polarized phase with a non-zero minority density, and it extends for around 15 pixels $\approx$ 90 μm on each side. The outermost shell is a fully polarized gas in the normal phase.
The general direction for the experiment is to explore many-body bulk systems using fermions. To this end, the group is now working on a single-atom quantum microscope able to take high resolution images for the atomic cloud, opening the way to study correlations leading to many-body phenomena which are not yet understood.

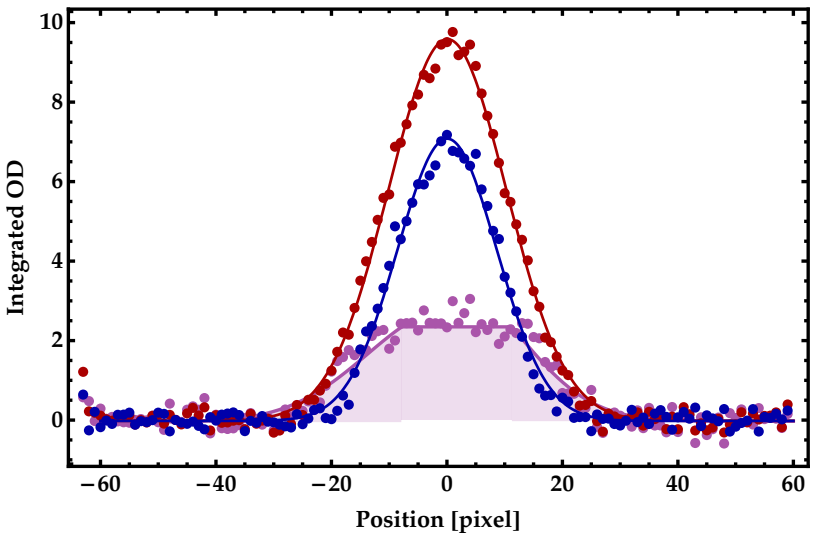

Figure 3.3: Spin imbalanced gas density profile. In red the profile density for atoms in state $|1\rangle$. In blue the profile density for atoms in state $|2\rangle$. In purple the difference between the two profiles is plotted. In this observation $N_\uparrow \approx 20000$ and $N_\downarrow \approx 12000$. A clear sign of superfluidity is observed in the center part of the cloud as the densities are equal due to pairing mechanisms. In the most outer shell a fully polarized ideal gas of atoms in state $|1\rangle$ is formed. In between a partially polarized phase is present with non-zero minority atoms density. Figure adapted from S. Jin's thesis [227].

3.4 Single-atom imaging of fermions

The next goal of the experimental setup is to achieve single-atom imaging of fermions as means to study bulk Fermi gases. Indeed, the last few years have seen many breakthroughs in quantum gas microscope experiments. These aim mainly to study 2D gases trapped in optical lattice potentials with resolutions attaining single-atom and single-lattice-site sizes [81–84, 285]. These experiments help probing variables which are otherwise unaccessible, which also helped revisiting long-standing questions, to cite a few observing the Mott insulator phase transition [286], and the study of fermion correlation in the 2D Fermi-Hubard model [88].

As the name suggests, single-atom imaging for a bulk system involves installing a high-resolution microscope objective able to reach resolutions on the order of the interatomic distance.

In this imaging scheme, fluorescence imaging technique is used, which relies on shining a resonant light on the cloud and collecting from another angle the scattered photons. The number of scattered photons and the quantum efficiency of the camera sensor determine the signal-to-noise ratio reached and whether it is sufficient to discern different atoms. While the scattering process takes place, the atoms attain higher temperatures because of the accumulative recoil energy. This is avoided by applying a cooling scheme simultaneously, and the chosen scheme is Raman sideband cooling.

Moreover, studying bulk systems differs from the case of optical lattice systems, where the system is left to evolve with a predetermined set of parameters and then imaged.
In order be able to capture the physics of the system, the imaged atoms distribution should reflect the results of the system's dynamics, which are non-trivially perturbed by the imaging and simultaneous cooling process. For this reason an optical lattice is ramped up before imaging to *pin* atoms in place and freeze their position for imaging. The subsequent cooling of atoms during imaging also takes advantage of the optical lattice in the Raman-sideband cooling technique as will be explained. This lattice is often called the pinning lattice.

3.5 Prospects of the ^{6}Li machine

The new experimental apparatus offers many interesting research paths to explore and help understanding the complex physics governing quantum many body systems. Using spin resolved single atom imaging will open the way to studying real time dynamics and spatial distributions in the gas which might help shed light on long-standing questions in the field. For instance one of the possible directions would be to study the physics of the FFLO transition in spin imbalanced Fermi gases.

In this chapter we started by the superfluid phase was characterized by comparison with the equation of state. We presented the methodology we followed and the obtained results of fitting the experimental density profile using the Equation of state of the strongly interacting gas with our density profiles.

Then we presented a further verification of the superfluid state by measuring the density profile of the cloud after having induced a spin imbalance and observing the constant value in the profile representing the difference between the densities of the two spin states in which we prepare the gas.

Finally, we described the prospective ingredients needed to achieve single-atom imaging of the fermionic gas in the bulk.

The presence of a high-resolution microscope and a box potential opens up many possibilities which were not technically available to other experiments.
One possibility is to use the box potential to determine the critical temperature dependence on the interaction strength across the BEC-BCS crossover by measuring the momentum distribution of fermion pairs after a rapid ramp towards the BEC side of the resonance [66, 188]. This measurement can be related to the critical temperature of the cloud since we are in a homogeneous potential.
In the Conclusion of this manuscript, a proposition to observe the phase diagram of an impurity immersed in a two-component Fermi sea is presented.
This chapter wraps up the experimental part of this thesis and we will then move on to describe our theoretical studies conducted in the last year of my PhD work.

Part II

Impurity immersed in a two-component Fermi sea

This part deals with two theoretical studies I have conducted starting from August 2019 until June 2020 under the supervision of Frédéric Chevy and Xavier Leyronas.
In the following, two aspects of the impurity problem in a double Fermi sea will be presented.
First, the case of an impurity immersed in an interacting fermionic superfluid is studied, and the main focus is to investigate the fundamental processes behind divergences present in the energy of the impurity. The presented part does not show yet the full answer to the problem as the work is still ongoing at the time of writing this chapter.
Second, the case of an impurity immersed in a non-interacting double Fermi sea is presented. The different phases of such a system are studied and the nature of the phase transitions that might take place is presented. This study has led to a publication focusing on the nature of transition between the polaron and trimer regime in such a system [118].

Chapter 4

Impurity in an interacting medium: a perturbative approach

The physics of an impurity immersed in a many-body ensemble is one of the simplest yet non trivial paradigms in many-body physics. In their seminal works, Landau and Pekar proposed that the properties of conduction electrons in a dielectric medium could be understood in terms of so-called polarons, i.e. quasi-particles resulting from the dressing of the electrons by collective excitations in the material identified to be the vibrations of the surrounding crystal i.e. optical phonons [97].
The properties of the polaron in different regimes has been an intriguing research field for decades. The case of an impurity immersed in a spin 1/2 superfluid was brought into light following experimental works on Bose-Fermi superfluids [111, 225, 226]. In these experiments, the impurity is weakly coupled to the background unpolarized superfluid. When the impurity is considered in a fermionic superfluid, two regimes arise depending on the nature of interactions in the superfluid. As the fermion-fermion interaction is varied in the BCS-BEC crossover, from a weakly attractive interaction on the BCS side of the crossover where fermions form loose Cooper pairs to a strongly attractive interaction on the BEC side where the Fermi gas condenses in a BEC of tightly bound dimers, the polaronic state switches from a Fermi polaron on the BCS side to a Bose polaron on the BEC side as was shown in Chapter 1.
When studying the phase diagram of the impurity in this setup assuming contact interactions between the impurity and the fermions, a peculiar UV-divergent term appears when treating the energy perturbatively with respect to the impurity-fermion interaction [117], this has been observed before in bosons [287] and is typical in three-body problems with contact interactions.
In this chapter, a quick overview of the problem is presented and then a more detailed treatment in the many-body regime is presented using the Green's function formalism.
We start by introducing basic theoretical tools which will be used to demonstrate important properties of the impurity system, mainly the Green's function formalism.

4.1 Perturbative expansion of the impurity energy

We study a regime of an impurity and two fermi seas without making any assumptions about the background fermions. In the Fermi polaron regime, the impurity-fermion interaction is weak and attractive $a \to 0^-$, so we can treat it pertubatively. In [117] this problem was studied perturbatively and as we will see, divergent terms appear in the limit of large impurity momentum. This was cured by introducing a three-body interaction in the problem and using a few-body approach an explicit form of this divergent term was obtained. This was used to renormalize the diverging term in the polaron energy.
We will be mainly interested in identifying processes leading to a divergent term in the polaron energy before introducing the three-body interaction.

4.1.1 Preliminary calculation

Consider an impurity with mass m_i immersed in a spin 1/2 fermions sea of mass m. The hamiltonian of the system is written as:

$$\begin{aligned}\hat{H} &= \hat{H}_f + \hat{H}_{imp} + \hat{H}_{int} + \hat{H}^f_{int} \\ &= \sum_{\boldsymbol{k},\sigma} \frac{\hbar^2 k^2}{2m} \hat{a}^\dagger_{\boldsymbol{k},\sigma} \hat{a}_{\boldsymbol{k},\sigma} + \sum_{\boldsymbol{q}} \frac{\hbar^2 q^2}{2m_i} \hat{c}^\dagger_{\boldsymbol{q}} \hat{c}_{\boldsymbol{q}} + \frac{g_0'}{\mathcal{V}} \sum_{\boldsymbol{k},\boldsymbol{q},\boldsymbol{k}',\boldsymbol{q}',\sigma} \delta_{\boldsymbol{k}+\boldsymbol{q},\boldsymbol{k}'+\boldsymbol{q}'} \hat{c}^\dagger_{\boldsymbol{q}'} \hat{a}^\dagger_{\boldsymbol{k}',\sigma} \hat{c}_{\boldsymbol{q}} \hat{a}_{\boldsymbol{k},\sigma} \\ &+ \frac{g_0}{\mathcal{V}} \sum_{\boldsymbol{k},\boldsymbol{q},\boldsymbol{k}',\boldsymbol{q}'} \delta_{\boldsymbol{k}+\boldsymbol{q},\boldsymbol{k}'+\boldsymbol{q}'} \hat{a}^\dagger_{\boldsymbol{q}',\uparrow} \hat{a}^\dagger_{\boldsymbol{k}',\downarrow} \hat{a}_{\boldsymbol{q},\downarrow} \hat{a}_{\boldsymbol{k},\uparrow}\end{aligned} \tag{4.1}$$

where $\hat{c}_{\boldsymbol{q}}$ is the annihilation operator of an impurity with momentum $\boldsymbol{q}$, $\hat{a}_{\boldsymbol{k},\sigma}$ is the annihilation operator of a fermion with momentum $\boldsymbol{k}$ and spin σ, and g_0' and g_0 are the bare coupling constants of the fermion-impurity and the fermion-fermion interactions respectively.
As seen in the Chapter 1, the contact potential coupling constant g_0' can be regularized by introducing a UV cutoff leading to an expression relating it to the scattering length through the following equation:

$$\frac{1}{g_0'} = \frac{1}{g'} - \frac{1}{\mathcal{V}} \sum_{k<\Lambda} \frac{2m^*}{\hbar^2 q^2} \tag{4.2}$$

where Λ is a UV cutoff, g' is the physical coupling constant between the impurity and background fermions, and it is related to the scattering length a using the relation: $g' = 2\pi\hbar^2 a'/m^*$, with m^* as the impurity-fermion reduced mass.
For weak interactions we can treat the coupling constant pertubatively, we find up to 2nd order:

$$g_0' = g' + \frac{g'^2}{\mathcal{V}} \sum_{k<\Lambda} \frac{2m^*}{\hbar^2 q^2} + o(g'^2) \tag{4.3}$$

We calculate the first order of perturbation of the energy of the impurity, with $|\Psi_0\rangle = |\phi_0\rangle \otimes |0\rangle$ the ground state of the superfluid with energy E_0 and the impurity respectively:

$$E^{(1)} = \langle \Psi_0 | \hat{H}_{int} | \Psi_0 \rangle = \frac{g_0' N_F}{\mathcal{V}} = g' n + \frac{g'^2 n}{\mathcal{V}} \sum_{k<\Lambda} \frac{2m^*}{q^2} \tag{4.4}$$

where N_F is the total number of fermions in both states. We see that we recover the mean field energy in the first term, and the second term will play a role in cancelling the divergence in the second term of the perturbative energy expansion which we calculate in the following:

$$E^{(2)} = \sum_{i\neq 0, \boldsymbol{q}\neq\boldsymbol{p}} \frac{|\langle \phi_i, \boldsymbol{q}|\hat{H}_{int}|\boldsymbol{p}, \phi_0\rangle|^2}{E_0 - E_i - \epsilon_q} = \frac{g_0'^2}{\mathcal{V}^2} \sum_{i\neq 0, \boldsymbol{q}\neq\boldsymbol{p}} \frac{|\langle \phi_i|\int d^3\boldsymbol{r}\, \psi_0^\dagger(\boldsymbol{r})\psi_0(\boldsymbol{r})e^{-i\boldsymbol{q}\boldsymbol{r}}|\phi_0\rangle|^2}{E_0 - E_i - \epsilon_q} \tag{4.5}$$

where $\psi_0^\dagger(\boldsymbol{r})$ is the field operator that creates a fermion at position $\boldsymbol{r}$ and E_0 is the ground state of the fermionic background, E_i is the energy of a state $|\phi_i\rangle$ of the fermionic background, ϵ_q is the impurity's unperturbed energy. We define:

$$\rho_{-\boldsymbol{q}} = \sum_\sigma \int d^3\boldsymbol{r}\psi_0^\dagger(\boldsymbol{r})\psi_0(\boldsymbol{r})e^{-i\boldsymbol{q}\boldsymbol{r}}, \tag{4.6}$$

as the Fourier transform of the density operator, and:

$$\chi(\boldsymbol{q}, E) = \frac{1}{N_F}\sum_{i\neq 0} \frac{|\langle \phi_i|\rho_{-\boldsymbol{q}}|\phi_0\rangle|^2}{E_i + E - E_0} \tag{4.7}$$

as the density response function. With these definitions we can write the energy as:

$$E = g'n + \frac{g'^2 n}{\mathcal{V}} \sum_{\boldsymbol{q}<\Lambda} [\frac{2m^*}{\hbar^2 q^2} - \chi(\boldsymbol{q}, \epsilon_{\boldsymbol{q}})] \tag{4.8}$$

where $\epsilon_{\boldsymbol{q}}$ is the energy of the impurity.

4.1.2 Asymptotic behavior

For large momenta $|\boldsymbol{q}|\to\infty$ of the impurity, the function χ has to behave as $1/q^2$ to cancel the otherwise divergent first term in the sum. At this limit, the energy of the excitations is mainly that of the particles since the holes are confined to the Fermi sphere and their energy becomes negligible, leading to the consideration that the eigenstates of the many-body hamiltonian correspond to free particle excitations of momentum $\boldsymbol{q}$ and energy $\hbar^2q^2/(2m)$. For an ideal Fermi gas, the response function then simplifies to:

$$\chi(\boldsymbol{q}, \epsilon_{\boldsymbol{q}}) \underset{|\boldsymbol{q}|\to\infty}{\simeq} \frac{1}{N_F}(\frac{1}{E_q + \epsilon_q})\sum_{i\neq 0}|\langle \psi_i|\rho_{-\boldsymbol{q}}|\psi_0\rangle|^2 = (\frac{1}{E_q + \epsilon_q})S(q) \tag{4.9}$$

where $E_q = \hbar^2q^2/2m$ is the Fermionic excitation energy, and $S(q)$ is the static structure factor, it characterizes the two body correlations in interacting systems and is measurable exactly. Its expression in the large momentum limit is [288, 289]:

$$S(q) \underset{|\boldsymbol{q}|\to\infty}{\simeq} 1 + \frac{\mathcal{C}_2}{4N_F q} + o(\frac{1}{q}) \tag{4.10}$$

where $\mathcal{C}_2$ is Tan's contact, first introduced by Shina Tan in 2008 [290, 291], a fundamental quantity that characterizes short-range two-body correlations. This simple analysis yields:

$$\chi(\boldsymbol{q}, \epsilon_{\boldsymbol{q}}) \underset{|\boldsymbol{q}|\to\infty}{\simeq} \frac{2m^*}{\hbar^2 q^2} + \frac{2m^*\mathcal{C}_2}{4\hbar^2 N_F q^3} + o(\frac{1}{q}) \tag{4.11}$$

The first term cancels with the term coming from regularizing the coupling constant in Eq. (4.2), but we see that the subdominant term presents a UV-logarithmic divergence in Eq. (4.8);
We also note that there are other terms in the expansion which come from the denominator in Eq. (4.9) that contribute to the subdominant term, for that we note that this formula only indicates the general behavior of $\chi(\boldsymbol{q}, E)$ when $|\boldsymbol{q}| \to \infty$ without accurately describing the coefficient of the divergent term. This result means that the regularization of the coupling constant was not enough.
This logarithmic divergence is typical of a singularity in the three-body problem for particles with contact interactions. This characteristic was first discovered by Wu [287] for a system of three bosons and was also investigated in the context of nuclear physics [106] or more recently with cold atoms [114, 292–294].
In the following, we present a diagrammatic calculation to understand the origin of the $1/q^3$ term in the function $\chi(\boldsymbol{q}, \epsilon_q)$. We start by extracting this function from the impurity's Green's function expansion and then by carefully going through the different diagrams and finding those at the origin of the logarithmic divergence.

4.2 Green's function for an interacting system

The Green's function formalism together with Feynman diagrams form one of the essential tools for modern quantum many-body physics, whether it is in particle physics, condensed matter or cold atoms physics.
The physics of quantum interacting systems becomes complex very fast, with the number of scattering processes in the Hilbert space increasing exponentially when the number of particles is increased when it is treated perturbatively. To that end, the Green's function formalism allows us to avoid the jumble of creation and annihilation operators encountered in perturbation theory calculations. This is done by ordering these operators in a way which allows us to map them to a unique intuitive graphical representation or *Feynman diagram* which helps writing these terms and extract useful features from them before moving to write their analytic expressions.
We start this section by defining the Green's function in a many-body system at zero temperature then we introduce briefly the time evolution operator and the adiabatic activation principles which will be handy in giving a general formula for the Green's function in a many-body regime.

4.2.1 Green's function: Definition

The Green's function, also called propagator in the path integral formalism, represents the amplitude that a single particle (hole) with momentum $\boldsymbol{k}$ added to the many-body system in a single particle state $\psi_{\boldsymbol{k}}$ at a time t' (t) will remain in the same single-particle state after a certain time $t - t'$ ($t' - t$). This probability is expressed by an expectation value:

$$G(\boldsymbol{k}; t - t') = -i\langle \mathcal{T} \hat{a}_{\boldsymbol{k}}(t) \hat{a}^{\dagger}_{\boldsymbol{k}}(t') \rangle \tag{4.12}$$

where $\hat{a}_{\boldsymbol{k}}$ and $\hat{a}^{\dagger}_{\boldsymbol{k}}$ are respectively the annihilation and creation operators for the particle, $\mathcal{T}$ is the time ordering operator which will order the operators that follow

it in a chronological order (with a minus sign in case of interchange of fermionic operators).
The expectation value is, at zero temperature, calculated in the many-body ground state $|\Psi_0\rangle$. For non-zero temperatures it becomes a quantum statistical expectation value where in addition to the usual quantum expectation value we also average over a suitable statistical ensemble of many-body states.
For interacting systems, the particle is created in the system and left to evolve and scatter with other particles, and then the Green's function measures the probability of this particle to stay in its original state.
This description fits perfectly with many experiments done in solid state physics for instance. There, a sample is exposed to a beam of electrons and then the number of electrons that come through from the original beam is measured, and how much is scattered [295].

4.2.2 Time evolution operator

For an interacting system we can write the hamiltonian of the system in the following way:

$$\hat{H} = \hat{H}_0 + \hat{H}_I \tag{4.13}$$

where $\hat{H}_0$ is an exactly solvable part describing the non-interacting system and $\hat{H}_I$ is treated as a perturbation and usually includes the interactions.

In the interaction picture (Dirac picture), operators transform according to $\hat{H}_0$, so that:

$$\hat{H}_I(t) = e^{i\hat{H}_0 t/\hbar}\hat{H}_I e^{-i\hat{H}_0 t/\hbar} \tag{4.14}$$

and wave-functions transform according to $\hat{H}_I$:

$$i\hbar\frac{d|\Psi(t)\rangle_I}{dt} = \hat{H}_I(t)|\Psi(t)\rangle_I \tag{4.15}$$

This differential equation can be integrated giving:

$$|\Psi(t)\rangle_I = \mathcal{T}\exp\Big\{-\frac{i}{\hbar}\int_{t_0}^{t} dt'\hat{H}_I(t')\Big\}|\Psi(t_0)\rangle_I \tag{4.16}$$

We define the time evolution operator as:

$$\hat{U}(t,t_0) = \mathcal{T}\exp\Big\{-\frac{i}{\hbar}\int_{t_0}^{t} dt'\hat{H}_I(t')\Big\} \tag{4.17}$$

We can check that it agrees with the simple definition of the time evolution operator of the time-independent Schrödinger equation $\hat{U}(t,t_0) = \exp\{-i(t-t_0)\hat{H}_I/\hbar\}$ in the case where $\hat{H}_I$ is time independent.
The last equation can be written in a more explicit form by using the Taylor's expansion of the exponential function as the following:

$$\hat{U}(t,t_0) = \sum_{n=0}^{\infty}\frac{1}{n!\,(i\hbar)^n}\int_{t_0}^{t} dt_1\int_{t_0}^{t} dt_2 ... \int_{t_0}^{t} dt_n \mathcal{T}[\hat{H}_I(t_1)\hat{H}_I(t_2)...\hat{H}_I(t_n)] \tag{4.18}$$

where $\mathcal{T}$ is the time ordering operator. We can verify that $\hat{U}^\dagger(t_0,t) = \hat{U}(t,t_0)$ and $\hat{U}(t,t_1)\hat{U}(t_1,t_0) = \hat{U}(t,t_0)$.

4.2.3 Adiabatic activation

The one particle Green's function in an interacting system is written as:

$$G(\boldsymbol{k}; t - t') = -i\frac{\langle \Psi_{GS}|\mathcal{T}\hat{a}_{\boldsymbol{k}}(t)\hat{a}^{\dagger}_{\boldsymbol{k}}(t')|\Psi_{GS}\rangle}{\langle \Psi_{GS}|\Psi_{GS}\rangle} \tag{4.19}$$

where $|\Psi_{GS}\rangle$ is the unknown many-body ground state of the interacting system described by the full hamiltonian $\hat{H}$ in Eq. (4.13), and $\hat{a}_{\boldsymbol{k}}$ and $\hat{a}^{\dagger}_{\boldsymbol{k}}$ are respectively the annihilation and creation operators for a particle with momentum $\boldsymbol{k}$.
We want to relate this function to the Green's function of the non-interacting system:

$$G_0(\boldsymbol{k}; t - t') = -i\langle \Psi_0|\mathcal{T}\hat{a}_{\boldsymbol{k}}(t)\hat{a}^{\dagger}_{\boldsymbol{k}}(t')|\Psi_0\rangle \tag{4.20}$$

where Ψ_0 is the ground state of the non-interacting system described by $\hat{H}_0$.
To establish the connection we will switch on the interactions adiabatically, this can be done by constructing the following hamiltonian:

$$\hat{H}(t) = \hat{H}_0 + e^{-\epsilon|t|}\hat{H}_I(t) \tag{4.21}$$

At time $t \to -\infty$ this represents the unperturbed system with ground state Ψ_0, while at time $t = 0$ it represents the full interacting system. The parameter ϵ is taken to be real and infinitesimally small, so that the changes occur adiabatically [1].
That means we can consider a time evolution operator corresponding to the hamiltonian in Eq. (4.21), the energy levels will shift and move continuously, but their occupation will not change. If a particle is in the ground state energy level, it will not transition to a higher level but follow the change of the wavefunction associated with the ground state.
With this we can write:

$$|\Psi_{GS}\rangle = \hat{U}(0, -\infty)|\Psi_0\rangle \tag{4.22}$$

This result is known as the **Gell-Mann and Low theorem** [296].
After transforming the creation and annihilation operators to the interaction picture using

$$[\hat{a}_k(t)]_H = \hat{U}(0, t)[\hat{a}_k(t)]_I\hat{U}(t, 0),$$

the Green's function in Eq. (4.19) for $t > t'$ is written as:

$$G(\boldsymbol{k}; t - t') = -i\frac{\langle \Psi_0|\hat{U}(\infty, 0)\hat{U}(0, t)\hat{a}_{\boldsymbol{k}}(t)\hat{U}(t, 0)\hat{U}(0, t')\hat{a}^{\dagger}_{\boldsymbol{k}}(t')\hat{U}(t', 0)\hat{U}(0, -\infty)|\Psi_0\rangle}{\langle \Psi_0|\hat{U}(\infty, 0)\hat{U}(0, -\infty)|\Psi_0\rangle} \tag{4.23}$$

Using the properties of the time evolution operator we can simplify the expression as follows:

$$G(\boldsymbol{k}; t - t') = -i\frac{\langle \Psi_0|\hat{U}(\infty, t)\hat{a}_{\boldsymbol{k}}(t)\hat{a}^{\dagger}_{\boldsymbol{k}}(t')\hat{U}(t', -\infty)|\Psi_0\rangle}{\langle \Psi_0|\hat{U}(\infty, -\infty)|\Psi_0\rangle} \tag{4.24}$$

[1] One must be careful when taking the limit $\epsilon \to 0$ as it might lead to an oscillating phase as explained in [295]

Finally we write the full expression of the Green's function used here with the help of the expression written for the time evolution operator in Eq. (4.18):

$$G(\boldsymbol{k}; t-t') = \frac{-i}{\langle\Psi_0|\hat{U}(\infty,-\infty)|\Psi_0\rangle}\langle\Psi_0|\sum_{n=0}^{\infty}\frac{1}{n!\,(i\hbar)^n}\int_{-\infty}^{\infty}dt_1\int_{-\infty}^{\infty}dt_2...\int_{-\infty}^{\infty}dt_n \quad (4.25)$$
$$e^{-\epsilon(|t_1|+...+|t_n|)}\mathcal{T}[\hat{a}_{\boldsymbol{k}}(t)\hat{H}_I(t_1)\hat{H}_I(t_2)...\hat{H}_I(t_n)\hat{a}^{\dagger}_{\boldsymbol{k}}(t')]|\Psi_0\rangle$$

Here we used the time reversal symmetry of the adiabatic activation, meaning that the hermitian conjugate of the time-evolution operator for a state evolving from $t \to -\infty$ to $t = 0$ is equal to the time-evolution operator evolving from $t = 0$ to $t \to \infty$.
The last two expressions only contain expectation values with respect to the ground state of the non-interacting system, which is the goal behind the adiabatic activation: no more expectation values with respect to the unknown many-body ground state. The exponential factor will be set to 1 when taking the limit $\epsilon \to 0$.
This expression allows the many-body problem to be treated iteratively in a manner similar to perturbation theory where for the first order the particle interacts only once with the bath and for the second it interacts twice and so on. This treatment allows us, if we are patient enough, to capture all physical processes allowed by quantum many-body physics and therefore describe the full system accurately. However, as we will see, the number of allowed combinations of these operators in the development of the Green's function explodes which restricts largely the analytical capabilities of this method.

4.2.4 Vacuum polarisation

We worked out the numerator in Eq. (4.19), as for the denominator we can write it as follows:

$$\begin{aligned} S_0 &= \langle\Psi_0|\hat{U}(\infty,-\infty)|\Psi_0\rangle \\ &= \sum_{n=0}^{\infty}\frac{1}{n!\,(i\hbar)^n}\int_{-\infty}^{\infty}dt_1\int_{-\infty}^{\infty}dt_2...\int_{-\infty}^{\infty}dt_n\langle\Psi_0|\mathcal{T}[\hat{H}_I(t_1)\hat{H}_I(t_2)...\hat{H}_I(t_n)]|\Psi_0\rangle \end{aligned} \quad (4.26)$$

The last expression describes interactions already happening in the background bath with no influence from the particle we are considering. Therefore, all terms in Eq. (4.25) containing non-interacting propagators of the concerned particles will have a part in which only bath interactions appear (disconnected diagrams) and will be canceled with the corresponding term in S_0, leaving only terms where the particle of interest is interacting with the bath (connected diagrams).
This term is called vacuum polarisation since it was inspired by Quantum Electrodynamics theory where virtual electron-positron pairs are created in vacuum and they change the distribution of charge in the system and therefore polarize it.

4.3 Perturbative expansion using Green's function formalism

As seen in the last section, the energy presents logarithmic divergences in the limit $|\boldsymbol{q}|\to\infty$ due to the presence of a $1/q^3$ term in $\chi(\boldsymbol{q},\epsilon_q)$. In the regime of weak attractive interactions between the impurity and the fermions, and by using the perturbative expansion of the Green's function of the impurity, we isolate the contribution of $\chi(\boldsymbol{q},\epsilon_q)$ in the second order term and then we try to identify the diagrams describing physical processes responsable for this divergence. We start by studying the Green's function of an impurity immersed in an interacting superfluid.

4.3.1 The impurity's Green function

Using the definition in Eq. (4.19) we can write the Green function of the impurity as follows:

$$G_I(\boldsymbol{p};t) = -i\frac{\langle\Psi_{GS}|\mathcal{T}\hat{c}_{\boldsymbol{p}}(t)\hat{c}^\dagger_{\boldsymbol{p}}(0)|\Psi_{GS}\rangle}{\langle\Psi_{GS}|\Psi_{GS}\rangle} \tag{4.27}$$

where the expectation value is taken on the function $|\Psi_{GS}\rangle = |\psi_0\rangle\otimes|0\rangle$, where $|0\rangle$ is the vacuum of the impurity and $|\psi_0\rangle$ is the ground state of the interacting bath.
Since we are studying the polaron's energy, we want to study the effect of an impurity's creation on the Fermi sea. That's why we start from a ground state of an interacting Fermi sea and no impurity. Note that for this, in Eq. (4.24) the $\hat{U}$ operators on the right and left of the impurity operators are equal to 1.

First order

Using Eq. (4.25) we can write the first order perturbation expansion of this function (which corresponds to the term of the sum with $n=1$ without the denominator):

$$\begin{aligned} G_{I,1}(\boldsymbol{p};t) &= -i\langle\Psi_0|\frac{1}{i\hbar}\int_{-\infty}^{\infty}dt_1\mathcal{T}[\hat{c}_{\boldsymbol{p}}(t)\hat{H}_I(t_1)\hat{c}^\dagger_{\boldsymbol{p}}(0)]|\Psi_0\rangle \\ &= -\frac{g_0'}{\hbar\mathcal{V}}\int_{-\infty}^{\infty}dt_1\sum_{\boldsymbol{k},\boldsymbol{q},\boldsymbol{k}',\boldsymbol{q}',\sigma}\delta_{\boldsymbol{k}+\boldsymbol{q},\boldsymbol{k}'+\boldsymbol{q}'}\langle\Psi_0|\mathcal{T}[\hat{c}_{\boldsymbol{p}}(t)\hat{c}^\dagger_{\boldsymbol{q}'}(t_1)\hat{c}_{\boldsymbol{q}}(t_1)\hat{a}^\dagger_{\boldsymbol{k}',\sigma}(t_1)\hat{a}_{\boldsymbol{k},\sigma}(t_1)\hat{c}^\dagger_{\boldsymbol{p}}(0)]|\Psi_0\rangle \end{aligned} \tag{4.28}$$

we calculate the expectation value, for that we observe that the expectation value of a product of an impurity operator and a bath operator factorizes.
Then, we use **Wick's theorem** which allows the expectation value of a product of creation and annihilation operators to be written as a product of expectation values of all possible pairs of creation and annihilation operators.
So we can write the expectation value as follows:

$$\begin{aligned} &\langle\Psi_0|\mathcal{T}[\hat{c}_{\boldsymbol{p}}(t)\hat{c}^\dagger_{\boldsymbol{q}'}(t_1)]|\Psi_0\rangle\langle\Psi_0|\mathcal{T}[\hat{c}_{\boldsymbol{q}}(t_1)\hat{c}^\dagger_{\boldsymbol{p}}(0)]|\Psi_0\rangle\langle\Psi_0|\mathcal{T}[\hat{a}^\dagger_{\boldsymbol{k}',\sigma}(t_1)\hat{a}_{\boldsymbol{k},\sigma}(t_1)]|\Psi_0\rangle \\ -&\langle\Psi_0|\mathcal{T}[\hat{c}_{\boldsymbol{p}}(t)\hat{c}^\dagger_{\boldsymbol{p}}(0)]|\Psi_0\rangle\langle\Psi_0|\mathcal{T}[\hat{c}_{\boldsymbol{q}}(t_1)\hat{c}^\dagger_{\boldsymbol{q}'}(t_1)]|\Psi_0\rangle\langle\Psi_0|\mathcal{T}[\hat{a}^\dagger_{\boldsymbol{k}',\sigma}(t_1)\hat{a}_{\boldsymbol{k},\sigma}(t_1)]|\Psi_0\rangle \\ =&i^2\delta_{\boldsymbol{p}\boldsymbol{q}'}\delta_{\boldsymbol{p}\boldsymbol{q}}\delta_{\boldsymbol{k}\boldsymbol{k}'}G_{I,0}(\boldsymbol{p},t-t_1)G_{I,0}(\boldsymbol{p},t_1)n_{\boldsymbol{k},\sigma}(t_1) - i^2\delta_{\boldsymbol{q}\boldsymbol{q}'}\delta_{\boldsymbol{k}\boldsymbol{k}'}G_{I,0}(\boldsymbol{p},t)G_{I,0}(\boldsymbol{p},t_1-t_1)n_{\boldsymbol{k},\sigma}(t_1) \end{aligned}$$

where $n_{\boldsymbol{k},\sigma}(t)$ is the number of fermions in single-particle state $\psi_{\boldsymbol{k},\sigma}$ at instant t, this observable does not depend explicitly on time.

We also leave out the second term since it represents a disconnected diagram which cancels with the denominator from Eq. (4.24) as was seen in Section 4.2.4. With this we can write Eq. (4.28) as:

$$G_{I,1}(\boldsymbol{p};t) = \frac{g_0' n}{\hbar}\int_{-\infty}^{\infty} dt_1 G_{I,0}(\boldsymbol{p}, t-t_1)G_{I,0}(\boldsymbol{p},t_1) \tag{4.29}$$

where $n = \sum_{k,\sigma} n_{k,\sigma}$ is the density of fermions in the bath, and:

$$G_{I,0}(\boldsymbol{p},t) = -i\theta(t)e^{-i\epsilon_p t/\hbar} \tag{4.30}$$

is the impurity's free particle Green's function, where $\epsilon_p = \hbar^2 p^2/(2m_i)$. We kept only the retarded part since we're studying the propagation of the impurity in a ground-state without the impurity (we start by creating the impurity and any term that does not take this into account is equal to zero). This term gives the mean-field contribution in the self-energy of the impurity (first term in Eq. (4.8)). In diagrammatic terms this gives a tadpole diagram and its middle part gives a contribution to the self energy $g_0' n/\hbar$.

Second order

Similar to the previous calculation, we can write the second order of perturbation for the impurity's Green's function as follows:

$$\begin{aligned} G_{I,2}(\boldsymbol{p},t) =& -i\langle\Psi_0|\frac{1}{2(i\hbar)^2}\int_{-\infty}^{\infty}dt_1\int_{-\infty}^{\infty}dt_2\mathcal{T}[\hat{c}_{\boldsymbol{p}}(t)\hat{H}_I(t_1)\hat{H}_I(t_2)\hat{c}^\dagger_{\boldsymbol{p}}(0)]|\Psi_0\rangle \\ =&\frac{ig_0'^2}{2\hbar^2\mathcal{V}^2}\int_{-\infty}^{\infty}dt_1\int_{-\infty}^{\infty}dt_2\sum_{\substack{\boldsymbol{k}\boldsymbol{q}\boldsymbol{k}'\boldsymbol{q}'\\ \boldsymbol{k}_1\boldsymbol{q}_1\boldsymbol{k}_1'\boldsymbol{q}_1',\sigma}}\delta_{\substack{\boldsymbol{k}+\boldsymbol{q}\\ \boldsymbol{k}'+\boldsymbol{q}'}}\delta_{\boldsymbol{k}_1+\boldsymbol{q}_1,\boldsymbol{k}_1'+\boldsymbol{q}_1'}\langle\mathcal{T}[\hat{c}_{\boldsymbol{p}}(t)\hat{c}^\dagger_{\boldsymbol{q}'}(t_1)\hat{c}_{\boldsymbol{q}}(t_1) \\ &\hat{a}^\dagger_{\boldsymbol{k}',\sigma}(t_1)\hat{a}_{\boldsymbol{k},\sigma}(t_1)\hat{c}^\dagger_{\boldsymbol{q}_1'}(t_2)\hat{c}_{\boldsymbol{q}_1}(t_2)\hat{a}^\dagger_{\boldsymbol{k}_1',\sigma}(t_2)\hat{a}_{\boldsymbol{k}_1,\sigma}(t_2)\hat{c}^\dagger_{\boldsymbol{p}}(0)]\rangle \end{aligned} \tag{4.31}$$

we evaluate the expectation value first, we leave out all terms containing loops of the impurity propagator (cf. Eq. (4.30)). We write the expectation value over the impurity operators as:

$$\begin{aligned} &\langle\mathcal{T}[\hat{c}_{\boldsymbol{p}}(t)\hat{c}^\dagger_{\boldsymbol{q}'}(t_1)\hat{c}_{\boldsymbol{q}}(t_1)\hat{c}^\dagger_{\boldsymbol{q}_1'}(t_2)\hat{c}_{\boldsymbol{q}_1}(t_2)\hat{c}^\dagger_{\boldsymbol{p}}(0)]\rangle = i^3\delta_{\boldsymbol{p},\boldsymbol{q}'}\delta_{\boldsymbol{q},\boldsymbol{q}_1'}\delta_{\boldsymbol{p},\boldsymbol{q}_1}G_{I,0}(\boldsymbol{p},t-t_1)G_{I,0}(\boldsymbol{q},t_1-t_2)G_{I,0}(\boldsymbol{p},t_2) \\ &+i^3\delta_{\boldsymbol{p},\boldsymbol{q}_1'}\delta_{\boldsymbol{q},\boldsymbol{p}}\delta_{\boldsymbol{q}_1,\boldsymbol{q}'}G_{I,0}(\boldsymbol{p},t-t_2)G_{I,0}(\boldsymbol{q},t_1)G_{I,0}(\boldsymbol{q}_1,t_2-t_1) \end{aligned}$$

where terms that also contain a fermionic loop were cancelled by the denominator of Eq. (4.27). For the other two terms they are equal if we replace t_1 by t_2. If we plug that in Eq. (4.31) we get:

$$G_{I,2}(\boldsymbol{p},t) = \frac{g_0'^2}{\hbar^2\mathcal{V}^2}\int_{-\infty}^{\infty}dt_1\int_{-\infty}^{\infty}dt_2\sum_{\boldsymbol{p}_1}\langle\mathcal{T}\hat{\rho}_{\boldsymbol{p}_1-\boldsymbol{p}}(t_1)\hat{\rho}_{\boldsymbol{p}-\boldsymbol{p}_1}(t_2)\rangle G_{I,0}(\boldsymbol{p},t-t_2)G_{I,0}(\boldsymbol{p},t_1)G_{I,0}(\boldsymbol{p}_1,t_2-t_1)$$

In case $\boldsymbol{p}=\boldsymbol{p}_1$, we get $\hat{\rho}_0 = \hat{N}$ the number operator in the bath, we find:

$$G_{I,2}(\boldsymbol{p},t) = \frac{g_0'^2 n^2}{\hbar^2}\int_{-\infty}^{\infty}dt_1\int_{-\infty}^{\infty}dt_2 G_{I,0}(\boldsymbol{p},t-t_2)G_{I,0}(\boldsymbol{p},t_1)G_{I,0}(\boldsymbol{p}_1,t_2-t_1)$$

In case $\boldsymbol{p} \neq \boldsymbol{p}_1$:

$$G_{I,2}(\boldsymbol{p},t) = \int_{-\infty}^{\infty} dt_1 \int_{-\infty}^{\infty} dt_2 \left[\frac{{g'}_0^2}{\hbar^2 \mathcal{V}^2} \sum_{p_1 \neq p} G_{I,0}(\boldsymbol{p}_1, t_2 - t_1) \langle \hat{\rho}_{p_1 - p}(t_2) \hat{\rho}_{p - p_1}(t_1) \rangle \right] \\ G_{I,0}(\boldsymbol{p}, t - t_2) G_{I,0}(\boldsymbol{p}, t_1) \tag{4.32}$$

where $\hat{\rho}_q = \sum_{k,\sigma} \hat{c}^\dagger_{k,\sigma} \hat{c}_{k+q,\sigma}$ is the Fourier transform of the bath density at wave-vector $\boldsymbol{q}$.
The quantity between brackets contributes to the self energy (the rest of the equation are the incoming and outgoing impurity particle and the bracketed part is the interaction with the bath).
We are going to limit ourselves to this order for the impurity's Green function (second order in ${g'}_0$), but we will follow the evolution of the fermionic expectation value to understand the divergence, for that we follow the same steps as before but with $\hat{H}^f_{int}$ as the interaction hamiltonian to capture the interactions between fermions.

As a sanity check, we insert a completeness relation $\sum_i |\psi_i\rangle\langle\psi_i| = 1$ between the two density operators. Then, we take the Fourier transform with respect to the time difference $t_2 - t_1$. We find

$$\begin{aligned} \Sigma^{(2)}_{\text{pol}}(\mathbf{p},t) &= \frac{{g'}_0^2}{\hbar^2 \mathcal{V}^2} \sum_{p_1 \neq p} G_{I,0}(\boldsymbol{p}_1, t) \langle \hat{\rho}_{p_1 - p}(t) \hat{\rho}_{p - p_1}(0) \rangle \\ &= \int_{-\infty}^{\infty} \frac{du}{2\pi} \frac{{g'}_0^2}{\hbar^2 \mathcal{V}^2} \frac{e^{-iut}}{u + i\eta} e^{-i\epsilon_{p_1} t/\hbar} \sum_{p_1 \neq p} \sum_{i \neq 0} e^{-i(E_i - E_0)t/\hbar} |\langle \psi_i | \hat{\rho}_{p - p_1} | \Psi_0 \rangle|^2 \end{aligned} \tag{4.33}$$

where $\eta \to 0^+$. We can see this as the Fourier transform of a function $\Sigma^{(2)}_{\text{pol}}(\mathbf{p},\omega)$ defined as:

$$\Sigma^{(2)}_{\text{pol}}(\mathbf{p},t) = \int_{-\infty}^{\infty} \frac{d\omega}{2\pi} e^{-i\omega t} \Sigma^{(2)}_{\text{pol}}(\mathbf{p},\omega)$$

with the variable change $\omega = u + \epsilon_p/\hbar - E_0/\hbar + E_i/\hbar$ with the same variables in Eq. (4.5) to get the following function (we put $\hbar = 1$):

$$\Sigma^{(2)}_{\text{pol}}(\mathbf{p},\omega) = \frac{{g'}_0^2}{\mathcal{V}^2} \sum_{p_1 \neq p} \sum_{i \neq 0} \frac{|\langle \psi_i | \hat{\rho}_{p - p_1} | \Psi_0 \rangle|^2}{\omega + i\,\eta - (E_i - E_0 + \epsilon_{p_1})} \tag{4.34}$$

For $\omega = 0$ and $\mathbf{p} = \mathbf{0}$, the result obtained by usual perturbation theory back in Eq. (4.5) is recovered.

4.3.2 Expectation value of the density-density correlation function

As seen in Eq. (4.33) and back in Eq. (4.8) the expectation value of the density-density correlation function is responsible for the divergent term for $|\boldsymbol{q}| \to \infty$.
We start by writing properly this expectation value defined for $\boldsymbol{q} \neq 0$, (notice that

the time ordering operator $\mathcal{T}$ always operates on what is inside the expectation brackets):

$$i\chi^T(\boldsymbol{q},t) = \langle \mathcal{T}\hat{\rho}_{\boldsymbol{q}}(t)\hat{\rho}_{-\boldsymbol{q}}(0)\rangle = \sum_{\boldsymbol{k},\boldsymbol{k}',\sigma,\sigma'} \langle \mathcal{T} a^\dagger_{\boldsymbol{k},\sigma}(t) a_{\boldsymbol{k}+\boldsymbol{q},\sigma}(t) a^\dagger_{\boldsymbol{k}',\sigma'}(0) a_{\boldsymbol{k}'-\boldsymbol{q},\sigma'}(0)\rangle \tag{4.35}$$

where the expectation value is taken over $|\Psi_0\rangle$ the ground state of the interacting bath. Its Fourrier transform can be written as:

$$\chi^T(\boldsymbol{q},\omega) = \sum_{i\neq 0} \frac{|\langle\phi_i|\rho_{-\boldsymbol{q}}|\phi_0\rangle|^2}{\omega + i\eta - E_i + E_0} - \sum_{i\neq 0} \frac{|\langle\phi_i|\rho_{\boldsymbol{q}}|\phi_0\rangle|^2}{\omega + i\eta + E_i - E_0} \tag{4.36}$$

This definition could be related to the one in Eq. (4.7) by the expression $\chi(\boldsymbol{q},E) = -N_F\,\chi^{T,R}(\boldsymbol{q},-E)$, where $\chi^{T,R}(\boldsymbol{q},-E)$ is the retarded part of $\chi^T(\boldsymbol{q},-E)$.
We would like to express this expectation value in terms of the non-interacting fermionic Green's function:

$$\begin{aligned} G_{0,\sigma}(\boldsymbol{k},t-t') &= -i\langle\Psi_{FS}|\mathcal{T}\hat{a}_{\boldsymbol{k},\sigma}(t)\hat{a}^\dagger_{\boldsymbol{k},\sigma}(t')|\Psi_{FS}\rangle \\ &= -ie^{-iE_{k,\sigma}(t-t')/\hbar}\Big[\theta(k_\sigma > k_{F,\sigma})\theta(t>t') - \theta(k_\sigma < k_{F,\sigma})\theta(t<t')\Big] \end{aligned} \tag{4.37}$$

where here we either treat a fermion propagating above the Fermi sea, or a hole propagating inside the Fermi sea.
In reciprocal space, the Green's function takes the following form:

$$G_{0,\sigma}(k) = \frac{\theta(|\boldsymbol{k}|>k_F)}{\omega - E_{\boldsymbol{k},\sigma} + i\eta} + \frac{\theta(|\boldsymbol{k}|<k_F)}{\omega - E_{\boldsymbol{k},\sigma} - i\eta} \tag{4.38}$$

where $E_k = \hbar^2k^2/(2m_\sigma)$ is the energy of the fermion added to the system.
In [117] the three-body regularization of the problem needs a $\propto 1/|\boldsymbol{q}|^3$ subdominant term in the expansion of $\chi(\boldsymbol{q},t)$ at $|\boldsymbol{q}|\to\infty$. Although the treatment there did not make any assumptions about the fermions interaction. For simplicity, we will start in the limit of a weakly interacting bath (BCS limit) for the time being.
As before, we use the adiabatic activation technique to treat the fermionic interactions considering that the fermion-fermion scattering length is small and negative (BCS side).

Zeroth order

The zeroth order is calculated by taking the expectation value of the expression directly over the non-interacting ket, we can use Wick's theorem to write as follows:

$$i\chi^T_0(\boldsymbol{q},t) = \sum_{\boldsymbol{k},\boldsymbol{k}',\sigma,\sigma'} \langle \mathcal{T} a^\dagger_{\boldsymbol{k},\sigma}(t) a_{\boldsymbol{k}+\boldsymbol{q},\sigma}(t) a^\dagger_{\boldsymbol{k}',\sigma'}(0) a_{\boldsymbol{k}'-\boldsymbol{q},\sigma'}(0)\rangle = \sum_{\boldsymbol{k},\sigma} G_{0,\sigma}(k,-t)G_{0,\sigma}(|k+q|,t) \tag{4.39}$$

Other contractions are zero since $|\boldsymbol{q}|\neq 0$. This term corresponds to two counter-propagating fermions, one with momentum $\boldsymbol{k}+\boldsymbol{q}$ and the other with momentum k:

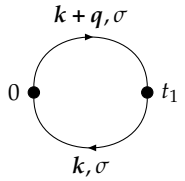

We take the Fourier transform to find:

$$\chi_0^T(\boldsymbol{q},\omega) = \sum_{\boldsymbol{k},\sigma}\left[\frac{\theta(|\boldsymbol{k}|<k_{F,\sigma})\theta(|\boldsymbol{k}+\boldsymbol{q}|>k_{F,\sigma})}{\omega+E_{\boldsymbol{k}}-E_{\boldsymbol{k}+\boldsymbol{q},\sigma}+i\eta} - \frac{\theta(|\boldsymbol{k}|>k_{F,\sigma})\theta(|\boldsymbol{k}+\boldsymbol{q}|<k_{F,\sigma})}{\omega+E_{\boldsymbol{k}}-E_{\boldsymbol{k}+\boldsymbol{q},\sigma}-i\eta}\right] \tag{4.40}$$

where we used following relation which can be proven using residue integrals:

$$\theta(t>0) = -\int_{-\infty}^{\infty}\frac{du}{2\pi i}\frac{e^{-iut}}{u+i\eta}$$

Now, since we were studying the propagation of the impurity starting from the impurity's vacuum state, only the retarded part of the function $G_0(\boldsymbol{p}_1, t_2-t_1)$ in Eq. (4.32) is taken, therefore $t_2 > t_1$. So the second term in the last equation (advanced part) will be discarded in the evaluation of $\Sigma^{(2)}_{\text{pol}}(\mathbf{p},\omega)$.
These functions are called in condensed matter theory the *Lindhard functions* and integrating them is an important step in many problems, i.e. Lindhard's dielectric functions for calculating response functions of an electron gas to external perturbations and the RPA's bubble.

Asymptotic behavior

How does the zeroth order of the density-density correlator behave at large $|\boldsymbol{q}|$ values? For that we go back to the self-energy of the impurity in Eq. (4.34). We replace χ^T by χ_0^T which is of particular interest here, then we can write:

$$\Sigma^{(2)}_{\text{pol}}(\mathbf{p},t) = i\frac{g'^2_0}{\hbar^2\mathcal{V}^2}\sum_{\boldsymbol{q}\neq 0}G_0(\boldsymbol{q},t)\chi_0^T(\boldsymbol{q},t) \tag{4.41}$$

Taking the Fourier Transform of this product of functions gives a convolution in the frequency domain, we will take $\omega = 0$ to match up the expression with the one obtained through the perturbative calculation in Eq. (4.32):

$$\begin{aligned}\Sigma^{(2)}_{\text{pol}}(\mathbf{p},\omega=0) &= i\frac{g'^2_0}{\hbar^2\mathcal{V}^2}\sum_{\boldsymbol{q}\neq 0}\int\frac{d\omega'}{2\pi}\chi_0^T(\boldsymbol{q},\omega')G_0(\boldsymbol{q},-\omega') \\ &= i\frac{g'^2_0}{\hbar^2\mathcal{V}^2}\sum_{\boldsymbol{q}\neq 0}\int\frac{d\omega'}{2\pi}\frac{\chi^T_{0,r}(\boldsymbol{q},\omega')-\chi^T_{0,a}(\boldsymbol{q},\omega')}{-\omega'-\epsilon_{\boldsymbol{q}}+i\eta}\end{aligned} \tag{4.42}$$

Where $\chi^T_{0,r}$ and $\chi^T_{0,a}$ are respectively the retarded and advanced parts shown in Eq. (4.40) and integrated over $\boldsymbol{k}$. By integrating over the advanced part, the integrand has two poles $\omega' = -\epsilon_{\boldsymbol{q}}+i\eta$ and $\omega' = E_{\boldsymbol{k}+\boldsymbol{q},\sigma}-E_{\boldsymbol{k}}+i\eta$, both in the upper half plane. So by integrating over the lower half plane, the function is holomorphic and it gives 0.
As for the first integration, the function has two poles $\omega' = -\epsilon_{\boldsymbol{q}}+i\eta$ and $\omega' = E_{\boldsymbol{k}+\boldsymbol{q},\sigma}-E_{\boldsymbol{k}}-i\eta$, so if we integrate over the upper half plane we will have one pole $\omega' = -\epsilon_{\boldsymbol{q}}+i\eta$ and we write this function as follows:

$$\chi^T_{0,r}(\boldsymbol{q},-\epsilon_q) = 2\int\frac{d^3\boldsymbol{k}}{(2\pi)^3}\frac{\theta(|\boldsymbol{k}|<k_F)\theta(|\boldsymbol{k}+\boldsymbol{q}|>k_F)}{-\epsilon_{\boldsymbol{q}}+E_{\boldsymbol{k}}-E_{\boldsymbol{k}+\boldsymbol{q}}+i\eta} = -2\int\frac{d^3\boldsymbol{k}}{(2\pi)^3}\frac{\theta(|\boldsymbol{k}|<k_F)\theta(|\boldsymbol{k}+\boldsymbol{q}|>k_F)}{q^2/2m^*+\boldsymbol{k}.\boldsymbol{q}/m-i\eta} \tag{4.43}$$

For $q \gg k_F$, the second step function equals 1 always. The integrand can be separated into real and imaginary parts using the following formula:

$$\frac{1}{x \pm i\eta} = \mathcal{P}\frac{1}{x} \mp i\pi\eta(x) \tag{4.44}$$

we notice that the principle value part has no poles and the imaginary term cancels when taking the limit $\eta \to 0$, with that the integration yields:

$$\begin{aligned}\chi^T_{0,r}(\boldsymbol{q}, -\epsilon_{\boldsymbol{q}}) = 2m\int_0^{k_F}\frac{dk}{(2\pi)^2}\frac{k}{q}\ln\left(\frac{q-k}{q+k}\right) &\underset{q\to\infty}{=} -\frac{m}{\pi^2}\int_0^{k_F} dk\frac{k}{q}\left[\frac{k}{q} + (\frac{k}{q})^3 + O((\frac{k}{q})^5)\right] \\ &\underset{|\boldsymbol{q}|\to\infty}{\propto} \frac{1}{q^2} + O(\frac{1}{q^4})\end{aligned} \tag{4.45}$$

So the leading term in $\chi^T_{0,r}$ is of order $1/q^2$ and the next order is $1/q^4$, none of these terms gives a logarithmic divergence, which is expected since we saw that the term responsible is proportional to Tan's contact $\mathcal{C}_2$ which needs at least second order interactions to appear.

First order

We write the first order as follows:

$$\begin{aligned}i\chi^T_1(\boldsymbol{q}, t) = -i\frac{g_0}{\mathcal{V}}\int dt_1 \sum_{\substack{\boldsymbol{k},\boldsymbol{k}',\sigma,\sigma' \\ \boldsymbol{k}_1,\boldsymbol{p},\boldsymbol{k}'_1,\boldsymbol{p}',\sigma_1}} &\delta_{\substack{\boldsymbol{k}_1+\boldsymbol{p} \\ \boldsymbol{k}'_1+\boldsymbol{p}'}}\langle \mathcal{T}\hat{a}^\dagger_{\boldsymbol{k},\sigma}(t)\hat{a}_{\boldsymbol{k}+\boldsymbol{q},\sigma}(t)\hat{a}^\dagger_{\boldsymbol{p}',-\sigma_1}(t_1)\hat{a}_{\boldsymbol{p},-\sigma_1}(t_1) \\ &\hat{a}^\dagger_{\boldsymbol{k}'_1,\sigma_1}(t_1)\hat{a}_{\boldsymbol{k}_1,\sigma_1}(t_1)\hat{a}^\dagger_{\boldsymbol{k}',\sigma'}(0)\hat{a}_{\boldsymbol{k}'-\boldsymbol{q},\sigma'}(0)\rangle\end{aligned} \tag{4.46}$$

We evaluate term by term Wick's contractions which result out of this term, all subsequent sums in front of each contraction are over all momenta and spin variables except $\boldsymbol{q}$. Then we evaluate the limit $\lim_{|\boldsymbol{q}|\to\infty}\chi_1(\boldsymbol{q}, -\epsilon_{\boldsymbol{q}})$ after each term in its turn:

$$i\chi^{T,(1)}_1(\boldsymbol{q}, t) = -i\frac{g_0}{\mathcal{V}}\sum_{\boldsymbol{k},\boldsymbol{p},\sigma}\int dt_1 G_{0,-\sigma}(\boldsymbol{p}, t_1 - t)G_{0,-\sigma}(\boldsymbol{p}+\boldsymbol{q}, t - t_1)G_{0,\sigma}(\boldsymbol{k}-\boldsymbol{q}, -t_1)G_{0,\sigma}(\boldsymbol{k}, t_1) \tag{4.47}$$

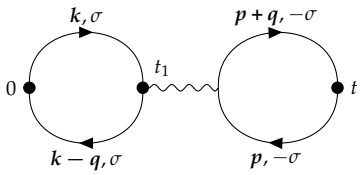

As before, we take the Fourier transform and we get for its asymptotic behavior:

$$\chi^{(1)}_1(\boldsymbol{q}, -\epsilon_{\boldsymbol{q}}) \underset{|\boldsymbol{q}|\to\infty}{\propto} \frac{1}{q^4} + O(\frac{1}{q^6})$$

The details of this calculation were reported in Appendix A.
Another possible diagram:

$$\chi_1^{T,(2)}(\boldsymbol{q},t) = \frac{g_0}{\mathcal{V}} \sum_{\boldsymbol{k},\boldsymbol{p},\sigma} \int dt_1 G_{0,\sigma}(\boldsymbol{k},-t) G_{0,-\sigma}(\boldsymbol{p},t_1-t_1) G_{0,\sigma}(\boldsymbol{k}+\boldsymbol{q},t-t_1) G_{0,\sigma}(\boldsymbol{k}+\boldsymbol{q},t_1) \tag{4.48}$$

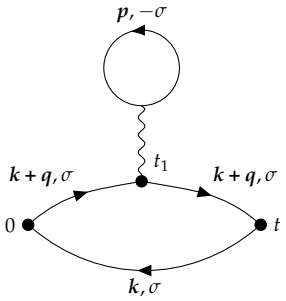

For its asymptotic behavior we can write:

$$\chi_{1,r}^{T,(2)}(\boldsymbol{q},-\epsilon_{\boldsymbol{q}}) = -g_0 n \sum_{\boldsymbol{k}} \frac{\theta(|\boldsymbol{k}|<k_F)\theta(|\boldsymbol{k}+\boldsymbol{q}|>k_F)}{(q^2+\boldsymbol{q}.\boldsymbol{k})^2} \propto \frac{1}{q^4} + O(\frac{1}{q^5})$$

Other diagrams resembling:

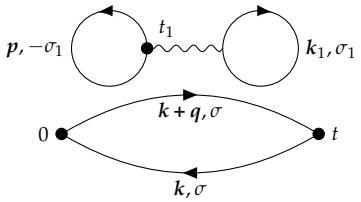

do not contribute since they are disconnected diagrams as we have mentioned before.

4.3.3 Ladder approximation

For the fermion-fermion scattering length to appear, we should regularize the interaction constant g_0 in each of the two significant first order diagrams we saw previously. This is done by considering the ladder approximation in which we consider that when taking the thermodynamic limit all diagrams containing fermions or impurity loops will go to zero since they are proportional the density. Meaning that all remaining diagrams must always have impurity-fermion interaction at each node. The subsequent series of diagrams is called the ladder series and the calculation involving all contributions is called the ladder resummation.
We start by a ladder resummation of the diagram in Eq. (4.47) by writing the sum over the ladder diagrams as two fermions interacting via an interaction vertex $\gamma_{\uparrow,\downarrow}$ as follows:

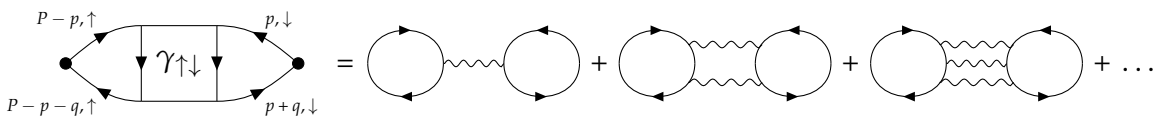

(4.49)

where $P = (\boldsymbol{P}, \Omega)$, $p = (\boldsymbol{p}, \omega_1)$ are internal four momenta we will sum on and $q = (\boldsymbol{q}, \omega)$ is the four momentum of the impurity.
We can then write a Bethe-Salpeter equation for $\gamma_{\uparrow,\downarrow}$:

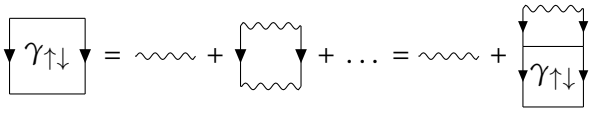

(4.50)

We can write an expression for the Bethe Salpeter equation for $\gamma_{\uparrow,\downarrow}$, recalling that at $T = 0$, Feynman rules add a factor i in front of the recursive part, as follows:

$$\begin{aligned}\gamma_{\uparrow,\downarrow}(P-p,p;P-p-q,p+q) = g_0 + ig_0 \sum_{p_1} G_{0,\uparrow}(P-p_1)G_{0,\downarrow}(p_1) \\ \gamma_{\uparrow,\downarrow}(P-p_1,p_1;P-p-q,p+q)\end{aligned} \tag{4.51}$$

By writing the Bethe Salpeter equation with $\gamma_{\uparrow,\downarrow}$ including the first interaction and followed by two fermion propagators, we can see that $\gamma_{\uparrow,\downarrow}$ only depends on the total four-momentum $P = (\boldsymbol{P}, \Omega)$, with that we can write:

$$\gamma^{-1}_{\uparrow,\downarrow}(\boldsymbol{P},\Omega) = g_0^{-1} - i\sum_{p_1} G_{0,\uparrow}(P-p_1)G_{0,\downarrow}(p_1)$$

We perform the residues integral over the two advanced and retarded parts of $G_{0,\downarrow}(p_1)$ to get:

$$\gamma^{-1}_{\uparrow,\downarrow}(\boldsymbol{P},\Omega) = g^{-1} - \sum_{p_1}\frac{2m^*}{p_1^2} - \sum_{|\boldsymbol{p}_1|>k_F}\frac{\theta(|\boldsymbol{P}-\boldsymbol{p}_1|>k_F)}{\Omega - E_{\boldsymbol{p}_1} - E_{\boldsymbol{P}-\boldsymbol{p}_1} + i\eta} + \sum_{|\boldsymbol{p}_1|<k_F}\frac{\theta(|\boldsymbol{P}-\boldsymbol{p}_1|<k_F)}{\Omega - E_{\boldsymbol{p}_1} - E_{\boldsymbol{P}-\boldsymbol{p}_1} - i\eta} \tag{4.52}$$

Inserting that into Eq. (4.47) we find:

$$\begin{aligned}\chi_1^{T,(1)}(\boldsymbol{q},\omega) = &\frac{2i}{V}\sum_{P,\boldsymbol{p}}\int_{-\infty}^{\infty}\frac{d\omega_1}{2\pi}\int_{-\infty}^{\infty}\frac{d\Omega}{2\pi}G_{0,\downarrow}(\boldsymbol{p},\omega_1)G_{0,\downarrow}(\boldsymbol{p}+\boldsymbol{q},\omega_1+\omega) \\ &G_{0,\uparrow}(\boldsymbol{P}-\boldsymbol{p}-\boldsymbol{q},\Omega-\omega-\omega_1)G_{0,\uparrow}(\boldsymbol{P}-\boldsymbol{p},\Omega-\omega_1)\gamma_{\uparrow,\downarrow}(P)\end{aligned} \tag{4.53}$$

We consider in the following that all fermions have the same mass m and drop the spin index. The product of four Green's functions of the form Eq. (4.38) gives $2^4 = 16$ terms.
We will focus mainly on the term resulting from multiplying only the retarded parts of the Green's functions. We dedicate Appendix B to discussing other terms. The term is written as:

$$\begin{aligned}\chi_{1,r}^{T,(1,1)}(\boldsymbol{q},\omega) = &\frac{2i}{V}\sum_{P,\boldsymbol{p}}\int_{-\infty}^{\infty}\frac{d\omega_1}{2\pi}\int_{-\infty}^{\infty}\frac{d\Omega}{2\pi}\frac{\theta(|\boldsymbol{p}|>k_F)}{\omega_1 - E_{\boldsymbol{p}} + i\eta}\frac{\theta(|\boldsymbol{P}-\boldsymbol{p}-\boldsymbol{q}|>k_F)}{\Omega-\omega_1-\omega-E_{\boldsymbol{P}-\boldsymbol{p}-\boldsymbol{q}}+i\eta} \\ &\frac{\theta(|\boldsymbol{p}+\boldsymbol{q}|>k_F)}{\omega+\omega_1-E_{\boldsymbol{p}+\boldsymbol{q}}+i\eta}\frac{\theta(|\boldsymbol{P}-\boldsymbol{p}|>k_F)}{\Omega-\omega_1-E_{\boldsymbol{P}-\boldsymbol{p}}+i\eta}\gamma_{\uparrow,\downarrow}(P)\end{aligned} \tag{4.54}$$

We notice that the second and third terms are retarded and advanced respectively with respect to the variable ω, we separate the product into a sum of a retarded and advanced term and we drop the advanced term.

The remaining integrand has three poles with respect to the variable ω_1, two of them in the lower half of the complex plane and one in the upper half. Thus, we perform the integral over ω_1 by closing the contour over the upper half of the complex plane, with that we get:

$$\chi^{(1,1)}_{1,r}(\boldsymbol{q},\omega) = \frac{2}{V}\sum_{P,\boldsymbol{p}}\int_{-\infty}^{\infty}\frac{d\Omega}{2\pi}\frac{\theta(|\boldsymbol{p}|>k_F)\theta(|\boldsymbol{P}-\boldsymbol{p}-\boldsymbol{q}|>k_F)}{(\Omega-E_{\boldsymbol{P}-\boldsymbol{p}}-E_{\boldsymbol{p}}+i\eta)(\Omega-E_{\boldsymbol{p}+\boldsymbol{q}}-E_{\boldsymbol{P}-\boldsymbol{p}-\boldsymbol{q}}+i\eta)} \\ \frac{\theta(|\boldsymbol{p}+\boldsymbol{q}|>k_F)\theta(|\boldsymbol{P}-\boldsymbol{p}|>k_F)}{(\Omega+\omega-E_{\boldsymbol{P}-\boldsymbol{p}}-E_{\boldsymbol{p}+\boldsymbol{q}}+i\eta)}\gamma_{\uparrow,\downarrow}(P) \tag{4.55}$$

We need to evaluate the function $\chi^{T,(1,1)}_{1,r}(\boldsymbol{q},\omega)$ at the frequency value $\omega=-\epsilon_{\boldsymbol{q}}$ which corresponds to the impurity's kinetic energy. Then we take the $|\boldsymbol{q}|\to\infty$ limit. For that we write the function as follows:

$$\chi^{T,(1,1)}_{1,r}(\boldsymbol{q},-\epsilon_{\boldsymbol{q}}) = \int\frac{d^3\boldsymbol{P}}{(2\pi)^3}\int_{-\infty}^{\infty}\frac{d\Omega}{2\pi}\gamma_{\uparrow,\downarrow}(\boldsymbol{P},\Omega)\ F(\Omega,\boldsymbol{P},q,k_F,m,m_i) \tag{4.56}$$

where the function F is given by:

$$F(\Omega,\boldsymbol{P},q,k_F,m,m_i) = \int\frac{d^3\boldsymbol{p}}{(2\pi)^3}\frac{\theta(|\boldsymbol{p}|>k_F)\theta(|\boldsymbol{P}-\boldsymbol{p}-\boldsymbol{q}|>k_F)}{(\Omega-E_{\boldsymbol{P}-\boldsymbol{p}}-E_{\boldsymbol{p}}+i\eta)(\Omega-E_{\boldsymbol{p}+\boldsymbol{q}}-E_{\boldsymbol{P}-\boldsymbol{p}-\boldsymbol{q}}+i\eta)} \\ \frac{\theta(|\boldsymbol{p}+\boldsymbol{q}|>k_F)\theta(|\boldsymbol{P}-\boldsymbol{p}|>k_F)}{(\Omega-\epsilon_{\boldsymbol{q}}-E_{\boldsymbol{P}-\boldsymbol{p}}-E_{\boldsymbol{p}+\boldsymbol{q}}+i\eta)} \tag{4.57}$$

We note that F is holomorphic in the upper half of the complex plane with respect to Ω. We split the complex function $\gamma_{\uparrow,\downarrow}(P)$ into a sum of an advanced and a retarded function: $\gamma_{\uparrow,\downarrow}(P)=\gamma^R_{\uparrow,\downarrow}(P)+\gamma^A_{\uparrow,\downarrow}(P)$.
The function $\gamma^R_{\uparrow,\downarrow}(P)$ is holomorphic in the upper-half of the complex plane and $\gamma^A_{\uparrow,\downarrow}(P)$ is holomorphic in the lower half of the complex plane. With that we find that only $\gamma^A_{\uparrow,\downarrow}(P)$ will contribute in Eq. (4.56) in order for the integrand to not be holomorphic in the lower-half plane and integrate to zero with respect to Ω.
We do the following rescaling $|\boldsymbol{p}|$ by $|\boldsymbol{q}|$ we find:

$$F(\Omega,|\boldsymbol{P}|,q,k_F,m,m_i) = \frac{(2m)^3}{q^3}F\left(\frac{\Omega}{q^2/(2m)},\frac{|\boldsymbol{P}|}{|\boldsymbol{q}|},1,\frac{k_F}{q},1,\frac{m}{m_i}\right)$$

By studying the behavior of the function $\gamma_{\uparrow,\downarrow}(\boldsymbol{P},\Omega)$ at $|\boldsymbol{P}|,\Omega\to\infty$ we find that its limit is zero. We prove that by noticing that the second sum in Eq. (4.52) is zero when $|\boldsymbol{P}|\to\infty$, we write the Heaviside function in the first sum as $1-\theta(|\boldsymbol{P}-\boldsymbol{p}_1|<k_F)$ and the second term subsequently goes to zero for $|\boldsymbol{P}|\to\infty$. For the remaining sum we can calculate it using the method detailed in Appendix D, to find that $\gamma^{-1}_{\uparrow,\downarrow}(\boldsymbol{P},\Omega)$ diverges for $|\boldsymbol{P}|,\Omega\to\infty$.
As a result, in F we can replace the first two arguments in the last expression by zero at lowest order and we find:

$$\chi^{T,(1,1)}_{1,r}(\boldsymbol{q},-\epsilon_{\boldsymbol{q}}) \underset{|\boldsymbol{q}|\to\infty}{\propto}\frac{A}{q^3} \tag{4.58}$$

with A given by:

$$A = \int \frac{d^3\boldsymbol{P}}{(2\pi)^3} \int_{-\infty}^{\infty} \frac{d\Omega}{2\pi} \gamma^A_{\uparrow,\downarrow}(\boldsymbol{P},\Omega)\ (2m)^3 F(0,0,1,0,m,m_i)$$

By definition we have

$$\int_{-\infty}^{\infty} \frac{d\Omega}{2\pi} \gamma^A_{\uparrow,\downarrow}(\boldsymbol{P},\Omega) = \gamma_{\uparrow,\downarrow}(\boldsymbol{P}, t=0^-)$$

and equivalently:

$$\int \frac{d^3\boldsymbol{P}}{(2\pi)^3} \gamma_{\uparrow,\downarrow}(\boldsymbol{P}, t=0^-) = \gamma_{\uparrow,\downarrow}(\boldsymbol{r}=\boldsymbol{0}, t=0^-)$$

The last expression can be related to the two-body contact as shown in [297, 298]:

$$\mathcal{C}_2 = -m^2\, \gamma_{\uparrow,\downarrow}(\boldsymbol{r}=\boldsymbol{0}, t=0^-)$$

In this context the contact $\mathcal{C}_2$ will help us identify diverging terms as it appears as a prefactor for these terms.
With that the coefficient of the divergent term becomes:

$$A = -8\, m\, \mathcal{C}_2 F(0,0,1,0,m,m_i)$$

This gives one of the contributions to the divergent term in Eq. (4.8). With the notations used in [117] we calculate the function $F(0,0,1,0,m,m_i)$ and we find:

$$F(0,0,1,0,m,m_i) = \frac{m^3}{\pi^2} \kappa_{II}(\eta)$$

where $\eta = m_i/m$ and $\kappa_{II}(\eta) = -\frac{\pi}{2}\eta \arctan\left(\frac{1}{\sqrt{\eta(\eta+2)}}\right)$.
The work on other terms is still under progress and other diagrams which are not included in ladder resummation with respect to the fermion-fermion interaction are being investigated.

Summary and future work

In this chapter we took a look at the logarithmic divergent terms which are present in the perturbative expansion of the energy of a polaron with respect to its interaction with an interacting Fermi gas.
A diagrammatic expansion was presented and we managed to identify one contribution to this divergence with the study of the ladder resummation of a diagram representing the propagation of two fermions.
Other terms are being investigated in order to find other divergent terms in the diagrammatic expansion of the fermion-fermion interaction.

An obvious prospective is to explore more diagrams and try to identify all the ones contributing to the $1/q^3$ term in $\chi^T(\boldsymbol{q}, -\epsilon_q)$ in the BCS limit of the impurity-fermion and fermion-fermion interaction. Second order diagrams will contribute to

the divergent term since it is proportional to the two-body contact $\mathcal{C}_2$ which appears only in second order perturbative expansions of this type.
The extension of the calculation to all values of interaction strength across the BEC-BCS crossover for the fermionic bath and the impurity-fermion interaction is an intriguing outlook.
Also, exploring values where $a' > R_e$ can be interesting, this is where a smooth crossover to a trimer state is predicted [130].

Chapter 5

Impurity immersed in a double non-interacting Fermi sea

Two-component Fermi systems are a fundamental tool in which a broad range of physical phenomena appear by exploiting their various interaction strengths and properties, as was presented in previous chapters.
At low temperature, when a weak attraction is present between the two components of fermions, typically two internal states of the same species (e.g. two spin 1/2 states), particles tend to form Cooper pairs and form a BCS superfluid. When increasing the attraction, the two components form a dimer, a diatomic bosonic molecule transforming the ensemble into a BEC.
Since the two regimes depend on the interaction strength between the two components when they are paired, the transition between them is a crossover. It was shown that the mean-field wavefunction smoothly interpolates the BEC and BCS superfluids [150, 151], in what became to be known as BCS-BEC crossover theory and which has become the subject of extensive studies theoretically and experimentally. For more details refer to Chapter 1.

Yet richer problems emerged when people started investigating three-component Fermi gases, initially motivated by its analogy to quark-hadron continuity in dense nuclear matter [299] and more so in the field of cold-atoms for the experimental realization of such systems using ^{6}Li atoms [143, 300].
Theoretically, the problem of three-component Fermi gases provides several challenges. The ordinary mean-field approximation treatment does not work since it misses completely Efimovian effects (See Chapter1) which play an essential role here [115].
Then, when considering the ground state of the three-component Fermi gas beyond mean-field, a serious problem arises when three distinguishable fermions can form an infinitely deep bound state in the zero-ranged potential limit, this previously mentioned phenomenon is known as the Thomas collapse [129], which was not present in two-component systems due to Pauli blocking. Therefore, a three-component Fermi gas in the zero range approximation does not have a many-body ground state and if it exists, it is bound to the potential range and thus is not universal. This echoes the results found for the Efimov trimer in the first chapter.

However, a ground state of the three-component Fermi gas can be found in the vicinity of a narrow Feshbach resonance where both the scattering length a and the resonance range R_e are much larger than the potential range, this results in it becoming irrelevant and not appearing in equations. This represents a universal ground state in the sense that it exists for any kind of interaction potential and is characterized completely by the density expressed by the Fermi wavevector $\boldsymbol{k}_F$, the scattering length a and the effective range R_e. The case of a broad Feshbach resonance, which is more relevant experimentally since in experiments working around a broad resonance is much simpler and allows fine control over interactions, was studied extensively [191,217,221,301].

Experiments in our group on Bose-Fermi mixtures brought focus on impurity physics in two and three component Fermi and Bose gases [109,111,112]. This started a theoretical effort trying to understand the phase diagram of an impurity immersed in a two-component Fermi sea, where the phase diagram now includes a trimer sector where Efimov physics comes into play [113–117]. For a more general introduction refer to Chapter 1.

In the weak impurity-fermions interaction regime, the impurity experiences a weak attractive interaction and can be described as a Fermionic polaron. In the regime of increased impurity-fermions interaction that does not support a two-body bound state (dimer), a three-body state, a trimer, forms. For strong interactions that support a two-body bound state the trimer state transitions into a dimer state [302]. A schematic phase diagram of the problem is presented in Fig. (1.5).

By using a mean-field description of the superfluid composed of the two majority fermions, a smooth crossover between the polaron and trimer regimes was proposed using the following ansatz [130]:

$$|\psi\rangle = \left(\alpha\hat{b}_0^\dagger + \sum_{\boldsymbol{k},\boldsymbol{k}'} \beta_{\boldsymbol{k},\boldsymbol{k}'}\hat{b}_{\boldsymbol{k}'}^\dagger \hat{\gamma}_{\boldsymbol{k},\uparrow}^\dagger \hat{\gamma}_{-\boldsymbol{k}-\boldsymbol{k}',\downarrow}^\dagger\right)|\text{BCS}\rangle$$

where $|\text{BCS}\rangle$ is the BCS mean-field ground state of majority fermions, $\hat{b}_{\boldsymbol{k}}^\dagger$ is the creation operator of an impurity of momentum $\boldsymbol{k}$ and $\hat{\gamma}_{\boldsymbol{k},\sigma}^\dagger$ is that of the Bogoliubov modes of the underlying superfluid.

The polaron-trimer crossover arises from the fact that the superfluid's excitations happen in pairs (the Bogoliubov excitations) and trimers arise as a bound state between the superfluid Cooper pairs and the impurity.

In light of the foregoing, an intriguing question is what would happen if there was no superfluid and the two majority components do not interact? What type of excitation would favor the trimer state appearance as the ground state of the system?

In Fig. (1.5) this would correspond to the limit of $R_e/a \to -\infty$, and the question is whether the shrinking trimer sector would still exist in this domain even in the absence of fermionic Cooper pairing.

Answering this question is the main goal of this chapter, where we will present a variational ansatz incorporating the physics of the polaron and trimer sectors in a system of an ideal gas of spin 1/2 fermions and an impurity. We will see that the type of coherence introduced by the presence of the superfluid in the previous case is not present in our system which leads to a dramatic change in the nature of the transition. The following work was reported in [118].

5.1 Variational ansatz of the full problem

We consider a system composed of non-interacting N spin up particles with N spin down particles of equal mass m and an impurity of mass m_i interacting with each component of the Fermi sea. An experimental setup to have in mind in this study is that of [111] where a mixture of ^{6}Li and ^{7}Li was studied.
We use a two-channel model to write the hamiltonian which as we saw in Chapter 1 gives rise to Efimov trimers without requiring additional physical ingredients. In this model the system is described as two scattering channels interacting with each other via a contact interaction potential defined as $V_{k-k'} = \Lambda\delta_{k,k'}$. We also assume periodic boundary conditions with quantization volume $\mathcal{V}$. The system's hamiltonian takes the general form:

$$\begin{aligned}\hat{H} = &\sum_{k,s} \epsilon_k a^\dagger_{k,s} a_{k,s} + \sum_k \mathcal{E}_k c^\dagger_k c_k + \sum_k (E_0 + E_k) b^\dagger_{k,s} b_{k,s} \\ &+ \frac{\Lambda}{\sqrt{\mathcal{V}}} \sum_{k,p,s} (b^\dagger_{p+k,s} c_k a_{p,s} + a^\dagger_{p,s} c^\dagger_k b_{p+k,s})\end{aligned} \tag{5.1}$$

where $a^\dagger_{k,s}$ and $a_{k,s}$ are creation and annihilation operators for an open channel fermion of momentum $\boldsymbol{k}$ and spin s, $c^\dagger_k$ and c_k are those of the open channel impurity, $b^\dagger_{k,s}$ and $b_{k,s}$ are those of the closed channel molecule made of a spin s fermion and an impurity.
We also have $\epsilon_k = \frac{\hbar^2 k^2}{2m}$, $\mathcal{E}_k = \frac{\hbar^2 k^2}{2m_i}$, $E_k = \frac{\hbar^2 k^2}{2(m+m_i)}$. E_0 is the binding energy of the molecule.
For simplicity, inspired by the experimental setup in [111], we consider interactions between the impurity and each spin component are the same and $m_i \simeq m$. The coupling Λ does not depend on momentum [303, 304], but a UV-cutoff k_c is introduced to match the scattering length a and the effective range R_e of the true potential. We remind the expressions in 1.22 and 1.26:

$$\frac{1}{a} = \frac{2k_c}{\pi} - \frac{2\pi\hbar^2 E_0}{m^*\Lambda^2}, \qquad R_e = \frac{\pi\hbar^4}{m^{*2}\Lambda^2} \tag{5.2}$$

where m^* is the reduced mass of the impurity/fermion pair.
We search for the ground state energy within a variational space spanned by the states depicted in Fig. (5.1). This space can be divided into two sectors. The polaron sector is spanned by state $|0\rangle$, which corresponds to the impurity sitting at the center of the two unperturbed Fermi seas, and single particle-hole states $|\boldsymbol{q}_1\rangle_s$ and $|\boldsymbol{q}_1, \boldsymbol{k}_1\rangle_s$ where a hole of spin s and momentum $\boldsymbol{q}_1$ is accompanied by either a bound or unbound impurity-fermion pair. The Efimov sector is characterized by states $|\boldsymbol{q}_1, \boldsymbol{q}_2, \boldsymbol{k}_1\rangle_s$ and $|\boldsymbol{q}_1, \boldsymbol{q}_2, \boldsymbol{k}_1, \boldsymbol{k}_2\rangle$ containing both one hole in each Fermi sea.
The general structure of a variational state is therefore

$$\begin{aligned}|\psi\rangle = A|0\rangle &+ \sum_{\boldsymbol{q}_1,s} B_s(\boldsymbol{q}_1)|\boldsymbol{q}_1\rangle_s + \sum_{\boldsymbol{q}_1,\boldsymbol{k}_1,s} C_s(\boldsymbol{q}_1,\boldsymbol{k}_1)|\boldsymbol{q}_1,\boldsymbol{k}_1\rangle_s + \sum_{\boldsymbol{q}_1,\boldsymbol{q}_2,\boldsymbol{k}_1,s} D_s(\boldsymbol{q}_1,\boldsymbol{q}_2,\boldsymbol{k}_1)|\boldsymbol{q}_1,\boldsymbol{q}_2,\boldsymbol{k}_1\rangle_s \\ &+ \sum_{\boldsymbol{q}_1,\boldsymbol{q}_2,\boldsymbol{k}_1,\boldsymbol{k}_2} E(\boldsymbol{q}_1,\boldsymbol{q}_2,\boldsymbol{k}_1,\boldsymbol{k}_2)|\boldsymbol{q}_1,\boldsymbol{q}_2,\boldsymbol{k}_1,\boldsymbol{k}_2\rangle.\end{aligned} \tag{5.3}$$

with $|\boldsymbol{q}_i| < k_F$ and $|\boldsymbol{k}_i| > k_F$ and where k_F is the norm of Fermi wavevector of the background fermions.
Here, A is the wavefunction of the impurity alone, B_s is the wavefunction of the molecule formed from an impurity and a fermion of spin s resulting from a particle-hole excitation in the Fermi sea, C_s is the wavefunction of one particle hole excitation of a fermion with spin s, when this molecule dissociates, D_s is the wavefunction when another molecule is formed from a second particle hole excitation, E is the wavefunction if this latter dissociates.

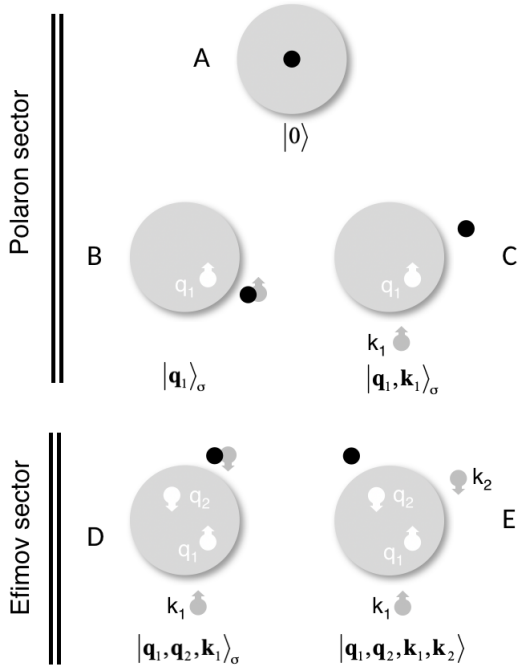

Figure 5.1: Structure of the variational Hilbert space. In the first two rows, the polaronic state is created by the impurity and one particle hole excitations, in the third row, a second particle hole excitation allows for the trimer to exist.

For spin balanced Fermi seas, the interactions of the impurity with the two spin components are identical. We can thus assume that the amplitudes B_s, C_s and D_s do not depend on s within this subspace, and we explore two families of variational states.
The trial wavefunction can be used to know the ground-state energy of the system in the subspace spanned by the wavefunction. To find this we perform a standard variational calculation which we detail in Appendix C.

5.2 Polaron sector

The polaronic sector corresponds to $D = E = 0$. The corresponding ansatz generalizes the approach succesfully used to describe the Fermi polaron problem, i.e. an impurity immersed in a spin-polarized Fermi sea [191].
In particular this trial wavefunction recovers the exact perturbative expansion of the

energy of the polaron up to second order in scattering length. In the following, we will assume that the impurity has the same mass as the fermions: $m_i = m$.
The minimization of the energy W with respect to A, B and C in the polaronic sector can be reduced to a single scalar equation $P_W = 0$ with:

$$P_W = W - \frac{2}{\mathcal{V}} \sum_{q<k_F} \frac{1}{\Delta_q(W)} \tag{5.4}$$

and

$$\Delta_q(W) = \frac{m}{4\pi\hbar^2}\left\{a^{-1} - R_e(\lambda^2 - \frac{q^2}{4}) - \frac{2}{\pi}k_F + \frac{4\pi}{\mathcal{V}} \sum_{|\boldsymbol{k}|>k_F} \frac{1}{\lambda^2 + k^2 - \boldsymbol{k}\cdot\boldsymbol{q}} - \frac{1}{k^2}\right\} \tag{5.5}$$

where $W = -\hbar^2\lambda^2/m$, is the ground state energy.
Since in this sector the impurity is coupled to a single atom of the Fermi sea (Sea Fig. (5.1), the zero-range limit does not suffer from any singularity and in this regime the polaron energy is a universal function of the dimensionless parameter $1/(k_F a)$ only that we display in Fig. (5.2).
In the perturbative regime $k_F a \to 0^-$, the energy of the polaron can be expanded as

$$W = \frac{8\pi\hbar^2 a}{m} n_F \left(1 + \frac{3}{2\pi}k_F a + \ldots\right). \tag{5.6}$$

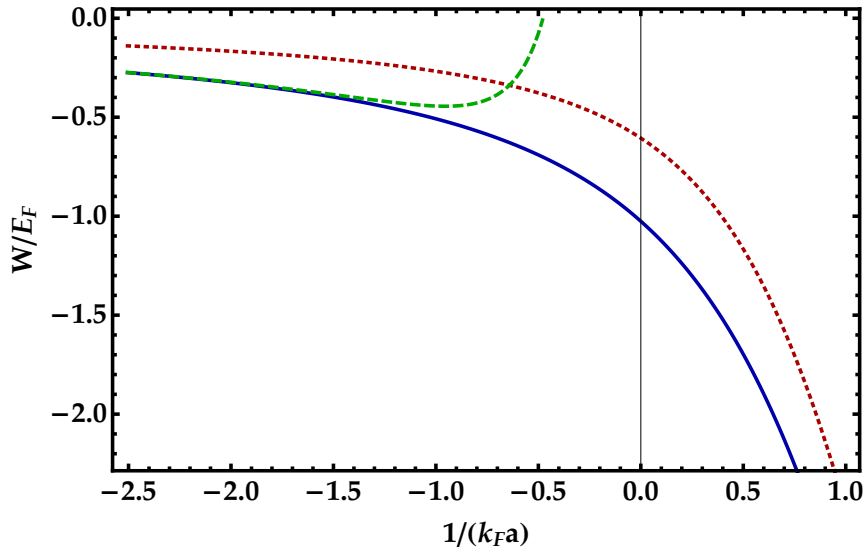

Figure 5.2: Energy of the purely polaronic ansatz for $R_e = 0$. The dashed green line corresponds to the second order perturbative expansion for $1/k_F a \to 0^-$. The dotted line corresponds to the polaron energy in a single component Fermi sea. The solid line corresponds to the polaron energy in a two component system described in Eq.(5.4).

At this order, the variational result recovers the exact perturbative expansion and amounts to twice the interaction energy with a single spin component. Because of the dependence of Δ_q with respect to the energy W, this coincidence does not extend

beyond that order though.
For instance, at the unitary limit $|a|=\infty$, we know that for a single component Fermi sea, the energy of the polaron is $W_{\rm FP} \simeq -0.606\, E_F$ [191,215,216], where $E_F = \hbar^2 k_F^2/2m$ is the Fermi energy of the background fermions, while for a two component system, we find $|W| \simeq 1.026 E_F < 2|W_{\rm FP}|$, meaning that, contrary to the perturbative expression, the interaction energy of the polaron with the two Fermi seas is not additive in the strong coupling regime.

5.3 Efimov sector

We now consider the opposite limit $A = B = C = 0$ corresponding to the formation of a ground state Efimov trimer above the Fermi surface. The trimer state dominates in an interval where the interaction is strong and attractive, however not strong enough to support a two-body bound state.

5.3.1 Trimer in vacuum

As a reference, we first consider the energy of the trimer in the absence of a Fermi sea that is obtained as a solution of Skornyakov-Ter-Martirosyan's equation [133]

$$\left[\frac{1}{4\pi}\left\{a^{-1} - R_e(\lambda^2 + \frac{3}{4}k^2)\right\} + \frac{1}{\mathcal{V}}\sum_{k'}\left(\frac{1}{\lambda^2 + k^2 + k'^2 + \boldsymbol{k}\cdot\boldsymbol{k}'} - \frac{1}{\boldsymbol{k}'^2}\right)\right] D(k) + \frac{1}{\mathcal{V}}\sum_{\boldsymbol{k}'}\frac{D(k')}{\lambda^2 + k^2 + k'^2 + \boldsymbol{k}\cdot\boldsymbol{k}'} = 0 \tag{5.7}$$

This equation is derived in Appendix C with $k_F = 0$, $q_1 = q_2 = 0$ and $f = g = 0$.
In this case, the only relevant dimensionless parameter is R_e/a and we observe that the trimer merges with the atomic continuum for a scattering length a_- such that $R_e/a_- = -2 \times 10^{-4}$. The energy of this state is plotted in Fig. (5.3) (blue solid line).

It means that in our situation, where only the impurity-fermion interactions are resonant, the three-body bound state essentially exists only in a regime where an impurity-fermion bound-state is also stable. This is to be contrasted with the more traditional three identical bosons problem shown in Chapter 1 for which all three interactions are resonant and Efimov trimers are stable deep in the domain where two-body bound states are unstable [131] (in that case we had $R_e/a_- \simeq -0.1$).

5.3.2 Cooper-like trimer

We consider next the effect of the Fermi sea on the energy of the trimer. In a first approach we simply assume that its role is to prevent the fermions above the Fermi surface from occupying states below k_F, in a manner very similar to the celebrated Cooper pairing problem for pairs of fermions in superconductors. The energy of the

trimer state is then solution of:

$$\left[\frac{1}{4\pi}\left\{a^{-1}-\frac{2}{\pi}k_F-R_e(\lambda^2-k_F^2+\frac{3}{4}k^2)\right\}+\frac{1}{\mathcal{V}}\sum_{|\boldsymbol{k}'|>k_F}(\frac{1}{\lambda^2-k_F^2+k^2+k'^2+\boldsymbol{k}\cdot\boldsymbol{k}'}-\frac{1}{k'^2})\right]D(k)$$
$$+\frac{1}{\mathcal{V}}\sum_{|\boldsymbol{k}'|>k_F}\frac{D(k')}{\lambda^2-k_F^2+k^2+k'^2+\boldsymbol{k}\cdot\boldsymbol{k}'}=0 \tag{5.8}$$

This equation is very similar to Eq. (5.7), the main difference stemming from the sums over momenta that are now restricted to $|\boldsymbol{k}|> k_F$ and the shift of the energy associated with the chemical potential of the two fermions that were removed from the Fermi seas to create the trimer (the term $\lambda^2-k_F^2$ in the equation).
The corresponding ground state energy is plotted in Fig. (5.3) for an experimentally relevant value $k_F R_e \simeq 10^{-2}$ ($k_F \approx 10^7\,\mathrm{m}^{-3}$ typically and we take R_e on the order of $50\,a_0$, where a_0 is the Bohr radius, that corresponds to a typical Van Der Waals length for alkali atoms [42]).
We observe that like for traditional Cooper pairing the presence of the Fermi sea stabilizes the trimer. Numerical precision did not allow to conclude if like in vacuum Efimov trimers do not exist beyond a critical scattering length a_- (see above), whether the presence of the Fermi Sea stabilizes the trimer for arbitrarily weak attraction, albeit with an exponentially small binding energy or there is exists a finite value for a_-.
To enrich the discussion regarding the Cooper-like trimer, we study in Appendix E the behavior of the energy curve with respect to $k_F R_e$.

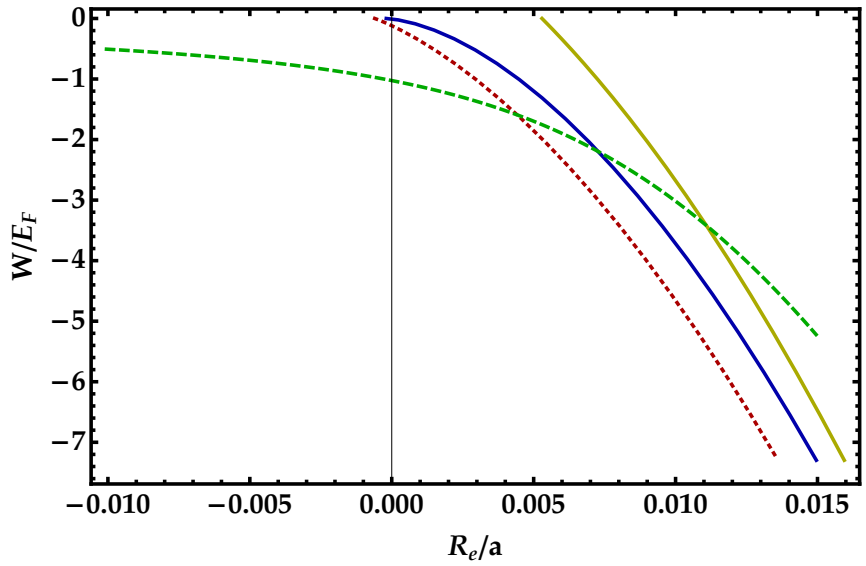

Figure 5.3: Variational energy for $k_F R_e = 10^{-2}$ of the trimer states. The Cooper-like trimer ground state energy (red, dotted) and polaron state (green, dashed), for comparison, we draw the Efimov ground state in vacuum described in Eq. (5.7) (solid, blue), and the trimer state considering a uniform hole distribution in the Fermi sea (solid, yellow).

5.3.3 General case

We can generalize this result by considering trimer amplitudes D_s and E of the form:

$$\begin{aligned} D_s(\boldsymbol{q}_1, \boldsymbol{q}_2, \boldsymbol{k}_1) &= F(\boldsymbol{q}_1, \boldsymbol{q}_2)\tilde{D}(\boldsymbol{k}_1) \\ E(\boldsymbol{q}_1, \boldsymbol{q}_2, \boldsymbol{k}_1, \boldsymbol{k}_2) &= F(\boldsymbol{q}_1, \boldsymbol{q}_2)\tilde{E}(\boldsymbol{k}_1, \boldsymbol{k}_2), \end{aligned} \tag{5.9}$$

The Cooper-like trimer corresponds to $F(\boldsymbol{q}_1, \boldsymbol{q}_2) = \delta_{\boldsymbol{q}_1,-\boldsymbol{q}_2}\widetilde{F}(q_1)$, where $\widetilde{F}$ is peaked near the Fermi surface. However, a restriction is present since we considered no correlations are present between particles and holes within this ansatz.
We choose the following normalization for the function $F(\boldsymbol{q}_1, \boldsymbol{q}_2)$: $\sum_{q_1,q_2}|F(\boldsymbol{q}_1, \boldsymbol{q}_2)|^2 = N_F^2$, where N_F is the total number of fermions per spin state.

Once again, we can eliminate E (the details of the derivation are presented in Appendix C). We see that at fixed F, $\tilde{D}$ is solution of a Skornyakov-Ter-Martirosyan like equation:

$$\begin{aligned} &\left[\frac{1}{4\pi}\left\{a^{-1} - \frac{2}{\pi}k_F - R_e(\lambda^2 + \frac{3}{4}k^2 - \frac{\langle(\boldsymbol{q}_1 - \boldsymbol{q}_2)^2\rangle}{4}) + \right\}\right. \\ &\quad \left. + \frac{1}{\mathcal{V}}\sum_{|\boldsymbol{k}'|>k_F}\left(\frac{1}{\lambda^2 + \langle \boldsymbol{q}_1 \cdot \boldsymbol{q}_2\rangle + k^2 + k'^2 + \boldsymbol{k}\cdot\boldsymbol{k}'} - \frac{1}{k'^2}\right)\right]\tilde{D}(k) \\ &\quad + \frac{1}{\mathcal{V}}\sum_{|\boldsymbol{k}'|>k_F}\frac{\tilde{D}(k')}{\lambda^2 + \langle \boldsymbol{q}_1 \cdot \boldsymbol{q}_2\rangle + k^2 + k'^2 + \boldsymbol{k}\cdot\boldsymbol{k}'} = 0 \end{aligned} \tag{5.10}$$

with $\langle f(\boldsymbol{q}_1, \boldsymbol{q}_2)\rangle = \sum_{\boldsymbol{q}_i}|F(\boldsymbol{q}_1, \boldsymbol{q}_2)|^2 f(\boldsymbol{q}_1, \boldsymbol{q}_2)/N_F^2$, and where we assumed that the distribution $|F|^2$ is an even function of $\boldsymbol{q}_1$ and $\boldsymbol{q}_2$.
Comparing Eq. (5.8) and Eq. (5.10) we see that their respective energies are simply translated one with respect to the other since we have:

$$W_F(R_e/a) = W_C(R_e/a + R_e^2\langle(\boldsymbol{q}_1 + \boldsymbol{q}_2)^2\rangle/4) - \frac{\hbar^2}{m}\left(k_F^2 + \langle \boldsymbol{q}_1 \cdot \boldsymbol{q}_2\rangle\right). \tag{5.11}$$

where W_F is the energy of the trimer using the ansatz in Eq. (5.9), and W_C is the energy of the Cooper-like trimer. This mapping corresponds to a translation of both the argument and the value of W_C and in practice we observe that the latter dominates. Since q_1 and q_2 are bounded by the Fermi wavevector k_F, we see that $k_F^2 + \langle \boldsymbol{q}_1 \cdot \boldsymbol{q}_2\rangle$ is always positive and the Cooper-like ansatz is always the optimal choice. We illustrate this property in Fig. (5.3) for a constant F corresponding to a uniform hole distribution in the Fermi sea.

5.4 Polaron-trimeron coupling

We now study the hybridization of the polaronic and Efimov sectors by minimizing the energy with respect to all five amplitudes A, B, C, D and E. From the previous analysis, we would expect that the optimal choice would be to mix the polaron wavefunction with the Cooper-like trimer. However, as we will show below, these

two sectors are not coupled at the thermodynamic limit. Indeed, the normalization of the state of a Cooper-like trimer requires that

$$\begin{aligned}|A|^2 + 2\sum_{\boldsymbol{q}_1}|B(\boldsymbol{q}_1)|^2 + 2\sum_{\boldsymbol{q}_1,\boldsymbol{k}_1}|C(\boldsymbol{q}_1,\boldsymbol{k}_1)|^2 + 2\sum_{\boldsymbol{q}_1,\boldsymbol{k}_1}|D(\boldsymbol{q}_1,-\boldsymbol{q}_1,\boldsymbol{k}_1)|^2 \\ + \sum_{\boldsymbol{q}_1,\boldsymbol{k}_1,\boldsymbol{k}_2}|E(\boldsymbol{q}_1,-\boldsymbol{q}_1,\boldsymbol{k}_1,\boldsymbol{k}_2)|^2 = 1\end{aligned} \tag{5.12}$$

For large quantization volumes, the sums are turned into integrals and in the normalization each sum gives rise to a density of state prefactor $\mathcal{V}/(2\pi)^3$. To recover results that do not depend on $\mathcal{V}$, we see that A should not depend on $\mathcal{V}$ and B, C, D and E should respectively scale like

$$\begin{aligned} B = \frac{b(\boldsymbol{q}_1)}{\sqrt{\mathcal{V}}},\ D(\boldsymbol{q}_1,-\boldsymbol{q}_1,\boldsymbol{k}_1) = \frac{d(\boldsymbol{q}_1,\boldsymbol{k}_1)}{\mathcal{V}} \\ C = \frac{c(\boldsymbol{q}_1,\boldsymbol{k}_1)}{\mathcal{V}},\ E(\boldsymbol{q}_1,-\boldsymbol{q}_1,\boldsymbol{k}_1,\boldsymbol{k}_2) = \frac{e(\boldsymbol{q}_1,\boldsymbol{k}_1,\boldsymbol{k}_2)}{\mathcal{V}^{3/2}}\end{aligned} \tag{5.13}$$

where b, c, d and e do not depend on the size of the system (For unrestricted hole momenta $\boldsymbol{q}_1$ and $\boldsymbol{q}_2$, C and D would scale as $1/\mathcal{V}^{3/2}$ and $1/\mathcal{V}^2$ respectively). Under this assumption, the expectation value of the interaction term of the Hamiltonian can be recast as

$$\begin{aligned}\langle\widehat{H}_{\text{int}}\rangle = \Lambda\Big[&\int\frac{d^3\boldsymbol{q}_1}{(2\pi)^3}A^*b(\boldsymbol{q}_1) + \int\frac{d^3\boldsymbol{q}_1 d^3\boldsymbol{k}_1}{(2\pi)^6}b(\boldsymbol{q}_1)^*c(\boldsymbol{q}_1,\boldsymbol{k}_1) \\ &+ \int\frac{d^3\boldsymbol{q}_1 d^3\boldsymbol{k}_1}{(2\pi)^6\sqrt{\mathcal{V}}}c(\boldsymbol{q}_1,\boldsymbol{k}_1)^*d(\boldsymbol{q}_1,\boldsymbol{k}_1) + \int\frac{d^3\boldsymbol{q}_1 d^3\boldsymbol{k}_1 d^3\boldsymbol{k}_2}{(2\pi)^9}d(\boldsymbol{q}_1,\boldsymbol{k}_1)^*e(\boldsymbol{q}_1,\boldsymbol{k}_1,\boldsymbol{k}_2)\Big] + \text{c.c.}\end{aligned} \tag{5.14}$$

In this expression, we see that the energy does not depend on the quantization volume, except for the term coupling the amplitudes c and d which vanishes as $1/\sqrt{\mathcal{V}}$ for diverging $\mathcal{V}$ thus showing that in this limit, the polaron and Cooper-like trimer sectors are decoupled.
This property was tested numerically using two ansatz wavefunctions reported in the final part of Appendix C. We observed the energy values would jump from the polaron branch to the Cooper-like trimer at the intersection point.

To explore a possible polaron-trimeron crossover we therefore need to relax the constraint on the vanishing center of mass momentum characterizing the Cooper-like trimer state. For this purpose we consider a trial wavefunction $F(\boldsymbol{q}_1,\boldsymbol{q}_2) = F_0\, e^{-\boldsymbol{q}_1\cdot\boldsymbol{q}_2/2\sigma^2}$, where F_0 is a normalization constant. Just like for the Cooper-like trimer, this amplitude is maximum when $\boldsymbol{q}_1 + \boldsymbol{q}_2 = 0$ and when both momenta are on the Fermi surface. The parameter σ allows us to tune continuously the width of the hole wave-function between a uniform distribution and the Cooper-like trimer configuration. The Cooper-like trimer corresponds to $\sigma = 0$ while the opposite limit ($\sigma = \infty$) corresponds to a uniform distribution F.

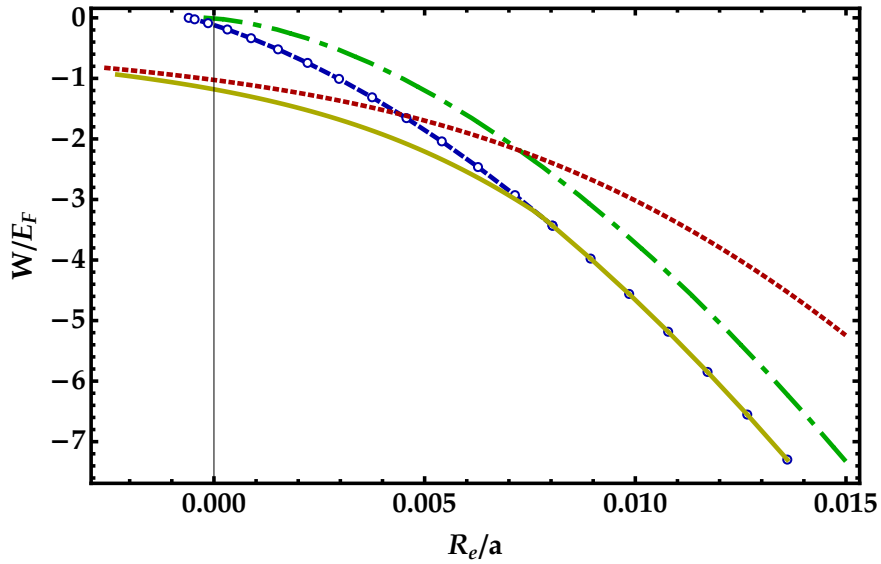

Figure 5.4: Variational ground state in the polaron-trimeron space for $k_F R_e = 10^{-2}$. We show the polaron energy for comparison (red dashed line). Cooper-like trimer ($\sigma = 0$, blue empty dots), compared to the energy of an Efimov trimer in vacuum (green, dash-dotted). The ground state associated with the optimal value of σ is the solid yellow line. The purely yellow section of the line corresponds to finite width hole pair wave functions F while the dotted section corresponds to Cooper-like trimers ($\sigma = 0$).

The minimization of the energy with respect to the amplitudes A, B, C, D, E yields the following set of coupled equations (See Appendix D for derivation) on $\tilde{A} = A/(\sqrt{\mathcal{V}} N_F \Lambda)$ and $\tilde{D}$ generalizing Eq. (5.4) and Eq. (5.10):

$$P_W \tilde{A} = \frac{2}{\mathcal{V}} \sum_{\mathbf{k}} h(k) \tilde{D}(k) \tag{5.15}$$

$$\mathcal{T}[\tilde{D}](k) = h(k)\tilde{A} + f(k)\tilde{D}(k) + \frac{1}{\mathcal{V}} \sum_{\mathbf{k}'} g(\mathbf{k}, \mathbf{k}') \tilde{D}(k') \tag{5.16}$$

where $\mathcal{T}$ is the operator from Eq. (5.10) (times $m/\hbar^2$), and the coupling functions h, f, g are the following:

$$\begin{aligned} h(k) &= -\frac{m}{\hbar^2 \mathcal{V}} \sum_{\mathbf{q}} \frac{\beta(q)}{(\lambda^2 + k^2 - \boldsymbol{q}\cdot\boldsymbol{k})\Delta_q}, \quad f(k) = -\frac{m}{\hbar^2 \mathcal{V}} \sum_{\mathbf{q}} \frac{\beta(q)^2}{\lambda^2 + k^2 - \boldsymbol{q}\cdot\boldsymbol{k}'} \\ g(\mathbf{k}, \mathbf{k}') &= \frac{m^2}{\hbar^4 \mathcal{V}} \sum_{\mathbf{q}} \frac{\beta(q)^2}{(\lambda^2 + k^2 - \boldsymbol{q}\cdot\boldsymbol{k})(\lambda^2 + k'^2 - \boldsymbol{q}\cdot\boldsymbol{k}')\Delta_q}, \quad \beta(q) = \frac{1}{N_F} \sum_{\mathbf{q}'} F(\mathbf{q}, \mathbf{q}') \end{aligned} \tag{5.17}$$

and where Δ_q is defined in Eq. (5.5). Functions f, g and h describe the coupling between the polaron and trimer sectors. If we set them equal to zero then Eq. (5.15) and (5.16) simply yield the equations of the polaron and trimeron sectors obtained earlier.

The results of the minimization are displayed in Fig. (5.5) (See Appendix D for details on the numerical calculation). For each value of R_e/a we solve Eq. (5.15) and

Eq. (5.16) for a fixed set of values of σ, here

$$\sigma \in \{0, 0.1, 0.125, 0.2, 0.25, 0.4, 0.5, 0.625, 0.67, 0.71, 0.77, 0.83, 0.91, 1\},$$

where $\sigma = 0$ corresponds to the Cooper-like trimer. For each value of R_e/a we search for the optimal value of σ_{opt} that minimizes the energy of the impurity. The corresponding values of σ_{opt} are displayed in Fig. (5.5). For $R_e/a \lesssim 7.7 \times 10^{-3}$, we observe that the optimum value decreases smoothly (in this regime the steps are just due to the discrete values of σ) and drops to $\sigma_{\text{opt}} = 0$ (corresponding to the Cooper-like trimer) at $R_e/a \simeq 7.7 \times 10^{-3}$ that suggests a sharp transition to the Cooper-like trimer state.

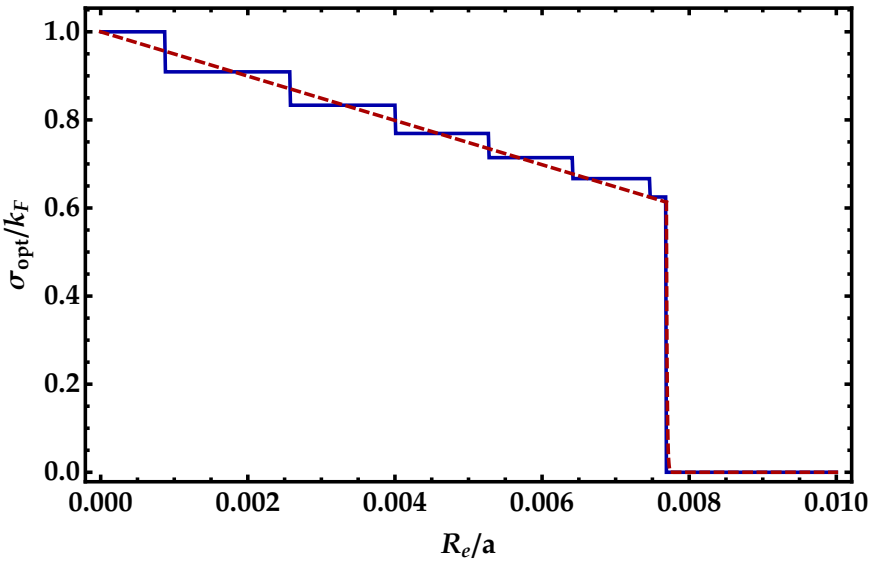

Figure 5.5: Optimal value of the width σ of the hole-pair wavefunction. Optimal value of the width σ of the hole-pair wavefunction (blue solid line). σ was varied over a finite set of values between between 0 and 1 (see text). For $R_e/a \lesssim 0.0077$, each step corresponds to a jump from one value of sigma to the next and is therefore an artefact of the discretization of σ. The red-dashed line corresponds to a smooth interpolation. For $R_e/a \simeq 0.0077$, we observe a jump of the value of σ which straddles several consecutive values of σ and thus marks a discontinuity between a Cooper-like trimer and a polaron-trimeron crossover state.

The variational ground state energy corresponding to $\sigma = \sigma_{\text{opt}}$ is displayed in Fig. (5.4), as well as the energy of the polaron state, and of the Cooper-like trimer. On this graph, we clearly see that for weak attractive interactions ($R_e/a \to -\infty$), the variational states converge to the polaron energy and that the ground state abruptly jumps to the Cooper-like trimer state in the vicinity of $R_e/a \simeq 7.7 \times 10^{-3}$. Note that this critical value depends on $k_F R_e$ and should converge to R_e/a_- for vanishing fermionic density.

5.5 Dimer energy

In the previous study we explored regions where the attractive interaction between the impurity and the fermions cannot support a two-body bound state, an important property for the formation of trimers due to their *Borromean* nature [133].
However, with increased attraction the trimer state will eventually merge into a dimer state and in this section we will explore more this possibility in order to complete our phase diagram.

The hamiltonian in Eq. (5.1) commutes with the spin operator, meaning that starting from the variation ansatz in Eq. (5.3), states with different spin number are not accessible in the Hilbert space. The polaron as well as the trimer have the spin number of the impurity, since the two fermions cancel each other's spin in the trimer case. However, the dimer has the spin of the impurity plus the spin of a fermion. This results in the exclusion of the dimer from the problem.

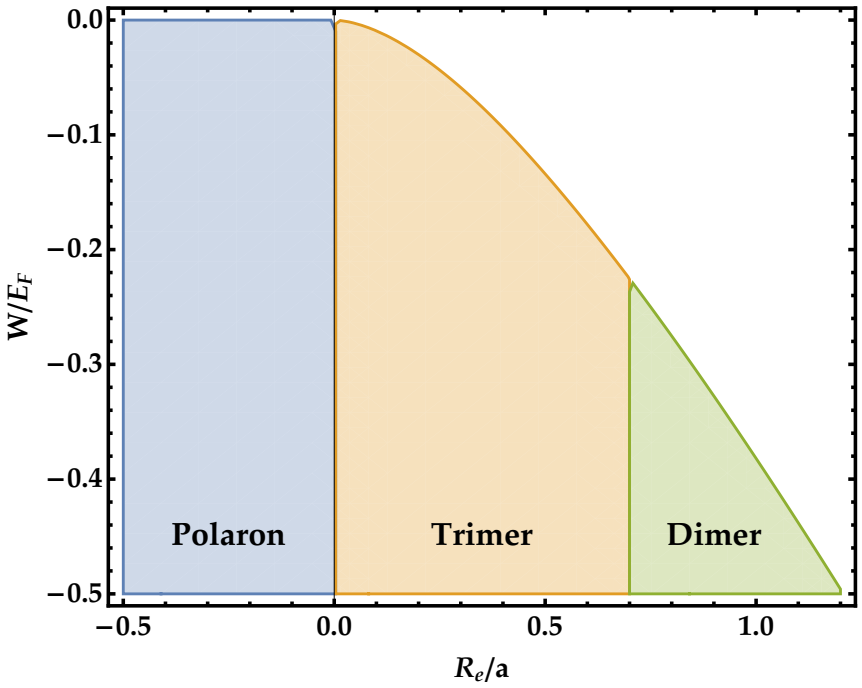

Figure 5.6: Phase diagram for an impurity immersed in a spin $1/2$ Fermi sea. We distinguish three regimes depending on the ratio between the resonance range R_e and the interaction strength a. When the impurity is interacting weakly with the spin components ($a \to 0^-$), a Fermi polaron state is the ground-state of the system, this state is composed of the impurity dressed by the particle-hole excitations it creates in the Fermi sea. For increased interactions ($a \to 0^-$), around $R_e/a = 0.0036$, the impurity binds to an existing Cooper pair and the polaronic branch connects to the resonant Cooper-like trimer states. In the strongly attractive regime $R_e/a \approx 0.7$ the Cooper pairing is overcome by the attraction between the impurity and the fermions and a dimer is formed.

Hence, to add the dimer to our treatment, we will treat it separately. We start by

writing a second variational ansatz that is written as follows

$$|\psi\rangle = (\beta\, b_0^\dagger + \sum_{\boldsymbol{k}} \alpha_{\boldsymbol{k}}\, a_{\boldsymbol{k}}^\dagger\, c_{-\boldsymbol{k}}^\dagger)|0\rangle \tag{5.18}$$

where β is the wavefunction of the dimer and α is the wavefunction for free impurity and a fermion both with momentum $\boldsymbol{k}$.
Solving the Shrödinger equation $(\hat{H} - E)|\psi\rangle = 0$ with $\hat{H}$ from Eq. (5.1) leads to the following set of coupled equations:

$$\begin{aligned} (E_0 - E)\beta + 2\frac{\Lambda}{\sqrt{\mathcal{V}}}\sum_{\boldsymbol{k}} \alpha_{\boldsymbol{k}} = 0, \\ \frac{\Lambda}{\sqrt{\mathcal{V}}}\beta + (2\epsilon_{\boldsymbol{k}} - E)\alpha_{\boldsymbol{k}} = 0. \end{aligned} \tag{5.19}$$

The energy of the dimer corresponds to the case $E < 0$. These equations can be solved simultaneously for β to find an equation for E, reminding the expression of E_0 in Eq. (5.2) and putting $m = m_i = 1$ and $\hbar = 1$ we find:

$$\frac{1}{4\pi a} - \frac{k_F}{2\pi^2} + \frac{E}{\Lambda^2} - \sum_{q>k_F}\left(\frac{1}{q^2} + \frac{1}{E - q^2}\right) = 0 \tag{5.20}$$

Reminding that $R_e = \frac{\pi\hbar^4}{m^{*2}\Lambda^2}$ we solve the last equation for E with $k_F R_e = 10^{-2}$ to find the energy of the dimer in our system. The results are presented in Fig. (5.5) where we see that for increased attractive interactions on the BEC side the dimer becomes the ground state of the system.

Summary and future work

In this chapter we used a variational approach to study the ground state of an impurity immersed in a non-interacting mixture of spin 1/2 fermions. We found that the impurity undergoes a first-order transition between a polaronic and a trimer state. This result differs from the case of an impurity immersed in a fermionic superfluid where fermionic Cooper pairing allows for a smooth crossover between those two states.
We explained our results by the absence of coupling between the two states in the thermodynamic limit. A similar situation seems to occur in the Fermi polaron for the transition between the polaron and dimer [305–308] and trimer [302] states.
Then to complete the phase diagram we followed a diagrammatic approach to calculate the energy of the dimer in our system and this led to the complete phase diagram. With increased interactions the trimer state is not stable anymore and it is no longer the ground state of the system.

For future work, one unanswered question is how does the excitations of the system play a role in the transition from a polaron state to a Cooper-like state in the thermodynamic limit. A careful analysis of the Hilbert space should be able to clearly see what is the main difference between the case of a superfluid, where Bogoliubov excitations help in creating a state of superposition between the impurity

and many particle-hole pairs which cannot be neglected when the system is scaled and the case of a Fermi gas in the normal phase where the impurity is the only catalyst for such an excitation and thus such excitations become negligible in the thermodynamic limit and therefore any coupling between the polaron and Efimov trimer states is killed off.
Another extension would be to study also the same problem with long-range interactions. This might have huge implications as the size of Efimov trimers could become much larger and therefore coupling might survive the thermodynamic limit.

Conclusion

The subject of this thesis is the study of ultracold Fermi gases, it was divided into two main parts. The first part focused on the experimental realization of fermionic superfluidity with ^{6}Li atoms. The design of the experimental setup is described with a quantitative characterization of each cooling and trapping step starting from the MOT to the science cell where the sample undergoes evaporative cooling to degeneracy. Then a characterization of the fermionic cloud beyond degeneracy is presented along with an overview of equation of state thermometry method and the interpolation realized in order to obtain the temperature of the cloud. Moreover, an additional step of directly observing superfluidity is presented where a spin imbalance is induced and the difference in spin populations is measured. The clear plateau at the center of the cloud is a signature of Cooper pairing and it shows a clear proof of superfluidity in our cloud.
As for the second part, it focused on a theoretical treatment involving two problems regarding an impurity in a two-component Fermi sea.
The first calculation showed that for an impurity immersed in an interacting superfluid, the divergent terms present in the perturbative expansion of the impurity's energy with respect to its interaction strength parameter with the bath can be traced back to processes including, among others, the scattering of an impurity and the creation of one particle hole pair and the subsequent interactions between this pair and the bath.
The second calculation studies more generally the physics of an impurity immersed in a two-component non-interacting Fermi sea. Using a variational ansatz, it was shown that the impurity state transitions sharply from a polaron state in the weak attractive limit to a trimer state of the impurity and two fermions lying close to the Fermi surface with opposite momenta.

General outlook: A quantum gas microscope to study impurity physics

With a high-resolution microscope and a box potential, the study of correlation functions of physical quantities in the gas becomes accessible.
For instance, to obtain the density-density correlation functions, the atoms in each region can be counted to establish a spatial distribution which, after being averaged, can give a measurement of $\langle n(\boldsymbol{r})n(\boldsymbol{r}')\rangle$.
The addition of an impurity to the system could open up the possibility to see for

the first time the modifications in the density of the system caused by the impurity. This addition can be done in our experiment either by using ^{7}Li atoms, which are present in the oven but are not being cooled for now, for a bosonic impurity, or by using a third internal state of ^{6}Li, state $|3\rangle$ for instance, for a fermionic impurity.
By stabilising the impurity we can study density-density correlations as a function of the interaction strength between the impurity and background fermions. In order to discern the nature of the impurity one can calculate the integral of the expectation value of the density distortion $\Delta n(\boldsymbol{r}) = n(\boldsymbol{r}) - n_0$ caused by the impurity [309] which will give, within statistical noise margins, an integer number q:

$$q = \int_{\mathcal{D}} d^3\boldsymbol{r}[n(\boldsymbol{r}) - n_0]$$

where $\mathcal{D}$ is the region of space limited by the characteristics of the microscope, $n(\boldsymbol{r})$ is the density at position $\boldsymbol{r}$ after adding the impurity, where $\boldsymbol{r} = 0$ corresponds to the position of the impurity, and n_0 is the density of the gas before its interaction with the impurity. One condition to fullfill is to take the thermodynamic limit before integrating for $\Delta n(\boldsymbol{r})$ to vanish when $|\boldsymbol{r}| \to \infty$.
When $q = 0$, this corresponds to the case where the impurity is in the polaron sector, $q = 1$ corresponds to the case of an impurity that has formed a dimer with one component of the Fermi sea, and $q = 3$ corresponds to the case of an impurity which has combined with two atoms from the fermionic background to form a trimer.
The basic idea behind this integer number is that for a big number of particles, the fermion that combines with the impurity will not leave an effect on the number of particles in the vicinity of the impurity, but it will be counted as an addition to the impurity.
A more simplified picture is that to form a dimer we take one particle from $+\infty$ and we glue it to the impurity making for a difference in the number of particles captured by the microscope which is equal to 1, and 2 in the case of a trimer. As for the polaron, no additional particles are needed so the number of particles stays the same. The value $q = 0$ in the polaron case was calculated analytically using the Chevy ansatz [191] by Trefzger and Castin [310].
Back to the experimental realization, methods to control the position of individual atoms have been successfully realized experimentally using optical tweezers [311]. Using that we can stabilise the impurity with respect to the microscope focal plane. The fact that a quantum gas microscope images a 2D sample only should not pose a problem since the same logic can apply to 2D case.
This measurement would provide an insight on the impurity phase diagram discussed in Chapter 5, and though limited by the relative tuning of the scattering length of the impurity-fermion and the fermion-fermion interaction, since both species are subject to the same magnetic field, it is still a very interesting possible measurement to observe the phase transition.

Appendix A

Calculation of $\chi_1^{(1)}(q, -\epsilon_q)$

We want to calculate the following diagram:

$$\chi_1^{T,(1)}(\boldsymbol{q}, t) = -i\frac{g_0'}{\mathcal{V}} \sum_{\boldsymbol{k},\boldsymbol{p},\sigma} \int dt_1 G_{0,-\sigma}(p, t_1 - t) G_{0,-\sigma}(p+q, t - t_1) G_{0,\sigma}(k-q, -t_1) G_{0,\sigma}(k, t_1) \tag{A.1}$$

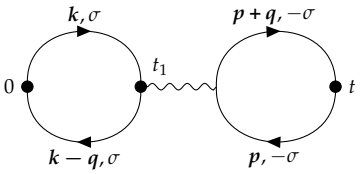

We take the Fourrier transform as follows::

$$\begin{aligned}\int_{-\infty}^{\infty} \frac{d\omega}{2\pi} e^{-i\omega t} \chi_1^{T,(1)}(q, \omega) = -2i\frac{g_0'}{\mathcal{V}} \int dt_1 \sum_{\boldsymbol{k},\boldsymbol{p},\sigma} \int_{-\infty}^{\infty} \frac{d\omega_1}{2\pi} e^{-i\omega_1(t_1 - t)} G_0(p, \omega_1) \\ \int_{-\infty}^{\infty} \frac{d\omega_2}{2\pi} e^{-i\omega_2(t - t_1)} G_0(p+q, \omega_2) \int_{-\infty}^{\infty} \frac{d\omega_3}{2\pi} e^{i\omega_3(t_1)} G_0(k-q, \omega_3) \int_{-\infty}^{\infty} \frac{d\omega_4}{2\pi} e^{-i\omega_4 t_1} G_0(k, \omega_4)\end{aligned} \tag{A.2}$$

The integration over t_1 gives a delta function which simplifies the expression, then we write the exponential in the RHS as $\int_{-\infty}^{\infty} d\omega e^{-i\omega t} \delta(\omega = \omega_2 - \omega_1)$, we eliminate ω_2 and with this we can write:

$$\chi_1^{T,(1)}(q, \omega) = 2i\frac{g_0'}{\mathcal{V}} \sum_{\boldsymbol{k},\boldsymbol{p}} \int_{-\infty}^{\infty} \frac{d\omega_1}{2\pi} \int_{-\infty}^{\infty} \frac{d\omega_3}{2\pi} G_0(p, \omega_1) G_0(p+q, \omega_1 + \omega) G_0(k-q, \omega_3) G_0(k, \omega_3 + \omega) \tag{A.3}$$

We remind that:

$$G_0(k, \omega) = \frac{\theta(k > k_F)}{\omega - E_k + i\delta} + \frac{\theta(k < k_F)}{\omega - E_k - i\delta} \tag{A.4}$$

With that we can write:

$$\begin{aligned}\chi_1^{T,(1)}(q, \omega) = 2i\frac{g_0'}{\mathcal{V}} \sum_{\boldsymbol{k},\boldsymbol{p}} \int_{-\infty}^{\infty} \frac{d\omega_1}{2\pi} \int_{-\infty}^{\infty} \frac{d\omega_3}{2\pi} \Big[\frac{\theta(p > k_F)}{\omega_1 - E_p + i\delta} + \frac{\theta(p < k_F)}{\omega_1 - E_p - i\delta}\Big] \\ \Big[\frac{\theta(p+q > k_F)}{\omega_1 + \omega - E_{p+q} + i\delta} + \frac{\theta(p+q < k_F)}{\omega_1 + \omega - E_{p+q} - i\delta}\Big] \Big[\frac{\theta(k-q > k_F)}{\omega_3 - E_{k-q} + i\delta} + \frac{\theta(k-q < k_F)}{\omega_3 - E_{k-q} - i\delta}\Big] \\ \Big[\frac{\theta(k > k_F)}{\omega_3 + \omega - E_k + i\delta} + \frac{\theta(k < k_F)}{\omega_3 + \omega - E_k - i\delta}\Big]\end{aligned} \tag{A.5}$$

We keep terms where ω_1 and ω_3 have poles above and below the real axis simultaneously to avoid a zero integral, we write the sum over $K = (\boldsymbol{k}, \omega_1)$ and $P = (\boldsymbol{p}, \omega_3)$:

$$\begin{aligned}\chi_1^{T,(1)}(q,\omega) = 2i\frac{g_0'}{\mathcal{V}}\sum_{K,P}\Big[&\frac{\theta(p>k_F)}{\omega_1 - E_p + i\delta}\frac{\theta(p+q<k_F)}{\omega_1+\omega-E_{p+q}-i\delta}\frac{\theta(k-q>k_F)}{\omega_3-E_{k-q}+i\delta}\frac{\theta(k<k_F)}{\omega_3+\omega-E_k-i\delta}\\ &+\frac{\theta(p>k_F)}{\omega_1 - E_p + i\delta}\frac{\theta(p+q<k_F)}{\omega_1+\omega-E_{p+q}-i\delta}\frac{\theta(k-q<k_F)}{\omega_3-E_{k-q}-i\delta}\frac{\theta(k>k_F)}{\omega_3+\omega-E_k+i\delta}\\ &+\frac{\theta(p<k_F)}{\omega_1 - E_p - i\delta}\frac{\theta(p+q>k_F)}{\omega_1+\omega-E_{p+q}+i\delta}\frac{\theta(k-q>k_F)}{\omega_3-E_{k-q}+i\delta}\frac{\theta(k<k_F)}{\omega_3+\omega-E_k-i\delta}\\ &+\frac{\theta(p<k_F)}{\omega_1 - E_p - i\delta}\frac{\theta(p+q>k_F)}{\omega_1+\omega-E_{p+q}+i\delta}\frac{\theta(k-q<k_F)}{\omega_3-E_{k-q}-i\delta}\frac{\theta(k>k_F)}{\omega_3+\omega-E_k+i\delta}\Big]\end{aligned}$$

We can now perform the integrals over ω_1 and ω_3 by closing the contour over the half-plane which does not contain ω in its pole, for example we close it over the lower half for both variables in the first term, resulting in residues at $\omega_1 = E_p - i\delta$ and $\omega_3 = E_{k-q} - i\delta$, we get the following:

$$\begin{aligned}\chi_1^{T,(1)}(q,\omega) = -2i\frac{g_0'}{\mathcal{V}}\sum_{\boldsymbol{k},\boldsymbol{p}}\Big[&\frac{\theta(p>k_F)\theta(p+q<k_F)}{\omega+E_p-E_{p+q}-i\delta}\frac{\theta(k-q>k_F)\theta(k<k_F)}{\omega+E_{k-q}-E_k-i\delta}\\ &-\frac{\theta(p>k_F)\theta(p+q<k_F)}{\omega+E_p-E_{p+q}-i\delta}\frac{\theta(k-q<k_F)\theta(k>k_F)}{\omega+E_{k-q}-E_k+i\delta}\\ &-\frac{\theta(p<k_F)\theta(p+q>k_F)}{\omega+E_p-E_{p+q}+i\delta}\frac{\theta(k-q>k_F)\theta(k<k_F)}{\omega+E_{k-q}-E_k-i\delta}\\ &+\frac{\theta(p<k_F)\theta(p+q>k_F)}{\omega+E_p-E_{p+q}+i\delta}\frac{\theta(k-q<k_F)\theta(k>k_F)}{\omega+E_{k-q}-E_k+i\delta}\Big]\end{aligned} \tag{A.6}$$

The minus sign results from the contour direction if the two poles are in different half-planes, one of the contours will be anti-clockwise.
We try to separate the function $\chi_1^{T,(1)}(q,\omega)$ into an advanced and a retarded part with respect to ω, clearly the first term is a purely advanced term, and the fourth term is a purely retarded term, as for the second and third terms, they both have two poles for ω in the upper and lower half-planes. So we separate them into retarded and advanced terms:

$$\begin{aligned}\chi_{1,r}^{(1)}(q,\omega) = -2i\frac{g_0'}{\mathcal{V}}\sum_{\boldsymbol{k},\boldsymbol{p}}\Big[&\frac{\theta(p<k_F)\theta(p+q>k_F)}{\omega+E_p-E_{p+q}+i\delta}\frac{\theta(k-q<k_F)\theta(k>k_F)}{\omega+E_{k-q}-E_k+i\delta}\\ &+\frac{\theta(p>k_F)\theta(p+q<k_F)\theta(k-q<k_F)\theta(k>k_F)}{(E_{k-q}-E_k-E_p+E_{p+q})(\omega+E_{k-q}-E_k+i\delta)}-\frac{\theta(p<k_F)\theta(p+q>k_F)\theta(k-q>k_F)\theta(k<k_F)}{(E_{k-q}-E_k-E_p+E_{p+q})(\omega+E_p-E_{p+q}+i\delta)}\Big]\end{aligned} \tag{A.7}$$

We take the limit of $\chi_{1,r}^{T,(1)}(q,-\epsilon_q)$ at $q\to\infty$:

$$\begin{aligned}\chi_{1,r}^{T,(1)}(q,-\epsilon_q) = -2i\frac{g_0'}{\mathcal{V}}\sum_{\boldsymbol{k},\boldsymbol{p}}\Big[&\frac{\theta(p<k_F)\theta(p+q>k_F)\theta(k-q<k_F)\theta(k>k_F)}{(q^2/2m^*+\boldsymbol{p}.\boldsymbol{q}/m)((1/m_i-1/m)q^2/2+\boldsymbol{k}.\boldsymbol{q}/m)}\\ &+m\frac{\theta(p>k_F)\theta(p+q<k_F)\theta(k-q<k_F)\theta(k>k_F)}{(q^2+\boldsymbol{p}.\boldsymbol{q}-\boldsymbol{k}.\boldsymbol{q})((1/m-1/m_i)q^2/2-\boldsymbol{k}.\boldsymbol{q}/m)}+m\frac{\theta(p<k_F)\theta(p+q>k_F)\theta(k-q>k_F)\theta(k<k_F)}{(q^2+\boldsymbol{p}.\boldsymbol{q}-\boldsymbol{k}.\boldsymbol{q})(q^2/2m^*+\boldsymbol{p}.\boldsymbol{q}/m)}\Big]\end{aligned} \tag{A.8}$$

In the first term p is limited by k_F but k is not, which gives a contribution in $1/q^4$, since the scalar product in the first multiplicant in the denominator is negligible but not in the second, with the same reasoning we treat the following terms and we find again a contribution of the order of $1/q^4$. This gives:

$$\chi_1^{T,(1)}(\boldsymbol{q}, -\epsilon_{\boldsymbol{q}}) \underset{|\boldsymbol{q}|\to\infty}{\propto} \frac{1}{q^4} + O(\frac{1}{q^5})$$

For a curious reader, can also verify the behavior of the advanced term.

$$\chi_{1,a}^{T,(1)}(q,\omega) = -2i\frac{g_0'}{\mathcal{V}}\sum_{\boldsymbol{k},\boldsymbol{p}}\Big[\frac{\theta(p>k_F)\theta(p+q<k_F)}{\omega+E_p-E_{p+q}-i\delta}\frac{\theta(k-q>k_F)\theta(k<k_F)}{\omega+E_{k-q}-E_k-i\delta} \tag{A.9}$$
$$-\frac{\theta(p>k_F)\theta(p+q<k_F)\theta(k-q<k_F)\theta(k>k_F)}{(E_{k-q}-E_k-E_p+E_{p+q})(\omega+E_p-E_{p+q}-i\delta)}+\frac{\theta(p<k_F)\theta(p+q>k_F)\theta(k-q>k_F)\theta(k<k_F)}{(E_{k-q}-E_k-E_p+E_{p+q})(\omega+E_{k-q}-E_k-i\delta)}\Big]$$

We take the limit of $\chi_{1,a}^{T,(1)}(q,-\epsilon_{\boldsymbol{q}})$ at $q\to\infty$:

$$\chi_{1,a}^{T,(1)}(q,-\epsilon_{\boldsymbol{q}}) = -2i\frac{g_0'}{\mathcal{V}}\sum_{\boldsymbol{k},\boldsymbol{p}}\Big[\frac{\theta(p<k_F)\theta(p+q>k_F)\theta(k-q<k_F)\theta(k>k_F)}{(q^2/2m^*+\boldsymbol{p}.\boldsymbol{q}/m)((1/m_i-1/m)q^2/2+\boldsymbol{k}.\boldsymbol{q}/m)} \tag{A.10}$$
$$-m\frac{\theta(p>k_F)\theta(p+q<k_F)\theta(k-q<k_F)\theta(k>k_F)}{(q^2+\boldsymbol{p}.\boldsymbol{q}-\boldsymbol{k}.\boldsymbol{q})(q^2/2m^*+\boldsymbol{p}.\boldsymbol{q}/m)}+m\frac{\theta(p<k_F)\theta(p+q>k_F)\theta(k-q>k_F)\theta(k<k_F)}{(q^2+\boldsymbol{p}.\boldsymbol{q}-\boldsymbol{k}.\boldsymbol{q})(1/m-1/m_i)q^2/2-\boldsymbol{k}.\boldsymbol{q}/m)}\Big]$$
$$\propto \frac{1}{(q^2/2m^*)(q^2/2m^*)}-\frac{1}{(q^2/m)q^2(1/2m^*-1/m)}+\frac{1}{(q^2/m)(1/m-1/m_i)q^2/2}$$

We note that the square of the momentum's amplitude in the summation (p^2 and k^2) does not count in the power counting since the volume of the integral sphere $dk\,k^2\,d\Omega$ has to remain finite, for example in the second term p is larger than k_F but the sum of the two vectors $p+q$ has to stay finite, so when $p\to\infty$ the solid angle $\Omega\to 0$ and the product remains finite.

Appendix B

Ladder diagram terms

We remind the following expression:

$$\chi_1^{(1)}(\boldsymbol{q},\omega) = \frac{2i}{V}\sum_{\boldsymbol{P},\boldsymbol{p}}\int_{-\infty}^{\infty}\frac{d\omega_1}{2\pi}\int_{-\infty}^{\infty}\frac{d\Omega}{2\pi}G_{0,\downarrow}(\boldsymbol{p},\omega_1)G_{0,\downarrow}(\boldsymbol{p}+\boldsymbol{q},\omega_1+\omega)G_{0,\uparrow}(\boldsymbol{P}-\boldsymbol{p}-\boldsymbol{q},\omega-\omega-\omega_1) \\ G_{0,\uparrow}(\boldsymbol{P}-\boldsymbol{p},\Omega-\omega_1)\gamma_{\uparrow,\downarrow}(P) \tag{B.1}$$

We develop the Green's functions as follows:

$$G_{0,\downarrow}(\boldsymbol{p},\omega_1)G_{0,\uparrow}(\boldsymbol{P}-\boldsymbol{p},\Omega-\omega_1)G_{0,\uparrow}(\boldsymbol{P}-\boldsymbol{p}-\boldsymbol{q},\omega-\omega-\omega_1)G_{0,\downarrow}(\boldsymbol{p}+\boldsymbol{q},\omega_1+\omega) \\ = \Big[\frac{\theta(|\boldsymbol{p}|>k_F)}{\omega_1-E_{\boldsymbol{p}}+i\eta}+\frac{\theta(|\boldsymbol{p}|<k_F)}{\omega_1-E_{\boldsymbol{p}}-i\eta}\Big]\Big[\frac{\theta(|\boldsymbol{P}-\boldsymbol{p}|>k_F)}{\Omega-\omega_1-E_{\boldsymbol{P}-\boldsymbol{p}}+i\eta}+\frac{\theta(|\boldsymbol{P}-\boldsymbol{p}|<k_F)}{\Omega-\omega_1-E_{\boldsymbol{P}-\boldsymbol{p}}-i\eta}\Big] \\ \Big[\frac{\theta(|\boldsymbol{P}-\boldsymbol{p}-\boldsymbol{q}|>k_F)}{\Omega-\omega-\omega_1-E_{\boldsymbol{P}-\boldsymbol{p}-\boldsymbol{q}}+i\eta}+\frac{\theta(|\boldsymbol{P}-\boldsymbol{p}-\boldsymbol{q}|<k_F)}{\Omega-\omega-\omega_1-E_{\boldsymbol{P}-\boldsymbol{p}-\boldsymbol{q}}-i\eta}\Big] \\ \Big[\frac{\theta(|\boldsymbol{p}+\boldsymbol{q}|>k_F)}{\omega+\omega_1-E_{\boldsymbol{p}+\boldsymbol{q}}+i\eta}+\frac{\theta(|\boldsymbol{p}+\boldsymbol{q}|<k_F)}{\omega+\omega_1-E_{\boldsymbol{p}+\boldsymbol{q}}-i\eta}\Big]$$

We call the retarded terms respectively A_1, B_1, C_1, D_1 and the advanced terms respectively A_2, B_2, C_2, D_2 and we write their poles with respect to different variables in the following table:

	ω_1	ω	Ω
A_1	$-i\eta$	X	X
B_1	$+i\eta$	X	$-i\eta$
C_1	$+i\eta$	$+i\eta$	$-i\eta$
D_1	$-i\eta$	$-i\eta$	X
A_2	$+i\eta$	X	X
B_2	$-i\eta$	X	$+i\eta$
C_2	$-i\eta$	$-i\eta$	$+i\eta$
D_2	$+i\eta$	$+i\eta$	X

where X means that no poles are present in the function with respect to this variable. We remind that we only accept terms with poles $\omega = -i\eta$ for the the function $\chi_1^{(1)}(\boldsymbol{q},\omega)$ to be retarded with respect to ω. We can detail the 16 resulting terms as follows:

- $A_1B_1C_1D_1 \underset{|\boldsymbol{q}|\to\infty}{\propto} \frac{1}{q^3}$ as shown in chapter 4.

- $A_1B_1C_1D_2 = 0$ since all poles of ω are in the upper half of the complex plane i.e. advanced with respect to ω.

- $A_1B_2C_1D_2 = 0$ since all poles of ω are in the upper half of the complex plane i.e. advanced with respect to ω.

- $A_1B_2C_2D_1 = 0$ since all poles of ω_1 are on one side of the complex plane leading to a zero integral over this variable.

- $A_2B_1C_1D_2 = 0$ since all poles of ω_1 are on one side of the complex plane leading to a zero integral over this variable.

- $A_2B_2C_1D_2 = 0$ since all poles of ω are in the upper half of the complex plane i.e. advanced with respect to ω.

- $A_2B_1C_2D_2 = A_1B_1C_2D_2 = A_1B_2C_2D_2 = A_2B_2C_2D_2 = 0$ since the product $\theta(|\boldsymbol{p}+\boldsymbol{q}|<k_F)\theta(|\boldsymbol{p}|<k_F)$ is zero since for the first Heaviside function to be verified $|\boldsymbol{p}|$ should be comparable to $|\boldsymbol{q}|$ when $|\boldsymbol{q}|\to\infty$. However $|\boldsymbol{p}|$ is limited to k_F.

- $A_2B_2C_2D_1 = 0$ similarly to the last expression with the product $\theta(|\boldsymbol{P}-\boldsymbol{p}|<k_F)\theta(|\boldsymbol{P}-\boldsymbol{p}-\boldsymbol{q}|<k_F)$ if we take $\boldsymbol{k} = \boldsymbol{p}-\boldsymbol{P}$ we recover the same product above.

For the remaining terms $A_2B_1C_1D_1, A_2B_1C_2D_1, A_2B_2C_1D_1, A_1B_1C_2D_1, A_1B_2C_1D_1$ we treat one of them in the following:

$$\begin{aligned} A_2B_1C_1D_1 =& \frac{2i}{V}\sum_{\boldsymbol{P},\boldsymbol{p}}\int_{-\infty}^{\infty}\frac{d\omega_1}{2\pi}\int_{-\infty}^{\infty}\frac{d\Omega}{2\pi}\frac{\theta(|\boldsymbol{p}|<k_F)}{\omega_1-E_{\boldsymbol{p}}-i\eta}\frac{\theta(|\boldsymbol{P}-\boldsymbol{p}|>k_F)}{\Omega-\omega_1-E_{\boldsymbol{P}-\boldsymbol{p}}+i\eta} \\ & \frac{\theta(|\boldsymbol{P}-\boldsymbol{p}-\boldsymbol{q}|>k_F)}{\Omega-\omega-\omega_1-E_{\boldsymbol{P}-\boldsymbol{p}-\boldsymbol{q}}+i\eta}\frac{\theta(|\boldsymbol{p}+\boldsymbol{q}|>k_F)}{\omega+\omega_1-E_{\boldsymbol{p}+\boldsymbol{q}}+i\eta}\gamma_{\uparrow,\downarrow}(P) \\ =& \frac{2i}{V}\sum_{\boldsymbol{P},\boldsymbol{p}}\int_{-\infty}^{\infty}\frac{d\Omega}{2\pi}\frac{\theta(|\boldsymbol{p}|<k_F)}{-\omega+E_{\boldsymbol{p}+\boldsymbol{q}}-E_{\boldsymbol{p}}-i\eta}\frac{\theta(|\boldsymbol{P}-\boldsymbol{p}|>k_F)}{\Omega+\omega-E_{\boldsymbol{p}+\boldsymbol{q}}-E_{\boldsymbol{P}-\boldsymbol{p}}+i\eta} \\ & \frac{\theta(|\boldsymbol{P}-\boldsymbol{p}-\boldsymbol{q}|>k_F)\theta(|\boldsymbol{p}+\boldsymbol{q}|>k_F)}{\Omega-E_{\boldsymbol{p}+\boldsymbol{q}}-E_{\boldsymbol{P}-\boldsymbol{p}-\boldsymbol{q}}+i\eta}\gamma_{\uparrow,\downarrow}(P) \end{aligned} \tag{B.2}$$

with $\omega = -\epsilon_{\boldsymbol{q}}$. We see that the first term in the product in the limit $|\boldsymbol{q}|\to\infty$ behaves as $1/q^2$ because with $|\boldsymbol{p}|<k_F$ we can make the change of variable $|\boldsymbol{p}+\boldsymbol{q}|\simeq|\boldsymbol{q}|$ in this limit.
We note the Ω has poles only in the lower half of the complex plane, $\gamma_{\uparrow,\downarrow}(P)$ has to have its poles in the upper half of the complex plane for the integral over Ω not to be zero.
From Eq. (4.52) we see that the second sum which constitutes the advanced part of the function is zero for $|\boldsymbol{P}|>2k_F$. This restricts the values of $\boldsymbol{P}$ and the second and third terms in Eq. (B.2) behave as $1/(\Omega - q^2/(2m) + o(q^2) + i\eta)$ so we can write the

term as:

$$A_2B_1C_1D_1 \underset{|\boldsymbol{q}|\to\infty}{\simeq} \frac{2i}{V}\sum_{\boldsymbol{P},|\boldsymbol{p}|<k_F}\int_{-\infty}^{\infty}\frac{d\Omega}{2\pi}\frac{1}{q^2} \frac{\theta(|\boldsymbol{P}-\boldsymbol{p}|>k_F)\theta(|\boldsymbol{P}-\boldsymbol{p}-\boldsymbol{q}|>k_F)}{\Omega - Aq^2/(2m)+o(q^2)+i\eta}\frac{\gamma^A_{\uparrow,\downarrow}(\boldsymbol{P},\Omega)}{\Omega - Bq^2/(2m)+o(q^2)+i\eta} \tag{B.3}$$

where $\theta(|\boldsymbol{p}+\boldsymbol{q}|>k_F)=1$ in the limit of a large impurity momentum.
The function $\gamma^A_{\uparrow,\downarrow}(\boldsymbol{P},\Omega)$ behaves as $1/\sqrt{\Omega}$ for $\Omega\to\infty$. Then by doing a change of variables $\Omega = q^2\tilde{\Omega}$ we can write finally:

$$\begin{aligned} A_2B_1C_1D_1 &\underset{|\boldsymbol{q}|\to\infty}{\simeq} \frac{2i}{V}\sum_{\boldsymbol{P},|\boldsymbol{p}|<k_F}\int_{-\infty}^{\infty}\frac{d\Omega}{2\pi}\frac{1}{\sqrt{\Omega}}\frac{1}{q^2}\frac{\theta(|\boldsymbol{P}-\boldsymbol{p}|>k_F)\theta(|\boldsymbol{P}-\boldsymbol{p}-\boldsymbol{q}|>k_F)}{(\Omega - Aq^2/(2m)+o(q^2)+i\eta)(\Omega - Bq^2/(2m)+o(q^2)+i\eta)} \\ &\underset{|\boldsymbol{q}|\to\infty}{\propto} \frac{1}{|\boldsymbol{q}|^5} \end{aligned} \tag{B.4}$$

which does not contribute to the divergent term in $\chi(\boldsymbol{q},-\epsilon_q)$.

In a similar manner we prove that the other terms in the expansion do not contribute to the divergent term, leaving only the term treated in Chapter 4.

Appendix C

Derivation of polaron-trimeron coupled equations

Variational solution

We minimize $\langle\psi|\hat{H}|\psi\rangle$ with the condition that we keep $\langle\psi|\psi\rangle$ constant, and for that we use a Lagrange multiplier which is the energy W in this case. We write this formally:

$$\delta\langle\psi|\hat{H}|\psi\rangle - W\delta\langle\psi|\psi\rangle = 0 \tag{C.1}$$

Since we have a wavefunction with five variables A, B, C, D, E, we need to solve a system of five equations resulting from deriving Eq. (C.1) with respect to each of the parameters. In the following we take $\hbar = 1$, we take also the masses of the impurity and the fermions to be equal to 1.
We remind the following form for the functions D and E:

$$\begin{aligned} D_s(\boldsymbol{q}_1, \boldsymbol{q}_2, \boldsymbol{k}_1) &= F(\boldsymbol{q}_1, \boldsymbol{q}_2)\tilde{D}(\boldsymbol{k}_1) \\ E(\boldsymbol{q}_1, \boldsymbol{q}_2, \boldsymbol{k}_1, \boldsymbol{k}_2) &= F(\boldsymbol{q}_1, \boldsymbol{q}_2)\tilde{E}(\boldsymbol{k}_1, \boldsymbol{k}_2), \end{aligned} \tag{C.2}$$

with $\sum_{q_1,q_2}|F(\boldsymbol{q}_1, \boldsymbol{q}_2)|^2 = N_F^2$ and where we assumed that the distribution $|F|^2$ is an even function of $\boldsymbol{q}_1$ and $\boldsymbol{q}_2$.
• With respect to $E^*(\boldsymbol{k}_1, \boldsymbol{k}_2)$

$$(W - k_1^2 - k_2^2 - \boldsymbol{k}_1.\boldsymbol{k}_2 - \langle \boldsymbol{q}_1.\boldsymbol{q}_2\rangle)E(\boldsymbol{k}_1, \boldsymbol{k}_2) = \frac{\Lambda}{\sqrt{\Omega}}(D(\boldsymbol{k}_1) + D(\boldsymbol{k}_2)) \tag{C.3}$$

with $\langle f(\boldsymbol{q}_1, \boldsymbol{q}_2)\rangle = \sum_{q_i}|F(\boldsymbol{q}_1, \boldsymbol{q}_2)|^2 f(\boldsymbol{q}_1, \boldsymbol{q}_2)/N_F^2$.
• With respect to $D^*(\boldsymbol{k}_1)$

$$\begin{aligned} &\left(W - E_0 - \frac{3k_1^2}{4} + \frac{1}{4}\langle(\boldsymbol{q}_1 - \boldsymbol{q}_2)^2\rangle\right)D(\boldsymbol{k}_1) = \frac{\Lambda}{\sqrt{\Omega}N_F}\sum_{\boldsymbol{q}_1}\beta(\boldsymbol{q}_1)C(\boldsymbol{q}_1, \boldsymbol{k}_1) \\ &+ \frac{\Lambda}{\sqrt{\Omega}}\sum_{k_2}E(\boldsymbol{k}_1, \boldsymbol{k}_2) \end{aligned} \tag{C.4}$$

with $\beta(q) = \frac{1}{N_F}\sum_{\mathbf{q}'} F(\mathbf{q},\mathbf{q}')$.
We can plug the expression of $E(\boldsymbol{k}_1,\boldsymbol{k}_2)$ from Eq. (C.3) to have a single expression for C and D:

$$\Big(W - E_0 - \frac{3k_1^2}{4} + \frac{1}{4}\langle(\boldsymbol{q}_1-\boldsymbol{q}_2)^2\rangle - \frac{\Lambda^2}{\Omega}\sum_{\boldsymbol{k}_2}\frac{1}{W - k_1^2 - k_2^2 - \boldsymbol{k}_1.\boldsymbol{k}_2 - \langle \boldsymbol{q}_1.\boldsymbol{q}_2\rangle}\Big)D(\boldsymbol{k}_1)$$
$$-\frac{\Lambda^2}{\Omega}\sum_{\boldsymbol{k}_2}\frac{D(\boldsymbol{k}_2)}{W - k_1^2 - k_2^2 - \boldsymbol{k}_1.\boldsymbol{k}_2 - \langle \boldsymbol{q}_1.\boldsymbol{q}_2\rangle} = \frac{\Lambda}{N_F\sqrt{\Omega}}\sum_{\boldsymbol{q}_1}\beta(\boldsymbol{q}_1)C(\boldsymbol{q}_1,\boldsymbol{k}_1) \tag{C.5}$$

When $C = 0$ this equation describes three particles with zero centre of mass momentum, which represents the trimer (Efimov problem).
• With respect to $C^*(\boldsymbol{q}_1,\boldsymbol{k}_1)$

$$C(\boldsymbol{q}_1,\boldsymbol{k}_1) = \frac{\Lambda}{\sqrt{\Omega}}\frac{B(\boldsymbol{q}_1) + N_F\beta(\boldsymbol{q}_1)D(\boldsymbol{k}_1)}{W - k_1^2 + \boldsymbol{q}_1.\boldsymbol{k}_1} \tag{C.6}$$

• With respect to $B^*(\boldsymbol{q}_1)$

$$B(\boldsymbol{q}_1) = \frac{\Lambda}{\sqrt{\Omega}}\frac{A + \sum_{\boldsymbol{k}_1} C(\boldsymbol{q}_1,\boldsymbol{k}_1)}{W - E_0 + \frac{q_1^2}{4}} \tag{C.7}$$

We can substitute the expression of C from Eq. (C.6):

$$B(\boldsymbol{q}_1) = \frac{1}{\Lambda\sqrt{\Omega}}\frac{A}{\Delta(\boldsymbol{q}_1)} + \frac{1}{\Omega}\frac{N_F}{\Delta(\boldsymbol{q}_1)}\sum_{\boldsymbol{k}_1}\frac{\beta(\boldsymbol{q}_1)D(\boldsymbol{k}_1)}{W - k_1^2 + \boldsymbol{q}_1.\boldsymbol{k}_1} \tag{C.8}$$

• With respect to A^*

$$WA = 2\frac{\Lambda}{\sqrt{\Omega}}\sum_{\boldsymbol{q}_1} B(\boldsymbol{q}_1) \tag{C.9}$$

We insert the expression B from Eq. (C.8):

$$\underbrace{(W - 2\frac{1}{\Omega}\sum_{\boldsymbol{q}_1}\frac{1}{\Delta(\boldsymbol{q}_1)})}_{\mathcal{P}_W} A = 2\frac{\Lambda N_F}{\Omega^{3/2}}\sum_{\boldsymbol{q}_1,\boldsymbol{k}_1}\frac{1}{\Delta(\boldsymbol{q}_1)}\frac{\beta(\boldsymbol{q}_1)D(\boldsymbol{k}_1)}{W - k_1^2 + \boldsymbol{q}_1.\boldsymbol{k}_1} \tag{C.10}$$

If $D = 0$ this would be the equation of the polaron. We can define:

$$\tilde{A} = \frac{A}{\Lambda\sqrt{\Omega}N_F}, \quad h(k_1) = \frac{1}{\Omega}\sum_{\boldsymbol{q}_1}\frac{\beta(\boldsymbol{q}_1)}{\Delta(\boldsymbol{q}_1)(W - k_1^2 + \boldsymbol{q}_1.\boldsymbol{k}_1)}$$

Then we can write Eq. (C.10) as:

$$\mathcal{P}_W\tilde{A} = \frac{2}{\Omega}\sum_{\boldsymbol{k}_1} h(k_1)D(\boldsymbol{k}_1) \tag{C.11}$$

Which is Eq. (5.15) in the main text.
Now that we have an expression which relates A with D, we will try to have another

one from Eq. (C.5), we write the RHS of Eq. (C.5) in the goal of writing it in terms of A and we obtain after writing:

$$f(\boldsymbol{k}_1) = \frac{1}{\Omega}\sum_{\boldsymbol{q}_1}\frac{\beta(\boldsymbol{q}_1)^2}{W - k_1^2 + \boldsymbol{q}_1.\boldsymbol{k}_1}$$

$$g(\boldsymbol{k}_1,\boldsymbol{k}_2) = \frac{1}{\Omega}\sum_{\boldsymbol{q}_1}\frac{\beta(\boldsymbol{q}_1)^2}{\Delta(\boldsymbol{q}_1)(W - k_1^2 + \boldsymbol{q}_1.\boldsymbol{k}_1)(W - k_2^2 + \boldsymbol{q}_1.\boldsymbol{k}_2)}$$

$$I(\boldsymbol{k}_1) = \frac{1}{\Lambda^2}\Big(W - E_0 - \frac{3k_1^2}{4} + \frac{1}{4}\langle(\boldsymbol{q}_1 - \boldsymbol{q}_2)^2\rangle - \frac{\Lambda^2}{\Omega}\sum_{\boldsymbol{k}_2}\frac{1}{W - k_1^2 - k_2^2 - \boldsymbol{k}_1.\boldsymbol{k}_2 - \langle\boldsymbol{q}_1.\boldsymbol{q}_2\rangle}\Big)$$

With this Eq. (C.5) becomes:

$$\begin{aligned} &I(\boldsymbol{k}_1)D(\boldsymbol{k}_1) - \frac{1}{\Omega}\sum_{\boldsymbol{k}_2}\frac{D(\boldsymbol{k}_2)}{W - k_1^2 - k_2^2 - \boldsymbol{k}_1.\boldsymbol{k}_2 - \langle\boldsymbol{q}_1.\boldsymbol{q}_2\rangle} \\ &= h(k_1)\tilde{A} + \frac{1}{\Omega}\sum_{\boldsymbol{k}_2} g(\boldsymbol{k}_1,\boldsymbol{k}_2)D(\boldsymbol{k}_2) + f(\boldsymbol{k}_1)D(\boldsymbol{k}_1), \end{aligned} \tag{C.12}$$

which corresponds to Eq. (5.16) from the main text.

Examples of $F(\boldsymbol{q}_1, \boldsymbol{q}_2)$

In order to verify numerically the problem with the vanishing coupling in the thermodynamic limit we choose two functions which introduce an explicit coupling between the case of a uniform hole distribution in the Fermi sea (the polaron state) and the case of holes localized at the Fermi surface (the Cooper-trimer state).

$F(\boldsymbol{q}_1, \boldsymbol{q}_2)$ as a linear superposition of uniformly distributed holes and localized holes at the Fermi surface

We take :

$$F(\boldsymbol{q}_1,\boldsymbol{q}_2) = \alpha + N\beta(q_1)\delta_{q_1,-q_2} \tag{C.13}$$

With $\beta(q_1)$ a function peaked at $q_1 = k_F$. The value of N could be calculated from the normalization condition:

$$\begin{aligned} &\sum_{q_1,q_2}|F(\boldsymbol{q}_1,\boldsymbol{q}_2)|^2 = N_F^2 \Rightarrow N^2 = N_F^2(1-\alpha^2)\sum_{q_1,}\beta^2(q_1) \\ &<\vec{q}_1.\vec{q}_2> = -(1-\alpha^2)k_F^2, <q_1^2> = 2\alpha^2\frac{U_F}{N_F} + (1-\alpha^2)k_F^2 \end{aligned} \tag{C.14}$$

All cross terms disappear at the thermodynamic limit since we have a delta Dirac function in the second term.
This leads to the following changes in the function above:

$$h(k_1), f(k_1), g(k_1,k_2) \to \alpha^2 h(k_1), \alpha^2 f(k_1), \alpha^2 g(k_1,k_2),\ \omega \to \omega + (1-\alpha^2)k_F^2,\ \frac{U_F}{N_F} \to \alpha^2\frac{U_F}{N_F} \tag{C.15}$$

By plugging these expressions and recalculating the energies we see that our ansatz did not improve the Cooper trimer, which means that our trial wave function simply move from the wave function we studied with uniform holes distribution and the wave function of the Cooper trimer without any underlying coupling between them which might lower the energy.

$F(\boldsymbol{q}_1, \boldsymbol{q}_2)$ as an exponential distribution of holes

To improve on the previous ansatz, we try a hole distribution which is not attenuated when taking the thermodynamic limit:

$$F(\boldsymbol{q}_1, \boldsymbol{q}_2) = Ne^{-\frac{\vec{q}_1.\vec{q}_2}{2\sigma^2}} \tag{C.16}$$

We normalize the expression, and we divide the final equation by N_F^2:

$$\sum_{q_1,q_2} |F(\boldsymbol{q}_1, \boldsymbol{q}_2)|^2 = N_F^2 \Rightarrow N^2 = \frac{4\pi^4}{\sigma^6(\sinh(\frac{k_F^2}{\sigma^2}) - \mathrm{shi}(\frac{k_F^2}{\sigma^2}))}, \text{ where } \quad \mathrm{shi}(x) = \int_0^x \frac{\sinh(t)}{t} dt \tag{C.17}$$

Then we calculate the term involved in f, g, h functions:

$$\beta(q_1) = \frac{1}{N_F} \sum_{q_2} F(\boldsymbol{q}_1, \boldsymbol{q}_2) = \frac{4\sigma}{q_1^3} \frac{k_F q_1 \cosh(\frac{k_F q_1}{2\sigma^2}) - 2\sigma^2 \sinh(\frac{k_F q_1}{2\sigma^2})}{\sqrt{\sinh(\frac{k_F^2}{\sigma^2}) - \mathrm{shi}(\frac{k_F^2}{\sigma^2}))}} \tag{C.18}$$

Now we have:

$$\begin{aligned} h(k_1) &= \frac{1}{\Omega} \sum_{q_1} \frac{\beta(q_1)}{\Delta(q_1)(\omega - k_1^2 + \vec{q}_1\vec{k}_1)}, \quad g(k_1, k_2) = \frac{1}{\Omega} \sum_{q_1} \frac{\beta(q_1)^2}{\Delta(q_1)(\omega - k_1^2 + \vec{q}_1\vec{k}_1)(\omega - k_2^2 + \vec{q}_1\vec{k}_2)} \\ f(k_1) &= \frac{1}{\Omega} \sum_{q_1} \frac{\beta(q_1)^2}{\omega - k_1^2 + \vec{q}_1\vec{k}_1} = \frac{1}{(2\pi)^2} \int_0^{k_F} dq_1 \frac{q_1}{k_1} \beta(q_1)^2 \ln(\frac{\omega - k_1^2 + q_1 k_1}{\omega - k_1^2 - q_1 k_1}) \end{aligned} \tag{C.19}$$

We calculate the moments involved in our full equation:

$$\begin{aligned} < \vec{q}_1.\vec{q}_2 > &= \frac{1}{N_F^2} \sum_{q_1,q_2} \vec{q}_1.\vec{q}_2 |F(\boldsymbol{q}_1, \boldsymbol{q}_2)|^2 = \frac{4\sigma^2 \sinh(\frac{k_F^2}{\sigma^2}) - k_F^2 \cosh(\frac{k_F^2}{\sigma^2}) - 3\sigma^2 \mathrm{shi}(\frac{k_F^2}{\sigma^2})}{\sinh(\frac{k_F^2}{\sigma^2}) - \mathrm{shi}(\frac{k_F^2}{\sigma^2})} \\ < q_1^2 > = < q_2^2 > &= \frac{1}{N_F^2} \sum_{q_1,q_2} q_1^2 |F(\boldsymbol{q}_1, \boldsymbol{q}_2)|^2 = \frac{-3\sigma^2 k_F^2 \cosh(\frac{k_F^2}{\sigma^2}) + (3\sigma^4 + k_F^4) \sinh(\frac{k_F^2}{\sigma^2})}{k_F^2(\sinh(\frac{k_F^2}{\sigma^2}) - \mathrm{shi}(\frac{k_F^2}{\sigma^2}))} \end{aligned} \tag{C.20}$$

Also we find by carefully calculating the energy that a first-order transition is still present.

Appendix D

Numercial solution of Skornyakov-Ter-Martirosyan's equation

Efimov part

Going back to the STM equation in the Cooper-like trimer state:

$$\left[\frac{1}{4\pi}\left\{a^{-1}-\frac{2}{\pi}k_F-R_e(\lambda^2-k_F^2+\frac{3}{4}k^2)\right\}+\frac{1}{\Omega}\sum_{K>k_F}(\frac{1}{\lambda^2-k_F^2+q^2+K^2+\vec{q}\cdot\vec{K}}-\frac{1}{K^2})\right]D(q)$$
$$+\frac{1}{\Omega}\sum_{K>k_F}\frac{D(K)}{\lambda^2-k_F^2+q^2+K^2+\vec{q}\cdot\vec{K}}=0 \tag{D.1}$$

We start by calculating the integral in the second term:

$$I_2=\sum_{q>k_F}\frac{1}{\lambda^2-k_F^2+K^2+q^2-\vec{q}.\vec{K}}=\frac{1}{4\pi^2}\int_{k_F}^{k_c}dq\frac{q}{K}\ln\left(\frac{K^2+q^2+qK+\lambda^2-k_F^2}{K^2+q^2-qK+\lambda^2-k_F^2}\right)$$

We perform a variable change $p=q/k_F$:

$$I_2=\frac{k_F}{8\pi^2A}\int_1^{k_c}dp\,p\ln\left(\frac{p^2+2Ap+B}{p^2-2Ap+B}\right)$$

With $A=\frac{K}{2k_F}$ and $B=\frac{K^2+\lambda^2}{k_F^2}-1$.

We integrate the last expression by parts putting: $u'=p$ and $v=\ln\left(\frac{p^2+2Ap+B}{p^2-2Ap+B}\right)$:

$$I_2=\frac{k_F}{8\pi^2A}\frac{k_c^2}{2}\ln\left(\frac{k_c^2+2Ak_c+B}{k_c^2-2Ak_c+B}\right)-\frac{k_F}{16\pi^2A}\ln\left(\frac{1+2A+B}{1-2A+B}\right)-\frac{k_F}{8\pi^2}I_3$$

where:

$$I_3=[-2p]_1^{k_c}+(A-\frac{B}{2A})\Big[\ln\left(\frac{p^2+2Ap+B}{p^2-2Ap+B}\right)\Big]_1^{k_c}$$
$$+2(B-A^2)\underbrace{\int_1^{k_c}dp\Big(\frac{1}{(p+A)^2+B-A^2}+\frac{1}{(p-A)^2+B-A^2}\Big)}_{I_4}$$

We calculate I_4 separately and we distinguish two cases:
1. $B - A^2 > 0$:

$$I_4 = \frac{1}{\sqrt{B-A^2}}\Big(\arctan(\frac{k_c+A}{\sqrt{B-A^2}}) + \arctan(\frac{k_c-A}{\sqrt{B-A^2}}) - \arctan(\frac{1+A}{\sqrt{B-A^2}}) - \arctan(\frac{1-A}{\sqrt{B-A^2}})\Big)$$

1. $B - A^2 < 0$:

$$I_4 = -\frac{1}{\sqrt{A^2-B}}\Big(\operatorname{arctanh}(\frac{k_c+A}{\sqrt{A^2-B}}) + \operatorname{arctanh}(\frac{k_c-A}{\sqrt{A^2-B}}) - \operatorname{arctanh}(\frac{1+A}{\sqrt{A^2-B}}) - \operatorname{arctanh}(\frac{1-A}{\sqrt{A^2-B}})\Big)$$

We inject the last expression in I_3 and then in I_2. The first term in I_2 gives a contribution of $2k_c + O(1/k_c)$, which adds to the first term in I_3 to give $4k_c$. The second term in I_3 when evaluated at k_c goes to zero and we get the following:
1. $B - A^2 > 0$:

$$\begin{aligned} I_2 = {} & \frac{k_F}{2\pi^2}k_c - \frac{k_F}{4\pi^2} + \frac{k_F}{8\pi^2}(A - \frac{B}{2A} - \frac{1}{2A})\ln\Big(\frac{1+2A+B}{1-2A+B}\Big) \\ & + \frac{k_F}{4\pi^2}\sqrt{B-A^2}(\arctan(\frac{1+A}{\sqrt{B-A^2}}) + \arctan(\frac{1-A}{\sqrt{B-A^2}}) - \pi) \end{aligned} \tag{D.2}$$

2. $B - A^2 < 0$:

$$\begin{aligned} I_2 = {} & \frac{k_F}{2\pi^2}k_c - \frac{k_F}{4\pi^2} + \frac{mk_F}{8\pi^2}(A - \frac{B}{2A} - \frac{1}{2A})\ln\Big(\frac{1+2A+B}{1-2A+B}\Big) \\ & + \frac{k_F}{8\pi^2}\sqrt{A^2-B}\ln\Big(\frac{1-B+2\sqrt{A^2-B}}{1-B-2\sqrt{A^2-B}}\Big) \end{aligned} \tag{D.3}$$

Remember for the terms linear in k_c that it should be scaled back to k_c/k_F before comparing it to k_c in E_0.

Final expressions

In case $B - A^2 > 0$

$$\begin{aligned} & K\beta_K\Bigg(R_e(3K^2/4+\lambda^2-k_F^2) + \frac{k_F}{\pi} - \frac{1}{\lambda a} + \sqrt{3K^2/4+\lambda^2-k_F^2}\Big[1 - \frac{1}{\pi}\Big(\arctan(\frac{k_F-K/2}{\sqrt{3K^2/4+\lambda^2-k_F^2}}) \\ & + \arctan(\frac{k_F+K/2}{\sqrt{3K^2/4+\lambda^2-k_F^2}})\Big)\Big] + \frac{K}{2\pi}(\frac{\lambda^2}{K^2}+\frac{1}{2})\ln\Big(\frac{K^2+\lambda^2+Kk_f}{K^2+\lambda^2-Kk_f}\Big) \\ & = \frac{1}{\pi}\int_{k_F}^{k_c} dK' \ln\Big(\frac{K'^2+K^2+K.K'+\lambda^2-k_F^2}{K'^2+K^2-K.K'+\lambda^2-k_F^2}\Big)K'\beta_{K'} \end{aligned} \tag{D.4}$$

We recall that in this equation both $|K|$ and $|K'|$ have to be larger than k_F. We first check that if $k_F = 0$ we regain the expression for 3 particles in vacuum, which is

indeed the case. We map the equation using $K = \frac{2\lambda}{\sqrt{3}}\sinh(\xi)$.
Then we try to write the equation in terms of variables which can help simplify the numerical solution, for that we divide by λ and we make the following variable changes: $x = R_e\lambda, y = k_F/\lambda$, writing equation Eq. (D.4) with the new variables :

$$\phi(\xi)\Bigg(x(\cosh^2(\xi)-y^2)+\frac{y}{\pi}-\frac{1}{\lambda a}+\sqrt{\cosh^2(\xi)-y^2}\Big[1-\frac{1}{\pi}\Big(\arctan\Big(\frac{y-\frac{1}{\sqrt{3}}\sinh(\xi)}{\sqrt{\cosh^2(\xi)-y^2}}\Big)$$
$$+\arctan\Big(\frac{y+\frac{1}{\sqrt{3}}\sinh(\xi)}{\sqrt{\cosh^2(\xi)-y^2}}\Big)\Big)\Big]+\frac{1}{4\sqrt{3}\pi}\frac{1+2\cosh^2(\xi)}{\sinh(\xi)}\ln\Big(\frac{4/3\sinh(\xi)^2+2/\sqrt{3}y\sinh(\xi)+1}{4/3\sinh(\xi)^2-2/\sqrt{3}y\sinh(\xi)+1}\Big)\Bigg)$$
$$=\frac{2}{\sqrt{3}\pi}\int_{\operatorname{arcsinh}(\sqrt{3}y/2)}^{k_c}d\xi'\cosh(\xi')\ln\Big(\frac{\sinh(\xi')^2+\sinh(\xi)^2+\sinh(\xi)\sinh(\xi')+3/4-3/4y^2}{\sinh(\xi')^2+\sinh(\xi)^2-\sinh(\xi)\sinh(\xi')+3/4-3/4y^2}\Big)\phi(\xi') \tag{D.5}$$

In case $B - A^2 < 0$

$$K\beta_K\Bigg(R_e(3K^2/4+\lambda^2-k_F^2)+\frac{k_F}{\pi}-\frac{1}{\lambda a}+\frac{K}{2\pi}(\frac{\lambda^2}{K^2}+\frac{1}{2})\ln\Big(\frac{K^2+\lambda^2+Kk_f}{K^2+\lambda^2-Kk_f}\Big)$$
$$-\frac{1}{2\pi}\sqrt{k_F^2-\lambda^2-3K^2/4}\ln\Big(\frac{2k_F^2-\lambda^2-K^2+2k_F\sqrt{k_F^2-\lambda^2-3K^2/4}}{2k_F^2-\lambda^2-K^2-2k_F\sqrt{k_F^2-\lambda^2-3K^2/4}}\Big)\Bigg) \tag{D.6}$$
$$=\frac{1}{\pi}\int_{k_F}^{k_c}dK'\ln\Big(\frac{K'^2+K^2+K.K'+\lambda^2-k_F^2}{K'^2+K^2-K.K'+\lambda^2-k_F^2}\Big)K'\beta_{K'}$$

We recall that in this equation both $|K|$ and $|K'|$ have to be larger than k_F. We first check that if $k_F = 0$ we regain the expression for 3 particles in vacuum, which is indeed the case. We map the equation using $K = \frac{2\lambda}{\sqrt{3}}\sinh(\xi)$.
Then we try to write the equation in terms of variables which can help simplify the numerical solution, for that we divide by λ and we make the following variable changes: $x = R_e\lambda, y = k_F/\lambda$, writing equation (D.6) with the new variables :

$$\phi(\xi)\Bigg(x(\cosh^2(\xi)-y^2)+\frac{y}{\pi}-\frac{1}{\lambda a}+\frac{1}{4\sqrt{3}\pi}\frac{1+2\cosh^2(\xi)}{\sinh(\xi)}\ln\Big(\frac{4/3\sinh^2(\xi)+2/\sqrt{3}y\sinh(\xi)+1}{4/3\sinh^2(\xi)-2/\sqrt{3}y\sinh(\xi)+1}\Big)$$
$$-\frac{1}{2\pi}\sqrt{y^2-\cosh^2(\xi)}\ln\Big(\frac{2y^2-1-4/3\sinh^2(\xi)+2y\sqrt{y^2-\cosh^2(\xi)}}{2y^2-1-4/3\sinh^2(\xi)-2y\sqrt{y^2-\cosh^2(\xi)}}\Big)\Bigg)$$
$$=\frac{2}{\sqrt{3}\pi}\int_{\operatorname{arcsinh}(\sqrt{3}y/2)}^{k_c}d\xi'\cosh(\xi')\ln\Big(\frac{\sinh(\xi')^2+\sinh(\xi)^2+\sinh(\xi)\sinh(\xi')+3/4-3/4y^2}{\sinh(\xi')^2+\sinh(\xi)^2-\sinh(\xi)\sinh(\xi')+3/4-3/4y^2}\Big)\phi(\xi') \tag{D.7}$$

Numerical implementation

We write a code to solve the last equation using the eigenvalues method. For that we need to write the equations in the following way:

$$\int_{\operatorname{arcsinh}(\sqrt{3}y/2)}^{\xi_c} d\xi' T(\xi,\xi')\phi(\xi') = \frac{1}{\lambda a}\phi(\xi) \tag{D.8}$$

With the kernel $T(\xi,\xi')$ which is written as:
1. In case $\cosh^2(\xi) - y^2 > 0$

$$\begin{aligned} T(\xi,\xi') = \delta(\xi-\xi')\Bigg[& x(\cosh^2(\xi')-y^2) + \frac{y}{\pi} + \sqrt{\cosh^2(\xi')-y^2} \\ & \Big[1 - \frac{1}{\pi}\Big(\arctan\Big(\frac{y-\frac{1}{\sqrt{3}}\sinh(\xi')}{\sqrt{\cosh^2(\xi')-y^2}}\Big) + \arctan\Big(\frac{y+\frac{1}{\sqrt{3}}\sinh(\xi')}{\sqrt{\cosh^2(\xi')-y^2}}\Big)\Big)\Big] \\ & + \frac{1}{4\sqrt{3}\pi}\frac{1+2\cosh^2(\xi')}{\sinh(\xi')}\ln\Big(\frac{4/3\sinh(\xi')^2 + 2/\sqrt{3}y\sinh(\xi') + 1}{4/3\sinh(\xi')^2 - 2/\sqrt{3}y\sinh(\xi') + 1}\Big)\Bigg] \\ & - \frac{2}{\sqrt{3}\pi}\ln\Big(\frac{\sinh(\xi')^2+\sinh(\xi)^2+\sinh(\xi)\sinh(\xi')+3/4-3/4y^2}{\sinh(\xi')^2+\sinh(\xi)^2-\sinh(\xi)\sinh(\xi')+3/4-3/4y^2}\Big)\Big)\cosh(\xi') \end{aligned} \tag{D.9}$$

In case $\cosh^2(\xi) - y^2 < 0$

$$\begin{aligned} T(\xi,\xi') = \delta(\xi-\xi')\Bigg[& x(\cosh^2(\xi')-y^2) + \frac{y}{\pi} \\ & + \frac{1}{4\sqrt{3}\pi}\frac{1+2\cosh^2(\xi')}{\sinh(\xi')}\ln\Big(\frac{4/3\sinh^2(\xi') + 2/\sqrt{3}y\sinh(\xi') + 1}{4/3\sinh^2(\xi') - 2/\sqrt{3}y\sinh(\xi') + 1}\Big) \\ & - \frac{1}{2\pi}\sqrt{y^2-\cosh^2(\xi')}\ln\Big(\frac{2y^2-1-4/3\sinh^2(\xi')+2y\sqrt{y^2-\cosh^2(\xi')}}{2y^2-1-4/3\sinh^2(\xi)-2y\sqrt{y^2-\cosh^2(\xi)}}\Big)\Bigg] \\ & - \frac{2}{\sqrt{3}\pi}\ln\Big(\frac{\sinh(\xi')^2+\sinh(\xi)^2+\sinh(\xi)\sinh(\xi')+3/4-3/4y^2}{\sinh(\xi')^2+\sinh(\xi)^2-\sinh(\xi)\sinh(\xi')+3/4-3/4y^2}\Big)\Big)\cosh(\xi') \end{aligned} \tag{D.10}$$

For the numerical implementation, we calculate $1/\lambda a$ for different values of $xy = k_F R_e$, since in a given experimental setup, the species has a given channel coupling (constant resonance width so R_e is constant) and k_F is constant a priori.

Numerical solution of the coupled equations

The energy spectrum of Eq. (5.16) can be obtained numerically. In the following we put $\hbar$ and m to unity for simplicity. We use the following parameters:

$$\begin{aligned} x = \lambda R_e, \quad & y = k_F/\lambda \\ k = \lambda\sinh(\xi), \quad & \phi(\xi) = \lambda\sinh(\xi)D(\lambda\sinh(\xi)) \end{aligned} \tag{D.11}$$

With this we can write Eq. (5.16) as follows:

$$\mathcal{M}(x, y, a)\tilde{\phi} = 0 \tag{D.12}$$

Where $\mathcal{M}$ is a non-symmetric square matrix. Its elements have the following form:

$$\begin{aligned}\mathcal{M}_i(\xi, \xi', x, y, a) &= \delta(\xi - \xi')\mathcal{M}_D(\xi, x, y, a) \\ &+ \epsilon \int_0^{2\pi} d\phi \int_0^{\pi} d\theta \sin(\theta) \cosh(\xi') \sinh^2(\xi')\mathcal{M}_N(\xi, \xi', x, y, a)\end{aligned} \tag{D.13}$$

Where ϵ is a discretization step we choose in order to have a convergent value of the unknown variable. We note that $\epsilon = \xi'_{max}/N_p$ where ξ' is the cutoff of the integral over ξ' and N_p is the number of points per row. Note also that $\xi, \xi' > \text{asinh}(y)$. We define the two functions $\mathcal{M}_D$ and $\mathcal{M}_N$ as follows:

$$\mathcal{M}_N(\xi, \xi', x, y, a) = \frac{1}{\lambda^2 I(\xi, \xi')} + \frac{2h(\xi)h(\xi')}{P_W} + g(\xi, \xi') \tag{D.14}$$

and

$$\begin{aligned}\mathcal{M}_D(\xi', x, y, a) = f(\xi) - \frac{\lambda}{4\pi}\Bigg\{\left(1 + \frac{3}{4}\sinh(\xi)^2 - \langle(\boldsymbol{q}_1 - \boldsymbol{q}_2)^2\rangle/(4\lambda^2)\right)\lambda R_e - \frac{1}{\lambda a} + \frac{2k_F}{\pi\lambda}\Bigg\} \\ - \frac{1}{\lambda^2\Omega}\sum_{\xi' > \text{asinh}(y)} \frac{1}{I(\xi, \xi')}\end{aligned} \tag{D.15}$$

Where:

$$I(\xi, \xi') = 1 + \langle \boldsymbol{q}_1 \cdot \boldsymbol{q}_2\rangle/\lambda^2 + \sinh^2(\xi) + \sinh^2(\xi') + \sinh(\xi)\sinh(\xi')\cos(\theta) \tag{D.16}$$

and g and h are functions defined in Eq. (5.17) , after the proper variable change.
If $f = g = 0$ the operators M and T are equal and the solution follows the reasoning in the previous section.
By fixing the value of $k_F R_e$ and for each value of $x = x_c$, we search the smallest value of $1/\lambda a$ which verifies the equation:

$$\det[\mathcal{M}(x_c, y_c, a)] = 0 \tag{D.17}$$

Note that the results in the Fig. (5.4) are obtained using a total number of points $N_p = 350$ and $\xi'_{max} = 10$.

Appendix E

Cooper-like trimer for different values of $k_F R_e$

The question of generalizing the previous calculation for the Cooper-like trimer to other values of $k_F R_e$ arises in order to see the limits of its stability with respect to the polaron.
To understand more this question we expand the STM equation (5.8) as in Appendix D and develop the resulting operator $T(\xi, \xi', y)$ with respect to $y = k_F R_e$:

First order correction

We write equation (D.8) in the following way:

$$\int_{g(y)}^{\infty} d\xi' T(\xi, \xi', y)\, \phi(\xi') = U(y)\, \phi(\xi) \tag{E.1}$$

The following expansions exist in case ($y \ll 1$), we choose to keep only linear terms in y:

$$\phi(\xi) = \phi_0(\xi) + y\phi_1(\xi) \quad , \quad U(y) = U_0 + yU_1 \tag{E.2}$$

Using (E.2) we can write (E.1) as:

$$\int_{g(y)}^{\infty} d\xi' T(\xi, \xi', y)\, \phi_0(\xi') + y \int_{g(y)}^{\infty} d\xi' T(\xi, \xi', y)\, \phi_1(\xi') = U_0\phi_0(\xi) + yU_0\, \phi_1(\xi) + yU_1\phi_0(\xi) \tag{E.3}$$

Symmetrization of $T(\xi, \xi', y)$

The operator $T(\xi, \xi', y)$ is not symmetric with respect to the variable change $\xi \to \xi'$ because of the $\cosh(\xi')$ term in the non-diagonal part. In order for the operator to be symmetric we do the following:

$$\int_{g(y)}^{\infty} d\xi' \underbrace{T(\xi, \xi', y) \frac{\sqrt{\cosh(\xi)}}{\sqrt{\cosh(\xi')}}}_{T_S(\xi, \xi', y)} \underbrace{\sqrt{\cosh(\xi')}\, \phi_0(\xi')}_{\tilde{\phi}(\xi')} = U(y)\, \underbrace{\sqrt{\cosh(\xi)}\phi(\xi)}_{\tilde{\phi}(\xi)} \tag{E.4}$$

Back to equation (E.3), we project it on $\tilde{\phi}_0(\xi)$, we find:

$$U_1 = \int_0^\infty d\xi \tilde{\phi}_0^*(\xi) \Big[\underbrace{\frac{\partial}{\partial y} \int_{g(y)}^\infty d\xi' T_S(\xi, \xi', y)\, \tilde{\phi}_0(\xi')}_{G(y)} \Big]_{y=0} \tag{E.5}$$

We can do the derivation using the Leibniz integral rule, we set:

$$G(y) = \int_{g(y)}^\infty d\xi' \frac{\partial}{\partial y} T_S(\xi, \xi', y)\, \tilde{\phi}_0(\xi') - T_S(\xi, g(y), y) g'(y) \tilde{\phi}_0(g(y)) \tag{E.6}$$

The partial derivative of the kernel with respect to y is linear in y so it cancels out when taking $y = 0$. With this we write, recalling that $g(y) = \operatorname{arcsinh}(\sqrt{3}y/2)$:

$$\begin{aligned} U_1 &= -\int_0^\infty d\xi \tilde{\phi}_0^*(\xi) T_S(\xi, g(0), 0) g'(0) \tilde{\phi}_0(g(0)) = -\frac{\sqrt{3}}{2} \int_0^\infty d\xi \tilde{\phi}_0^*(\xi) T_S(\xi, 0, 0) \tilde{\phi}_0(0) \\ &= -\frac{\sqrt{3}}{2} \int_0^\infty d\xi \tilde{\phi}_0^*(\xi) \delta(\xi)(1 + \lambda R_e) \tilde{\phi}_0(0) = -\frac{\sqrt{3}}{2}(1 + \lambda R_e) |\tilde{\phi}_0(0)|^2 \end{aligned} \tag{E.7}$$

Since $\tilde{\phi}_0(\xi)$ is an odd function, $\tilde{\phi}_0(0) = 0$ which gives $U_1 = 0$.

Second order correction

Abusing the notation we can write equation (E.1) after symmetrizing $\hat{T}$ and then develop all terms with respect to y:

$$\begin{aligned} &(\hat{T}_{S0} + y\hat{T}_{S1} + y^2 \hat{T}_{S2}/2)(|\tilde{\phi}_0\rangle + y|\tilde{\phi}_1\rangle + y^2/2|\tilde{\phi}_2\rangle) \\ &= (U_0 + yU_1 + y^2 U_2/2)(|\tilde{\phi}_0\rangle + y|\tilde{\phi}_1\rangle + y^2/2|\tilde{\phi}_2\rangle) \end{aligned} \tag{E.8}$$

We project the equation on $|\tilde{\phi}_0\rangle$ to get:

$$U_2 = \langle \tilde{\phi}_0 | \hat{T}_{S2} | \tilde{\phi}_0 \rangle \tag{E.9}$$

Where T_{S2} is the second order perturbation term of the symmetrized $\hat{T}$ operator. We can write equation (E.9) like :

$$U_2 = \int_0^\infty d\xi \tilde{\phi}_0^*(\xi) \Big[\underbrace{\frac{\partial^2}{\partial y^2} \int_{g(y)}^\infty d\xi' T_S(\xi, \xi', y)\, \tilde{\phi}_0(\xi')}_{H(y)} \Big]_{y=0} \tag{E.10}$$

We calculate $H(y)$ seperately and then put $y = 0$:

$$\begin{aligned} H(y) = &\int_{g(y)}^\infty \frac{\partial^2}{\partial y^2} T_S(\xi, \xi', y) \tilde{\phi}_0(\xi')\, d\xi' - \tilde{\phi}_0(g(y)) g'(y) \left(g'(y) \frac{\partial}{\partial y} T_S(\xi, g(y), y) + 2 \frac{\partial}{\partial y} T_S(\xi, g(y), y) \right) \\ &- T_S(\xi, g(y), y) \left(\tilde{\phi}_0(g(y)) g''(y) + g'(y)^2 \tilde{\phi}_0'(g(y)) \right) \end{aligned} \tag{E.11}$$

The next step after calculating $H(y)$ is to put $y = 0$ in (E.10), which leads to the second term cancelling since $\tilde{\phi}_0(0) = 0$, the same for the first part of the third term, but for

the last part of the third term, we have only a diagonal term in $T(\xi, 0, 0)$ which leads to $\tilde{\phi}^*(0) = 0$ with the integral in (E.10) which is also 0, after all of that we get:

$$H(y) = \int_{g(y)}^{\infty} d\xi' \frac{\partial^2}{\partial y^2} T_S(\xi, \xi', y)\, \tilde{\phi}_0(\xi') \tag{E.12}$$

We calculate the derivative and we put $y = 0$:

$$\begin{aligned} H(0) = &- \int_0^{\infty} d\xi' \frac{\sqrt{\cosh(\xi)}}{\sqrt{\cosh(\xi')}} \delta(\xi, \xi')\left(\frac{1}{\cosh(\xi)} + 2x\right) \\ &- \int_0^{\infty} d\xi' \frac{\sqrt{\cosh(\xi)}}{\sqrt{\cosh(\xi')}} \frac{16\sqrt{3}\sinh(\xi)\sinh(\xi')\cosh(\xi')}{\pi(2\cosh(2\xi)\cosh(2\xi') + \cosh(4\xi) + \cosh(4\xi') + 1/2)} \tilde{\phi}_0(\xi') \end{aligned} \tag{E.13}$$

Plugging this back in (E.10) and showing the explicit dependence on x we find:

$$U_2(x) = \int_0^{\infty} d\xi \tilde{\phi}_0^*(\xi) H(0) \tag{E.14}$$

The kernel (without the minus sign) is an all positive matrix leading to a positive eigenvalue, and that leaves the integration of the norm of $\tilde{\phi}_0$ which is also positive. We conclude from this quick analysis that $U_2(x)$ is an all negative function.
We can contrast this result to a fit function of the following type:

$$\frac{R_e}{\lambda a} = \frac{R_e \lambda}{\lambda_0 a} + \frac{U_2}{2\lambda R_e} k_F^2 R^{*2} \tag{E.15}$$

with U_2 as the fit parameter for different values of $x = R_e\lambda$. The results are shown in Fig.(E.1).

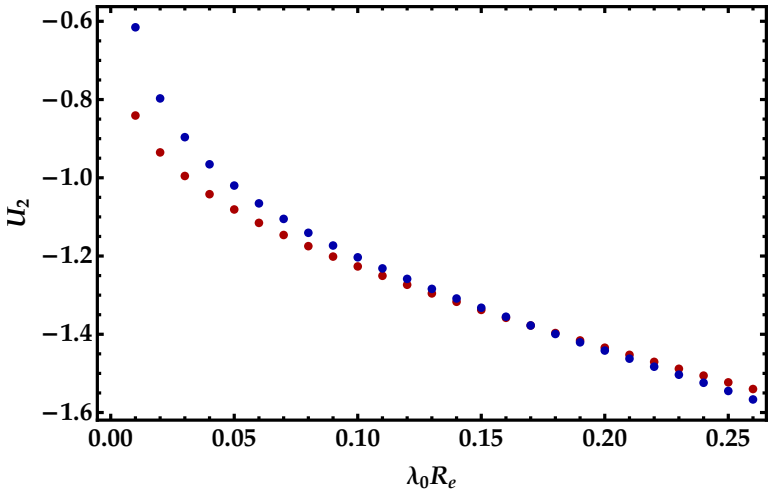

Figure E.1: Second order perturbation correction of the Cooper-like trimer energy with respect to $y = k_F R_e$. In red, data points from curves calculated using Eq. (5.8) for different values of y and fitted with a parabola of the form in Eq. (E.15) to extract U_2. In blue, actual U_2 points calculated from Eq. (E.14).

We see a pretty good match. The discrepancy in small $\lambda_0 R_e$ values is due to the high sensitivity of the data on the precision in this region since we approach lower values of $\delta\xi'$ (here it is 0.02).

Bibliography

[1] W Pauli. Über den Zusammenhang des Abschlusses der Elektronengruppen im Atom mit der Komplexstruktur der Spektren. *Zeitschrift für Physik*, 31(1):765–783, 1925.

[2] Freeman J Dyson. Ground-State Energy of a Finite System of Charged Particles. *Journal of Mathematical Physics*, 8(8):1538–1545, aug 1967.

[3] Freeman J Dyson and A Lenard. Stability of Matter. I. *Journal of Mathematical Physics*, 8(3):423–434, mar 1967.

[4] Heike Kamerlingh Onnes. Investigations into the properties of substances at low temperatures, which have led, amongst other things, to the preparation of liquid helium. *Nobel Lecture*, pages 306–336, 1913.

[5] P Kapitza. Viscosity of Liquid Helium below the λ-Point. *Nature*, 141(3558):74, 1938.

[6] J F Allen and A D Misener. Flow of Liquid Helium II. *Nature*, 141(3558):75, 1938.

[7] D D Osheroff, R C Richardson, and D M Lee. Evidence for a New Phase of Solid He 3. *Phys. Rev. Lett.*, 28(14):885–888, apr 1972.

[8] K v. Klitzing, G Dorda, and M Pepper. New Method for High-Accuracy Determination of the Fine-Structure Constant Based on Quantized Hall Resistance. *Phys. Rev. Lett.*, 45(6):494–497, aug 1980.

[9] I Bloch, J Dalibard, and W Zwerger. Many-body physics with ultracold gases. *Rev. Mod. Phys.*, 80(3):885–964, 2008.

[10] Richard P Feynman. Simulating physics with computers. *International Journal of Theoretical Physics*, 21(6):467–488, 1982.

[11] T W Hänsch and A L Schawlow. Cooling of gases by laser radiation. *Optics Communications*, 13(1):68–69, 1975.

[12] D J Wineland, R E Drullinger, and F L Walls. Radiation-Pressure Cooling of Bound Resonant Absorbers. *Phys. Rev. Lett.*, 40(25):1639–1642, jun 1978.

[13] W Neuhauser, M Hohenstatt, P Toschek, and H Dehmelt. Optical-Sideband Cooling of Visible Atom Cloud Confined in Parabolic Well. *Phys. Rev. Lett.*, 41(4):233–236, jul 1978.

[14] Steven Chu, L Hollberg, J E Bjorkholm, Alex Cable, and A Ashkin. Three-dimensional viscous confinement and cooling of atoms by resonance radiation pressure. *Phys. Rev. Lett.*, 55(1):48–51, jul 1985.

[15] E. L. Raab, M. Prentiss, Alex Cable, Steven Chu, and D. E. Pritchard. Trapping of Neutral Sodium Atoms with Radiation Pressure. *Physical Review Letters*, 59(23):2631–2634, 1987.

[16] Paul D. Lett, Richard N. Watts, Christoph I. Westbrook, William D. Phillips, Phillip L. Gould, and Harold J. Metcalf. Observation of atoms laser cooled below the doppler limit. *Physical Review Letters*, 61(2):169–172, 1988.

[17] J. Dalibard and C. Cohen-Tannoudji. Laser cooling below the Doppler limit by polarization gradients: simple theoretical models. *Journal of the Optical Society of America B*, 6(11):2023, 1989.

[18] A. Aspect, E. Arimondo, R. Kaiser, N. Vansteenkiste, and C. Cohen-Tannoudji. Laser cooling below the one-photon recoil energy by velocity-selective coherent population trapping. *Phys. Rev. Lett.*, 61(7):826–829, 1988.

[19] F Diedrich, J C Bergquist, Wayne M Itano, and D J Wineland. Laser Cooling to the Zero-Point Energy of Motion. *Phys. Rev. Lett.*, 62(4):403–406, jan 1989.

[20] Alan L Migdall, John V Prodan, William D Phillips, Thomas H Bergeman, and Harold J Metcalf. First Observation of Magnetically Trapped Neutral Atoms. *Phys. Rev. Lett.*, 54(24):2596–2599, jun 1985.

[21] Wolfgang Petrich, Michael H Anderson, Jason R Ensher, and Eric A Cornell. Stable, Tightly Confining Magnetic Trap for Evaporative Cooling of Neutral Atoms. *Phys. Rev. Lett.*, 74(17):3352–3355, apr 1995.

[22] Kendall B Davis, Marc-Oliver Mewes, Michael A Joffe, Michael R Andrews, and Wolfgang Ketterle. Evaporative Cooling of Sodium Atoms. *Phys. Rev. Lett.*, 74(26):5202–5205, jun 1995.

[23] M H Anderson, J R Ensher, M R Matthews, C E Wieman, and E A Cornell. Observation of Bose-Einstein Condensation in a Dilute Atomic Vapor. *Science*, 269(5221):198–201, 1995.

[24] C C Bradley, C A Sackett, J J Tollett, and R G Hulet. Evidence of Bose-Einstein Condensation in an Atomic Gas with Attractive Interactions. *Phys. Rev. Lett.*, 75(9):1687–1690, aug 1995.

[25] K B Davis, M O. Mewes, M R Andrews, N J van Druten, D S Durfee, D M Kurn, and W Ketterle. Bose-Einstein Condensation in a Gas of Sodium Atoms. *Phys. Rev. Lett.*, 75(22):3969–3973, nov 1995.

[26] Steven Chu, J E Bjorkholm, A Ashkin, and A Cable. Experimental Observation of Optically Trapped Atoms. *Phys. Rev. Lett.*, 57(3):314–317, jul 1986.

[27] Charles S Adams, Heun Jin Lee, Nir Davidson, Mark Kasevich, and Steven Chu. Evaporative Cooling in a Crossed Dipole Trap. *Phys. Rev. Lett.*, 74(18):3577–3580, may 1995.

[28] M R Andrews, C G Townsend, H.J. Miesner, D S Durfee, D M Kurn, and W Ketterle. Observation of Interference Between Two Bose Condensates. *Science*, 275(5300):637 LP – 641, jan 1997.

[29] Immanuel Bloch, Theodor W Hansch, and Tilman Esslinger. Atom Laser with a cw Output Coupler. *Phys. Rev. Lett.*, 82(15):3008–3011, apr 1999.

[30] M.-O. Mewes, M R Andrews, D M Kurn, D S Durfee, C G Townsend, and W Ketterle. Output Coupler for Bose-Einstein Condensed Atoms. *Phys. Rev. Lett.*, 78(4):582–585, jan 1997.

[31] E W Hagley, L Deng, M Kozuma, J Wen, K Helmerson, S L Rolston, and W D Phillips. A Well-Collimated Quasi-Continuous Atom Laser. *Science*, 283(5408):1706 LP – 1709, mar 1999.

[32] D S Jin, J R Ensher, M R Matthews, C E Wieman, and E A Cornell. Collective Excitations of a Bose-Einstein Condensate in a Dilute Gas. *Phys. Rev. Lett.*, 77(3):420–423, jul 1996.

[33] M R Andrews, D M Kurn, H.J. Miesner, D S Durfee, C G Townsend, S Inouye, and W Ketterle. Propagation of Sound in a Bose-Einstein Condensate. *Phys. Rev. Lett.*, 79(4):553–556, jul 1997.

[34] M.-O. Mewes, M R Andrews, N J van Druten, D M Kurn, D S Durfee, C G Townsend, and W Ketterle. Collective Excitations of a Bose-Einstein Condensate in a Magnetic Trap. *Phys. Rev. Lett.*, 77(6):988–991, aug 1996.

[35] D M Stamper-Kurn, A P Chikkatur, A Gorlitz, S Inouye, S Gupta, D E Pritchard, and W Ketterle. Excitation of Phonons in a Bose-Einstein Condensate by Light Scattering. *Phys. Rev. Lett.*, 83(15):2876–2879, oct 1999.

[36] Michael Robin Matthews, Brian P Anderson, P C Haljan, D S Hall, C E Wieman, and E A Cornell. Vortices in a Bose-Einstein condensate. *Physical Review Letters*, 83(13):2498, 1999.

[37] K W Madison, F Chevy, W Wohlleben, and J Dalibard. Vortex formation in a stirred Bose-Einstein condensate. *Physical Review Letters*, 84(5):806, 2000.

[38] J R Abo-Shaeer, C Raman, J M Vogels, and Wolfgang Ketterle. Observation of vortex lattices in Bose-Einstein condensates. *Science*, 292(5516):476–479, 2001.

[39] Stefan Burger, K Bongs, S Dettmer, W Ertmer, K Sengstock, A Sanpera, G V Shlyapnikov, and M Lewenstein. Dark solitons in Bose-Einstein condensates. *Physical Review Letters*, 83(25):5198, 1999.

[40] J Denschlag, J E Simsarian, D L Feder, Charles W Clark, L A Collins, J Cubizolles, L Deng, E W Hagley, K Helmerson, William P Reinhardt, and Others.

Generating solitons by phase engineering of a Bose-Einstein condensate. *Science*, 287(5450):97–101, 2000.

[41] Herman Feshbach. Unified theory of nuclear reactions. *Annals of Physics*, 5(4):357–390, 1958.

[42] Cheng Chin, Rudolf Grimm, Paul Julienne, and Eite Tiesinga. Feshbach resonances in ultracold gases. *Reviews of Modern Physics*, 82(2):1225, 2010.

[43] S Inouye, M R Andrews, J Stenger, H-J Miesner, D M Stamper-Kurn, and W Ketterle. Observation of Feshbach resonances in a Bose–Einstein condensate. *Nature*, 392(6672):151–154, 1998.

[44] Ph Courteille, R S Freeland, D J Heinzen, F A Van Abeelen, and B J Verhaar. Observation of a Feshbach resonance in cold atom scattering. *Physical Review Letters*, 81(1):69, 1998.

[45] B S Rem, A T Grier, I Ferrier-Barbut, U Eismann, T Langen, N Navon, L Khaykovich, F Werner, D S Petrov, F Chevy, and Others. Lifetime of the Bose gas with resonant interactions. *Physical review letters*, 110(16):163202, 2013.

[46] Richard J Fletcher, Alexander L Gaunt, Nir Navon, Robert P Smith, and Zoran Hadzibabic. Stability of a unitary Bose gas. *Physical review letters*, 111(12):125303, 2013.

[47] Philip Makotyn, Catherine E Klauss, David L Goldberger, E A Cornell, and Deborah S Jin. Universal dynamics of a degenerate unitary Bose gas. *Nature Physics*, 10(2):116–119, 2014.

[48] Ulrich Eismann, Lev Khaykovich, Sébastien Laurent, Igor Ferrier-Barbut, Benno S Rem, Andrew T Grier, Marion Delehaye, Frédéric Chevy, Christophe Salomon, Li-Chung Ha, and Cheng Chin. Universal Loss Dynamics in a Unitary Bose Gas. *Phys. Rev. X*, 6(2):21025, may 2016.

[49] R Chang, Q Bouton, H Cayla, C Qu, A Aspect, C.I. Westbrook, and Clément D. Momentum-resolved observation of quantum depletion in an interacting Bose gas. *arXiv preprint arXiv:1608.04693*, 2016.

[50] S Basu and E J Mueller. Final-state effects in the radio frequency spectrum of strongly interacting fermions. *Phys. Rev. Lett.*, 101(6):60405, 2008.

[51] Fei Zhou and Mohammad S Mashayekhi. Bose gases near resonance: Renormalized interactions in a condensate. *Annals of Physics*, 328:83–102, 2013.

[52] Shao-Jian Jiang, Wu-Ming Liu, Gordon W Semenoff, and Fei Zhou. Universal Bose gases near resonance: A rigorous solution. *Physical Review A*, 89(3):33614, 2014.

[53] A G Sykes, J P Corson, J P D'Incao, A P Koller, C H Greene, A M Rey, K R A Hazzard, and J L Bohn. Quenching to unitarity: Quantum dynamics in a three-dimensional Bose gas. *Physical Review A*, 89(2):21601, 2014.

[54] Swann Piatecki and Werner Krauth. Efimov-driven phase transitions of the unitary Bose gas. *Nature communications*, 5, 2014.

[55] Elliott Lieb and Daniel Mattis. Theory of Ferromagnetism and the Ordering of Electronic Energy Levels. *Phys. Rev.*, 125(1):164–172, jan 1962.

[56] B DeMarco and D S Jin. Onset of Fermi degeneracy in a trapped atomic gas. *Science*, 285(5434):1703, 1999.

[57] A G Truscott, K E Strecker, W I McAlexander, G B Partridge, and R G Hulet. Observation of Fermi pressure in a gas of trapped atoms. *Science*, 291(5513):2570–2572, 2001.

[58] F Schreck, L Khaykovich, K L Corwin, G Ferrari, T Bourdel, J Cubizolles, and C Salomon. Quasipure Bose-Einstein Condensate Immersed in a Fermi Sea. *Phys. Rev. Lett.*, 87(8):80403, aug 2001.

[59] G Roati, F Riboli, G Modugno, and M Inguscio. Fermi-Bose Quantum Degenerate 40K-87Rb Mixture with Attractive Interaction. *Phys. Rev. Lett.*, 89(15):150403, sep 2002.

[60] Z Hadzibabic, C A Stan, K Dieckmann, S Gupta, M W Zwierlein, A Görlitz, and W Ketterle. Two-Species Mixture of Quantum Degenerate Bose and Fermi Gases. *Phys. Rev. Lett.*, 88(16):160401, apr 2002.

[61] S R Granade, M E Gehm, K M O'Hara, and J E Thomas. All-Optical Production of a Degenerate Fermi Gas. *Phys. Rev. Lett.*, 88(12):120405, mar 2002.

[62] D S Petrov, C Salomon, and G V Shlyapnikov. Weakly bound dimers of fermionic atoms. *Phys. Rev. Lett.*, 93(9):90404, 2004.

[63] S Giorgini, L P Pitaevskii, and S Stringari. Theory of ultracold atomic Fermi gases. *Rev. Mod. Phys.*, 80(4):1215–1274, 2008.

[64] K.M. O'Hara, S.L. Hemmer, M.E. Gehm, S.R. Granade, and J.E. Thomas. Observation of a strongly interacting degenerate Fermi gas of atoms. *Science*, 298(5601):2179, 2002.

[65] T Bourdel, J Cubizolles, L Khaykovich, K M F Magalhães, S J J M F Kokkelmans, G V Shlyapnikov, and C Salomon. Measurement of the Interaction Energy near a Feshbach Resonance in a 6Li Fermi Gas. *Phys. Rev. Lett.*, 91(2):20402, jul 2003.

[66] M Greiner, C A Regal, and D S Jin. Emergence of a molecular Bose-Einstein condensate from a Fermi gas. *Nature*, 426(6966):537–540, 2003.

[67] S Jochim, M Bartenstein, A Altmeyer, G Hendl, S Riedl, C Chin, J Hecker Denschlag, and R Grimm. Bose-Einstein condensation of molecules. *Science*, 302(5653):2101, 2003.

[68] M W Zwierlein, C A Stan, C H Schunck, S M F Raupach, S Gupta, Z Hadzibabic, and W Ketterle. Observation of Bose-Einstein Condensation of Molecules. *Phys. Rev. Lett.*, 91(25):250401, dec 2003.

[69] Regal C.A., M Greiner, and D.S. Jin. Observation of resonance condensation of fermionic atom pairs. *Phys. Rev. Lett.*, 92:40403, 2004.

[70] C Chin, M Bartenstein, A Altmeyer, S Riedl, S Jochim, J Hecker Denschlag, and R Grimm. Observation of the pairing gap in a strongly interacting Fermi gas. *Science*, 305(5687):1128, 2004.

[71] M W Zwierlein, J R Abo-Shaeer, A Schirotzek, C H Schunck, and W Ketterle. Vortices and superfluidity in a strongly interacting Fermi gas. *Nature*, 435(7045):1047–1051, 2005.

[72] B J DeSalvo, M Yan, P G Mickelson, Y N de Escobar, and T C Killian. Degenerate Fermi Gas of 87Sr. *Phys. Rev. Lett.*, 105(3):30402, jul 2010.

[73] Meng Khoon Tey, Simon Stellmer, Rudolf Grimm, and Florian Schreck. Double-degenerate Bose-Fermi mixture of strontium. *Phys. Rev. A*, 82(1):11608, jul 2010.

[74] Mingwu Lu, Nathaniel Q Burdick, and Benjamin L Lev. Quantum Degenerate Dipolar Fermi Gas. *Phys. Rev. Lett.*, 108(21):215301, may 2012.

[75] T Fukuhara, Y Takasu, S Sugawa, and Y Takahashi. Quantum Degenerate Fermi Gases of Ytterbium Atoms. *Journal of Low Temperature Physics*, 148(3):441–445, 2007.

[76] Shintaro Taie, Yosuke Takasu, Seiji Sugawa, Rekishu Yamazaki, Takuya Tsujimoto, Ryo Murakami, and Yoshiro Takahashi. Realization of a SU(2)XSU(6) System of Fermions in a Cold Atomic Gas. *Phys. Rev. Lett.*, 105(19):190401, nov 2010.

[77] J Hubbard and Brian Hilton Flowers. Electron correlations in narrow energy bands. *Proceedings of the Royal Society of London. Series A. Mathematical and Physical Sciences*, 276(1365):238–257, nov 1963.

[78] D. Jaksch, C. Bruder, J. I. Cirac, C. W. Gardiner, and P. Zoller. Cold bosonic atoms in optical lattices. *Phys. Rev. Lett.*, 81:3108–3111, Oct 1998.

[79] W. Vincent Liu, Frank Wilczek, and Peter Zoller. Spin-dependent hubbard model and a quantum phase transition in cold atoms. *Phys. Rev. A*, 70:033603, Sep 2004.

[80] Tilman Esslinger. Fermi-Hubbard Physics with Atoms in an Optical Lattice. *Annual Review of Condensed Matter Physics*, 1(1):129–152, jul 2010.

[81] Lawrence W Cheuk, Matthew A Nichols, Melih Okan, Thomas Gersdorf, Vinay V Ramasesh, Waseem S Bakr, Thomas Lompe, and Martin W Zwierlein. Quantum-Gas Microscope for Fermionic Atoms. *Phys. Rev. Lett.*, 114(19):193001, may 2015.

[82] Elmar Haller, James Hudson, Andrew Kelly, Dylan A Cotta, Bruno Peaudecerf, Graham D Bruce, and Stefan Kuhr. Single-atom imaging of fermions in a quantum-gas microscope. *Nature Physics*, 11(9):738–742, 2015.

[83] Maxwell F Parsons, Florian Huber, Anton Mazurenko, Christie S Chiu, Widagdo Setiawan, Katherine Wooley-Brown, Sebastian Blatt, and Markus Greiner. Site-Resolved Imaging of Fermionic 6Li in an Optical Lattice. *Phys. Rev. Lett.*, 114(21):213002, may 2015.

[84] Ahmed Omran, Martin Boll, Timon A Hilker, Katharina Kleinlein, Guillaume Salomon, Immanuel Bloch, and Christian Gross. Microscopic Observation of Pauli Blocking in Degenerate Fermionic Lattice Gases. *Phys. Rev. Lett.*, 115(26):263001, dec 2015.

[85] Peter T Brown, Debayan Mitra, Elmer Guardado-Sanchez, Peter Schauß, Stanimir S Kondov, Ehsan Khatami, Thereza Paiva, Nandini Trivedi, David A Huse, and Waseem S Bakr. Spin-imbalance in a 2D Fermi-Hubbard system. *Science (New York, N.Y.)*, 357(6358):1385–1388, sep 2017.

[86] Eugenio Cocchi, Luke A Miller, Jan H Drewes, Marco Koschorreck, Daniel Pertot, Ferdinand Brennecke, and Michael Köhl. Equation of State of the Two-Dimensional Hubbard Model. *Phys. Rev. Lett.*, 116(17):175301, apr 2016.

[87] Christian Hofrichter, Luis Riegger, Francesco Scazza, Moritz Höfer, Diogo Rio Fernandes, Immanuel Bloch, and Simon Fölling. Direct Probing of the Mott Crossover in the SU(N) Fermi-Hubbard Model. *Phys. Rev. X*, 6(2):21030, jun 2016.

[88] Lawrence W Cheuk, Matthew A Nichols, Katherine R Lawrence, Melih Okan, Hao Zhang, Ehsan Khatami, Nandini Trivedi, Thereza Paiva, Marcos Rigol, and Martin W Zwierlein. Observation of spatial charge and spin correlations in the 2D Fermi-Hubbard model. *Science*, 353(6305):1260–1264, 2016.

[89] Martin Boll, Timon A Hilker, Guillaume Salomon, Ahmed Omran, Jacopo Nespolo, Lode Pollet, Immanuel Bloch, and Christian Gross. Spin- and density-resolved microscopy of antiferromagnetic correlations in Fermi-Hubbard chains. *Science*, 353(6305):1257 LP – 1260, sep 2016.

[90] Maxwell F Parsons, Anton Mazurenko, Christie S Chiu, Geoffrey Ji, Daniel Greif, and Markus Greiner. Site-resolved measurement of the spin-correlation function in the Fermi-Hubbard model. *Science (New York, N.Y.)*, 353(6305):1253–1256, sep 2016.

[91] Matthew A Nichols, Lawrence W Cheuk, Melih Okan, Thomas R Hartke, Enrique Mendez, T Senthil, Ehsan Khatami, Hao Zhang, and Martin W Zwierlein. Spin transport in a Mott insulator of ultracold fermions. *Science*, 363(6425):383 LP – 387, jan 2019.

[92] Alexander L Gaunt, Tobias F Schmidutz, Igor Gotlibovych, Robert P Smith, and Zoran Hadzibabic. Bose-Einstein condensation of atoms in a uniform potential. *Phys. Rev. Lett.*, 110(20):200406, 2013.

[93] Biswaroop Mukherjee, Zhenjie Yan, Parth B Patel, Zoran Hadzibabic, Tarik Yefsah, Julian Struck, and Martin W Zwierlein. Homogeneous atomic Fermi gases. *Physical review letters*, 118(12):123401, 2017.

[94] P Fulde and R A Ferrell. Superconductivity in a strong spin-exchange field. *Phys. Rev*, 135:A550, 1964.

[95] A I Larkin and Y N Ovchinnikov. Nonuniform state of superconductors. *Zh. Eksp. Teor. Fiz*, 47:1136, 1964.

[96] L D Landau. Über Die Bewegung der Elektronen in Kristallgitter. *Phys. Z. Sowjetunion*, 3:644–645, 1933.

[97] L D Landau and S I Pekar. Effective mass of a polaron. *Zh. Eksp. Teor. Fiz*, 18(5):419–423, 1948.

[98] H Frohlich. Electrons in lattice fields. *Advances in Physics*, 3(11):325–361, 1954.

[99] Jun Kondo. Resistance minimum in dilute magnetic alloys. *Progress of theoretical physics*, 32(1):37–49, 1964.

[100] W J de Haas, J de Boer, and G J van dën Berg. The electrical resistance of gold, copper and lead at low temperatures. *Physica*, 1:1115–1124, may 1934.

[101] Kenneth G Wilson. The renormalization group: Critical phenomena and the Kondo problem. *Rev. Mod. Phys.*, 47(4):773–840, oct 1975.

[102] Philip Warren Anderson. Localized magnetic states in metals. *Physical Review*, 124(1):41, 1961.

[103] P. W. Anderson. Infrared catastrophe in fermi gases with local scattering potentials. *Physical Review Letters*, 18(24):1049–1051, 1967.

[104] Marko Cetina, Michael Jag, Rianne S Lous, Jook T M Walraven, Rudolf Grimm, Rasmus S Christensen, and Georg M Bruun. Decoherence of Impurities in a Fermi Sea of Ultracold Atoms. *Phys. Rev. Lett.*, 115(13):135302, sep 2015.

[105] Marko Cetina, Michael Jag, Rianne S Lous, Isabella Fritsche, Jook T M Walraven, Rudolf Grimm, Jesper Levinsen, Meera M Parish, Richard Schmidt, Michael Knap, and Eugene Demler. Ultrafast many-body interferometry of impurities coupled to a Fermi sea. *Science*, 354(6308):96 LP – 99, oct 2016.

[106] Marek Kutschera and Wlodzimierz Wojcik. Proton impurity in the neutron matter: A nuclear polaron problem. *Phys. Rev. C*, 47(3):1077–1085, mar 1993.

[107] W Zuo, Z H Li, G C Lu, J Q Li, W Scheid, U Lombardo, H-J Schulze, and C W Shen. 1S0 proton and neutron superfluidity in Beta-stable neutron star matter. *Physics Letters B*, 595(1-4):44–49, 2004.

[108] Kenji Fukushima and Vladimir Skokov. Polyakov loop modeling for hot QCD. *Progress in Particle and Nuclear Physics*, 96:154–199, 2017.

[109] Sebastien Laurent, Matthieu Pierce, Marion Delehaye, Tarik Yefsah, Frédéric Chevy, and Christophe Salomon. Connecting Few-Body Inelastic Decay to Quantum Correlations in a Many-Body System: A Weakly Coupled Impurity in a Resonant Fermi Gas. *Phys. Rev. Lett.*, 118(10):103403, mar 2017.

[110] A N Wenz, G Zurn, S Murmann, I Brouzos, T Lompe, and S Jochim. From Few to Many: Observing the Formation of a Fermi Sea One Atom at a Time. *Science*, 342(6157):457 LP – 460, oct 2013.

[111] I Ferrier-Barbut, M Delehaye, S Laurent, A T Grier, M Pierce, B S Rem, F Chevy, and C Salomon. A mixture of Bose and Fermi superfluids. *Science*, 345:1035–1038, 2014.

[112] Marion Delehaye, Sébastien Laurent, Igor Ferrier-Barbut, Shuwei Jin, Frédéric Chevy, and Christophe Salomon. Critical Velocity and Dissipation of an ultracold Bose-Fermi Counterflow. *Phys. Rev. Lett.*, 115(26):265303, 2015.

[113] Mingyuan Sun and Xiaoling Cui. Efimov physics in the presence of a Fermi sea. *Physical Review A*, 99(6):1–6, 2019.

[114] Wei Yi and Xiaoling Cui. Polarons in ultracold Fermi superfluids. *Phys. Rev. A*, 92(1):13620, 2015.

[115] Yusuke Nishida. New type of crossover physics in three-component Fermi gases. *Physical Review Letters*, 109(24):240401, 2012.

[116] Y Nishida and S Tan. Universal Fermi gases in mixed dimensions. *Phys. Rev. Lett.*, 101(17):170401, 2008.

[117] M Pierce, X Leyronas, and F Chevy. Few Versus Many-Body Physics of an Impurity Immersed in a Superfluid of Spin 1/2 Attractive Fermions. *Phys. Rev. Lett.*, 123(8):80403, aug 2019.

[118] R Alhyder, X Leyronas, and F Chevy. Impurity immersed in a double Fermi sea. *Phys. Rev. A*, 102(3):33322, sep 2020.

[119] Louis de Broglie. A tentative theory of light quanta. *The London, Edinburgh, and Dublin Philosophical Magazine and Journal of Science*, 47(278):446–458, 1924.

[120] J J Sakurai and J Napolitano. *Modern Quantum Mechanics*. Addison-Wesley, 2011.

[121] Peter Schwerdtfeger. The Pseudopotential Approximation in Electronic Structure Theory. *ChemPhysChem*, 12(17):3143–3155, 2011.

[122] U Fano. Effects of Configuration Interaction on Intensities and Phase Shifts. *Phys. Rev.*, 124(6):1866–1878, dec 1961.

[123] J. C. Lehmann. *Laser Spectroscopy and Predissociation of Molecules*.

[124] A J Moerdijk, B J Verhaar, and A Axelsson. Resonances in ultracold collisions of 6Li, 7Li, and 23Na. *Phys. Rev. A*, 51(6):4852–4861, jun 1995.

[125] M Bartenstein, A Altmeyer, S Riedl, R Geursen, S Jochim, C Chin, J Hecker Denschlag, R Grimm, A Simoni, E Tiesinga, C J Williams, and P S Julienne. Precise Determination of 6Li Cold Collision Parameters by Radio-Frequency Spectroscopy on Weakly Bound Molecules. *Phys. Rev. Lett.*, 94(10):103201, mar 2005.

[126] Michael E. Gehm. *Properties of Lithium 6*, 2003.

[127] Eddy Timmermans, Paolo Tommasini, Mahir Hussein, and Arthur Kerman. Feshbach resonances in atomic Bose–Einstein condensates. *Physics Reports*, 315(1):199–230, 1999.

[128] W Ketterle and M Zwierlein. *Making, probing and understanding ultra-cold Fermi gases in Proceedings of the International School of Physics, Enrico Fermi, Course CLXIV, Varenna*. Società Italiana di Fisica, 2008.

[129] L H Thomas. The Interaction Between a Neutron and a Proton and the Structure of H3. *Phys. Rev.*, 47(12):903–909, jun 1935.

[130] Yusuke Nishida. Polaronic atom-trimer continuity in three-component Fermi gases. *Physical Review Letters*, 114(11):115302, 2015.

[131] Alexander O Gogolin, Christophe Mora, and Reinhold Egger. Analytical solution of the bosonic three-body problem. *Physical Review Letters*, 100(14):140404, 2008.

[132] Vitaly Efimov. Energy levels arising from resonant two-body forces in a three-body system. *Physics Letters B*, 33(8):563–564, 1970.

[133] Pascal Naidon and Shimpei Endo. Efimov physics: a Review. *Reports on Progress in Physics*, 80(5):56001, 2017.

[134] G V Skorniakov and K A Ter-Martirosian. Three body problem for short range forces. I. Scattering of low energy neutrons by deuterons. *Sov. Phys. JETP*, 4, 1957.

[135] G S Danilov. On the three-body problem with short-range forces. *Sov. Phys. JETP*, 13(349):3, 1961.

[136] Christian Langmack, Richard Schmidt, and Wilhelm Zwerger. Efimov states near a Feshbach resonance and the limits of van der Waals universality at finite background scattering length. *Phys. Rev. A*, 97(3):33623, mar 2018.

[137] D S Petrov. Three-Boson Problem near a Narrow Feshbach Resonance. *Phys. Rev. Lett.*, 93(14):143201, sep 2004.

[138] T Kraemer, M Mark, P Waldburger, J G Danzl, C Chin, B Engeser, A D Lange, K Pilch, A Jaakkola, H C Nägerl, and Others. Evidence for Efimov quantum states in an ultracold gas of caesium atoms. *Nature*, 440(7082):315–318, 2006.

[139] F Ferlaino, A Zenesini, M Berninger, B Huang, H-C Nagerl, and R Grimm. Efimov resonances in ultracold quantum gases. *Few-Body Systems*, 51(2-4):113–133, 2011.

[140] Noam Gross, Zav Shotan, Servaas Kokkelmans, and Lev Khaykovich. Observation of Universality in Ultracold Li 7 Three-Body Recombination. *Physical review letters*, 103(16):163202, 2009.

[141] Scott E Pollack, Daniel Dries, and Randall G Hulet. Universality in three-and four-body bound states of ultracold atoms. *Science*, 326(5960):1683–1685, 2009.

[142] Matteo Zaccanti, Benjamin Deissler, Chiara D Errico, Marco Fattori, Mattia Jona-Lasinio, Stefan Müller, Giacomo Roati, Massimo Inguscio, and Giovanni Modugno. Observation of an Efimov spectrum in an atomic system. *Nature Physics*, 5(8):586–591, 2009.

[143] Thomas Lompe, Timo B Ottenstein, Friedhelm Serwane, Andre N Wenz, Gerhard Zurn, and Selim Jochim. Radio-Frequency Association of Efimov Trimers. *Science*, 330(6006):940 LP – 944, nov 2010.

[144] Shuta Nakajima, Munekazu Horikoshi, Takashi Mukaiyama, Pascal Naidon, and Masahito Ueda. Measurement of an Efimov Trimer Binding Energy in a Three-Component Mixture of 6Li. *Phys. Rev. Lett.*, 106(14):143201, apr 2011.

[145] P Drude. Zur Elektronentheorie der Metalle. *Annalen der Physik*, 306(3):566–613, 1900.

[146] L N Cooper. Bound electron pairs in a degenerate Fermi gas. *Phys. Rev.*, 104(4):1189–1190, 1956.

[147] J Bardeen, L N Cooper, and J R Schrieffer. Theory of superconductivity. *Phys. Rev.*, 108(5):1175–1204, 1957.

[148] V.N. Popov. Theory of a Bose gas produced by bound states of Fermi particles. *Eksp. Teor. Fiz.*, 50, 1966.

[149] A.J. Leggett. Cooper pairing in spin-polarized Fermi systems. *J. Phys. Colloques*, 41(C7):19–26, 1980.

[150] D.M. Eagles. Possible Pairing without Superconductivity at Low Carrier Concentrations in Bulk and Thin-Film Superconducting Semiconductors. *Phys. Rev.*, 186(2):456–463, oct 1969.

[151] A J Leggett. Diatomic molecules and cooper pairs BT - Modern Trends in the Theory of Condensed Matter. pages 13–27, Berlin, Heidelberg, 1980. Springer Berlin Heidelberg.

[152] V Galitskii. The energy spectrum of a non-ideal fermi gas. *Sov. Phys. JETP*, 7:104, 1958.

[153] T D Lee and C N Yang. Many-Body Problem in Quantum Mechanics and Quantum Statistical Mechanics. *Phys. Rev.*, 105(3):1119–1120, 1957.

[154] R B Diener, R Sensarma, and M Randeria. Quantum fluctuations in the superfluid state of the BCS-BEC crossover. *Phys. Rev. A*, 77(2):23626, 2008.

[155] I V Brodsky, M Y Kagan, A V Klaptsov, R Combescot, and X Leyronas. Exact diagrammatic approach for dimer-dimer scattering and bound states of three and four resonantly interacting particles. *Phys. Rev. A*, 73(3):32724, 2006.

[156] X Leyronas and R Combescot. Superfluid equation of state of dilute composite bosons. *Phys. Rev. Lett.*, 99(17):170402, 2007.

[157] Mark J H Ku, Ariel T Sommer, Lawrence W Cheuk, and Martin W Zwierlein. Revealing the superfluid lambda transition in the universal thermodynamics of a unitary Fermi gas. *Science*, 335(6068):563–567, 2012.

[158] Sascha Hoinka, Marcus Lingham, Kristian Fenech, Hui Hu, Chris J Vale, Joaquin E Drut, and Stefano Gandolfi. Precise Determination of the Structure Factor and Contact in a Unitary Fermi Gas. *Phys. Rev. Lett.*, 110(5):55305, jan 2013.

[159] W Zwerger, editor. *The BCS-BEC Crossover and the Unitary Fermi Gas*, volume 836 of *Lecture Notes in Physics*. Springer, Berlin, 2012.

[160] T Holstein. Studies of polaron motion: Part II. The "small" polaron. *Annals of Physics*, 8(3):343–389, 1959.

[161] Alexandre S Alexandrov. *Polarons in advanced materials*, volume 103. Springer Science & Business Media, 2008.

[162] Alexandre S Alexandrov and Jozef T Devreese. *Advances in Polaron Physics*, volume 159. 2010.

[163] Gerald D. Mahan. *Many-Particle Physics*. 2000.

[164] Jozef T. Devreese and Alexandre S. Alexandrov. Fröhlich polaron and bipolaron: Recent developments. *Reports on Progress in Physics*, 72(6), 2009.

[165] A S Mishchenko, N Nagaosa, K M Shen, Z.-X. Shen, X J Zhou, and T P Devereaux. Polaronic metal in lightly doped high-T c cuprates. *{EPL} (Europhysics Letters)*, 95(5):57007, aug 2011.

[166] VB Shikin and YP Monarkha. Free electrons on the surface of liquid helium in the presence of external fields. *Soviet Journal of Experimental and . . .*, 38(2):373–377, 1974.

[167] M E Gershenson, V Podzorov, and A F Morpurgo. Colloquium: Electronic transport in single-crystal organic transistors. *Rev. Mod. Phys.*, 78(3):973–989, sep 2006.

[168] Frank Ortmann, Friedhelm Bechstedt, and Karsten Hannewald. Charge transport in organic crystals: Theory and modelling. *physica status solidi (b)*, 248(3):511–525, mar 2011.

[169] E.L. Nagaev. Ground State and Anomalous Magnetic Moment of Conduction Electrons in an Antiferromagnetic Semiconductor. *ZhETF Pisma Redaktsiiu*, 6:484, jul 1967.

[170] Elbio Dagotto. Correlated electrons in high-temperature superconductors. *Rev. Mod. Phys.*, 66(3):763–840, jul 1994.

[171] Gregory A Fiete, Gergely Zarand, and Kedar Damle. Effective Hamiltonian for Ga_(1-x)Mn_xAs in the Dilute Limit. *Phys. Lett.*, 91(9):97202, aug 2003.

[172] A Kaminski and S Das Sarma. Polaron Percolation in Diluted Magnetic Semiconductors. *Phys. Rev. Lett.*, 88(24):247202, may 2002.

[173] Peter W Higgs. Broken symmetries, massless particles and gauge fields. *Phys. Lett.*, 12:132–133, 1964.

[174] Peter W Higgs. Broken Symmetries and the Masses of Gauge Bosons. *Phys. Rev. Lett.*, 13(16):508–509, oct 1964.

[175] Thierry Giamarchi. *Quantum physics in one dimension*, volume 121. Clarendon press, 2003.

[176] A O Gogolin, A A Nersesyan, and A M Tsvelik. *Bosonization and Strongly Correlated Systems*. Cambridge University Press, 2004.

[177] P W Anderson. A poor man's derivation of scaling laws for the Kondo problem. *Journal of Physics C: Solid State Physics*, 3(12):2436–2441, dec 1970.

[178] Alexander Cyril Hewson. *The Kondo Problem to Heavy Fermions*. Cambridge University Press, Cambridge, 1993.

[179] P. B. Wiegmann and A. M. Tsvelik. Solution of the Kondo problem for an orbital singlet, 1996.

[180] N Andrei. Diagonalization of the Kondo Hamiltonian. *Phys. Rev. Lett.*, 45(5):379–382, aug 1980.

[181] Fabian Grusdt and Michael Fleischhauer. Tunable Polarons of Slow-Light Polaritons in a Two-Dimensional Bose-Einstein Condensate. *Phys. Rev. Lett.*, 116(5):53602, feb 2016.

[182] Nils B Jorgensen, Lars Wacker, Kristoffer T Skalmstang, Meera M Parish, Jesper Levinsen, Rasmus S Christensen, Georg M Bruun, and Jan J Arlt. Observation of Attractive and Repulsive Polarons in a Bose-Einstein Condensate. *Phys. Rev. Lett.*, 117(5):55302, jul 2016.

[183] Nicolas Spethmann, Farina Kindermann, Shincy John, Claudia Weber, Dieter Meschede, and Artur Widera. Dynamics of Single Neutral Impurity Atoms Immersed in an Ultracold Gas. *Phys. Rev. Lett.*, 109(23):235301, dec 2012.

[184] Takeshi Fukuhara, Adrian Kantian, Manuel Endres, Marc Cheneau, Peter Schauß, Sebastian Hild, David Bellem, Ulrich Schollwöck, Thierry Giamarchi, Christian Gross, Immanuel Bloch, and Stefan Kuhr. Quantum dynamics of a mobile spin impurity. *Nature Physics*, 9(4):235–241, 2013.

[185] R Scelle, T Rentrop, A Trautmann, T Schuster, and M K Oberthaler. Motional Coherence of Fermions Immersed in a Bose Gas. *Phys. Rev. Lett.*, 111(7):70401, aug 2013.

[186] Michael Hohmann, Farina Kindermann, Benjamin Gänger, Tobias Lausch, Daniel Mayer, Felix Schmidt, and Artur Widera. Neutral impurities in a Bose-Einstein condensate for simulation of the Fröhlich-polaron. *EPJ Quantum Technology*, 2(1):23, 2015.

[187] Zoe Z Yan, Yiqi Ni, Carsten Robens, and Martin W Zwierlein. Bose polarons near quantum criticality. *Science*, 368(6487):190 LP – 194, apr 2020.

[188] M W Zwierlein, C H Schunck, A Schirotzek, and W Ketterle. Direct observation of the superfluid phase transition in ultracold Fermi gases. *Nature*, 442(7098):54–58, 2006.

[189] G B Partridge, W Li, R I Kamar, Y Liao, and R G Hulet. Pairing and phase separation in a polarized Fermi gas. *Science*, 311(5760):503–505, 2006.

[190] F Chevy. Density profile of a trapped strongly interacting Fermi gas with unbalanced spin populations. *Phys. Rev. Lett.*, 96(13):130401, 2006.

[191] F Chevy. Universal phase diagram of a strongly interacting Fermi gas with unbalanced spin populations. *Phys. Rev. A*, 74(6):63628, 2006.

[192] P Pieri and G C Strinati. Trapped Fermions with Density Imbalance in the Bose-Einstein Condensate Limit. *Phys. Rev. Lett.*, 96(15):150404, apr 2006.

[193] W. Yi and L. M. Duan. Trapped fermions across a Feshbach resonance with population imbalance. *Physical Review A - Atomic, Molecular, and Optical Physics*, 73(3):031604, mar 2006.

[194] T N De Silva and E J Mueller. Profiles of near-resonant population-imbalanced trapped Fermi gases. *Phys. Rev. A*, 73(5), 2006.

[195] Masudul Haque and H. T.C. Stoof. Pairing of a trapped resonantly interacting fermion mixture with unequal spin populations. *Physical Review A - Atomic, Molecular, and Optical Physics*, 74(1):011602, jul 2006.

[196] H Hu, X.-J. Liu, and P D Drummond. Phase Diagram of a Strongly Interacting Polarized Fermi Gas in One Dimension. *Phys. Rev. Lett.*, 98(7):70403, feb 2007.

[197] Christoph Kohstall, Mattheo Zaccanti, Matthias Jag, Andreas Trenkwalder, Pietro Massignan, Georg M Bruun, Florian Schreck, and Rudolf Grimm. Metastability and coherence of repulsive polarons in a strongly interacting Fermi mixture. *Nature*, 485(7400):615–618, 2012.

[198] A Schirotzek, C-H Wu, A Sommer, and M W Zwierlein. Observation of Fermi Polarons in a Tunable Fermi Liquid of Ultracold Atoms. *Phys. Rev. Lett.*, 102(23):230402, 2009.

[199] Marco Koschorreck, Daniel Pertot, Enrico Vogt, Bernd Frohlich, Michael Feld, and Michael Köhl. Attractive and repulsive Fermi polarons in two dimensions. *Nature*, 485(7400):619–622, may 2012.

[200] F Grusdt and E Demler. New theoretical approaches to Bose polarons. *arXiv: Quantum Gases*, 2015.

[201] J Tempere, W Casteels, M K Oberthaler, S Knoop, E Timmermans, and J T Devreese. Feynman path-integral treatment of the BEC-impurity polaron. *Phys. Rev. B*, 80(18):184504, nov 2009.

[202] F M Cucchietti and E Timmermans. Strong-Coupling Polarons in Dilute Gas Bose-Einstein Condensates. *Phys. Rev. Lett.*, 96(21):210401, jun 2006.

[203] T D Lee, F E Low, and D Pines. The Motion of Slow Electrons in a Polar Crystal. *Phys. Rev.*, 90(2):297–302, apr 1953.

[204] Rasmus Sogaard Christensen, Jesper Levinsen, and Georg M Bruun. Quasiparticle Properties of a Mobile Impurity in a Bose-Einstein Condensate. *Phys. Rev. Lett.*, 115(16):160401, oct 2015.

[205] Jesper Levinsen, Meera M Parish, and Georg M Bruun. Impurity in a Bose-Einstein condensate and the Efimov effect. *Physical Review Letters*, 115(12):125302, 2015.

[206] Nils B Jørgensen, Lars Wacker, Kristoffer T Skalmstang, Meera M Parish, Jesper Levinsen, Rasmus S Christensen, Georg M Bruun, and Jan J Arlt. Observation of attractive and repulsive polarons in a Bose-Einstein condensate. *Physical review letters*, 117(5):55302, 2016.

[207] Weiran Li and S. Das Sarma. Variational study of polarons in Bose-Einstein condensates. *Physical Review A - Atomic, Molecular, and Optical Physics*, 90(1):013618, jul 2014.

[208] Steffen Patrick Rath and Richard Schmidt. Field-theoretical study of the Bose polaron. *Physical Review A - Atomic, Molecular, and Optical Physics*, 88(5):053632, nov 2013.

[209] Shuhei M Yoshida, Shimpei Endo, Jesper Levinsen, and Meera M Parish. Universality of an Impurity in a Bose-Einstein Condensate. *Phys. Rev. X*, 8(1):11024, feb 2018.

[210] Ming-Guang Hu, Michael J de Graaff, Dhruv Kedar, John P Corson, Eric A Cornell, and Deborah S Jin. Bose polarons in the strongly interacting regime. *Physical review letters*, 117(5):55301, 2016.

[211] B S Chandrasekhar. A note on the maximum critical field of high-field superconductors. *App. Phys. Lett.*, 1(1):7–8, 1962.

[212] A M Clogston. Upper limit for the critical field in hard superconductors. *Phys. Rev. Lett.*, 9(6):266–267, 1962.

[213] M W Zwierlein, A Schirotzek, C H Schunck, and W Ketterle. Fermionic superfluidity with imbalanced spin populations. *Science*, 311(5760):492–496, 2006.

[214] Pietro Massignan, Matteo Zaccanti, and Georg M Bruun. Polarons, dressed molecules and itinerant ferromagnetism in ultracold Fermi gases. *Reports on Progress in Physics*, 77(3):34401, 2014.

[215] C Lobo, A Recati, S Giorgini, and S Stringari. Normal state of a polarized Fermi gas at unitarity. *Phys. Rev. Lett.*, 97(20):200403, 2006.

[216] Nikolay Prokof'ev and Boris Svistunov. Fermi-polaron problem: Diagrammatic Monte Carlo method for divergent sign-alternating series. *Phys. Rev. B*, 77(2):20408, jan 2008.

[217] R Combescot and S Giraud. Normal state of highly polarized Fermi gases: full many-body treatment. *Phys. Rev. Lett.*, 101(5):50404, 2008.

[218] Y Shin, M W Zwierlein, C H Schunck, A Schirotzek, and W Ketterle. Observation of phase separation in a strongly interacting imbalanced Fermi gas. *Phys. Rev. Lett.*, 97(3):30401, 2006.

[219] Y I Shin. Determination of the equation of state of a polarized Fermi gas at unitarity. *Phys. Rev. A*, 77(4):41603, 2008.

[220] S Nascimbène, N Navon, K Jiang, L Tarruell, M Teichmann, J McKeever, F Chevy, and C Salomon. Collective Oscillations of an Imbalanced Fermi Gas: Axial Compression Modes and Polaron Effective Mass. *Phys. Rev. Lett.*, 103(17):170402, 2009.

[221] R Combescot, A Recati, C Lobo, and F Chevy. Normal state of highly polarized Fermi gases: simple many-body approaches. *Phys. Rev. Lett.*, 98(18):180402, 2007.

[222] S Pilati and S Giorgini. Phase separation in a polarized Fermi gas at zero temperature. *Phys. Rev. Lett.*, 100(3):30401, 2008.

[223] C Mora and F Chevy. Ground state of a tightly bound composite dimer immersed in a Fermi Sea. *Phys. Rev. A*, 80(3):33607–33617, 2009.

[224] R Combescot, S Giraud, and X Leyronas. Analytical theory of the dressed bound state in highly polarized Fermi gases. *Europhys. Lett.*, 88(6):6007, 2009.

[225] Richard Roy, Alaina Green, Ryan Bowler, and Subhadeep Gupta. Two-element mixture of Bose and Fermi superfluids. *Physical review letters*, 118(5):55301, 2017.

[226] Xing-Can Yao, Hao-Ze Chen, Yu-Ping Wu, Xiang-Pei Liu, Xiao-Qiong Wang, Xiao Jiang, Youjin Deng, Yu-Ao Chen, and Jian-Wei Pan. Observation of Coupled Vortex Lattices in a Mass-Imbalance Bose and Fermi Superfluid Mixture. *Phys. Rev. Lett.*, 117(14):145301, sep 2016.

[227] S Jin. *A New Generation Experiment for the Study of Strongly Interacting Fermi Gases*. PhD thesis, 2019.

[228] G. Breit and I. I. Rabi. Measurement of nuclear spin. *Physical Review*, 38(11):2082–2083, 1931.

[229] G Zürn, T Lompe, A N Wenz, S Jochim, P S Julienne, and J M Hutson. Precise Characterization of 6Li Feshbach Resonances Using Trap-Sideband-Resolved RF Spectroscopy of Weakly Bound Molecules. *Phys. Rev. Lett.*, 110(13):135301, 2013.

[230] S. Jochim, M. Bartenstein, G. Hendl, J. Hecker Denschlag, R. Grimm, A. Mosk, and M. Weidemüller. Magnetic Field Control of Elastic Scattering in a Cold Gas of Fermionic Lithium Atoms. *Physical Review Letters*, 89(27):1–4, 2002.

[231] Ulrich Eismann, Andrea Bergschneider, F Sievers, N Kretzschmar, C Salomon, and F Chevy. 2.1-watts intracavity-frequency-doubled all-solid-state light source at 671 nm for laser cooling of lithium. *Optics express*, 21(7):9091–9102, 2013.

[232] D J McCarron, S A King, and S L Cornish. Modulation transfer spectroscopy in atomic rubidium. *Measurement Science and Technology*, 19(10):105601, aug 2008.

[233] G Ritt, G Cennini, C Geckeler, and M Weitz. Laser frequency offset locking using a side of filter technique. *Applied Physics B*, 79(3):363–365, 2004.

[234] K. Dai. Laser frequency offset lock for Raman sideband cooling and site-resolved imaging of Li6 atoms in a pinning lattice. Technical report, 2018.

[235] Leticia Tarruell. *Superfluidité dans un gaz de fermions ultrafroids*. PhD thesis, 2009.

[236] William D. Phillips and Harold Metcalf. Laser deceleration of an atomic beam. *Physical Review Letters*, 48(9):596–599, mar 1982.

[237] Marion Delehaye. *Mixtures of superfluids*. PhD thesis, 2016.

[238] Thomas Salez. *Towards quantum degenerate atomic Fermi mixtures*. PhD thesis, 2011.

[239] Thad Walker, David Sesko, and Carl Wieman. Collective behavior of optically trapped neutral atoms. *Physical Review Letters*, 64(4):408–411, 1990.

[240] Wolfgang Ketterle, Kendall B. Davis, Michael A. Joffe, Alex Martin, and David E. Pritchard. High densities of cold atoms in a dark spontaneous-force optical trap. *Physical Review Letters*, 70(15):2253–2256, 1993.

[241] Claude Cohen-Tannoudji and Jacques Dupont-Roc. Experimental study of Zeeman light shifts in weak magnetic fields. *Physical Review A*, 5(2):968–984, 1972.

[242] P. M. Duarte, R. A. Hart, J. M. Hitchcock, T. A. Corcovilos, T. L. Yang, A. Reed, and R. G. Hulet. All-optical production of a lithium quantum gas using narrow-line laser cooling. *Physical Review A - Atomic, Molecular, and Optical Physics*, 84(6):61406, dec 2011.

[243] P D Lett, W D Phillips, S L Rolston, C E Tanner, R N Watts, and C I Westbrook. Optical molasses. *J. Opt. Soc. Am. B*, 6(11):2084–2107, nov 1989.

[244] P J Ungar, D S Weiss, E Riis, and Steven Chu. Optical molasses and multilevel atoms: theory. *J. Opt. Soc. Am. B*, 6(11):2058–2071, nov 1989.

[245] G Grynberg and J Y Courtois. Proposal for a magneto-optical lattice for trapping atoms in nearly-dark states. *Euro. Phys. Lett.*, 27:41, 1994.

[246] M. Weidemüller, T. Esslinger, M. A. Ol'shanii, A. Hemmerich, and T. W. Hänsch. A novel scheme for efficient cooling below the photon recoil limit. *Epl*, 27(2):109–114, 1994.

[247] M S Shahriar, P R Hemmer, M G Prentiss, P Marte, J Mervis, D P Katz, N P Bigelow, and T Cai. Continuous polarization-gradient precooling-assisted velocity-selective coherent population trapping. *Phys. Rev. A*, 48(6):R4035—-R4038, dec 1993.

[248] J. Dalibard. Une brève histoire des atomes froids, Lecture Notes., 2014.

[249] A Hemmerich, M Weidemüller, T Esslinger, C Zimmermann, and T Hänsch. Trapping Atoms in a Dark Optical Lattice. *Phys. Rev. Lett.*, 75(1):37–40, jul 1995.

[250] D Boiron, C Triché, D R Meacher, P Verkerk, and G Grynberg. Three-dimensional cooling of cesium atoms in four-beam gray optical molasses. *Phys. Rev. A*, 52(5):R3425—-R3428, nov 1995.

[251] D Rio Fernandes, F Sievers, N Kretzschmar, S Wu, C Salomon, and F Chevy. Sub-Doppler laser cooling of fermionic 40K atoms in three-dimensional gray optical molasses. *EPL*, 100(6):63001, 2012.

[252] Andrew T Grier, Igor Ferrier-Barbut, Benno S Rem, Marion Delehaye, Lev Khaykovich, Frédéric Chevy, and Christophe Salomon. Λ-enhanced sub-Doppler cooling of lithium atoms in D 1 gray molasses. *Physical Review A*, 87(6):63411, 2013.

[253] T Bergeman, Gidon Erez, and Harold J Metcalf. Magnetostatic trapping fields for neutral atoms. *Phys. Rev. A*, 35(4):1535–1546, feb 1987.

[254] A Ashkin. Acceleration and Trapping of Particles by Radiation Pressure. *Phys. Rev. Lett.*, 24(4):156–159, jan 1970.

[255] T L Gustavson, A P Chikkatur, A E Leanhardt, A Görlitz, S Gupta, D E Pritchard, and W Ketterle. Transport of Bose-Einstein Condensates with Optical Tweezers. *Phys. Rev. Lett.*, 88(2):20401, dec 2001.

[256] D Boiron, A Michaud, J M Fournier, L Simard, M Sprenger, G Grynberg, and C Salomon. Cold and dense cesium clouds in far-detuned dipole traps. *Phys. Rev. A*, 57(6):R4106—-R4109, jun 1998.

[257] Rudolf Grimm, Matthias Weidemüller, and Yurii B. Ovchinnikov. Optical Dipole Traps for Neutral Atoms. *Advances in Atomic, Molecular and Optical Physics*, 42(C):95–170, 2000.

[258] Franz Sievers, Norman Kretzschmar, Diogo Rio Fernandes, Daniel Suchet, Michael Rabinovic, Saijun Wu, Colin V Parker, Lev Khaykovich, Christophe Salomon, and Frédéric Chevy. Simultaneous sub-doppler laser cooling of fermionic {L}i 6 and {K} 40 on the D1 line: Theory and experiment. *Phys. Rev. A*, 91(2):23426, 2015.

[259] T A Savard, K M O'Hara, and J E Thomas. Laser-noise-induced heating in far-off resonance optical traps. *Phys. Rev. A*, 56(2):R1095—-R1098, aug 1997.

[260] S Stringari. Collective Excitations of a Trapped Bose-Condensed Gas. *Phys. Rev. Lett.*, 77(12):2360–2363, sep 1996.

[261] F Chevy, V Bretin, P Rosenbusch, K W Madison, and J Dalibard. Transverse Breathing Mode of an Elongated Bose-Einstein Condensate. *Phys. Rev. Lett.*, 88(25):250402, jun 2002.

[262] A Couvert, T Kawalec, G Reinaudi, and D Guéry-Odelin. Optimal transport of ultracold atoms in the non-adiabatic regime. *{EPL} (Europhysics Letters)*, 83(1):13001, jun 2008.

[263] Wolfgang Ketterle and N. J. Van Druten. *Evaporative Cooling of Trapped Atoms*. 1996.

[264] Harald F Hess. Evaporative cooling of magnetically trapped and compressed spin-polarized hydrogen. *Phys. Rev. B*, 34(5):3476–3479, sep 1986.

[265] M E Gehm, S L Hemmer, K M O'Hara, and J E Thomas. Unitarity-limited elastic collision rate in a harmonically trapped Fermi gas. *Phys. Rev. A*, 68(1):11603, jul 2003.

[266] L. D. Landau. A theory of energy transfer II. *Phys. Z. USSR 2, 46*, 1932.

[267] C. Zener Fowler and R. H. Non-adiabatic crossing of energy levels. *Proceedings of the Royal Society of London. Series A, Containing Papers of a Mathematical and Physical Character 137 (1932), 833, 696.*

[268] S Jochim, M Bartenstein, A Altmeyer, G Hendl, C Chin, J. H. Denschlag, and R Grimm. Pure gas of optically trapped molecules created from fermionic atoms. *Phys. Rev. Lett.*, 91(24):240402, 2003.

[269] T Bourdel, L Khaykovich, J Cubizolles, J Zhang, F Chevy, M Teichmann, L Tarruell, S.J.J.M.F. Kokkelmans, and C Salomon. Experimental Study of the BEC-BCS Crossover Region in Lithium 6. *Phys. Rev. Lett.*, 93(5):50401, 2004.

[270] T L Ho. Universal thermodynamics of degenerate quantum gases in the unitarity limit. *Phys. Rev. Lett.*, 92(9):90402, 2004.

[271] S Nascimbene, N Navon, K Jiang, F Chevy, and C Salomon. Exploring the Thermodynamics of a Universal Fermi Gas. *Nature*, 463:1057–1060, 2010.

[272] M Horikoshi, S Nakajima, M Ueda, and T Mukaiyama. Measurement of universal thermodynamic functions for a unitary Fermi gas. *Science*, 327(5964):442, 2010.

[273] H Heiselberg. Fermi systems with long scattering lengths. *Phys. Rev. A*, 63(4):43606, 2001.

[274] T Ho and Q Zhou. Obtaining phase diagram and thermodynamic quantities of bulk systems from the densities of trapped gases. *Nature Physics*, 6:131, 2010.

[275] A Bulgac, J E Drut, and P Magierski. Spin 1/2 fermions in the unitary regime: A superfluid of a new type. *Phys. Rev. Lett.*, 96(9):90404, 2006.

[276] O Goulko and M Wingate. Thermodynamics of balanced and slightly spin-imbalanced Fermi gases at unitarity. *Phys. Rev. A*, 82(5):53621, 2010.

[277] X J Liu, H Hu, and P D Drummond. Virial expansion for a strongly correlated Fermi gas. *Phys. Rev. Lett.*, 102(16):160401, 2009.

[278] Erich Beth and George E Uhlenbeck. The quantum theory of the non-ideal gas. II. Behaviour at low temperatures. *Physica*, 4(10):915–924, 1937.

[279] D Guéry-Odelin and S Stringari. Scissors Mode and Superfluidity of a Trapped Bose-Einstein Condensed Gas. *Phys. Rev. Lett.*, 83(22):4452–4455, nov 1999.

[280] Bason Clancy, Le Luo, and John E Thomas. Observation of Nearly Perfect Irrotational Flow in Normal and Superfluid Strongly Interacting Fermi Gases. *Phys. Rev. Lett.*, 99(14):140401, oct 2007.

[281] M J Wright, S Riedl, A Altmeyer, C Kohstall, E R Sánchez Guajardo, J Hecker Denschlag, and R Grimm. Finite-Temperature Collective Dynamics of a Fermi Gas in the BEC-BCS Crossover. *Phys. Rev. Lett.*, 99(15):150403, oct 2007.

[282] M Bartenstein, A Altmeyer, S Riedl, S Jochim, C Chin, J Hecker Denschlag, and R Grimm. Crossover from a Molecular Bose-Einstein Condensate to a Degenerate Fermi Gas. *Phys. Rev. Lett.*, 92(12):120401, mar 2004.

[283] M.W. Zwierlein, C.A. Stan, C.H. Schunck, S.M.F. Raupach, A.J. Kerman, and W Ketterle. Condensation of pairs of fermionic atoms near a Feshbach resonance. *Phys. Rev. Lett.*, 92:120403, 2004.

[284] Chevy F. and C Mora. Ultra-cold Polarized Fermi Gases. *Rep. Prog. Phys.*, 73:112401, 2010.

[285] B Peaudecerf, M Andia, M Brown, E Haller, and S Kuhr. Microwave preparation of two-dimensional fermionic spin mixtures. *New Journal of Physics*, 21(1):13020, jan 2019.

[286] Daniel Greif, Maxwell F Parsons, Anton Mazurenko, Christie S Chiu, Sebastian Blatt, Florian Huber, Geoffrey Ji, and Markus Greiner. Site-resolved imaging of a fermionic Mott insulator. *Science*, 351(6276):953–957, 2016.

[287] T T Wu. Ground state of a Bose system of hard spheres. *Phys. Rev.*, 115(6):1390–1404, 1959.

[288] E D Kuhnle, H Hu, X.-J. Liu, P Dyke, M Mark, P D Drummond, P Hannaford, and C.J. Vale. Universal Behavior of Pair Correlations in a Strongly Interacting Fermi Gas. *Phys. Rev. Lett.*, 105(7):70402, aug 2010.

[289] V Borisovich Bobrov. The relation between the static structure factor and the density-density response function in the long-wave limit. *Journal of Physics: Condensed Matter*, 2(13):3115–3118, apr 1990.

[290] S Tan. Large momentum part of a strongly correlated Fermi gas. *Ann. Phys.*, 323(12):2971–2986, 2008.

[291] Shina Tan. Energetics of a strongly correlated Fermi gas. *Annals of Physics*, 323(12):2952–2970, 2008.

[292] Eric Braaten and Agustin Nieto. Quantum corrections to the energy density of a homogeneous Bose gas. *The European Physical Journal B-Condensed Matter and Complex Systems*, 11(1):143–159, 1999.

[293] Shina Tan. Three-boson problem at low energy and implications for dilute Bose-Einstein condensates. *Phys. Rev. A*, 78(1):13636, jul 2008.

[294] Hans-Werner Hammer, Andreas Nogga, and Achim Schwenk. Three-body forces: From cold atoms to nuclei. *Rev. Mod. Phys.*, 85:197, 2013.

[295] Alexander L Fetter and John D Walecka. *Quantum Theory of Many-Particle Systems*. Dover Publications, jun 2003.

[296] Murray Gell-Mann and Francis Low. Bound States in Quantum Field Theory. *Phys. Rev.*, 84(2):350–354, oct 1951.

[297] R Rossi, T Ohgoe, E Kozik, N Prokof'ev, B Svistunov, K Van Houcke, and F Werner. Contact and Momentum Distribution of the Unitary Fermi Gas. *Phys. Rev. Lett.*, 121(13):130406, sep 2018.

[298] K Van Houcke, F Werner, T Ohgoe, N V Prokof'ev, and B V Svistunov. Diagrammatic Monte Carlo algorithm for the resonant Fermi gas. *Phys. Rev. B*, 99(3):35140, jan 2019.

[299] Mikhail Stephanov. QCD Phase Diagram and the Critical Point. *Progress of Theoretical Physics Supplement*, 153:139–156, 2004.

[300] T B Ottenstein, T Lompe, M Kohnen, A N Wenz, and S Jochim. Collisional Stability of a Three-Component Degenerate Fermi Gas. *Phys. Rev. Lett.*, 101(20):203202, nov 2008.

[301] N V Prokof'ev and B V Svistunov. Bold diagrammatic Monte Carlo: A generic sign-problem tolerant technique for polaron models and possibly interacting many-body problems. *Phys. Rev. B*, 77:125101, 2008.

[302] C.J.M. Mathy, M.M. Parish, and D.A. Huse. Polarons, molecules and trimers in highly-polarized Fermi gases. *arXiv:1002.0101*, 2010.

[303] M Jona-Lasinio, L Pricoupenko, and Y Castin. Three fully polarized fermions close to a p-wave Feshbach resonance. *Phys. Rev. A*, 77(4):43611, apr 2008.

[304] M Holland, S J J M F Kokkelmans, M L Chiofalo, and R Walser. Resonance Superfluidity in a Quantum Degenerate Fermi Gas. *Phys. Rev. Lett.*, 87(12):120406, aug 2001.

[305] Zhihao Lan and Carlos Lobo. A Single Impurity in an Ideal Atomic Fermi Gas: Current Understanding and Some Open Problems. *Journal of the Indian Institute of Science*, 94(2):179, 2014.

[306] D M Edwards. A smooth polaron–molecule crossover in a Fermi system. *Journal of Physics: Condensed Matter*, 25(42):425602, 2013.

[307] Gal Ness, Constantine Shkedrov, Yanay Florshaim, and Yoav Sagi. Observation of a smooth polaron-molecule transition in a degenerate Fermi gas. *arXiv preprint arXiv:2001.10450*, 2020.

[308] Xiaoling Cui. Fermi polaron revisited: polaron-molecule transition and coexistence. *arXiv preprint arXiv:2003.11710*, 2020.

[309] Kun Chen, Yuan Huang, Youjin Deng, and Boris Svistunov. Halon: A quasiparticle featuring critical charge fractionalization. *Phys. Rev. B*, 98:214516, Dec 2018.

[310] Christian Trefzger and Yvan Castin. Polaron residue and spatial structure in a fermi gas. *EPL (Europhysics Letters)*, 101(3):30006, feb 2013.

[311] Manuel Endres, Hannes Bernien, Alexander Keesling, Harry Levine, Eric R. Anschuetz, Alexandre Krajenbrink, Crystal Senko, Vladan Vuletic, Markus Greiner, and Mikhail D. Lukin. Atom-by-atom assembly of defect-free one-dimensional cold atom arrays. *Science*, 354(6315):1024–1027, 2016.

Acknowledgement

Many people have contributed to this work and I would like to thank them all. A non-exhaustive list would be:

- Christophe Salomon for having accepted me in his team, for being always there when needed, for the various interesting discussions regarding the physics of Fermi gases and for the father he was during the hard times.
- Frédéric Chevy for making all of this possible and for teaching me a whole lot of things, scientifically as well as personally.
- Xavier Leyronas for the countless discussions, long calculations and pedagogic insight which for sure helped me a lot.
- Tarik Yefsah for his experimental supervision.
- Julian Struck for many discussions which helped me many times in putting my work in perspective and for his outstanding physical insight and patience whenever asked.
- My colleagues in the experimental lab: Shuwei Jin, Kunlun Dai, Joris Verstraeten, Darby Bates, Yann Kiefer. Working with you all has been a great experience, and it has certainly paid off.
- Bruno Peaudecerf, for being able to teach me a lot about dipole traps, thermometry and single-atom microscopes.
- Felix Werner for the great prospects our discussions have opened to me and for helpful advice on all fronts.
- All members of the mechanical and electronic workshop at ENS for their extremely professional and hard work.
- I also thank all members of the administrative staff at LKB and ENS for their efficiency.
- Toufik Elatmani and Lionel Perennes for discussions regarding the many electronic devices I needed to build.
- Sébastian Laurent, Mathieu Pierce, Cedric Enesa, Thomas Riemann, Gentle Dash, Marin Tharrault and Mohamed Baghdad for the friendly discussions and humor. Going through long working hours has been much easier with you all around at some time or another.

Finally I would like to thank my girlfriend, my family members and friends for standing with me and supporting me during all of the past years.

RÉSUMÉ

Une partie de la thèse porte sur la description d'une expérience de nouvelle génération construite au sein de l'équipe des gaz de fermions ultra-froids au laboratoire Kastler Brossel.
Les étapes expérimentales qui mènent à la réalisation et la caractérisation d'un superfluide fermionique sont décrite ainsi que les principes physiques derrière ces méthodes qui sont bien établies dans le domaine.
La deuxième partie porte sur deux études théoriques concernant la physique d'une impureté. Lorsqu'une impureté s'introduit dans un milieu en interaction, son énergie présente des divergences logarithmiques dans son développement perturbatif. Nous utilisons la méthode des fonctions de Green pour comprendre les processus fondamentaux à l'origine de ces divergences.
Pour le deuxième projet, on étudie le diagramme de phase d'une impureté immergée dans une double mer de Fermi sans interactions. Nous utilisons une méthode variationelle pour montrer qu'il existe une transition de phase du premier degré entre la limite de faible interaction impureté-fermion où une quasi-particule appelée le polaron est présente, et la limite des interaction plus forte où existe un état lié de trois particules, appelé un trimer, proche de la surface de Fermi.

MOTS CLÉS

Gas de Fermi, Superfluide, Impureté, Polaron, Efimov, Trimer, Atomes froids.

ABSTRACT

Part of the thesis concerns the description of a new generation experiment built within the ultra-cold fermion gas team at the Kastler Brossel laboratory.
The experimental steps that lead to the realization and characterization of a fermionic superfluid are described along with the physical principles behind these methods which are well established in the field.
The second part deals with two theoretical studies concerning the physics of an impurity. When an impurity enters an interacting medium, its energy exhibits logarithmic divergences in its perturbative development. We use the method of Green's functions to understand the fundamental processes at the origin of these divergences.
For the second project, we study the phase diagram of an impurity submerged in a double Fermi sea without interactions. We use a variational method to show that there is a first degree phase transition between the limit of weak impurity-fermion interaction where a quasi-particle called the polaron is present, and the limit of stronger interaction where there is a bound state of three particles, called a trimer, close to the Fermi surface.

KEYWORDS

Fermi gases, Superfluid, Impurity, Polaron, Efimov, Trimer, Cold atoms.